ENHANCING MAGNETIC PROPERTIES OF MOLECULAR MAGNETIC MATERIALS: THE ROLE OF SINGLE-ION ANISOTROPY

A Dissertation

by

MOHAMED RASHAD MOHAMED SABER

Submitted to the Office of Graduate Studies of
Texas A&M University
in partial fulfillment of the requirements for the degree of

DOCTOR OF PHILOSOPHY

Chair of Committee,	Kim R. Dunbar
Committee Members,	Francois P. Gabbai
	Hong-Cai Zhou
	Donald G. Naugle
Head of Department,	David H. Russell

August 2013

Major Subject: Chemistry

ABSTRACT

Considerable efforts are being devoted to designing enhanced molecular magnetic materials, in particular single molecule magnets (SMMs) that can meet the requirements for future technologies such as quantum computing and spintronics. A current trend in the field is enhancing the global anisotropy in metal complexes using single-ion anisotropy. The work in this dissertation is devoted to the synthesis and characterization of new building blocks of the highly anisotropic early transition metal ion V(III) with the aim of incorporating them into heterometallic molecular materials. The results underscore the importance of tuning the local coordination environments of metal ions in order to ensure enhanced single ion anisotropy.

A family of mononuclear axially distorted vanadium (III) compounds, $A[L_3VX_3]$ (**3-9**) (X = F, Cl or Br, $A^+ = Et_4N^+$, nBu_4N^+ or PPN^+ , L_3 = Tp or Tp* (Tp = *tris*(*-1*-pyrazolyl)borohydride), Tp* = *tris*(*3*,*5*-dimethyl-*1*-pyrazolyl)borohydride)), and $[Tp^*V(DMF)_3](PF_6)_2$ were studied. Replacement of the Tp ligand in **3** with the stronger π-donor Tp* results in a near doubling of the magnitude of the axial zero-field splitting parameter D_z (D_z = -16.0 cm^{-1} in **3**, and -30.0 cm^{-1} in **4**) as determined by magnetic measurements. Such findings support the idea that controlling the axial crystal field distortion is an excellent way to enhance single-ion anisotropy. High Field-High Frequency EPR measurements on **4** revealed an even higher D value, -40.0 cm^{-1}. Interestingly, compound **4** exhibits evidence for an out-of-phase ac signal under dc field.

In another effort, a new series of vanadium cyanide building blocks, $PPN[V(acac)_2(CN)_2]\cdot PPNCl$ (**13**) (acac = acetylacetonate), $A[V(L)(CN)_2]$ ($A^+ = Et_4N^+$,

L = N,N'-Ethylenebis(salicylimine) (**14**), A = PPN^+, L = N,N'-Ethylenebis(salicylimine) (**15**), L = N,N'-Phenylenebis(salicylimine) (**16**), and L = N,N'-Ethylenebis(2-methoxysalicylimine) (**17**)) were synthesized. Magnetic studies revealed moderate D_z values (-10.0, 5.89, 3.7, 4.05 and 4.36 cm^{-1} for **13-17** respectively).

The first family of cyanide-bridged lanthanide containing molecules with a trigonal bipyramidal (TBP) geometry, $(Et_4N)_2[(Re(triphos)(CN)_3)_2(Ln(NO_3)_3)_3]$-·$4CH_3CN$ (**19-27** with Ln = La, Ce, Pr, Nd, Sm, Gd, Tb, Dy and Ho) were prepared using the $[(triphos)Re(CN)_3]^-$ building block, results that add valuable information to our database of compounds with a TBP geometry. Magnetic studies revealed diverse magnetic responses including slow relaxation of the magnetization at zero field for **25** and **26** , an indication of SMM behavior.

DEDICATION

To My Family

ACKNOWLEDGEMENTS

First and foremost I would like to thank my advisor Prof. Kim R. Dunbar for her support, advice and guidance throughout this process and for providing the opportunity for me to learn a great deal and to perform the work contained in this dissertation. I would also like to thank my committee members, Prof. Francois P. Gabbai, Prof. Zhou, and Prof. Donald G. Naugle for their guidance and support throughout the course of this research, specially, Dr Gabbai for his support during my work in his laboratories in my first visit to Texas A&M. I am really grateful for the experience and advice I received at this time.

I also want to extend my gratitude to Prof. Winfred Teizer for being on my committee for most of the process and for Prof. Donald Darensbourg for being on my defense committee. Many thanks go to Prof. Wolfgang Wernsdorfer for the micro-SQUID measurements and Prof. Steve Hill and Dr Komalavalli Thirunavukkuarasu for HF-HFEPR measurements which are essential data for the success of my projects which would not have been possible without them.

I can't forget the Dunbar group members, all of them. I am really grateful to their friendship, help and support - day in and day out. Thanks also go to the department faculty and staff for making my time at Texas A&M University a great experience.

I also thank the Egyptian community here at Texas A&M for their wonderful help and support. Despite the very small number, they were really helpful and supportive in a way that made me feel that I was at home. And thanks to all my friends back home

especially those who were able to keep in touch and provide support with words, prayers and feelings.

Finally, thanks to my family, especially my parents, for their love, encouragement and prayers, I wish I were able to make it so you all could have shared this moment with me, and to my wife and daughter for their patience and love, I know how tough it was for them all this time when I was always busy and not available.

NOMENCLATURE

SMM	Single Molecule Magnet
ZFS	Zero-Field Splitting
S	Spin
D_z	Axial zero-field splitting parameter
E	Rhombic zero-field splitting parameter
T_B	Blocking temperature
U	Energy barrier
U_{eff}	Effective energy barrier
λ	Spin-orbit coupling parameter
HDVV	Heisenberg, Dirac, Van Vleck Hamiltonian
emu	Electromagnetic unit
χ	The molar magnetic susceptibility
TIP	temperature-independent paramagnetic
M	Magnetization
H	Magnetic field
Tp	*Tris*(-*1*-pyrazolyl)borohydride)
Tp*	*Tris*(*3*,*5*-dimethyl-*1*-pyrazolyl)borohydride)
PPN	Bis(triphenylphosphoranylidene)ammonium
salen	N, N'-Ethylenebis(salicylimine)
salphen	N,N'-Phenylenebis(salicylimine)

TABLE OF CONTENTS

Page

LIST OF FIGURES

Page

LIST OF SCHEMES

Page

LIST OF TABLES

Page

CHAPTER I

INTRODUCTION

Molecular Magnetism

Molecular magnetism is a fascinating, interdisciplinary field of research that incorporates basic concepts of chemistry, physics, and materials science. The evolution of the field has been described in detail in several reviews and books.[1-15] To date, technologically important conventional magnetic materials are exclusively based on simple robust and cheap inorganic materials including pure magnetic metals such as Fe, Mn, Co, and Nd, metallic alloys such as $SmCo_5$ and $Nd_2Fe_{14}B$, and simple metal oxides.[16-18] Such materials currently form the basis for important technological applications of magnets, but the quest for new materials to overcome the current limitations of the size and functionality of magnetic particles has fueled an interest in molecule-based materials from a "bottom-up" approach.[5] Practical advantages of molecular magnetic materials as a potential alternative to traditional, atomically simple solid-state magnets include lower densities and ease of synthesis and processing due to higher solubilities, lower temperature self-assembly, and mechanical flexibility.[19-21] Also, molecular materials offer systematic approaches for the study of structure-property relationships which leads to a deeper understanding of the factors that affect magnetic interactions which ultimately makes it easier to tune the properties. Furthermore, the molecular nature of these materials opens up new horizons for combining different physical properties which leads to multifunctional magnetic materials.[21-29]

The field of molecular magnetism began with the study of the exchange interactions in simple metal complexes such as the dinuclear copper(II) acetate complex by Bleany and Bowers in 1951.[30] It was not long after this study before molecular magnetic materials expanded into different arenas by the development of many new types of materials that exhibit unusual behavior including high T_c molecule-based ferromagnets,[20,31-36] spin cross-over compounds, and photomagnets.[37,38] The discovery of molecule-based materials that exhibit slow relaxation of magnetization, known as single molecule magnets (SMMs), by Gatteschi and Sessoli in 1993 and simultaneously by Christou and Hendrickson represented a major breakthrough in the field.[39,40] The intermolecular magnetic interactions in these materials are negligible as compared to the intramolecular interactions therefore their properties are attributed to single molecules. The incredible variety of available molecular materials with different dimensionalities, nuclearities, and compositions has opened up important new venues for chemical approaches to the preparation of electronic and magnetic devices with unprecedented precision at the nanoscale.[41] These devices represent potential candidates for use as memory storage units of molecular size,[6,7] including "non-volatile" memory with bistability induced by a resistance change rather than current flow which makes them capable of operating at increased speeds with less energy expenditure.[42] They are also excellent candidates as carriers of quantum bits of information for quantum computing purposes[43-56] and as components of spintronic devices (Figure 1.1).[57-62]

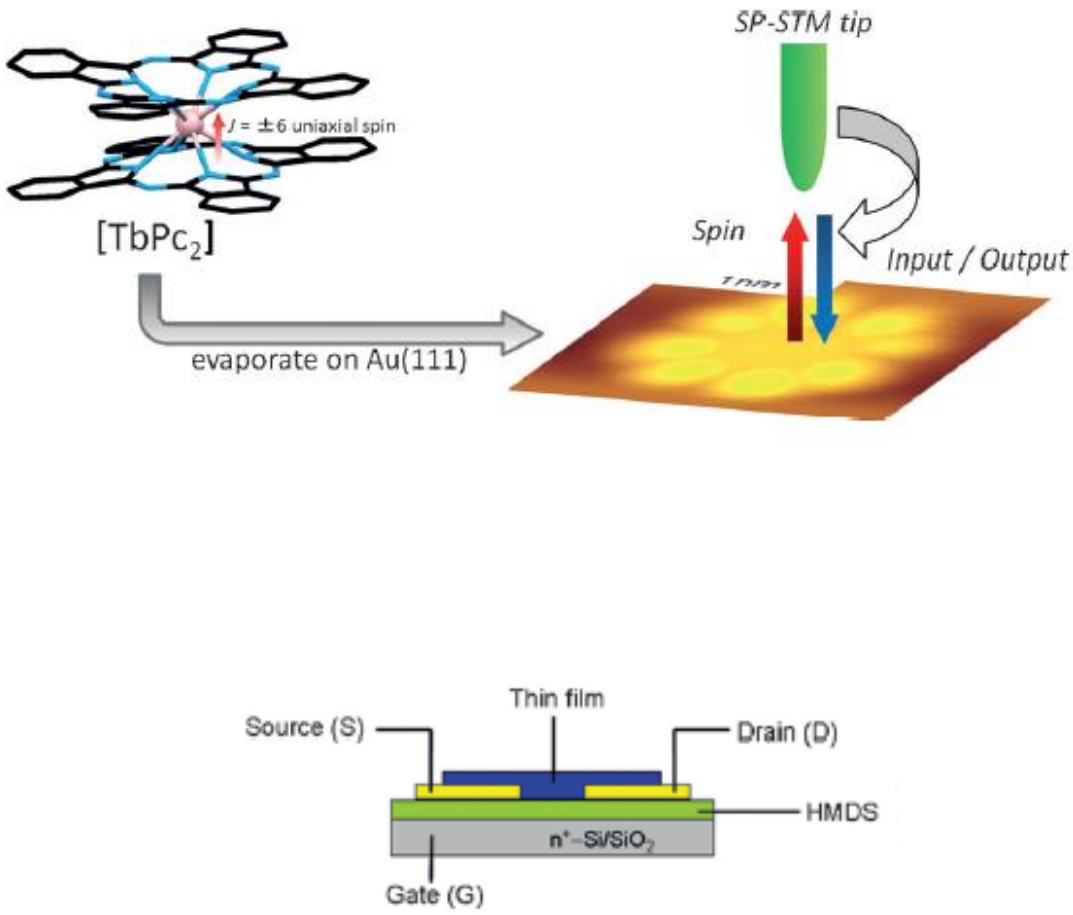

Figure 1.1 Single-molecule memory device based on [$TbPc_2$] SMMs on Au (111) (top). Spin direction can be controlled using spin-polarized STM. A bottom-contact type field effect transistor device based on [$TbPc_2$] SMMs (bottom). Adapted from (59)

Basic Concepts in Molecular Magnetism

Magnetic moment is a physical quantity related to the motion of charged particles in an electric field. The spin of protons and electrons in atoms gives rise to spin magnetic moment while their motion relative to each other results in an orbital magnetic moment. The coupling of both types of magnetic moments in an atom or a molecule results in the magnetic ground state of the atom or the molecule. A magnetic spin ground state in purely isolated individual atoms or molecules gives rise to discrete atomic or molecular magnetic moments. Such magnetic moments can engage in interatomic/intermolecular interactions of different types and ranges, which govern the macroscopic behavior of the magnetic material.

The effect of an applied magnetic field on the magnetic moments of the atoms or molecules in a material can be used to reveal the nature of the magnetic interactions between them. The magnetization of a substance (magnetic moment per unit volume; M) can be measured as a function of temperature under an applied field (H). The molar magnetic susceptibility ($\chi = M/\mathrm{H}$) and χT product can then be calculated and plotted vs. T to reveal the magnetic behavior of the material (Figure 1.2). In a material of non-interacting atoms with paired electrons, the field-induced electron circulations of the paired electrons generate a field opposite to the applied field resulting in diamagnetic molar susceptibility (χ_D) that is negative and typically ranges from -1 to -100×10^{-6} emu·mol^{-1}(emu = electromagnetic unit). Such a response is temperature independent, thus, a diamagnetic contribution, known as *Pascal's constant,* can be calculated for any atom based on its atomic number.[63]

For a material of non-interacting, discrete atomic or molecular spins, the atomic magnetic moments align with the external field and the material is referred to as *paramagnetic*. The non-interacting spins in paramagnets thermally relax to random orientations upon the removal of external field and lose their magnetization. Paramagnetic molar susceptibilities (χ_P) are typically positive and temperature dependent. Temperature independent paramagnetism (TIP) can exist in magnetic systems wherein there is a permanent mixing of the wavefunctions of the ground state and a paramagnetic excited state or states regardless of the temperature. Typically being on the order of 10^{-4} emu/mol, however, TIP is significantly smaller than temperature dependent paramagnetism at low temperatures.

In discrete molecules, the interatomic interactions that lead to a parallel alignment of spins is called *ferromagnetic coupling* whereas the interaction that favors antiparallel alignment is known as *antiferromagnetic coupling*. The latter can lead to either an antiferromagnetic (nonmagnetic) ground state or a ferrimagnetic state depending on the magnitude of different spins (Figure 1.2). The presence of nearest neighbor interatomic/intermolecular interactions in materials with extended structures often leads to long-range magnetic ordering that favors certain alignment of spins even upon removal of the external field resulting in retention of magnetization in the absence of an applied field below a certain critical temperature. When the magnetic moments interact in such a way that favors parallel alignment (*ferromagnetically coupled)* the material is a *ferromagnet*.

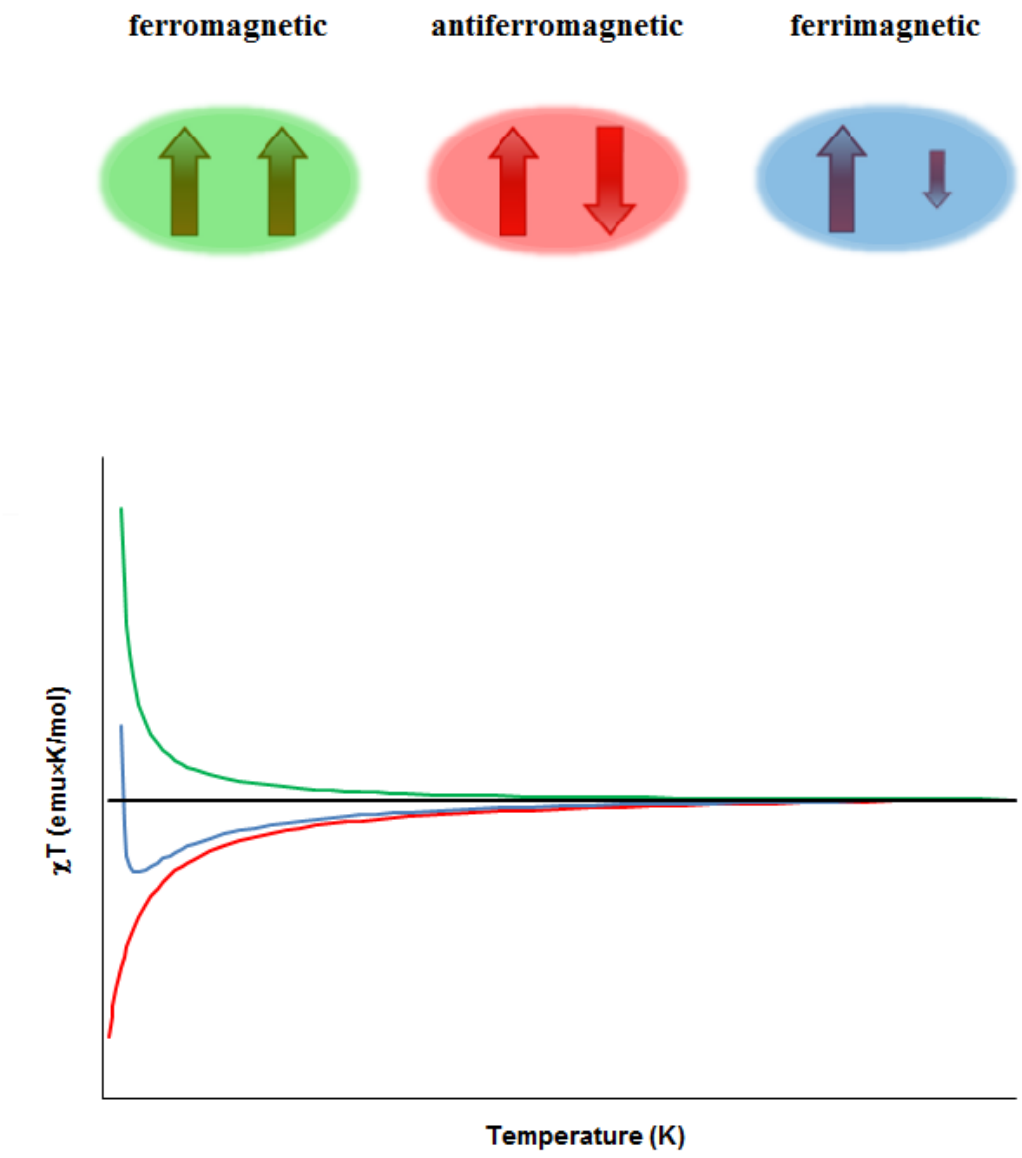

Figure 1.2 Different types of interactions (top). χT vs. *T plot* for different responses to an external field paramagnetic (black), ferromagnetic (green), antiferromagnetic (red) and ferrimagnetic (blue) (bottom).

Above the critical temperature (known as the Curie temperature, T_C) thermal fluctuations overcome the energy of the interactions between the spins and the material will relax to a paramagnetic state.

An interaction that favors antiparallel alignment of spins (*antiferromagnetic coupling*) can result in two different magnetic behaviors based on the magnitude of the interacting spins. Antiferromagnetically coupled spins of equal magnitude will cancel each other resulting in an *antiferromagnet,* whereas spins of unequal magnitude will have an overall magnetic moment resulting in a *ferrimagnet.* In a similar fashion to ferromagnets, above the critical temperature (Neel Temperature, T_N), antiferromagnets and ferrimagnets revert to a paramagnetic state.

The nature of the exchange interactions between spins can be classified into four categories: direct exchange, super-exchange, indirect exchange and itinerant exchange. Indirect and itinerant exchange pertain to the coupling via the conduction electrons in magnetic conductors. Direct exchange and *super-exchange* pertain to insulator cases where the magnetic moments are strongly localized on the magnetic centers. In such cases, the interaction occurs directly through space or through bridging chemical bonds.

Super-exchange is an orbital overlap interaction. When the overlap leads to non - orthogonal orbital ground state, spins pair up in a bonding fashion resulting in antiferromagnetic coupling (Scheme 1.1). On the other hand, the overlap that leads to orthogonal orbitals will lead to single occupation of electrons in a parallel alignment, and a ferromagnetic coupling is established (Scheme 1.1).

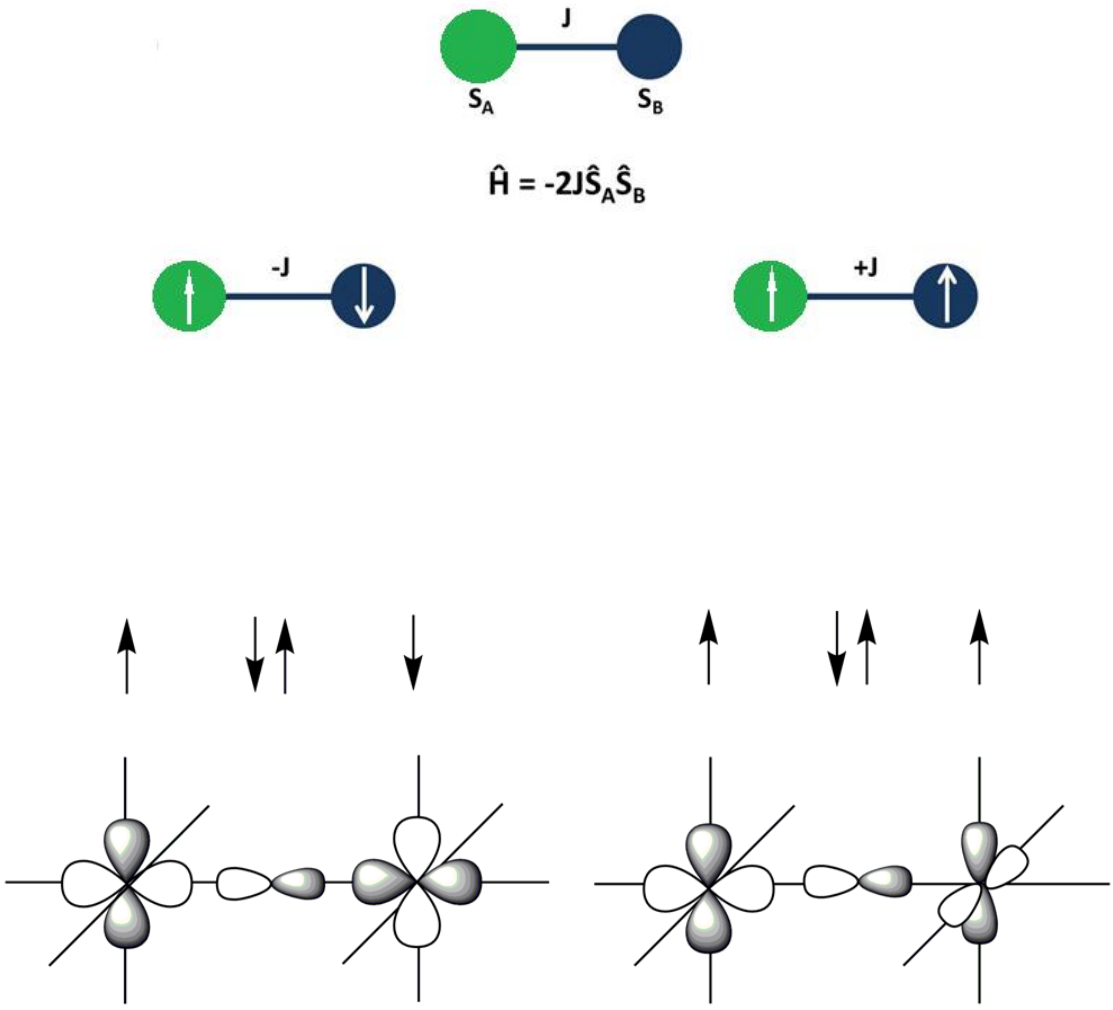

Scheme 1.1 The Heisenberg Hamiltonian: $\hat{H} = -2J\hat{S}_A\hat{S}_B$, where the two spins of the electron are coupled by the exchange interaction parameter ***J***.
$J < 0$ for antiferromagnetic coupling (interactions of non-orthogonal orbitals) while orthogonal orbitals result in ferromagnetic coupling ($J > 0$).

In both cases, the Heisenberg, Dirac, Van Vleck Hamiltonian (HDVV), $H = -2JS_1S_2$, where S_1 and S_2 are the two interacting spin centers and J is the exchange interaction parameter, is used to describe the magnetic exchange interaction between the spin centers. With this Hamiltonian, positive *J* values indicate ferromagnetic coupling whereas negative values indicate antiferromagnetic coupling (Scheme 1.1).[63]

In the 1950's, Bleaney and Bowers achieved what is considered a pioneering discovery in molecular magnetism by predicting the singlet-triplet gap in $Cu_2(O_2CCH_3)_4L_2$ (L = solvent) by employing the Van Vleck equation for two S=1/2 interacting spin centers to fit the temperature dependent magnetic behavior of the sample. This prediction was experimentally verified by subsequent magnetic, crystallographic and spectroscopic studies.[64-70] Later on, models relating chemical bonding to exchange interactions were described by Anderson[71], Goodenough[72], and Kanamori[73] for three-dimensional solids. Hoffman[74] introduced a description of the interaction of unpaired electrons in a molecule in terms of molecular orbital theory. In the case of the exchange coupling for spin ½ dimers, the antiferromagnetic contribution is expressed in terms of $(\varepsilon_a-\varepsilon_b)$, where ε_a and ε_b are the energies of the bonding and antibonding combinations of the magnetic orbitals respectively. Similarly, Kahn used an approach based on a different quantum mechanical basis set to more clearly delineate the role of the overlap in determining the value of the exchange coupling[75] based on rational design of specific systems,[76] work that underscored the success and promise of the field of Molecular Magnetism for the design of magnets with tailored properties.

Origins of Bistability in Single Molecule Magnets

One of the most important breakthroughs in the field of molecular magnetism is the discovery of slow paramagnetic relaxation of magnetization in discrete molecules known as *Single Molecule Magnets* (SMMs) wherein a single molecule retains its magnetization and exhibit magnetic hysteresis of molecular origin below a blocking temperature (T_B).[77-80] This discovery triggered a renaissance in the field of molecular magnetism, which opens interesting venues for magnetic data storage device miniaturization as well as other interesting future technologies based on quantum phenomena[81-83] such as quantum computing [43-56] and spintronics.[57-62]

Magnetic bistability in SMMs is of molecular origin. It arises from the combination of a high ground state electron spin (S) and a large negative global anisotropy (Δ) (axial zero-field splitting (D) in the classical case) within this ground state.[78,80,84] The highest spin (Ms) sub-levels are stabilized by the negative axial anisotropy creating a bistability gap with an energy barrier (U) to the reversal of the magnetization (M) (Scheme 1.2). Below a certain blocking temperature (T_B), the thermal energy is not sufficient to overcome the energy barrier (U) on the time scale of the experiment. In such a situation, trapping one of the two spin configurations is possible by applying a magnetic field (H_{dc}) below T_B, which leads to a saturation of magnetization (M). Upon removing the applied field, a slow relaxation of magnetization occurs with a certain relaxation time, (τ). For thermally activated relaxation of magnetization, the energy barrier is proportional to $S^2|\Delta|$ or $(S^2 - 1/4)|\Delta|$ for molecules with integer and non-integer S, respectively.

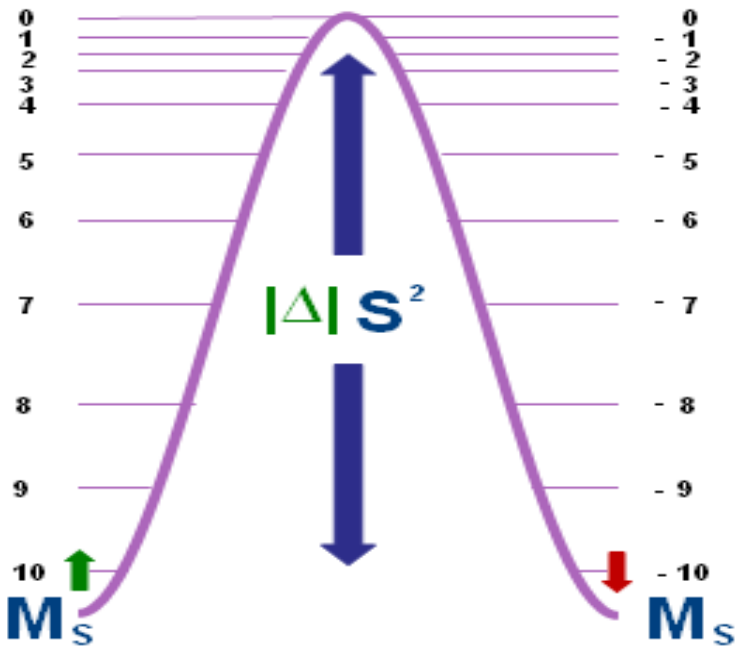

Scheme 1.2 Energy diagram for an SMM with S = 10 ground state in zero field reflecting the energy barrier ($\Delta E = U = S^2|\Delta|$) where S is the total spin and Δ is the global anisotropy.

Even below $T_{B,}$ faster relaxation rates (U_{eff} < U) are possible due to quantum tunneling of the magnetization. These quantum tunneling pathways increase with decreasing temperature, however, they can be partially or totally circumvented by applying small dc field in order to remove the degeneracy of ±Ms sublevels. The relaxation mechanism in bulk magnets is different. In a bulk magnet, hysteresis results from the magneto-crystalline anisotropy and domain wall motion. A bulk magnet can retain its magnetization (remnant magnetization) upon the removal of the external field; an application of a magnetic field in the opposite direction (coercive field) is required to demagnetize the material.

The first example of an SMM, $[Mn_{12}O_{12}(O_2CMe)_{16}(H_2O)_4]\cdot 2MeCO_2H\cdot 4H_2O$ ($Mn_{12}OAc$), was synthesized by Lis.[85] It took 13 years for Gatteschi and coworkers to make the discovery by magnetically characterizing the compound and observing slow relaxation of magnetization up to 3.5K (Figure 1.3a).[39,40] Later on, a whole family of the mixed-valent Mn_{12} SMMs with the general formula $[Mn_{12}O_{12}(O_2\text{-}CR)_{16}(H_2O)_4]$ (R = Et, Ph, etc.) was reported with an S = 10 ground state, T_B = 3.5 K and U_{eff} values up to 74 K.[86-101]

The vast majority of single-molecule magnets have anisotropy barriers to spin reversal lower than 60 cm^{-1} (86 K), which corresponds to a 2 months relaxation time at 2K,[81] or 4 K relaxation time of approximately 2 s.[102] Thus, a major challenge in this field is to design and synthesize molecules that have higher blocking temperatures. Numerous efforts have been launched in response to the quest for enhanced barriers for magnetization reversal.

In the early stages of investigation most of these efforts focused on traditional oxo - based SMMs in an attempt to increase the total spin of the cluster as the main strategy.[103-108] Numerous clusters with huge nuclearities and large spins have been reported such as a Mn_{19} molecule exhibiting a ground state of 83/2 reported by Powell *et al*,[109] and Mn_{25} and Mn_{84} molecules, by Christou *et al*., having spin ground states of S = 51/2 and S = 6, respectively (Figure 1.3c).[110,111] Another very large cluster is $Mo_{72}Fe_{30}$ reported by Müller and coworkers with 30 Fe(III) centers but it only has an S=5/2 ground state.[105-108] Increasing spin value, however, has not led to an appreciable increase in the barrier height, since the low local symmetry of metal ions in these clusters significantly reduces the anisotropy.

Another route towards designing improved SMMs is controlling the type and magnitude of magnetic coupling within the cluster in order to ensure a ground state isolation that switches quantum tunneling pathways. In this vein, Christou and coworkers were successfully able to switch the magnetic interaction between metal centers in the hexametallic complex $[Mn^{III}_6O_2(sao)_6(O_2CPh)_2(EtOH)_4]$ ($saoH_2$ = salicylaldoxime) into ferromagnetic coupling through partial replacement of acetate ligands. The resulting molecule had S = 12 and D = -0.43 cm^{-1} in the ground state resulting in a U_{eff} = 86.4 K and a T_B ~ 4.5 K (Figure 1.3b).[112]

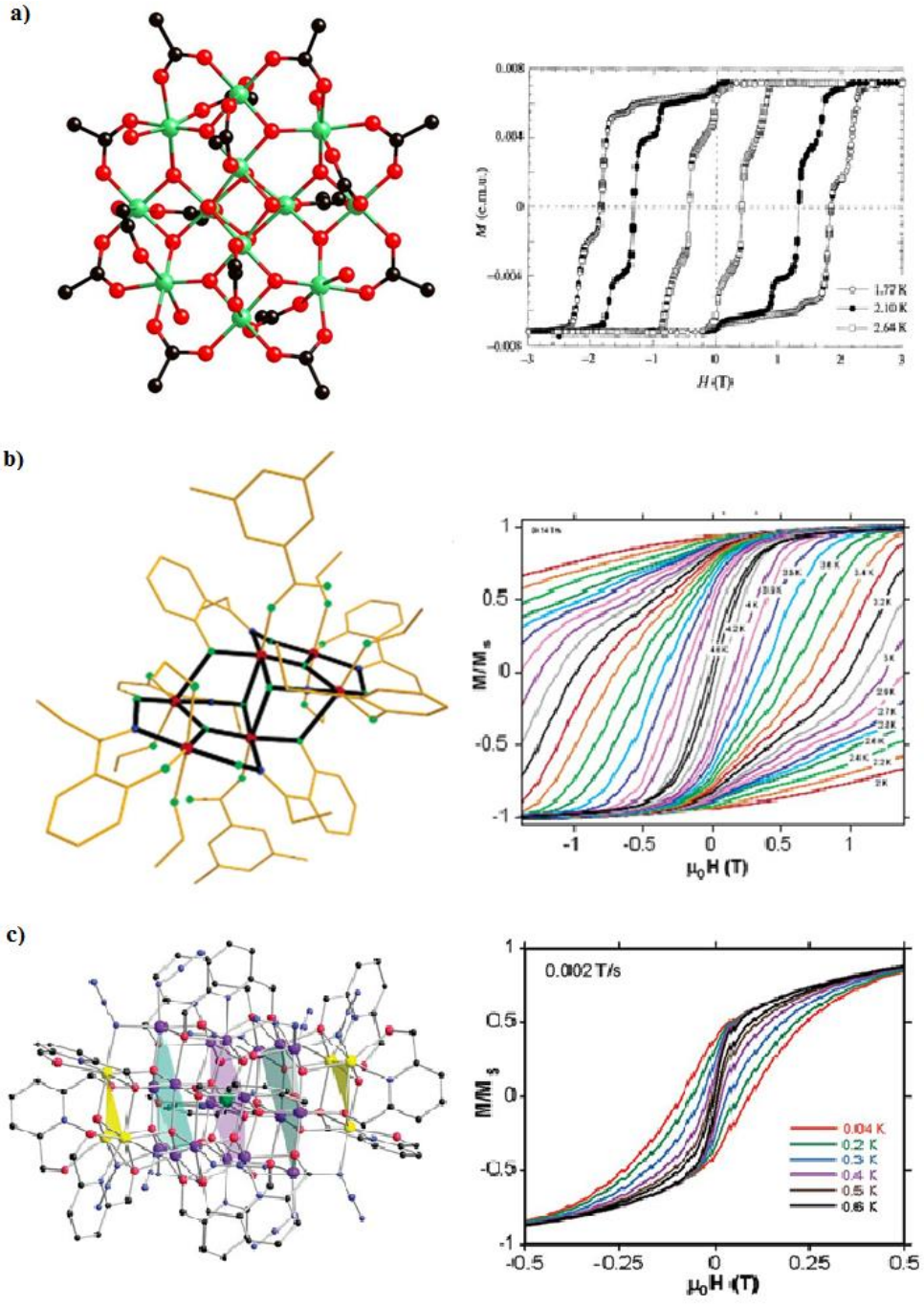

Figure 1.3 Single molecule magnets; (a) $[Mn_{12}O_{12}(O_2CMe)_{16}(H_2O)_4]\cdot 2MeCO_2H\cdot 4H_2O$ ($Mn_{12}OAc$) first SMM with a barrier of 43.2 cm^{-1} and τ_0 = 2.1 x 10^{-7} s. (b) $[Mn^{III}_6O_2(sao)_6(O_2CPh)_2(EtOH)_4]$ with ferromagnetic coupling. (c) Mn_{25}, large spin SMM (S = 51/2) molecule. Adapted from references (110,112,113).

Recent theoretical work has championed the idea of focusing on strong single-ion anisotropy of the clusters as a method for increasing the blocking temperature, T_B, of SMM materials wherein relatively large ZFS values provide a chance to design SMMs based on smaller complexes with smaller number of spins. In his discussion of this issue,[114] Waldmann pointed out that the direct proportionality of the energy barrier height to the square of spin value, according to the formula $U = S^2|D|$, is not technically correct. He also pointed out, along with others,[115] that the coexistence of high spin value along with large anisotropy is not possible due to the inverse proportionality between them.[114] These theoretical findings clearly suggest that we should focus synthetic efforts towards enhancing the global anisotropy in metal complexes rather than the spin, S, for obtaining higher barriers in SMMs. In order to achieve this goal, a greater structural control on cluster architectures is required to ensure certain local symmetries for metal ions with larger single ion anisotropies. Such control can be achieved using the building block strategy, wherein pre-designed molecular precursors are synthesized using capping ligands to prevent the growth toward one-, two-, or three-dimensional extended structures. These building blocks are then allowed to react into a pre-designed structural motif.[116] This need for more structurally controlled chemical syntheses requires the use of other bridging ligands with less tendency for serendipitous bridging modes, such as cyanide.[117] Cyanide is known for its tendency to form linear M-CN-M' bridges between two transition metal atoms and the unsymmetrical nature of cyanide with a harder carbon and a relatively softer nitrogen end allows for the selective binding of two different transition metals which enriches the available varieties of metal combinations in cyanide

bridged heterometallic complexes. Moreover the polycyanometallate precursors are typically stable in solution rendering them excellent building blocks for further chemical modifications. In addition, in terms of magnetic properties, the cyanide ligand allows for predictable exchange coupling between the spin carriers because of the linear configuration of the M-CN-M' unit by considering the symmetry of the metal-based magnetic orbitals involved.[118]

The Effect of Single-ion Anisotropy

The unquenched orbital momenta in degenerate ground states and their mixing with the spin *via* first order spin-orbit coupling were reported to result in a strong anisotropy in Fe^{III}-CN-Cu^{II} and Fe^{III}-CN-Ni^{II} model complexes.[119,120] When these dinuclear units are incorporated into poly-nuclear cyanometalate, large negative zero-field splitting, ZFS, |D| values could be achieved depending on the geometry.[119] In addition, the incorporation of this type of anisotropic metal ion into magnetic clusters induces antisymmetric exchange interactions which represent another interesting source of global anisotropy for the molecule.[121-124]

Early 3d transition metals as well as 4d and 5d transition metals are excellent candidates that can introduce large single-ion anisotropy into clusters potentially resulting in a large negative value of D. Moreover, the diffuse d orbitals can give rise to improved overlap with the π and π^* orbitals of the cyanide ligand resulting in larger superexchange constants |J| between metal centers [125,126] which ensures that the magnetic ground state is well-isolated from higher spin states to prevent relaxation via population of excited states. Indeed, the combination of V^{II} (t_{2g}^3) and Cr^{III} (t_{2g}^3) metal centers in

Prussian blue analogues has led to bulk magnets with ordering temperatures well above room temperature. [34,127,128] Similarly, Ruiz *et al*., in theoretical treatments of cyanide bridged model compounds, predicted that super-exchange interactions between the hexacyanomolybdate(III) ion and the early 3d metal centers V^{II} and Cr^{II} should be extremely strong (J = -422 cm^{-1} for $Mo^{III}V^{II}$ and J = -186 cm^{-1} for $Mo^{III}Cr^{II}$).[118] Impressive manifestations of the single ion anisotropy effect on U_{eff} have been reported including slow relaxation of magnetization in low nuclearity molecules such as the pentanuclear TBP $\{[Mn^{II}(tmphen)_2]_3[Mn^{III}(CN)_6]_2\}$,[129] the pentanuclear $\{[Mn^{II}(py_5Me_2)]_4[Re^{IV}(CN)_7](PF_6)_5$,[130] the heptanuclear $K\{[(Me_3tacn)Mo^{III}(CN)_3]_6\text{-}Mn^{II}\}(ClO_4)_3$,[131] and octanuclear $\{[(triphos)Re^{II}(CN)_3]_4[Mn^{II}Cl]_4\}$(triphos = 1,1,1-tris(diphenylphosphino-methyl)ethane))[132] clusters, all of which behave as SMMs (Figure 1.10). The literature is witnessing increasingly larger numbers of SMMs with smaller sizes and spin states, with notable examples being based on the linear trinuclear $[Mn^{III}{}_2M^{III}]$ units (M = Fe: S = 9/2 ground state, ferromagnetic coupling; M = Cr: S = 5/2 ground state, antiferromagnetic coupling), with U_{eff} values of 9.3 cm^{-1} and 16 cm^{-1}, respectively.[133-135] Studies of the heavier 4d and 5d congeners by Bendix *et al*., $NEt_4[Mn^{III}{}_2(5\text{-}Brsalen)_2(MeOH)_2M^{III}(CN)_2]$ (M = Fe, Ru, Os), has led to enhanced barriers, as predicted, to 11.8 cm^{-1} and 13.2 cm^{-1} for the Ru and Os compounds respectively (Figure 1.4).[136-139] Recently, Long *et al.* reported a record ferromagnetic exchange through cyanide by incorporating the highly anisotropic 5d metal ion (Re^{IV}) into cyanide bridged chain with (Cu^{II}).[140]

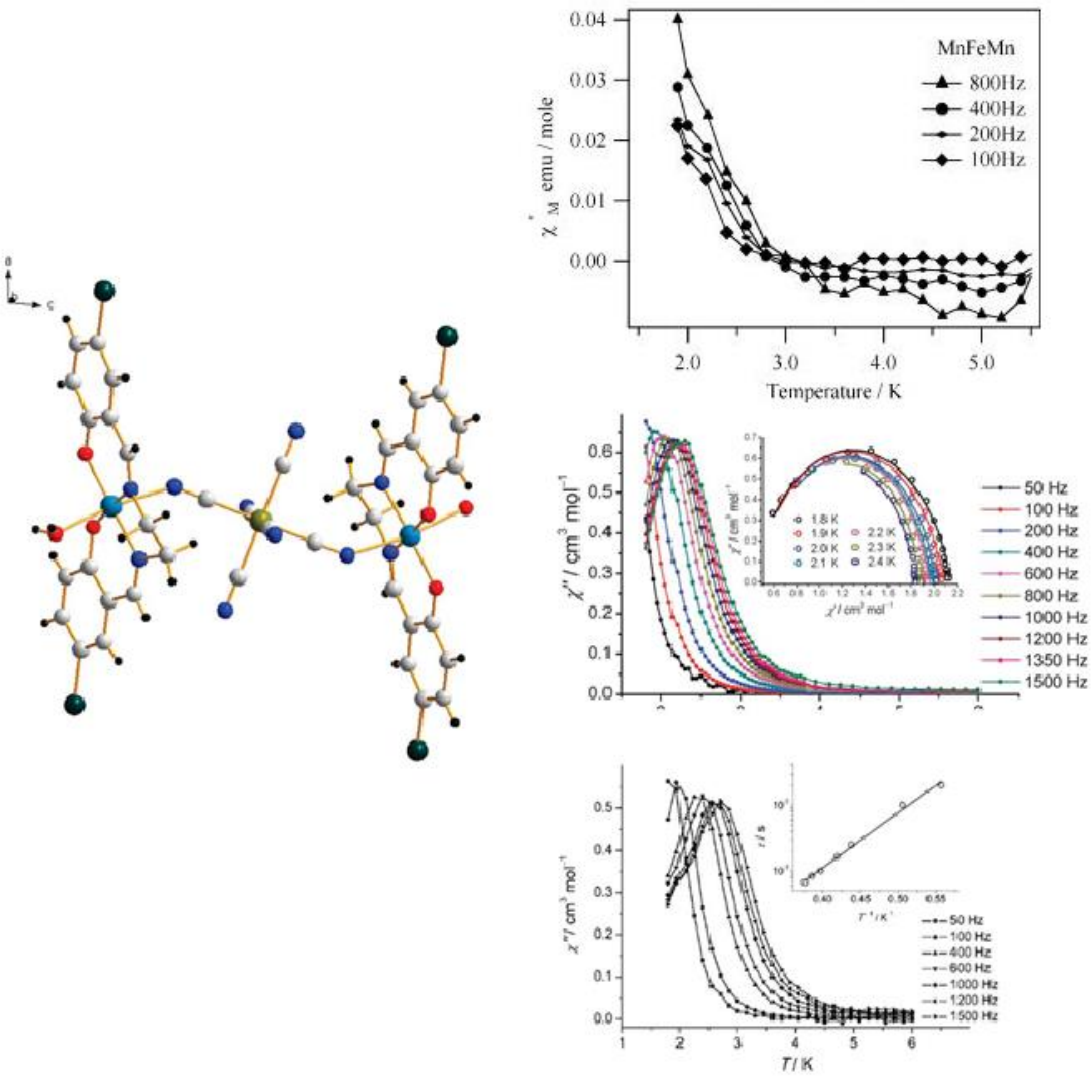

Figure 1.4 Structure of the Mn-M-Mn unit (M = Ru, Os).[138] Top right: out-of-phase ac susceptibility of the Mn_2Ru SMM with an effective barrier of 11.8 cm^{-1}.[136] Bottom right: out-of-phase ac susceptibility of the Mn_2Os SMM giving a U_{eff} = 13.2 cm^{-1}.[137]

More interestingly, efforts towards making anisotropy-enhanced SMMs led to the observation of slow relaxation of magnetization in mononuclear complexes (Table 1.1).[141-151] Long and coworkers reported the first family of mononuclear SMMs based on trigonal pyramidal iron(II) complexes of the general formula [M(solv)n][(tpaR)Fe] (tpa = tris(pyrrolyl-R-methyl)amine, M = Na, R = tert-butyl (1), phenyl (4); M = K, R = mesityl (2)).[141,142] In this family, the height of the anisotropy barrier was found to be directly proportional to ligand field strength. Jurca and coworkers reported slow relaxation in smaller spin (3/2) system based on mononuclear cobalt(II) complexes, (2,6-$\{ArN=C(R)\}_2NC_5H_3$)$Co(NCS)_2$ (R=Me or Ph).[143] Mossin et al. reported that the five coordinate trigonal bipyramid Fe(III) complex (PNP)$FeCl_2$ (PNP = N[2-$P(CHMe_2)_2$-4-methyl-phenyl]$_2^-$) also exhibited slow relaxation without the need to apply a dc field with an energy barrier of 47 K.[144] More recently, Long et al. developed a series of two-coordinate Fe(II) complexes with the highest anisotropy barrier reported to date for a mononuclear SMM, as high as 181 cm^{-1}(Figure 1.5b).[149]

In the vein of increasing single-ion anisotropy, heavy lanthanide and actinide ions are of special interest due to their large spin states accompanied by large Ising-type single ion anisotropy. Several early examples of the high-profile family of double decker complexes by Ishikawa[152-155] revealed that individual 4f centers can exhibit SMM behavior up to 40 K. Recently, more efforts have been directed towards understanding and improving SMM behavior in single lanthanide ions by controlling the crystal field environment.[156-165] Exciting examples have emerged including organometallic lanthanide complexes[159,160] as well as actinide complexes (Figure 1.6).[164-168]

Table 1.1 Transition metal mononuclear (Single Ion) single molecule magnets

Formula	**Ground State**	U_{eff} **(cm^{-1})**	τ_0 **(s)**	**Ref.**
[Na(solv)n][(tpa(tBu))Fe^{II}]	2	65	$6.7\cdot10^{-11}$	[142]
[K(solv)n][(tpa(Mes))Fe^{II}]	2	42	-	[142]
[Na(solv)n][(tpa(Ph))Fe^{II}]	2	25	-	[142]
Fe^{II} [$N(SiMe_3)(C_6H_3$-2,6-$Pr^i_2)]_2$	2	181	$1\cdot10^{-11}$	[149]
Fe^{II} [$C(SiMe_3)_3]_2$	2	146	$4\cdot10^{-9}$	[149]
Fe^{II} [$N(H)(C_6H_3$-2,6-$(C_6H_3$-2,6-$Pr^i_2)_2)]_2$	2	109	$5\cdot10^{-9}$	[149]
Fe^{II} [$N(H)(C_6H_3$-2,6-$(C_6H_2$-2,4,6-$Pr^i_2)_2)]_2$	2	104	$4\cdot10^{-8}$	[149]
Fe^{II} [$O(C_6H_3$-2,6-$(C_6H_3$-2,6-$Pr^i_2)_2]_2$	2	43	$3\cdot10^{-7}$	[149]
(2,6-{ArN=C(Me)}$_2NC_5H_3$)Co^{II} $(NCS)_2$	3/2	16	$3.6\cdot10^{-6}$	[143]
(2,6-{ArN=C(Ph)}$_2NC_5H_3$)Co^{II} $(NCS)_2$	3/2	24	$5.1\cdot10^{-7}$	[143]
$(Ph_4P)_2$[Co^{II} $(SPh)_4$]	3/2	21	$1\cdot10^{-7}$	[145]
Co^{II} ((4,5-diph-1H-imidazolyl)phenol)$_2$	3/2	34	$7.5\cdot10^{-8}$	[151]
Co^{II}((4,5-diph-imidazolyl)methoxyphenol)$_2$	3/2	29	$1.4\cdot10^{-7}$	[151]
[(PNP)$Fe^{III}Cl_2$]	3/2	36	$2\cdot10^{-8}$	[144]
($HNEt_3$)($Co^{II}Co^{III}{}_3L_6$)	3/2	86	$1\cdot10^{-7}$	[147]
cis-[Co^{II} $(dmphen)_2(NCS)_2$]·0.25EtOH	1/2	17	$4\cdot10^{-7}$	[148]
[(3G)Co^{II}Cl](CF_3SO_3)	1/2	24	$1.9\cdot10^{-10}$	[146]

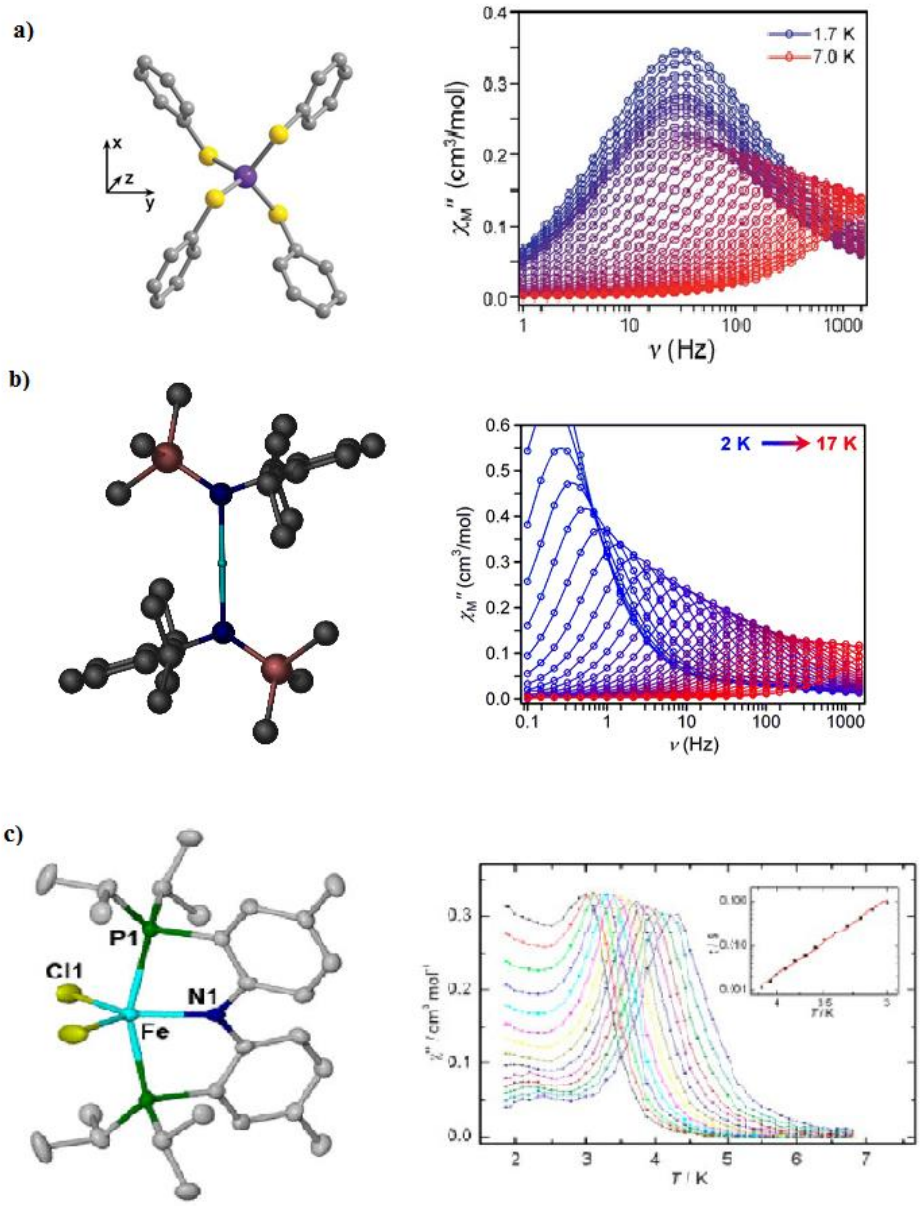

Figure 1.5 Examples of transition metal mononuclear single molecule magnets; $(Ph_4P)_2[Co^{II}(SPh)_4]$,[145] $Fe^{II}[N(SiMe_3)(C_6H_3\text{-}2,6\text{-}Pr^i_2)]_2$[149] and $[(PNP)Fe^{III}Cl_2]$.[144]

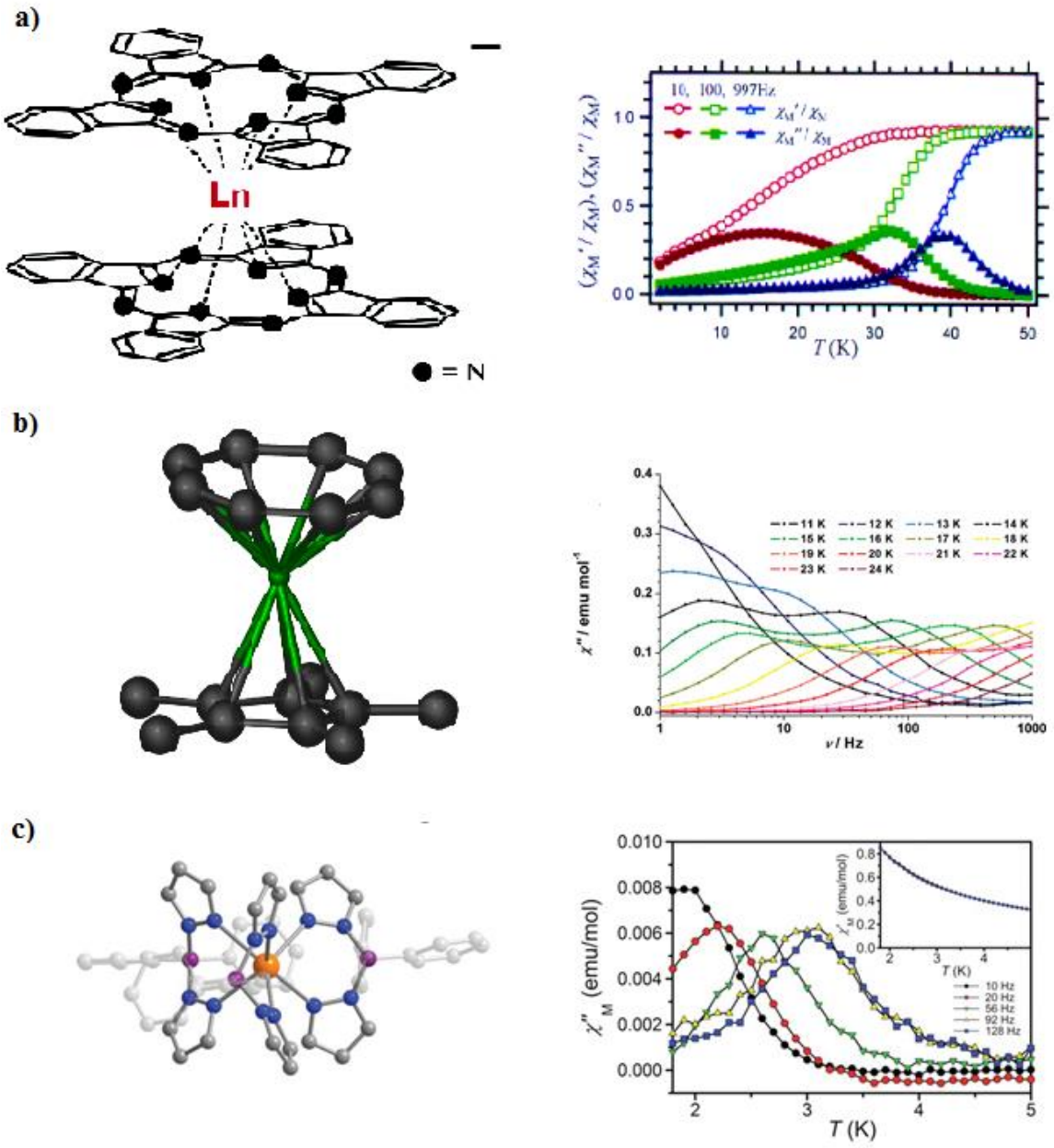

Figure 1.6 Examples of lanthanide mononuclear (single ion) single molecule magnets; (a) double decker family.[152-155] (b) ErCp*COD (Cp* = pentamethyl-cyclopentadienide, COD = cyclooctatetraenide.[159,160] (c) $U(tp)_3$ (tp = diphenylbis(pyrazolylborate).[204]

Enhancing Single-ion Anisotropy in Metal Complexes

The axial zero-field splitting parameter, D, one of the main types of single-ion anisotropy, is typically described as resulting from the mutual effect of both trigonal crystal field distortion, Δ, and spin orbit coupling, λ, according to the equation ($D = \lambda^2/\Delta$).[14] Recent studies revealed that ligand spin-orbit coupling can contribute to the overall λ and significantly alter both the sign and magnitude of D in a metal complex.[169,170] Moreover, theoretical studies have predicted that the relationship between D and Δ depends on the orbital degeneracy of the system where it could be directly proportional in case of complexes with orbitally degenerate ground states.[124,171,172]

The vanadium (III) ion is an excellent candidate for probing these issues as it is known to exhibit very large zero-field splitting with axial components |D| up to - 20 cm^{-1}.[173-178] Additionally, V(III) has been reported to give rise to very strong ferromagnetic interactions in dinuclear species,[173,174] which makes it very promising to introduce single ion anisotropy into magnetic clusters as supported by several interesting examples including the first room temperature molecule-based magnet, $V(TCNE)_2$(T_C = 350K), reported by Miller,[36] and the first room temperature cyanide-based magnet, $V^{II}_{0.42}V^{III}_{0.58}[Cr^{III}(CN)_6]_{0.86}\bullet 2.8H_2O$ (T_C = 315K), reported by Verdaguer's group.[34] Despite these interesting properties and achievements, there is very little literature on V^{III} molecular magnetic materials.[32,34,173-185] The incorporation of hexacyanovanadate (III) anion $[V^{III}(CN)_6]^{3-}$ into PB-structured materials has proven to be synthetically challenging, presumably due to the ease of oxidation of V^{III} to V^{IV}.[33,186-188] Discrete magnetic molecules based on cyanovanadate building blocks are quite rare.[183,189]

The work described in this dissertation highlights our recent efforts to develop new building blocks suitable for incorporating highly anisotropic early transition metals (V(III)), 5d metals (Re(II)) and lanthanides into heterometallic molecular magnetic materials, and gives insight into the different factors affecting zero-field splitting as a source for single ion anisotropy. In Chapter II, attempts at rational control of the local coordination environment of metal ions in order to ensure larger orbital contributions to their magnetic moments is described. The synthesis of a series of trigonally distorted mononuclear vanadium(III) complexes is described with emphasis on the effect of both the magnitude of the trigonal field and the ligand spin-orbit coupling contribution on zfs parameters. The results presented in Chapter III describe the syntheses along with the structural, spectroscopic and magnetic studies of a new series of vanadium cyanide building blocks suitable for incorporating the highly anisotropic vanadium(III) ion into cyanide bridged molecular materials. Chapter IV outlines a building block approach that involves the use of capping ligands as a viable synthetic route to various heterometallic discrete molecules. The results presented in this chapter describe the structural and magnetic properties of an unprecedented series of trigonal bipyramidal molecules containing lanthanides with various magnetic responses. Overall, the work presented in this dissertation provides insight into new methods for enhancing magnetic properties via control of metal ion coordination environments (Chapter II) and highlights the use of metal cyanide precursors for the synthesis of new magnetic molecular materials (Chapters III and IV).

CHAPTER II

EXPLORING THE FACTORS CONTROLLING ZERO-FIELD SPLITTING PARAMETERS AS A SOURCE FOR SINGLE ION ANISOTROPY

Magnetic bistability in single molecule magnets (SMMs), in a classical case, arises from the combination of a high ground state electron spin (S) and a large negative axial zero-field splitting (D) within this ground state.[78,80,84] The best route towards SMMs with more readily accessible blocking temperatures has been debated for some time now.[78,114,119,190-192] Recent theoretical work has suggested that, rather than a high spin value, we should focus on the inherent magnetic anisotropy of the molecules as a method for increasing the blocking temperature, T_b, of SMM materials wherein relatively large values of D translate into smaller complexes with relatively smaller S values behaving comparably if not better than larger spin molecules.[119,192-194] This strategy has led to remarkable new examples of SMMs based on mononuclear transition metal complexes, which capitalize on the large single ion anisotropy of metals with unquenched orbital angular momenta.[141-146,172,195] The examples reported in this vein underscore the fact that controlling local symmetries of the metal ions is crucial for engendering larger orbital contributions to the magnetic moment, and hence, a higher degree of anisotropy which is a key factor in the realization of single molecule magnetic behavior. This strategy was successfully employed to prepare several families of mononuclear SMMs based on iron(II),[141,142,172] iron(III)[144] and cobalt(II)[143,145,195,196].

In order to better understand the origins of zero-field splitting as one of the main types of single ion anisotropy, several studies have been reported on model compounds

revealing that it is a result of the mutual effect of both trigonal crystal field distortion Δ and spin orbit coupling λ according to the equation ($D = \lambda^2/\Delta$) (Figure 2.1).[14]

The significance of the global spin-orbit coupling in the system has been supported by the fact that ligand spin-orbit coupling can contribute to and significantly alter both the sign and magnitude of D in a metal complex.[169,170] In our recent work, the axial trigonal distortion of the crystal field was shown to be crucial for the presence of an energy barrier in the $[triphosRe(CN)_3]_4[MnCl]_4$ SMM.[197] Moreover, theoretical studies of the first cyanide-based SMM prepared in our laboratories, $[Mn(CN)_6]_2[Mn(tmphen)_2]_3$, predicted that a great enhancement in the energy barrier could be achieved by increasing the magnitude of the trigonal distortion of the crystal field of Mn(III) ions.[124,171,172]

The vanadium (III) ion is an excellent candidate for probing these issues for two reasons; it is known to exhibit very large zero-field splitting with axial components |D| up to - 20 cm^{-1} which makes it a very promising ion for enhancing SMMs[173-178] and it has been reported to give rise to very strong ferromagnetic interactions in dinuclear species which is also an attractive feature.[173,174]

Studying the electronic structure of such a complicated system requires a combination of experimental techniques. V(III) has been the subject of a number of studies using optical and magnetic resonance spectroscopy.[198-201] Properties of Vanadium(III) hexa-aqua complexes have been previously investigated using electronic absorption,[202,203] Raman spectroscopy techniques[204] as well as by theory.[202,205] Single-crystal electronic spectra for Vanadium(III) doped into $Al(acac)_3$ has been reported

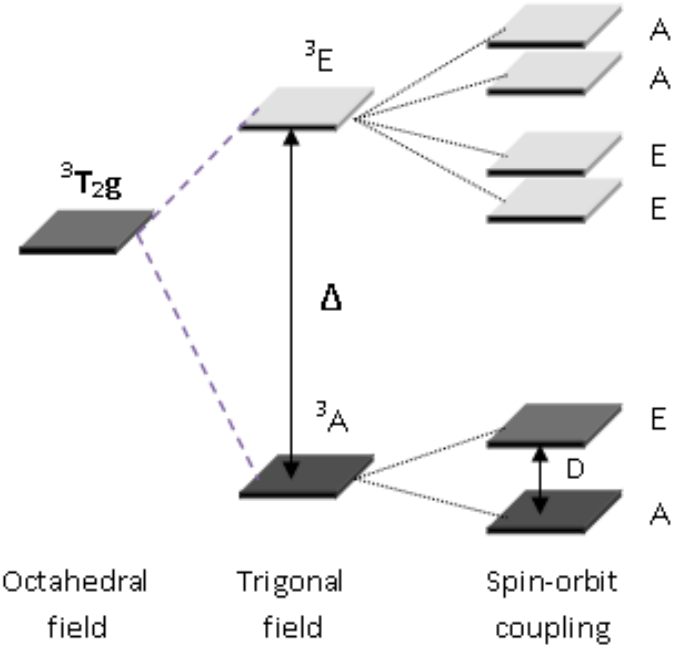

Figure 2. 1 Zero-field splitting of a d^2 metal ion in trigonally distorted coordination environment.

by Piper and Carlin[206] and electronic spectra for $V(acac)_3$ and $VCl_3(thf)_3$ have been reported by Machin and Murray.

EPR studies are of special importance for vanadium complexes. As an $S = 1$ system, vanadium (III) ion exhibits zfs that depends on its local symmetry. In a high symmetry environment, zfs is small enough to make spin-allowed ($\Delta M_S = \pm 1$) EPR transitions measurable with conventional X band EPR methods.[207] Introducing axial distortions that cause a lowering of the cubic symmetry leads to "EPR silent" vanadium (III) systems since zero-field splitting in such systems usually becomes well above the microwave frequency (~0.3 cm^{-1} for X-band EPR). In such a case, all spin-allowed ($\Delta M_S = \pm 1$) EPR transitions are far higher than the field/ frequency range.

The emergence of high-field and high- frequency EPR (HFEPR; $\nu > 94$ GHz; B_0 up to ~35 T) spectrometers has promoted a renaissance of traditional "EPR silent" systems.[208,209] HFEPR spectroscopy has been recently reported for V (III) compounds in pure RbV alum and as a CsGa alum dopant.[210] Krzystek and coworkers reported an excellent study for a family of V(III) molecular complexes with S=1 ground state that exhibit significant zfs due to their highly distorted pseudo-octahedral environments.[211] The results revealed large axial zfs, with D values of ~ 8 cm^{-1} for $V(acac)_3$ upto ~ -16 cm^{-1} in $VBr_3(thf)_3$.[212] HFEPR studies the "hole" counterpart, Ni (II) ($3d^8$), have been reported also both as a dopant into diamagnetic hosts[213] and as pure molecular complexes.[214-217] Ruamps and coworkers were able to measure a Ni(II) molecule with D value as high as -180 cm^{-1} using HFEPR.[217]

In view of these principles, the effects of both axial crystal-field distortions and spin-orbit coupling on the magnitude of zero field splitting parameters have been explored in a family of mononuclear trigonally distorted vanadium complexes. In this series, the magnitude of the trigonal field distortion was systematically varied depending on the difference of ligand field strength for different ligand combinations while the magnitude of spin-orbit coupling in the system was varied using ligand spin-orbit coupling contributions (the heavy halide effect). Herein we report the syntheses, structural characterization and properties investigation of a family of mononuclear trigonally distorted vanadium complexes of the general type $A[LVX_3]$ (X = F, Cl or Br, A^+ = Et_4N^+, $^{n-}Bu_4N^+$ or PPN^+, PPN = bis(triphenylphosphoranylidene)ammonium, L = Tp or Tp*, Tp = *tris*(*-1*-pyrazolyl)borohydride), Tp* = *tris*(*3*,*5*-dimethyl-*1*-pyrazolyl)borohydride) and $[Tp^*V(DMF)_3](PF_6)_2$.

Experimental

Syntheses

Starting Materials. All chemicals and solvents used are of reagent grade quality. $VCl_3(THF)_3$ (Aldrich), $(Et_4N)Cl$ (Aldrich), $(nBu_4N)Cl$ (Aldrich), (PPN)Cl (Aldrich), KTp and KTp* (Strem) were used as received. Anhydrous $(Et_4N)F$ was prepared by distillation from anhydrous ethanol. Acetonitrile and CH_2Cl_2 were pre-dried over 4 Å molecular sieves and freshly distilled under a nitrogen atmosphere. Anhydrous DMF (Alpha Aesar), THF and diethyl ether (Aldrich) were used as received. All reactions were performed under nitrogen using standard dry box and Schlenk-line techniques.

Physical Measurements. Elemental analyses were performed by Atlantic Microlab Inc. (Norcross, GA). Infrared spectra were recorded as Nujol mulls in the range 220-4000 cm^{-1} on a Nicolet Nexus 470 FTIR spectrophotometer.

[$TpVCl_2THF$] (1). The compound was synthesized by modification of a previously reported procedure.[218] A quantity of KTp (1.35 g, 5.35 mmol) was added slowly to a solution of $VCl_3(THF)_3$ (2.0 g, 5.35 mmol) in 30 mL of CH_2Cl_2 which was stirred overnight. The green mixture was filtered through ™Celite to remove KCl. The filtrate was reduced under vacuum at room temperature to 5 mL and treated with 50 mL of hexanes with stirring to precipitate a blue green powder. The product was collected by filtration, washed with hexanes (3x5 mL) and dried under vacuum (Yield =1.53 g, 72%) IR(Nujol): (νB-H) 2490(m) cm^{-1}.

[Tp^*VCl_2THF] (2). The compound was synthesized as previously reported.[219] A quantity of KTp* (1.8 g, 5.35 mmol) was added slowly to a solution of $VCl_3(THF)_3$ (2.0 g, 5.35 mmol) in 30 mL of THF. The resulting solution was stirred overnight, to give a green mixture which was evacuated to dryness. The green residue was extracted with 20 mL of CH_2Cl_2 and filtered through ™Celite to remove KCl. The volume of the green filtrate was reduced under vacuum at room temperature to 5 mL after which time 50 mL of hexanes were added with stirring to effect the precipitation of a lime green powder. The product was collected by filtration and washed with hexanes (3x5 mL) and finally dried under vacuum (Yield = 1.35 g, 51.3%) IR(Nujol): (νB-H) 2544(m) cm^{-1}.

(PPN)[$TpVCl_3$]·CH_2Cl_2 (3). A solution of (PPN)Cl (230 mg, 0.4 mmol) and **1** (162 mg, 0.4 mmol) in 10 mL of CH_3CN was stirred for 2 hours. The volume of the green solution

was reduced under vacuum at room temperature to 5 mL and treated with 20 mL of diethyl ether to give pale green needles of the product which were filtered, washed with diethyl ether (2x3 mL) and recrystallized from CH_2Cl_2/ diethyl ether mixture to give pale green crystals suitable for single crystal X-ray crystallography (Yield = 331 mg, 77%). Elemental analysis: Calcd. for $C_{46}H_{42}BN_7P_2Cl_5V$ (**3**): C, 55.59; H, 4.26; N, 9.87; Found: C, 55.41; H, 4.45; N, 10.26 %. IR(Nujol): ν(B-H) 2520(m); ν(P=N) 1587(s), ν(V-Cl) 324(s), 281(s) cm^{-1}.

(PPN)[Tp*VCl$_3$] (4). A solution of (PPN)Cl (230 mg, 0.4 mmol) and **2** (197 mg, 0.4 mmol) in 10 mL of CH_3CN was refluxed for 1 hour. The volume of the green solution was reduced under vacuum at room temperature to 5 mL and treated with 20 mL of diethyl ether which resulted in the formation of green crystals which were collected by filtration, washed with diethyl ether (2x3 mL) and then recrystallized from CH_3CN/diethyl ether at room temperature which produced green crystals suitable for single crystal X-ray crystallography (Yield = 290 mg, 73%). Elemental analysis: Calcd. for $C_{51}H_{52}BN_7P_2Cl_3V$ (**4**): C, 61.63; H, 5.23; N, 9.87; Cl, 10.71; Found: C, 61.41; H, 5.16; N, 9.30; Cl, 10.30 %. IR(Nujol): ν(B-H) 2550(m); ν(P=N) 1587(s), ν(V-Cl) 327(s), 303(s) cm^{-1}.

(Et$_4$N)[Tp*VCl$_3$] (5). A solution of (Et_4N)Cl (66 mg, 0.4 mmol) and **2** (197 mg, 0.4 mmol) in 10 mL of CH_3CN was refluxed for 30 minutes. The volume of the green solution was reduced to 3 mL which led to a color change to purple. Upon cooling down to room temperature, green crystals of the product suitable for single crystal X-ray crystallography formed. The crystals were filtered off and washed with diethyl ether

(2x3 mL) (Yield = 155 mg, 66%). Elemental analysis: Calcd. for $C_{23}H_{42}BN_7Cl_3V$ (**5**): C, 47.20; H, 7.18; N, 16.76; Found: C, 47.52; H, 7.21; N,17.19%. IR(Nujol): ν(B-H) 2548(m); ν(V-Cl) 326(s), 303(s) cm^{-1}.

$(nBu_4N)[Tp^*VCl_3]$ (6). A solution of $(nBu_4N)Cl$ (113 mg, 0.4 mmol) and **2** (0.2 g, 0.4 mmol) in 10 mL of CH_3CN was stirred for 2 hours. The volume of the green solution was reduced under vacuum at room temperature to 5 ml then 20 ml diethyl ether were added and left overnight resulting in green crystals of the product which was collected by filtration, washed with diethyl ether (2x3 mL) (Yield = 193 mg, 69%). Elemental analysis: Calcd. for $C_{31}H_{58}BN_7P_2Cl_3V$ (**6**): C, 53.37; H, 8.32; N, 14.06; Found: C, 53.81; H, 8.56; N, 13.36%. IR(Nujol): ν(B-H) 2534(m); ν(V-Cl) 330(s), 299(s) cm^{-1}.

$(Et_4N)[Tp^*VBr_3]$ (7). A solution of KTp* (580 mg, 1.72 mmol) in 10 mL of CH_3CN was slowly added to a solution of VBr_3 (500 mg, 1.72 mmol) in 15 mL of CH_3CN. The resultant mixture was stirred overnight then filtered through ™Celite into Et_4NBr (361 mg, 1.72 mmol). The yellow solution was refluxed for 2 hours and then reduced in volume at room temperature to 5 mL. Addition of 25 mL of Et_2O resulted in an orange product which was collected by filtration, washed with diethyl ether (2x3 mL) and recrystallized from an CH_3CN/ diethyl ether mixture to give orange crystals suitable for single crystal X-ray crystallography (Yield = 567 mg, 46%). Elemental analysis: Calcd. for $C_{23}H_{42}BN_7Br_3V$ (**7**): C, 38.44; H, 5.84; N, 13.65; Found: C, 38.37; H, 5.76; N, 13.66 %. IR(Nujol): ν(B-H) 2553(m); ν(V-Br)279(s), 254(s) cm^{-1}.

$(Et_4N)[Tp^*VF_3]\cdot H_2O$ (8). A solution of $(Et_4N)F$ (181 mg, 1.21 mmol) and **2** (197 mg, 0.4 mmol) in 20 mL of CH_3CN was stirred overnight. The resulting green solution was

reduced under vacuum at room temperature to 5 mL and treated with 20 mL diethyl ether to yield green crystals of the product which were filtered, washed with diethyl ether (2x3 mL) and recrystallized from CH_3CN/ diethyl ether to give bright green crystals suitable for single crystal X-ray crystallography (Yield = 139 mg, 60%). Elemental analysis: Calcd. for $C_{23}H_{44}BN_7F_3OV$ (**8**): C, 49.92; H, 8.01; N, 17.72; Found: C, 50.11; H, 7.86; N, 17.89 %. IR(Nujol): ν(B-H) 2522(m); ν(V-F) 775(s) cm^{-1}.

$[Tp^*V(DMF)_3](PF_6)_2$ (9). A solution of $TlPF_6$ (70 mg, 0.2mmol) in 3 mL of DMF was added to **2** (50 mg, 0.1 mmol) in 5 mL of DMF which led to the instantaneous precipitation of a white solid with the color of the solution slowly changing to red. The solution was stirred overnight, filtered through ™Celite then layered with benzene which diffused into the red filtrate to yield red crystals suitable for single crystal X-ray crystallography which were filtered and washed with diethyl ether (2x3 mL) (Yield = 45 mg, 52.5%). Elemental analysis: Calcd. for $C_{24}H_{42}BN_9O_3P_2F_{12}V$ (**9**): C, 33.63; H, 4.90; N, 14.71; Found: C, 33.47; H, 5.01; N,14.76 %. IR(Nujol): ν(B-H) 2561(m), ν(C=O) 1652(s) cm^{-1}.

Single Crystal X-Ray Diffraction

The X-ray single crystal data were collected on a Bruker-APEX CCD diffractometer at 110 K. Crystals were mounted on cryoloops in oil. The data sets were collected with Mo-Kα radiation (k = 0.71073 Å) as four *ω*-scans at a 0.3–0.4° step width. Data integration and processing, Lorentz-polarization and absorption corrections were performed using the Bruker SAINT[220] and SADABS[221] software packages. Solutions and refinements of the crystal structures were performed using the SHELXL[222] suite of programs within the graphical interface X-SEED.[223] The structures were solved by direct methods and refined by alternating cycles of full-matrix least-squares methods on F^2, using SHELXL which resolved all non-hydrogen atoms. All non-hydrogen atoms were refined anisotropically for the final refinement cycles. The hydrogen atoms were located using difference Fourier maps, assigned with isotropic displacement factors and included in the final refinement cycles by use of either geometrical constraints (HFIX for hydrogen atoms with parent carbon atoms) or restraints (DFIX for hydrogen atoms with parent nitrogen or oxygen atoms). A summary of the crystallographic data and unit cell parameters, conditions related to data collection and some features of the structural refinements are provided in Table 2.1 and Table 2.2. Selected metal–ligand bond distances and angles are provided in Table 2.3 for compounds **3-5** and in Table 2.4 for compound **6-8**.

Table 2.1 Crystal structural data and refinement parameters for compounds **3–6**

Compound	**(3)**	**(4)**	**(5)**	**(6)**
Space group	P-1	$P2_1/c$	Cc	$P2_1/c$
Unit cell	a = 8.9587(18) Å b =15.589(3) Å c =17.465(4) Å α=*101.16*(3)° β =95.83(3)° γ=95.02°	a = 9.7417(19) Å b = 61.577(12) Å c =16.864(3) Å β = 95.53(3)°	a = 17.598(4)Å b = 10.385(2)Å c = 16.984(3) Å β =111.87(3)°	a = 28.470(6) Å b = 14.224(3) Å c = 18.359(4) Å β = 90.83(3)°
Unit cell volume, V	2366.2(8) Å^3	10069(3) Å^3	2880.5(10) Å^3	7434(3) Å^3
Z	2	8	4	8
Density, ρ_{calc}	1.417 g/cm^3	1.310 g/cm^3	1.348 g/cm^3	1.245 g/cm^3
Abs. coeff., μ	0.604mm^{-1}	0.462 mm^{-1}	0.648 mm^{-1}	0.518 mm^{-1}
Crystal color and habit	green block	Green block	dark-green block	green block
Crystal size	0.20 x 0.20 x 0.10 mm	0.18 x 0.13 x 0.12 mm	0.16 x 0.13 x 0.10 mm	0.18x0.17x0.07 mm
Temperature	110 K	110 K	110 K	110 K
Radiation, λ	Mo-Kα, 0.71073 Å	Mo-Kα, 0.71073 Å	Mo-Kα, 0.71073 Å	Mo-Kα, 0.71073 Å
Min. and max. θ	1.97 to 27.51º	1.79 to 21.05º	2.32 to 24.31º	1.60 to 20.93º
Reflections collected	15525[R_{int} =0.0163]	67346 [R_{int} =0.0628]	12623 [R_{int} =0.0312]	46894 [R_{int} = 0.0790]
Independent reflections	10411	10847	4613	7842
Data/parameters/restraints	10411/572/0	10847/1191/0	4613/330/2	7842/803/0
R [$F_o > 4\sigma(F_o)$]	R_1 = 0.0519 wR_2 = 0.116	R_1 = 0.0567 wR_2 = 0.0818	R_1 = 0.0302 wR_2 = 0.0641	R_1 = 0.0693 wR_2 = 0.1403
G.o.f. on F^2	1.026	1.117	1.069	1.028
Max./min. residual densities, e·Å^{-3}	1.14, -0.68	0.33, -0.37	0.2, -0.3	1.2, –0.57

$R_1 = \Sigma [(F_o - F_o)] / \Sigma (F_o)$. $wR_2 (F_{o2}) = \{ \Sigma [w(F_{o2} - F_{c2})_2 / \Sigma [w(F_{o2})_2] \}_{1/2}$.

Table 2.2 Crystal structural data and refinement parameters for compounds **7–9**

Compound	**(7)**	**(8)**	(9**)**
Space group	*Cc*	*Cmc2$_1$*	*P-3*
Unit cell	*a* = 17.686(4) Å *b* = 10.535(2) Å *c* = 17.163(3) Å β = 111.24(3)°	*a* = 12.169(2) Å *b* = 15.627(3) Å *c* = 15.320(3) Å	*a* = 12.3550(17) Å *b* = 12.3550(17) Å *c* = 14.651(3) Å β = 120.00 °
Unit cell volume, *V*	2980.6(10) Å^3	2913.4(10) Å^3	1936.8(5) Å^3
Z	4	4	2
Density, ρ_{calc}	1.600 g/cm^3	1.303 g/cm^3	1.470 g/cm^3
Abs. coeff., μ	4.380 mm^{-1}	0.392 mm^{-1}	0.436 mm^{-1}
Crystal color and habit	Bright orange block	Bright green needle	red-brown block
Crystal size	0.18 x 0.10 x 0.08 mm	0.16 x 0.11 x 0.07 mm	0.11x0.10x0.09 mm
Temperature	110 K	110 K	110 K
Radiation, λ	Mo-Kα, 0.71073 Å	Mo-Kα, 0.71073 Å	Mo-Kα, 0.71073 Å
Min. and max. θ	2.29 to 19.73º	2.12 to 27.67º	1.39 to 27.57º
Reflections collected	7912 [R_{int} =0.0292]	16994 [R_{int} =0.2242]	21837 [R_{int} = 0.1142]
Independent reflections	2646	3545	2968
Data/parameters/restraints	2646/330/2	3545 /208 /1	2968 /219/0
R [$F_o > 4\sigma(F_o)$]	R_1 = 0.0248 wR_2 = 0.0570	R_1 = 0.0271 wR_2 = 0.0724	R_1 = 0.1427 wR_2 = 0.3951
G.o.f. on F^2	1.023	1.085	1.558
Max./min. residual densities, e·Å^{-3}	0.38, -0.3	1.23, -0.92	1.06, –0.9

$R_1 = \Sigma [(F_o - F_o)] / \Sigma (F_o)$. $wR_2 = \{ \Sigma [w(F_{o2} - F_{c2})_2 / \Sigma [w(F_{o2})_2] \}_{1/2}$.

Table 2.3 Selected bond distances (Å) and bond angles (°) for **3-5**

Compound **3**	Distance (Å)		Angle (°)
V(1)–N(1)	2.136(2)	Cl(1)-V(1)-Cl(2)	97.51(2)
V(1)–N(3)	2.116(2)	Cl(1)-V(1)-Cl(3)	92.26(2)
V(1)–N(5)	2.125(2)	Cl(2)-V(1)-Cl(3)	93.19(2)
V(1)– Cl(1)	2.3238(9)	Cl(1)-V(1)-N(1)	91.42(5)
V(1)– Cl(2)	2.347(1)	Cl(1)-V(1)-N(3)	90.53(5)
V(1)– Cl(3)	2.376(1)	Cl(1)-V(1)-N(5)	171.58(6)
V(1) … V(2)	8.629(1)	N(1)-V(1)-N(3)	84.93(7)
Compound **4**	Distance (Å)		Angle (°)
V(1)–N(1)	2.137(3)	Cl(1)-V(1)-Cl(2)	92.06(4)
V(1)–N(3)	2.143(3)	Cl(1)-V(1)-Cl(3)	94.65(4)
V(1)–N(5)	2.158(3)	Cl(2)-V(1)-Cl(3)	93.54(4)
V(1)– Cl(1)	2.334(1)	Cl(1)-V(1)-N(1)	175.74(9)
V(1)– Cl(2)	2.362(1)	Cl(1)-V(1)-N(3)	92.38(9)
V(1)– Cl(3)	2.363(1)	Cl(1)-V(1)-N(5)	90.12(9)
V(1) … V(2)	12.853(1)	N(1)-V(1)-N(3)	85.1(1)
		N(1)-V(1)-N(5)	86.3(1)
Compound **5**	Distance (Å)		Angle (°)
V(1)–N(1)	2.138(2)	Cl(1)-V(1)-Cl(2)	93.07(3)
V(1)–N(3)	2.148(2)	Cl(1)-V(1)-Cl(3)	92.79(3)
V(1)–N(5)	2.151(3)	Cl(2)-V(1)-Cl(3)	94.23(3)
V(1)– Cl(1)	2.3422(8)	Cl(1)-V(1)-N(1)	90.97(6)
V(1)– Cl(2)	2.367(1)	Cl(1)-V(1)-N(3)	176.22(6)
V(1)– Cl(3)	2.354(1)	Cl(1)-V(1)-N(5)	90.84(6)
V(1) … V(2)	10.175(1)	N(1)-V(1)-N(3)	86.21(8)
		N(1)-V(1)-N(5)	83.68(8)

Table 2.4 Selected bond distances (Å) and bond angles (°) for **6**-**8**

Compound **6**	Distance (Å)		Angle (°)
V(1)–N(1)	2.184(4)	Cl(1)-V(1)-Cl(2)	93.56(6)
V(1)–N(3)	2.135(4)	Cl(1)-V(1)-Cl(3)	93.03(5)
V(1)–N(5)	2.134(4)	Cl(2)-V(1)-Cl(3)	92.09(6)
V(1)– Cl(1)	2.349(2)	Cl(1)-V(1)-N(1)	89.8(1)
V(1)– Cl(2)	2.287(2)	Cl(1)-V(1)-N(3)	88.9(1)
V(1)– Cl(3)	2.344(2)	Cl(1)-V(1)-N(5)	172.5(1)
V(1) … V(2)	8. 84(4)	N(1)-V(1)-N(3)	85.1(1)
Compound **7**	Distance (Å)		Angle (°)
V(1)–N(1)	2.147(5)	Br(1)-V(1)-Br(2)	92.07(4)
V(1)–N(2)	2.149(5)	Br(1)-V(1)-Br(3)	93.91(4)
V(1)–N(3)	2.157(6)	Br(2)-V(1)-Br(3)	92.15(4)
V(1)– Br(1)	2.521(1)	Br(1)-V(1)-N(1)	174.6(1)
V(1)– Br(2)	2.486(1)	Br(1)-V(1)-N(3)	89.5(1)
V(1)– Br(3)	2.519(2)	Br(1)-V(1)-N(5)	91.6(1)
V(1) … V(2)	10.293(1)	N(1)-V(1)-N(3)	87.0(2)
Compound **8**	Distance (Å)		Angle (°)
V(1)–F(1)	1.929(1)	F(1)-V(1)-N(1)	90.93(6)
V(1)–F(2)	1.843(1)	F(1)-V(1)-N(2)	174.64(5)
V(1)–N(1)	2.148(2)	F(1)-V(1)-F(2)	92.12(5)
V(1)– N(2)	2.116(1)	N(1)-V(1)-N(2)	83.73(6)
V(1) … V(2)	9.903(1)		
Compound **9**	Distance (Å)		Angle (°)
V(1)–O(1)	1.994(4)	O(1)-V(1)-O(1A)	89.8(2)
V(1)–O(1A)	1.993(7)	O(1)-V(1)-N(1)	90.9(1)
V(1)–N(1)	2.083(3)	O(1)-V(1)-N(1A)	92.1(2)
V(1)– N(1A)	2.082(2)		
V(1) … V(2)	9.72(1)		

Results and Discussion

Syntheses and Infrared Spectral Studies

The precursors **1-2** were synthesized following reported procedures.[218,224] Compounds **3-8** were synthesized by a substitution reaction of the coordinated solvent molecule in $TpVX_2THF$ {where X = Cl or Br) with the corresponding halide in a molar ratio of 1:1 in acetonitrile. Compound **9** was prepared by abstracting chloride from Tp^*VCl_2THF in DMF using $TlPF_6$. All compounds are air-sensitive in solution but more stable in the solid state. Exposing an acetonitrile solution of **4** to air then layering with Et_2O results in bright green crystals of the decomposition product $PPN[VO_2Cl_2]$ whose composition was determined using single crystal X-ray methods.

Compounds **3-9** exhibit characteristic bands in the *ν*(B-H) stretching region (Table 2.5).[67,72] The IR spectrum of **3** exhibits *ν*(B-H) stretches at 2520 cm^{-1}. Similarly, the *ν*(B-H) stretches observed for **4, 5** and **6** appear at 2550, 2547 and 2536 cm^{-1} respectively which are slightly shifted compared to the corresponding mode of the precursor **1** (2543 cm^{-1}).[72] For other compounds, the energies vary from 2522 cm^{-1} for **8** to 2553 cm^{-1} for **7** and 2561 cm^{-1} for **9**. The ν(C=N) (imine) stretching frequency of the pyrazol ring appears at ~1540 for the Tp* complexes and 1500 for the Tp complex.

The halide stretching *ν*(V-Cl) for **3** appears at 324 cm^{-1} whereas for **4-6** it is located at 327 cm^{-1}. In the case of **8** the metal fluoride feature appears at 775 cm^{-1} and for the weaker bromide ligand in **7** it shifts to 280 cm^{-1}.[225] The stretching mode of the ν(P=N) for the PPN^+ cation is observed for both **3** and **4** at 1587 cm^{-1} and the ν(C=O) stretch for DMF in **9** appears at 1652 cm^{-1}.

Table 2.5 Selected IR frequencies (cm^{-1}) for **1-9**

Compound	νB-H	ν(C=N)	ν(P=N)	ν(C=O)	ν(X) [225]	
1	2489(m)	1540(s)	-	-		
2	2542(m)	1544(s)	-	-		
3	2520(m)	1500(s)	1587(s)	-	323(s)	281(s)
4	2550(m)	1543(s)	1587(s)	-	327(s)	303(s)
5	2547(m)	1540(s)	-	-	329(s)	299(s)
6	2536(m)	1541(s)	-	-	327(s)	303(s)
7	2553(m)	1540(s)	-	-	280(s)	254(s)
8	2522(m)	1539(s)	-	-	775(s)	
9	2561(m)	1542(s)	-	1652(s)	-	-

s = strong, m = medium

Single Crystal X-Ray Diffraction Study

X-ray crystallographic studies of **3** revealed that it crystallizes in the triclinic space group P-1 (Table 2.1) with trigonally distorted coordination geometry for the complex anion consisting of three nitrogen atoms from the Tp ligand and three terminal chlorides (Figure 2.2). The local symmetry deviates from the C_{3v} with bond angles, Cl1-V-Cl2 97.51(2), Cl1-V-Cl3 92.26(2), Cl2-V-Cl3 93.19(2) and distances V(1)–Cl(1) 2.3238(9), V(1)–Cl(2) 2.347(1), V(1)–Cl(3) 2.376(1). Both bond lengths and angles lie within the values for previously reported vanadium Tp or Tp* complexes.[218,219,224] The crystal contains a dichloromethane molecule of crystallization and the V----V separation is 8.629Å.

Complex **4** crystallizes in the monoclinic space group $P2_1/c$ (Table 2.1). The asymmetric unit contains two vanadium centers with a trigonally distorted octahedral environment for the complex anion consisting of three nitrogen atoms from the Tp* ligand and three terminal chlorides (Figure 2.3). The local symmetry of both centers is almost identical and deviates from ideal C_3v symmetry with a smaller variation in bond angles than **3**; Cl1-V-Cl2 92.06(4), Cl1-V-Cl3 94.65(4), Cl2-V-Cl3 93.54(4) and bond lengths; V(1)–Cl(1) 2.334(1), V(1)–Cl(2) 2.362(1), V(1)–Cl(3) 2.363(1) being evident. Both bond distances and angles lie within the values for previously reported vanadium Tp or Tp* complexes.[218,219,224] The large size of the PPN^+ cation is convenient as it reduces the V----V intermolecular distances [12.7Å] which is helpful for minimizing the dipolar zero-field quantum tunneling relaxation pathway.

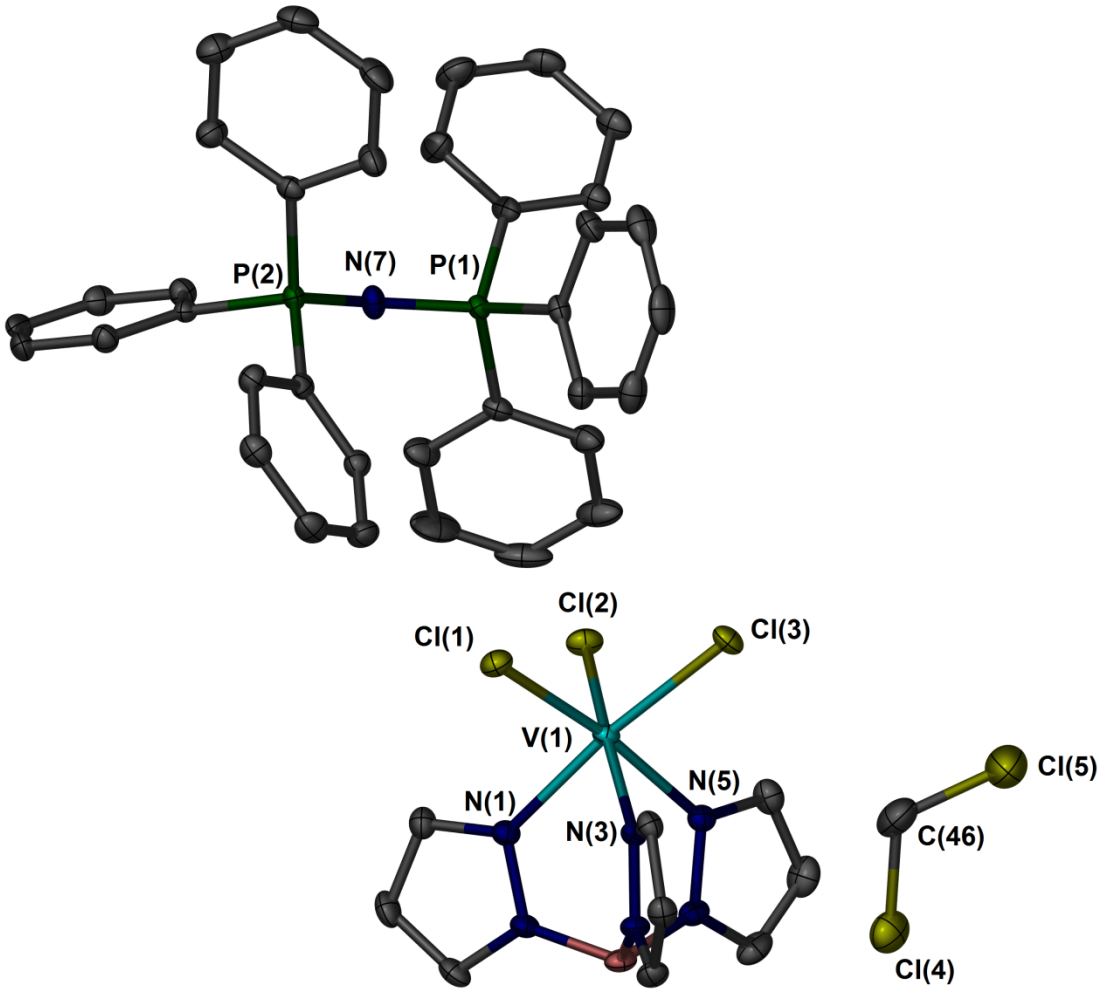

Figure 2.2 Thermal ellipsoid plots of PPN[$TpVCl_3$]·CH_2Cl_2 **3**. Ellipsoids are projected at the 50% probability level. Hydrogen atoms are omitted for the sake of clarity.

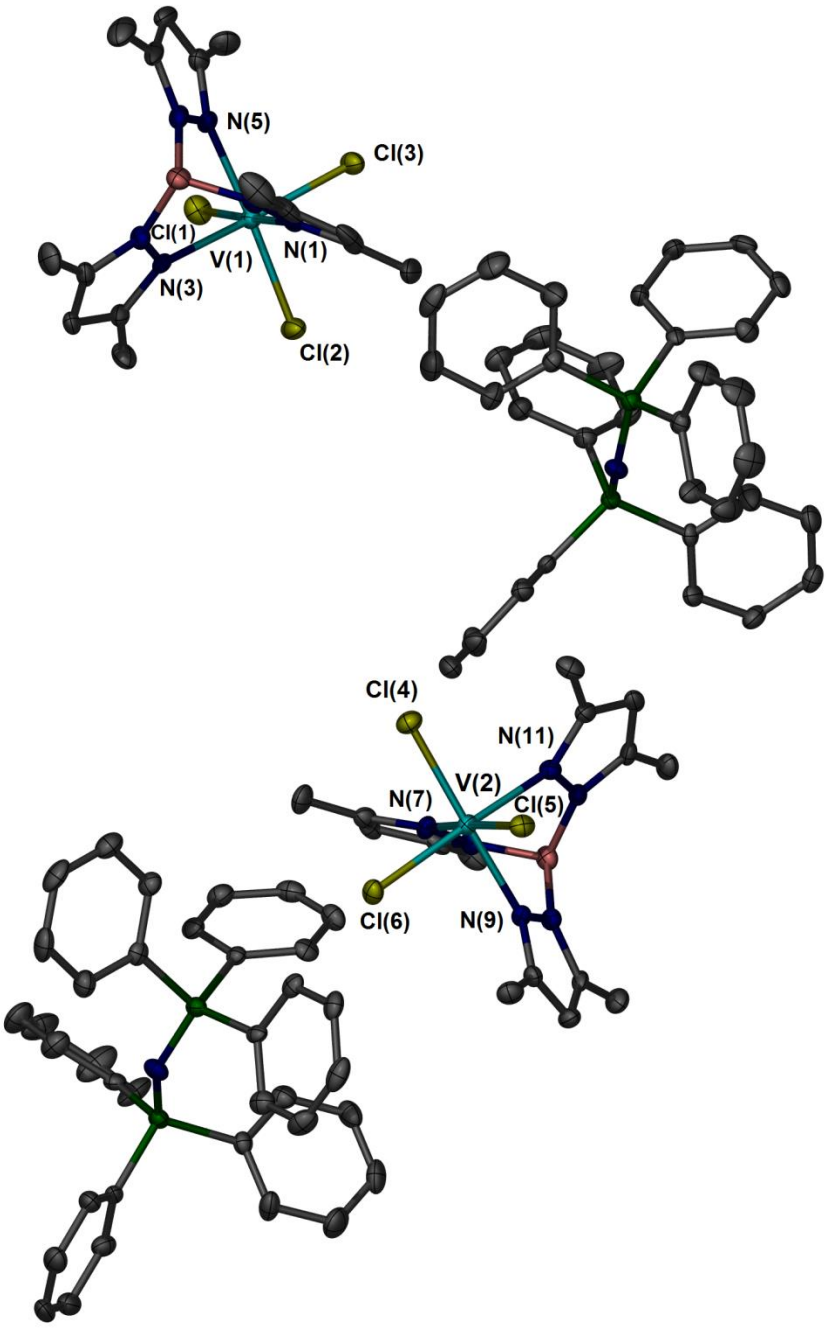

Figure 2.3 Thermal ellipsoid plots of PPN[Tp*VCl_3], **4**. Ellipsoids are projected at the 50% probability level. Hydrogen atoms are omitted for the sake of clarity.

The single crystal structure of **5** reveals that it crystallizes in the monoclinic space group C_c (Table 2.1). The coordination environment is essentially identical to **4** with a trigonally distorted octahedral environment of three nitrogen atoms from the Tp* ligand and three terminal chlorides (Figure 2.4). Similarly, the local symmetry deviates from ideal C_{3v} as evidenced by the angles, Cl1-V-Cl2 92.73(4), Cl1-V-Cl3 93.11(4), Cl2-V-Cl3 94.25(4), N1-V-N3 84.94(1), N1-V-N5 85.43(1), N3-V-N5 85.7(1) and distances V(1)–Cl(1) 2.3422(8), V(1)–Cl(2) 2.367(1), V(1)–Cl(3) 2.354(1). Both bond lengths and angles lie within the values for previously reported vanadium Tp or Tp* complexes.[218,219,224] Compound **5** has a smaller V-----V spacing of 10.17 Å.

Complex **6** crystallizes in the monoclinic space group $P2_1/c$ (Table 2.1) with an asymmetric unit similar to **4** with two vanadium centers with trigonally distorted octahedral environments consisting of three nitrogen atoms from Tp* ligand and three terminal chlorides (Figure 2.5). Similarly the local symmetry slightly deviates from C_{3v}: Cl1-V-Cl2 93.56(6), Cl1-V-Cl3 93.03(5), Cl2-V-Cl3 92.09(6), N1-V-N3 85.10(1), N1-V-N5 85.43(1), N3-V-N5 85.7(1) and V(1)–Cl(1) 2.349(2), V(1)–Cl(2) 2.287(2), V(1)–Cl(3) 2.344(2). Both sets of metrical parameters lie within the values for previously reported vanadium Tp and Tp* complexes.[218,219,224] The V-----V spacing in **6** is 8.84 Å.

Complex **7** is iso-structural with **5** and crystallizes in the monoclinic space group C_c (Table 2.2). The coordination environment is essentially identical to **4** with a trigonally distorted octahedral environment of three nitrogen atoms from a Tp* ligand and three terminal bromide ligands (Figure 2.6).

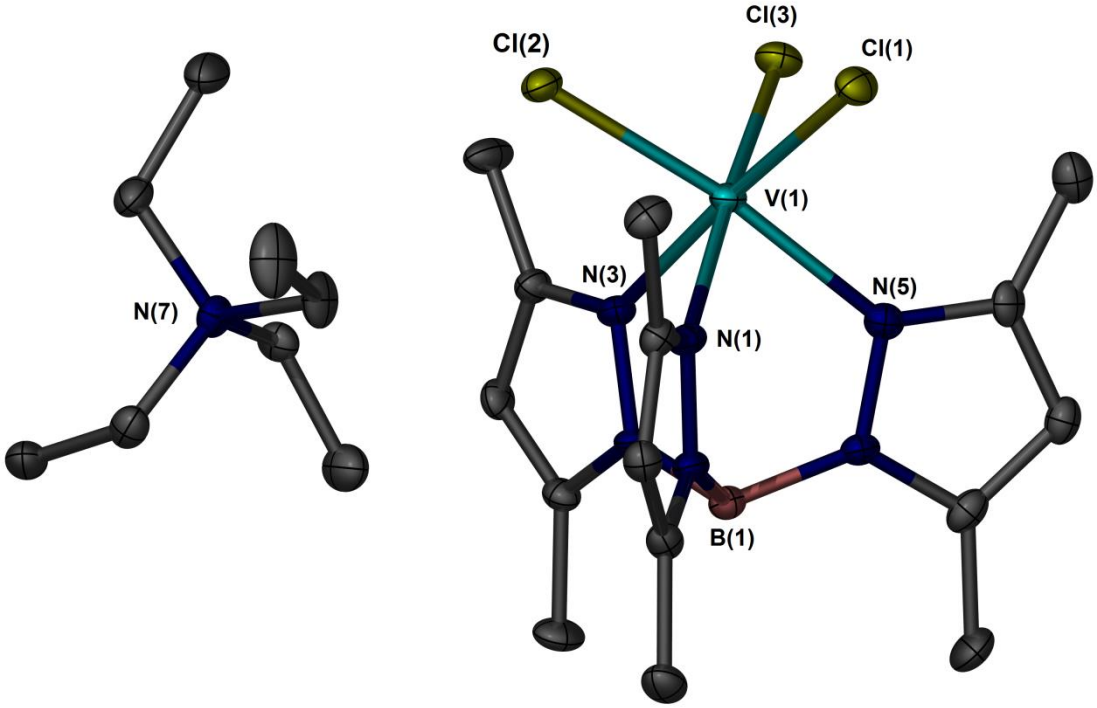

Figure 2.4 Thermal ellipsoid plots of $(Et_4N)[Tp^*VCl_3]$ **5**. Ellipsoids are projected at the 50% probability level. Hydrogen atoms are omitted for the sake of clarity.

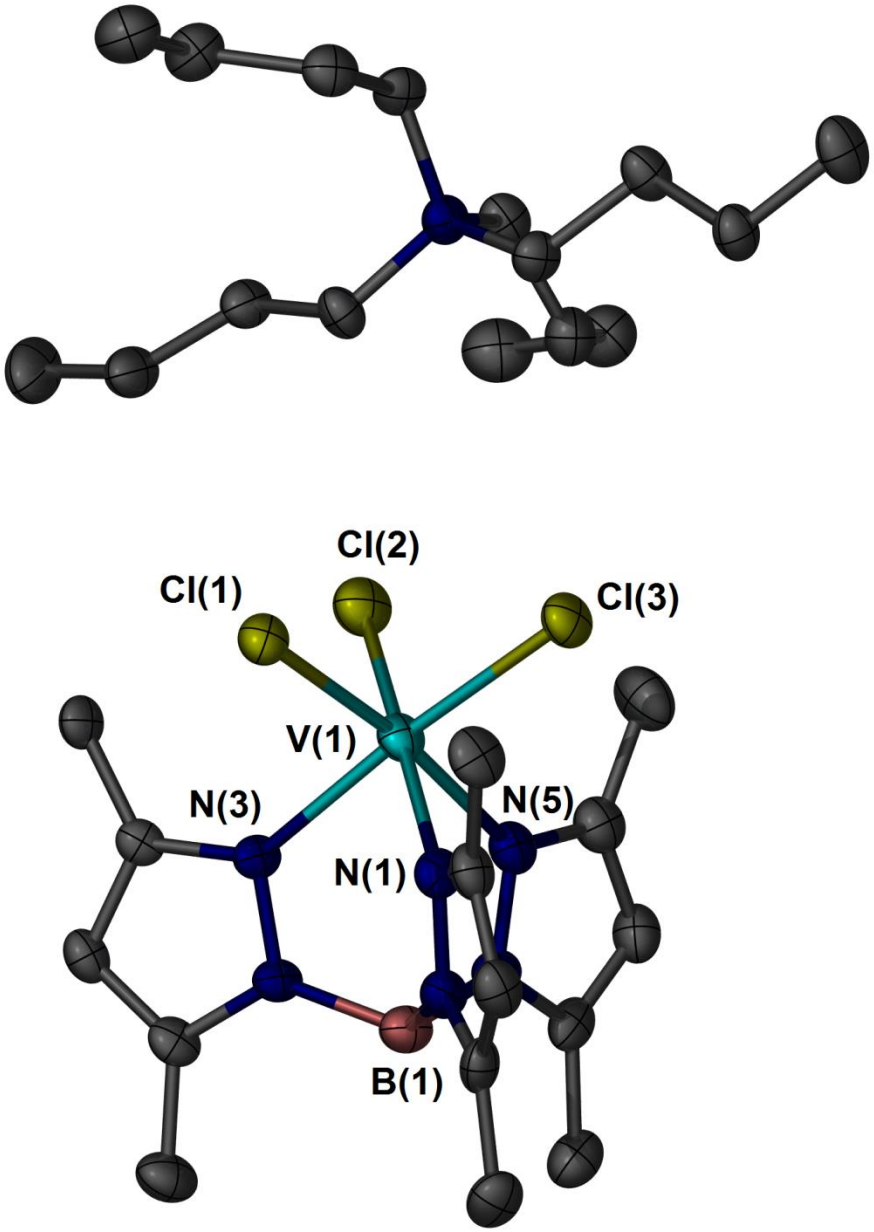

Figure 2.5 Thermal ellipsoid plots of $(Bu_4N)[Tp^*VCl_3]$ **6**. Ellipsoids are projected at the 50% probability level. Hydrogen atoms are omitted for the sake of clarity.

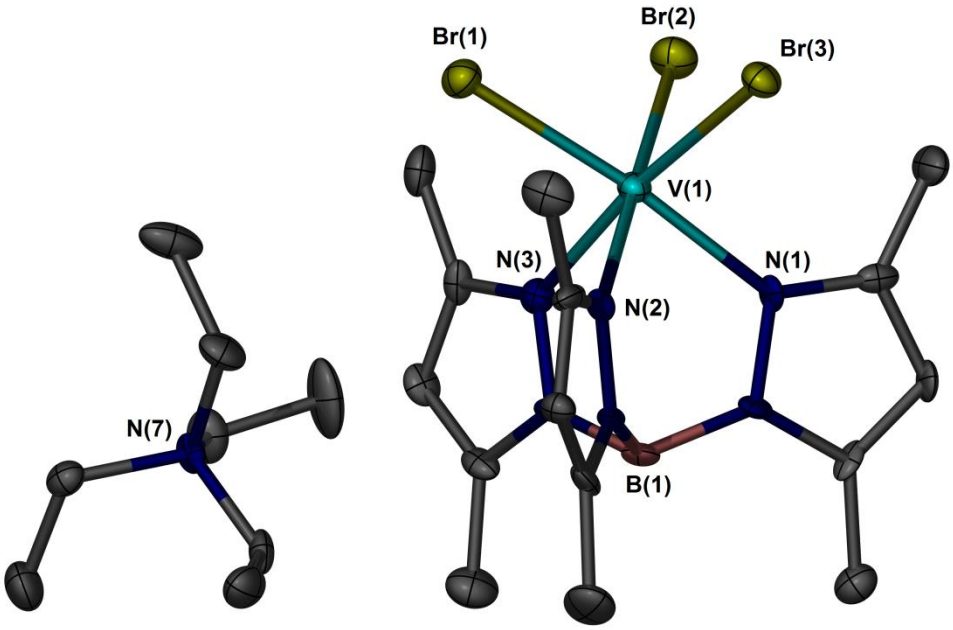

Figure 2.6 Thermal ellipsoid plots of $(Et_4N)[Tp^*VBr_3]$ **7**. Ellipsoids are projected at the 50% probability level. Hydrogen atoms are omitted for the sake of clarity.

The angles and distances within the immediate coordination sphere indicate distortion from ideal C_{3v} symmetry: Br1-V-Br2 92.07(4), Br1-V-Br3 93.91(4), Br2-V-Br3 92.15(4), and bond angles, V(1)–Br(1) 2.521(1), V(1)–Br(2) 2.486(1), V(1)–Br(3) 2.519(2). The V-Br distances lie within the values for previously reported vanadium bromide complexes.[226,227] The metal - metal spacing in **7** is 10.29 Å.

Complex **8** crystallizes in the orthorhombic space group $Cmc2_1$ (Table 2.2) in a trignoally distorted octahedral environment of three nitrogen atoms from the Tp* ligand and three terminal fluoride ligands (Figure 2.7). The local symmetry deviates from C_{3v} with slight differences in the bond angles, namely F1-V-F2 92.12(5), F1-V-F3 88.88(6), F2-V-F3 92.12(5) and bond distances V(1)–F(1) 1.929(1) Å, V(1)–F(2) 1.843(1) Å, V(1)–F(3) 1.929(1) Å. The V-F bond distances are slightly shorter than the values for previously reported vanadium(III) fluoride complexes.[228,229] The asymmetric unit contains a water molecule of crystallization that is engaged in hydrogen bonding with terminal fluoride ligands. The V------V spacing is 9.90 Å.

Complex **9** crystallizes in the hexagonal space group P-3 (Table 2.2) in a trignoally distorted octahedral environment of three nitrogen atoms from the Tp* ligand and three oxygen atoms of DMF ligands (Figure 2.8). The local symmetry is almost C_{3v} with practically identical bond angles, O1-V-O1A 89.8(2) and bond distances V(1)–O(1) 1.994(4) Å, V(1)–O(1A) 1.993(7) Å, V(1)–O(1B) 1.994(7) Å. The V-O bond distances lie within the values for previously reported vanadium(III) DMF complexes.[230] The V-------V spacing is 9.72 Å. Both the coordinated DMF molecules and the PF_6^- anions suffer from disorder which was solved by division over two sites with 50% occupancy.

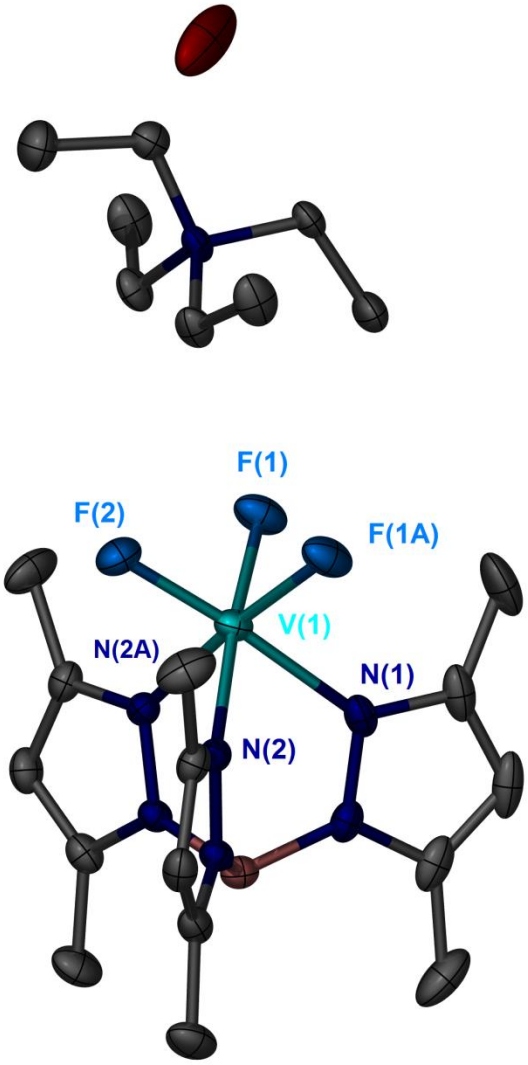

Figure 2.7 Thermal ellipsoid plots of $(Et_4N)[Tp^*VF_3]\cdot H_2O$ **8**. Ellipsoids are projected at the 50% probability level. Hydrogen atoms are omitted for the sake of clarity.

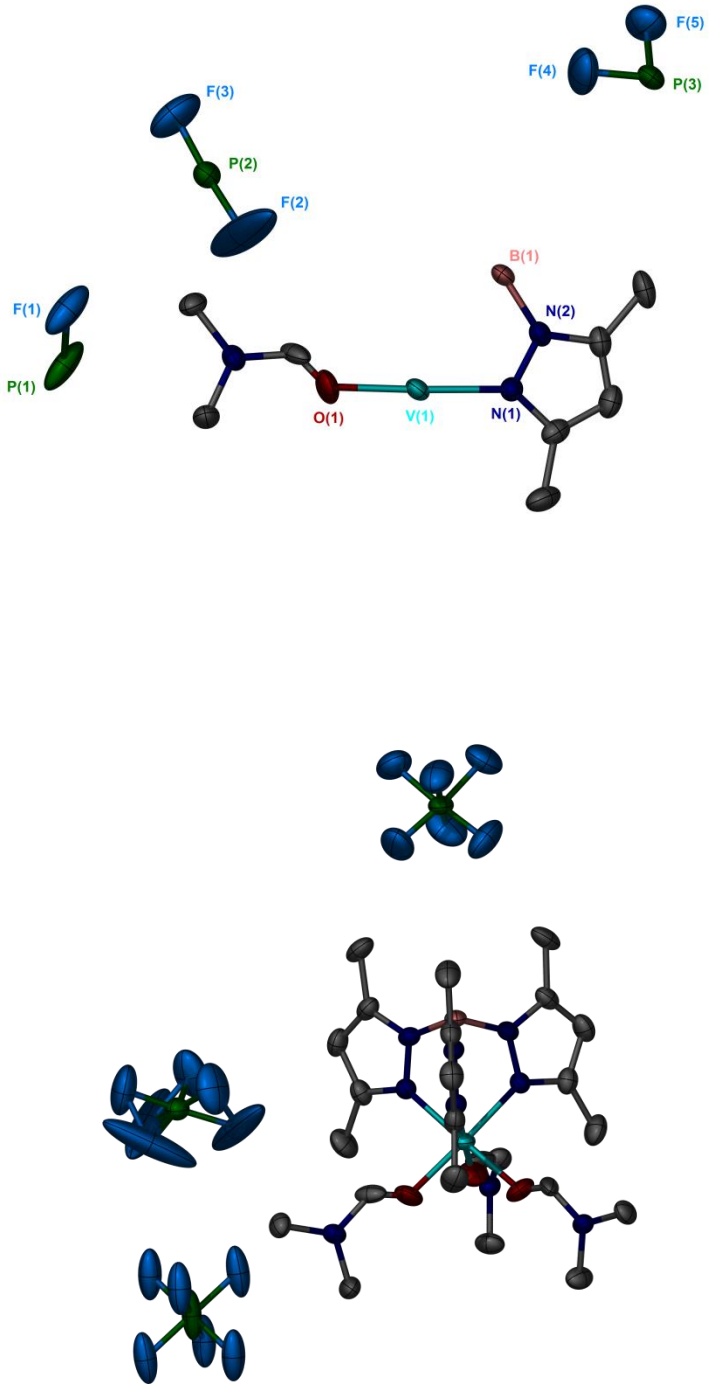

Figure 2.8 Thermal ellipsoid plots of; asymmetric unit of **9** (top), molecular structure of $[Tp^*V(DMF)_3](PF_6)_2$ **9** (bottom). Ellipsoids are projected at the 30% probability level. Hydrogen atoms are omitted for the sake of clarity.

Electronic Spectroscopy

Electronic absorption spectra were performed on a Shimadzu UV-1601PC spectrophotometer using air-free cuvette. Compounds **3-8** were measured in CH_2Cl_2, compound **9** was measured in anhydrous DMF (Figure 2.9, 2.10 and 2.11). The observed electronic absorption features for complexes **3-9** are listed in Table 2.6 along with their assignments. Typical electronic transitions for a d^2 octahedral molecule were observed.[225] The band corresponding to the $^3T_1g \rightarrow {}^3T_2g$ transition appeared at ~14,500 cm^{-1} whereas the $^3T_1g(P) \rightarrow {}^3T_1g(F)$ transitions were observed at ~21,500 cm^{-1}. The $^3T_1g \rightarrow {}^3A_2g$ is expected to lie at approximately 30,000 cm^{-1}, but they are obscured by the strong band at ~25,500 cm^{-1} which is assigned to a CT transition. Based on these observed transitions, the octahedral splitting parameters (B and 10 Dq) were determined using the Tanabe-Sugano diagram. Analysis of the spectrum for **3** revealed an octahedral splitting (10 Dq) of 15,986 cm^{-1}. Complexes **4-6** exhibit relatively similar 10 Dq values of 15,653, 15,608 and 15,585 cm^{-1} respectively. The octahedral field splittings (10 Dq) for complex **8** and **9** were found to be 17,512 cm^{-1} and 15,276 cm^{-1} respectively. These values of 10 Dq lies within the range of previously reported vanadium complexes. [225]

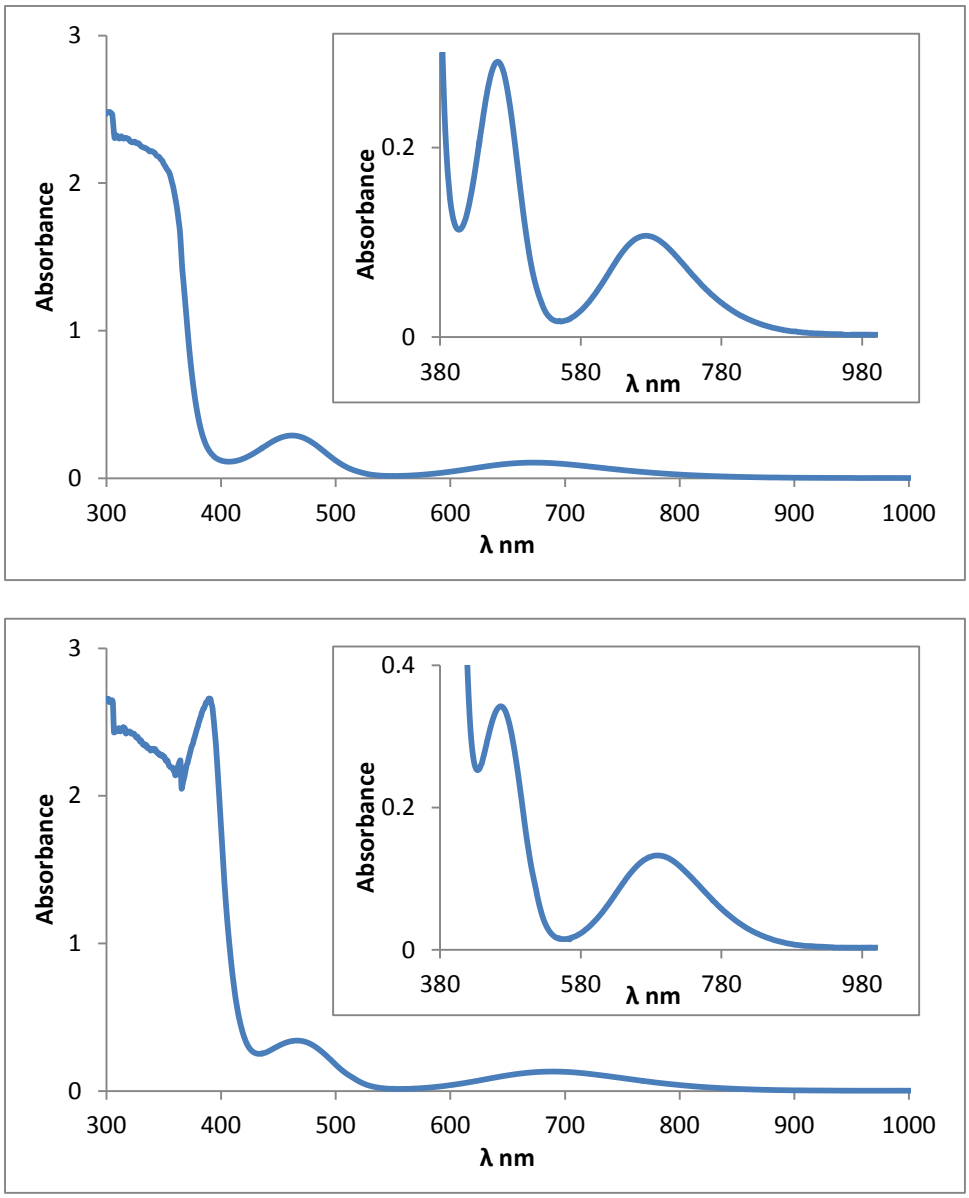

Figure 2.9 Electronic spectra of **3** (top) and **4** (bottom).

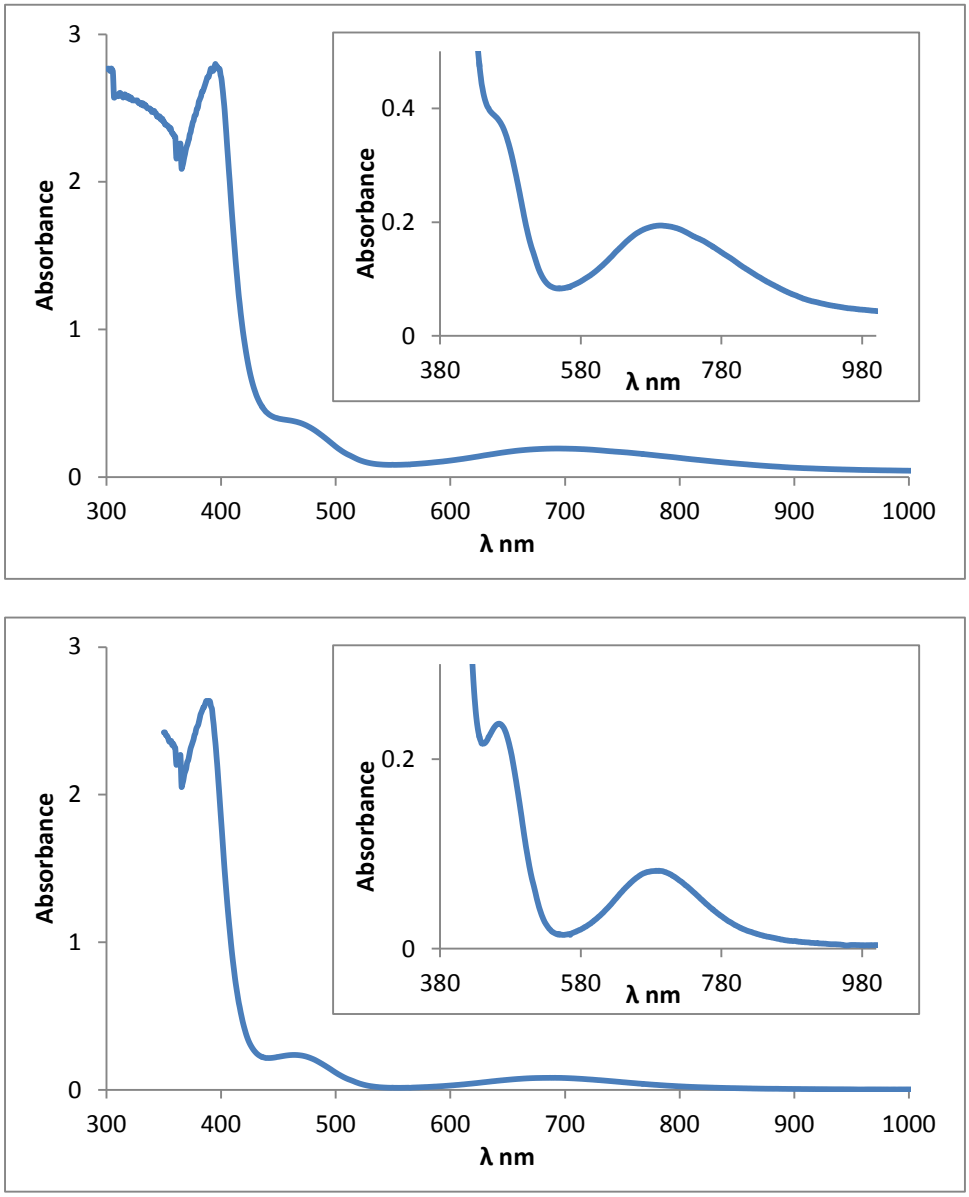

Figure 2.10 Electronic spectra of **5** (top) and **6** (bottom).

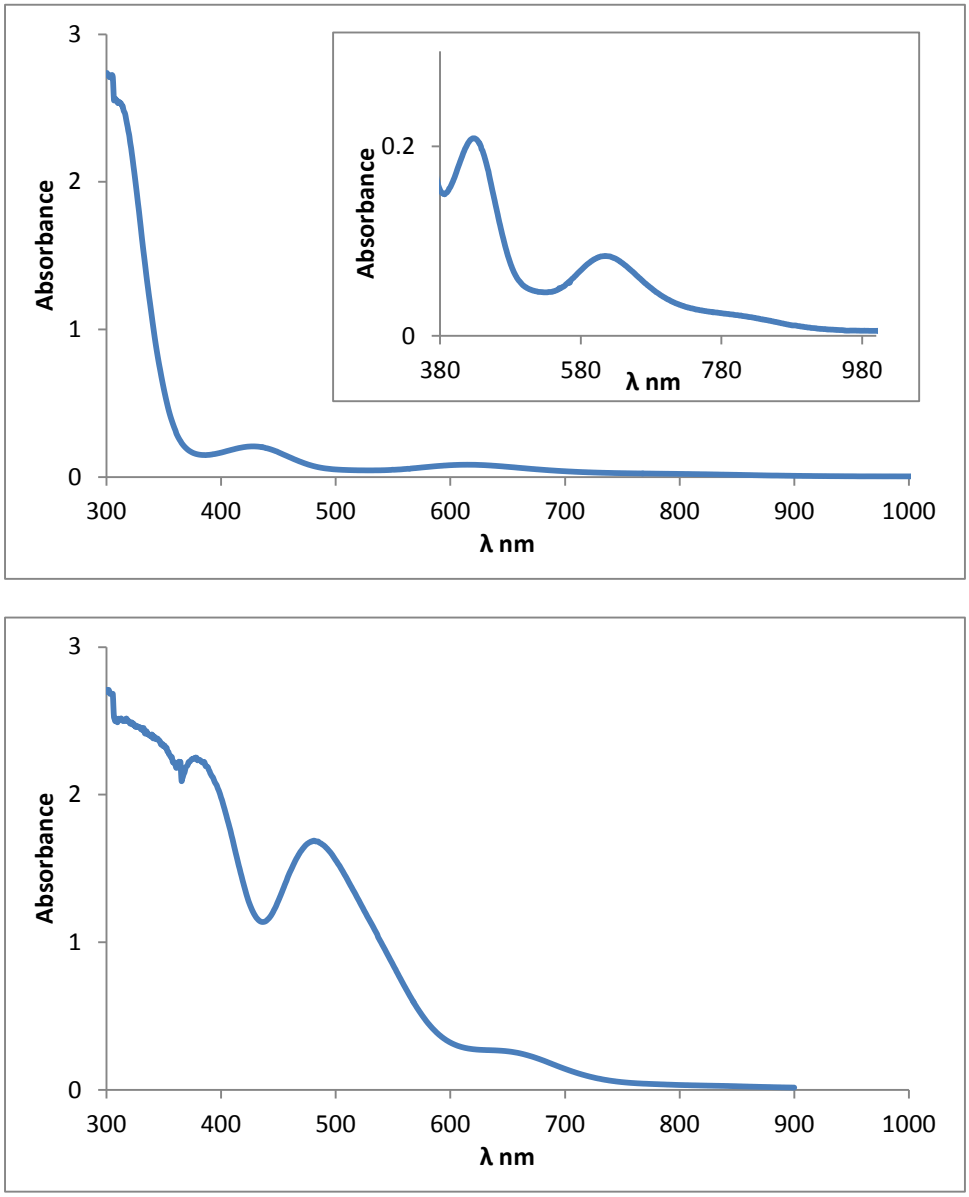

Figure 2.11 Electronic spectra of **8** (top) and **9** (bottom).

Table 2.6 Electronic transitions for complexes **3-9**

Compound	$^3T_1g \rightarrow {}^3T_2g$			$^3T_1g(P) \rightarrow {}^3T_1g(F)$			V_3 / $^3T_1g \rightarrow {}^3A_2g$				B (cm^{-1})	10 Dq (cm^{-1})
	nm	cm^{-1}	ε	nm	cm^{-1}	ε	nm	cm^{-1}	ε	predicted		
3	672	14,880	35	462	21,645	96	-	-	-	30,867	524	15986
4	688	14,534	28	465	21,505	68	390	25,641	350	30,188	539	15653
5	690	14,492	31	466	21,459	71	395	25,641	352	30,101	537	15608
6	691	14,471	20	464	21,551	59	388	25,773	355	30,057	536	15585
8	615	16,260	45	428	23,364	90	314	31,847	360	33,772	603	17,512
9	705	14,184	21	481	20,790	130	-	-	-	29,460	525	15,276

Magnetic Properties

The DC susceptibility data for samples of crushed crystals of compounds **1-9** were measured from 2-300 K using a plastic bag in an applied dc field of 1000 G on a Quantum Design SQUID, Model MPMS. The measurements at mK temperatures were performed in collaboration with Dr. Wolfgang Wernsdorfer in Grenoble, France using micro-SQUID techniques. All compounds showed a decrease in χT as the temperature is lowered, which, in this case, is an indication of large zero-field splitting. Zero field splitting parameters were calculated by fitting the reduced magnetization data using *ANISOFIT*.[231]

$TpVCl_2THF$ (1). The temperature dependent magnetic susceptibility of **1** exhibits a similar behavior to **1** (Figure 2.12a)**.**The room-temperature χT value of 0.92 emu·K·mol^{-1} is consistent with an isolated V^{III} ion with g = 1.8, Weiss constant, Θ = -6.5K and TIP of 0.48x10^{-3} emu·K·mol^{-1} (C= 0.81 emu·K·mol^{-1}). The χT value decreases with temperature which could be attributed to zero field splitting with a minor contribution of intermolecular dipole-dipole interactions. The field dependence of the magnetization data at temperatures between 2 and 4.5 K reveal a non-superposition of the iso-field lines indicating the presence of significant zero-field splitting (Figure 2.12b). Additionally, even at 7 T and 2 K, the magnetization is well below the saturation value of 2.0 μ_B expected for an S = 1 ground state with a g = 2.0 in the absence of zero-field splitting (Figure 2.12b, inset). The magnitude of zero-field splitting parameters were estimated using *ANISOFIT* which gave D = -8.8 cm^{-1} and E = 2.62 cm^{-1} with g = 1.46.

Tp*VCl$_2$THF (2). The room-temperature χT value of 0.93 emu·K·mol^{-1} for **2** (Figure 2.13a) is consistent with an isolated V^{III} ion with g = 1.74, Weiss constant, Θ = -3.5K and Temperature independent paramagnetism TIP of $7.0 \cdot 10^{-4}$ emu·K·mol^{-1} (C= 0.75 emu·K·mol^{-1}). The χT value decreases with temperature which could be attributed to zero field splitting with a minor contribution of intermolecular dipole-dipole interactions. The field dependence of the magnetization data at temperatures between 2 and 4.5 K reveal a non-superposition of the iso-field lines indicating the presence of significant zero-field splitting (Figure 2.13b). Additionally, even at 7 T and 2 K, the magnetization is well below the saturation value of 2.0 μ_B expected for an S = 1 ground state with a g = 2.0 in the absence of zero-field splitting (Figure 2.13b, inset). The calculated zero-field splitting parameters were found to be D = -18.53 cm^{-1} and E = 2.79 cm^{-1} with g = 1.63. The comparison of the axial zero field splitting parameter D in **1** (-8.8 cm^{-1}) and **2** (-18.53 cm^{-1}) suggests a direct relationship between the D value and the trigonal crystal field which is larger for the stronger π-donor Tp* ligand in **2.**

PPN[TpVCl$_3$]·CH$_2$Cl$_2$ (3). The room-temperature χT vs. T value of 0.85 emu·K·mol^{-1} is consistent with one isolated V^{III} spin center with g = 2.0 and Θ = -50K (Figure 2.14a). The value of χT decreases as the temperature is lowered which is attributable to zero-field splitting and/or intermolecular interactions. The non-superposition of the iso-field lines at temperatures between 2 and 4.5 K (Figure 2.14b) and the lack of saturation of the magnetization curve indicate the presence of significant zero-field splitting. ANISOFIT led to values of D = -16.0 cm^{-1}, E = 3.0 cm^{-1} and g = 1.26. The ac magnetic susceptibility data under an applied dc field did not show a signal.

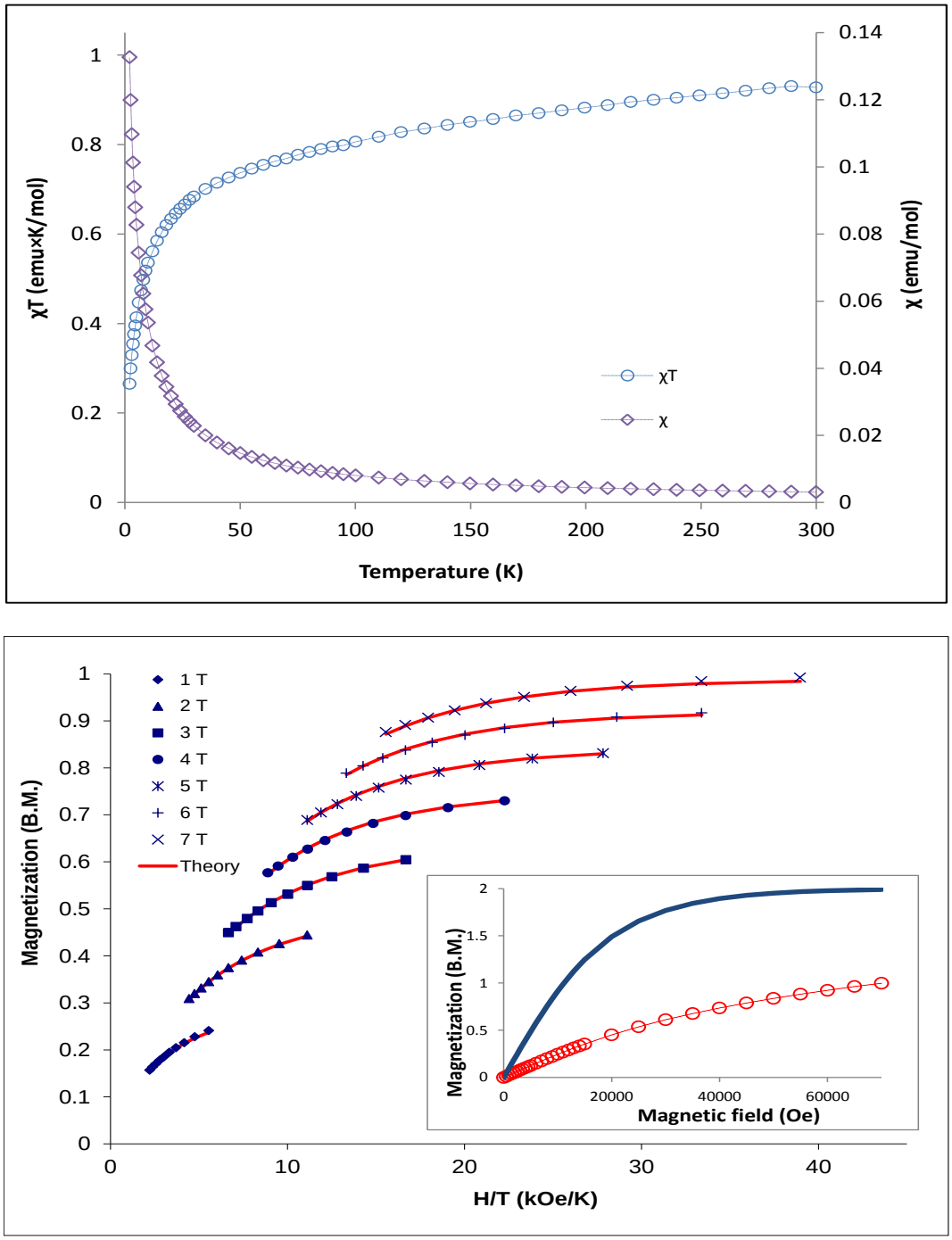

Figure 2.12 (a) Temperature dependence of χ (◊) and χT product (o) for **1**. (b) Reduced magnetization data at different external fields. Solid lines correspond to the best-fit curves using *ANISOFIT* (D = -8.8 cm^{-1}, E = 2.62 cm^{-1}, g = 1.46). Inset: Field dependent magnetization for **1** (o). The solid line corresponds to the Brillouin function (S = 1, g_{avg} = 2.0).

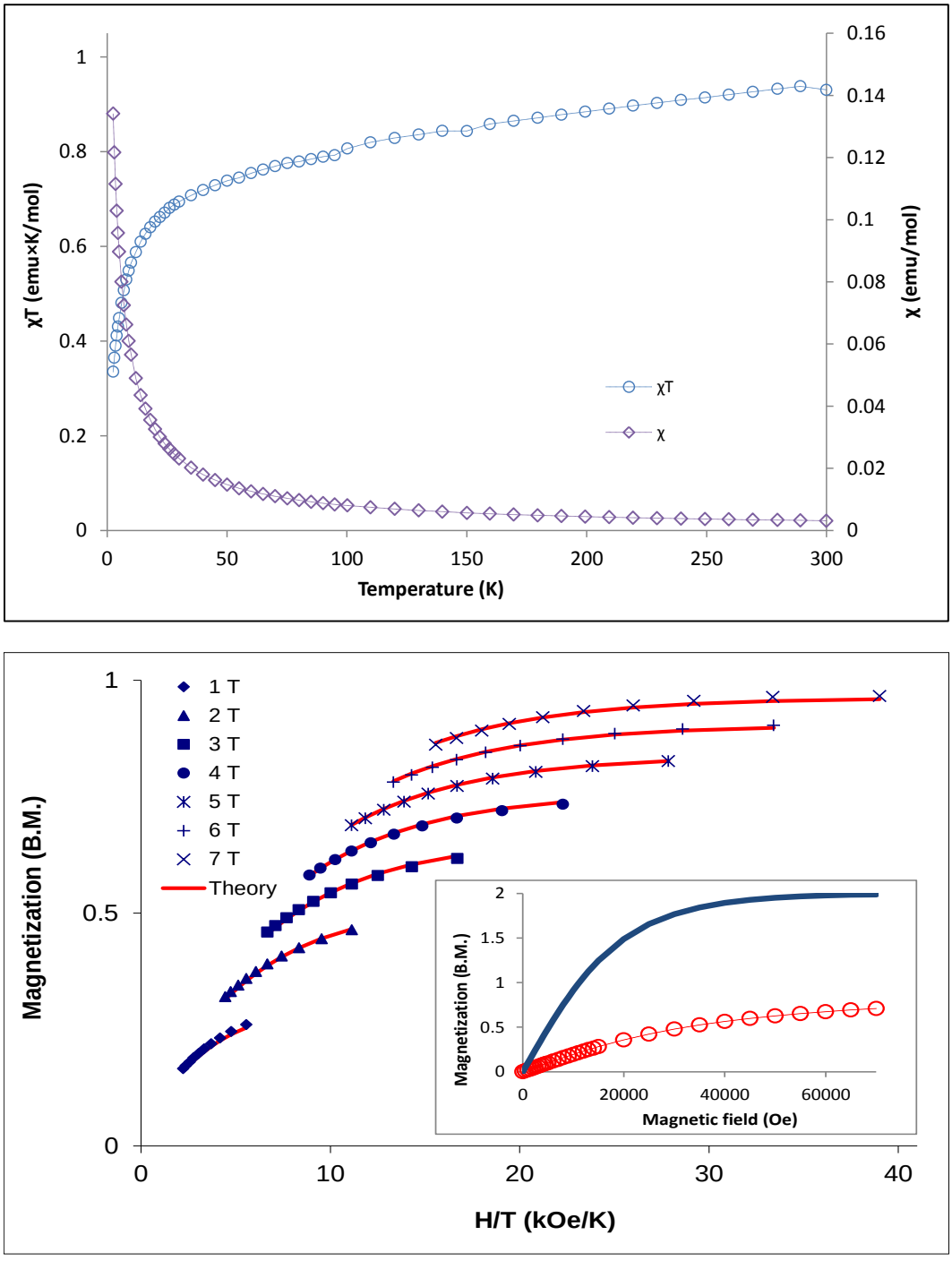

Figure 2.13 (a) Temperature dependence of χ (◊) and χT product (o) for **2**. (b) Reduced magnetization data at different external fields. Solid lines correspond to the best-fit curves using *ANISOFIT* (D = -18.53 cm^{-1}, E = 2.79 cm^{-1}, g = 1.63). Inset: Field dependent magnetization for **2** (o). The solid line corresponds to the Brillouin function (S = 1, g_{avg} = 2.0).

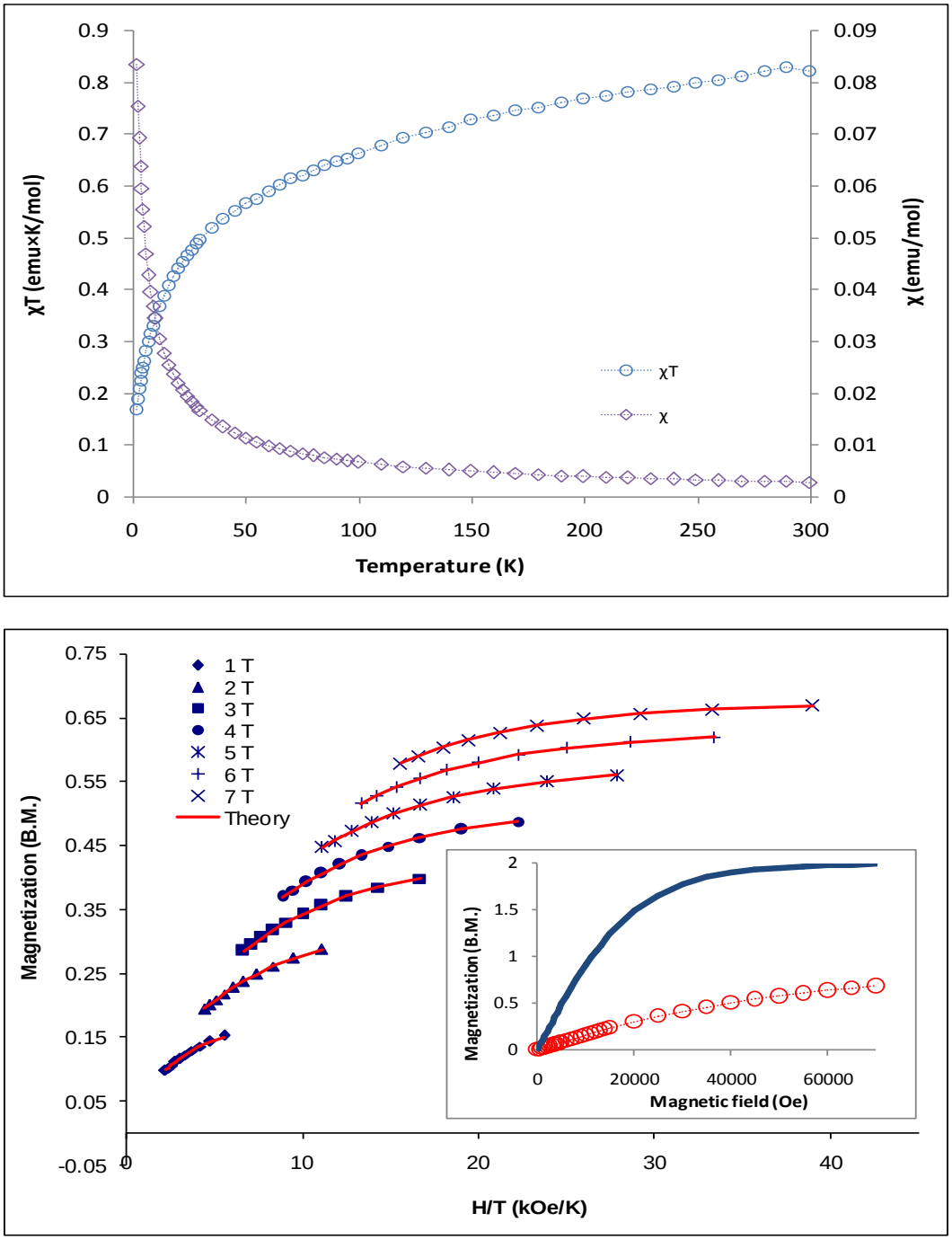

Figure 2.14 (a) Temperature dependence of χ (◊) and χT product (o) for **3**. (b) Reduced magnetization data at different external fields. Solid lines correspond to the best-fit curves using *ANISOFIT* (D = -16.0 cm^{-1}, E = 3.0 cm^{-1}, g = 1.26). Inset: Field dependent magnetization for **3** (o). The solid line corresponds to the Brillouin function (S = 1, g_{avg} = 2.0).

PPN[Tp*VCl$_3$] (4). Temperature-dependent magnetic susceptibility data for **4** are dominated by the signature of large zero-field splitting for the S = 1 state (Figure 2.15a). The room-temperature χT value of 0.87 emu·K·mol^{-1} is consistent with an isolated V^{III} ion with g = 2.0 and a Weiss constant, Θ = -50K (C= 1 emu·K·mol^{-1}). The χT value decreases with temperature which could be attributed to zero field splitting with a minor contribution of intermolecular dipole-dipole interactions which should not be appreciable given the large V---V intermolecular distances (12.7 A). The field dependence of the magnetization data at temperatures between 2 and 4.5 K reveal a non-superposition of the iso-field lines indicating the presence of significant zero-field splitting (Figure 2.15b). Additionally, even at 7 T and 2 K, the magnetization is well below the saturation value of 2.0 μ_B expected for an S = 1 ground state with a g = 2.0 in the absence of zero-field splitting (Figure 2.15b, inset). The magnitude of zero-field splitting parameters were estimated using *ANISOFIT* which gave D = -30.0 cm^{-1} and E = -0.8 cm^{-1} with g = 1.54. Similarly, the larger D value of **4** compared to **3** indicates a direct relationship between the D value and the magnitude of the trigonal crystal field which is larger for the stronger π-donor Tp* ligand in **4.**

Given that mononuclear complexes with large zero field splittings recently have been found to exhibit SMM behavior[142,143,146,172,232], the magnetization reversal dynamics of compound **4** were probed with the use of AC susceptometry. The ac magnetic susceptibility data under a 1000 Oe applied dc field manifest slow relaxation of the magnetization (Figure 2.16a).

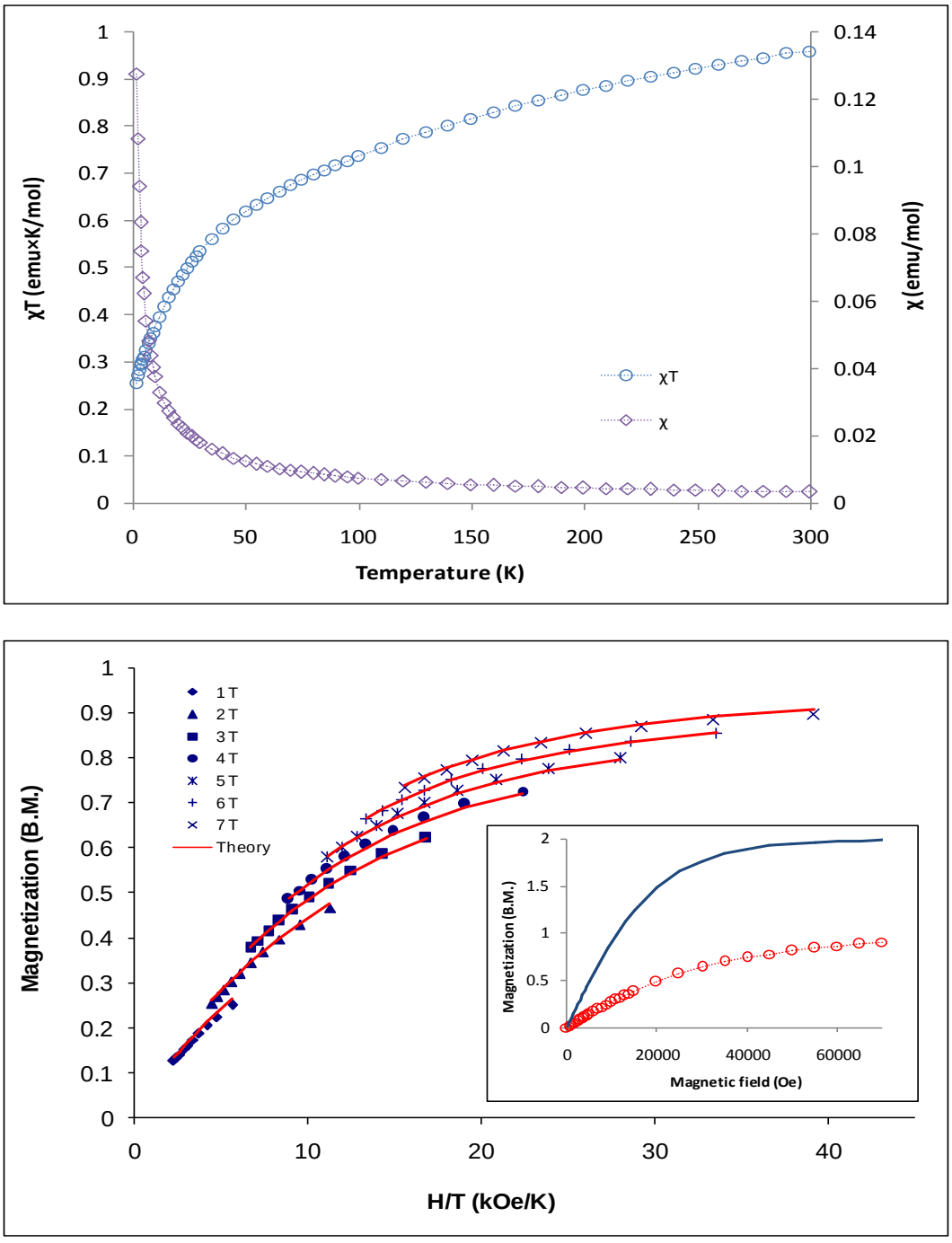

Figure 2.15 (a) Temperature dependence of χ (◊) and χT product (o) for **4**. (b) Reduced magnetization data at different external fields. Solid lines correspond to the best-fit curves using *ANISOFIT* (D = -30.0 cm^{-1}, E = -0.81 cm^{-1}, g = 1.85). Inset: Field dependent magnetization for **4** (o). The solid line corresponds to the Brillouin function (S = 1, g_{avg} = 2.0).

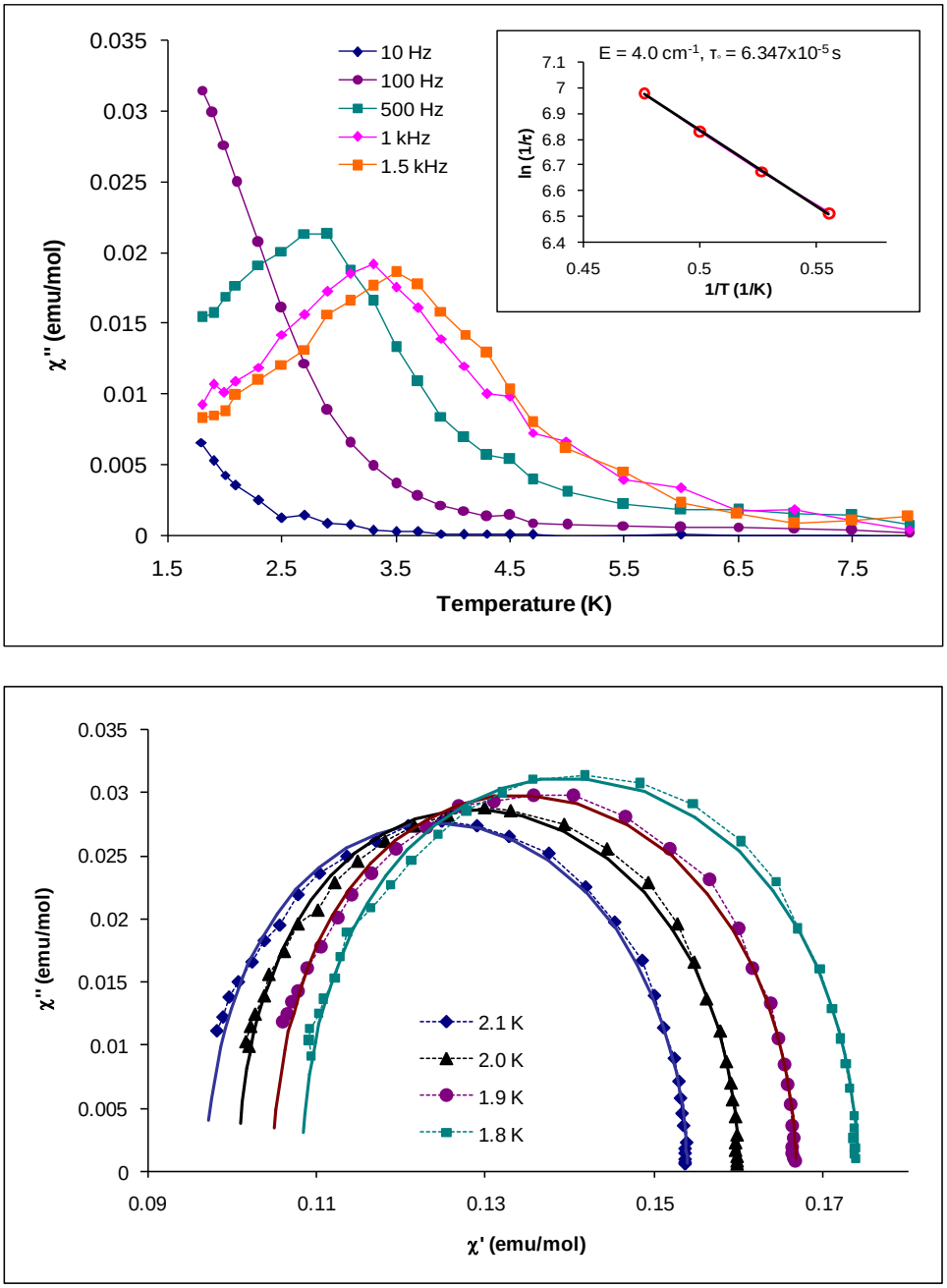

Figure 2.16 (a) Temperature dependence of the imaginary (χ′′) part of the ac susceptibility for **4** measured under various oscillating frequencies (1-1500 Hz). The solid lines are a guide for the eye. Inset: dependence of the logarithm of the relaxation rate ($1/\tau$) on the inverse temperature ($1/T$). The solid line represents the best linear fit to the Arrhenius law (U_{eff} = 4 cm^{-1} and τ_0 = 6.34 x 10^{-5} s). (b) Cole-Cole plot for **4**. The solid line represents the least squares fit by a generalized Debye model.

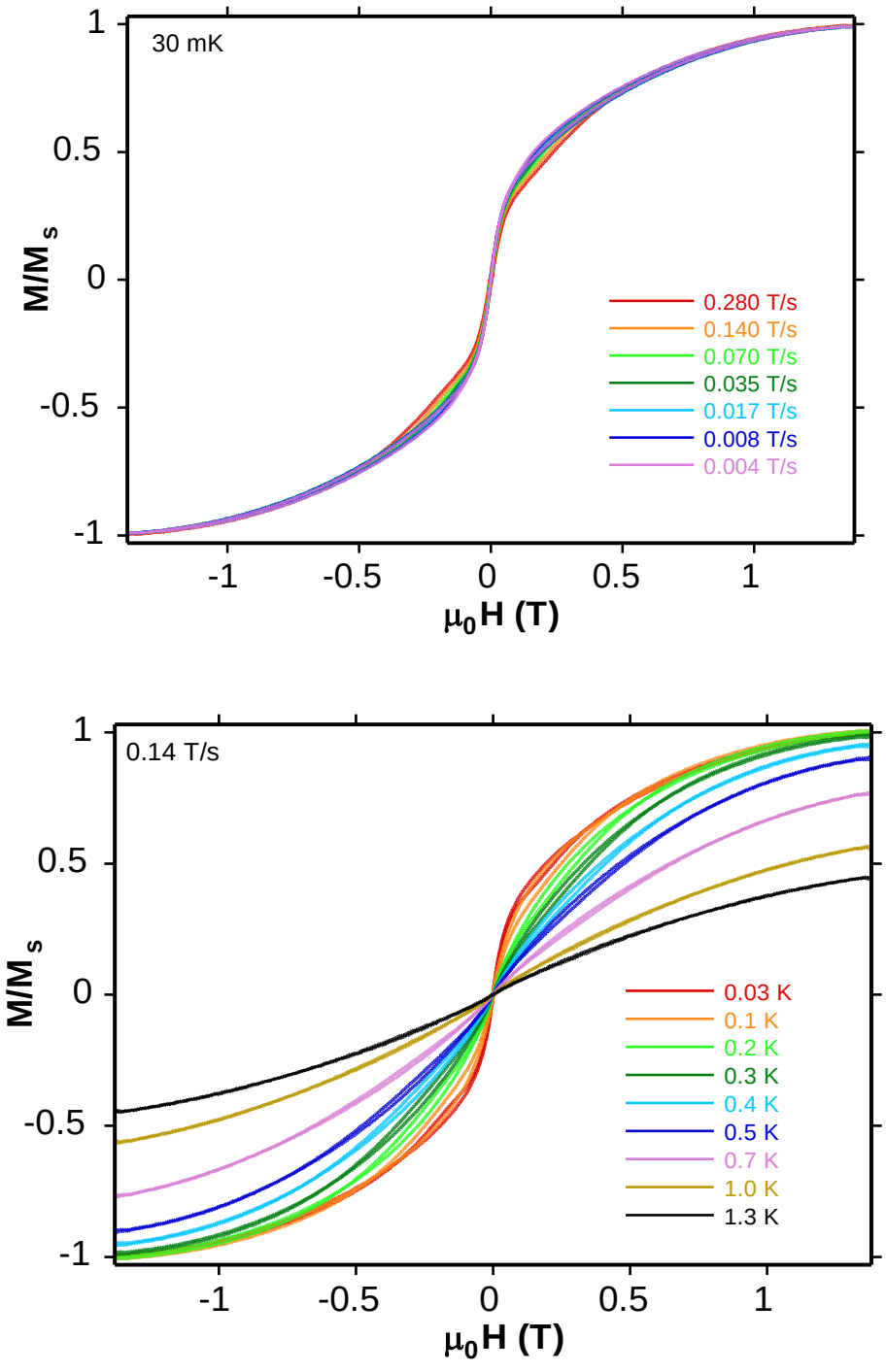

Figure 2.17 Field dependence of the magnetization on an oriented crystal of **4** measured on a micro-SQUID along the *b* axis (a) below 1.3 K with a sweep field rate of 0.14 T/s and (b) below a sweep rate of 0.280 T/s at 0.03 K.

The corresponding rise in the "out-of-phase" susceptibility, χ_M'', is shown in Figure 2.16 for frequencies of 100, 500, 1000, and 1500 Hz. In each case, χ_M'' achieves a maximum at a temperature at which the switching of the magnetic field matches the relaxation rate, $1/\tau$, for the magnetization of the molecule. The χ_M'' data indicates a blocking temperature, T_B, of 3.5 K at 1 kHz. In addition, the shape of the Cole-Cole plot is nearly symmetrical (Figure 2.16b) indicating that a single relaxation time, τ, can be considered. As for typical SMMs, the relaxation times follow an Arrhenius relationship: $\tau = \tau_o \exp(U_{eff}/k_BT)$. Accordingly, a plot of $\ln(1/\tau)$ vs. $1/T$ is linear (Figure 2.16a, inset) with a least-square fit yielding $\tau_o = 5 \times 10^{-5}$ s and $U_{eff} = 4.0$ cm^{-1}. Hysteresis loops were collected using a micro-SQUID on easy-axis oriented single crystal samples. Temperature dependent scans reveal butterfly shape hysteretic behavior for **4** at low temperatures (Figure 2.17), which is a typical behavior in mononuclear SMMs due to quantum tunneling.[76]

In conclusion, the combined ac and dc measurements gathered at low temperatures on **4** using SQUID and Micro-SQUID indicate unambiguously that it exhibits SMM behavior induced by a large zero-field splitting, $D = -30.0$ cm^{-1}. These measurements clearly indicate that compound **4** represent the first mononuclear SMM based on vanadium. Such interesting findings reveals the importance of careful tuning of the local coordination environment for a simple trigonally distorted pseudooctahedral complex in order to increase the orbital contribution to the magnetic moment resulting in a significant D value as a basis for molecular magnetic bistability.

(ET_4N)[Tp*VCl_3] (5). The magnetic properties of **5** behave similarly to compound **4**. The room-temperature χT vs. T value of 0.86 emu·K·mol^{-1} is consistent with one isolated V^{III} ion with g = 2.0 and Θ = -50K (C=1.0 emu·K·mol^{-1}; Figure 2.18). The value of χT decreases as the temperature is lowered which is attributable to zero-field splitting and/or intermolecular interactions. As in the case of compound **4**, the non-superposition of the iso-field lines of the field dependence of the magnetization data at temperatures between 2 and 4.5 K (Figure 2.18) and the lack of saturation of the magnetization curve for compound **5** indicate the presence of significant zero-field splitting. The *ANISOFIT* calculation for zfs parameters resulted in D = -30.0 cm^{-1} and E = -0.85 with g = 1.5. The ac susceptibility data under an applied dc field showed only a weak and noisy signal.

(nBu_4N)[Tp*VCl_3] (6). The magnetic properties of **6** behave similarly to compound **4**. The room-temperature χT vs. T value of 0.85 emu·K·mol^{-1} is consistent with one isolated V^{III} spin center with g = 2.0 and Θ = -50K (C = 1.0 emu·K·mol^{-1}; Figure 2.19a). The value of χT decreases with decreasing temperature which is attributable to zero-field splitting and/or intermolecular interactions. As in the case of compound **4**, the non-superposition of the iso-field lines from the magnetization data at temperatures between 2 and 4.5 K (Figure 2.19b) and the lack of saturation of the magnetization curve for compound **5** indicate the presence of significant zero-field splitting which was calculated by *ANISOFIT* to give D = -22.7 cm^{-1}, E = -1. 53 cm^{-1} and g = 1.36. The ac magnetic susceptibility data under an applied dc field did not show a signal probably due to the increased dipole-dipole interaction as a result of the closer V-----V intermolecular distances.

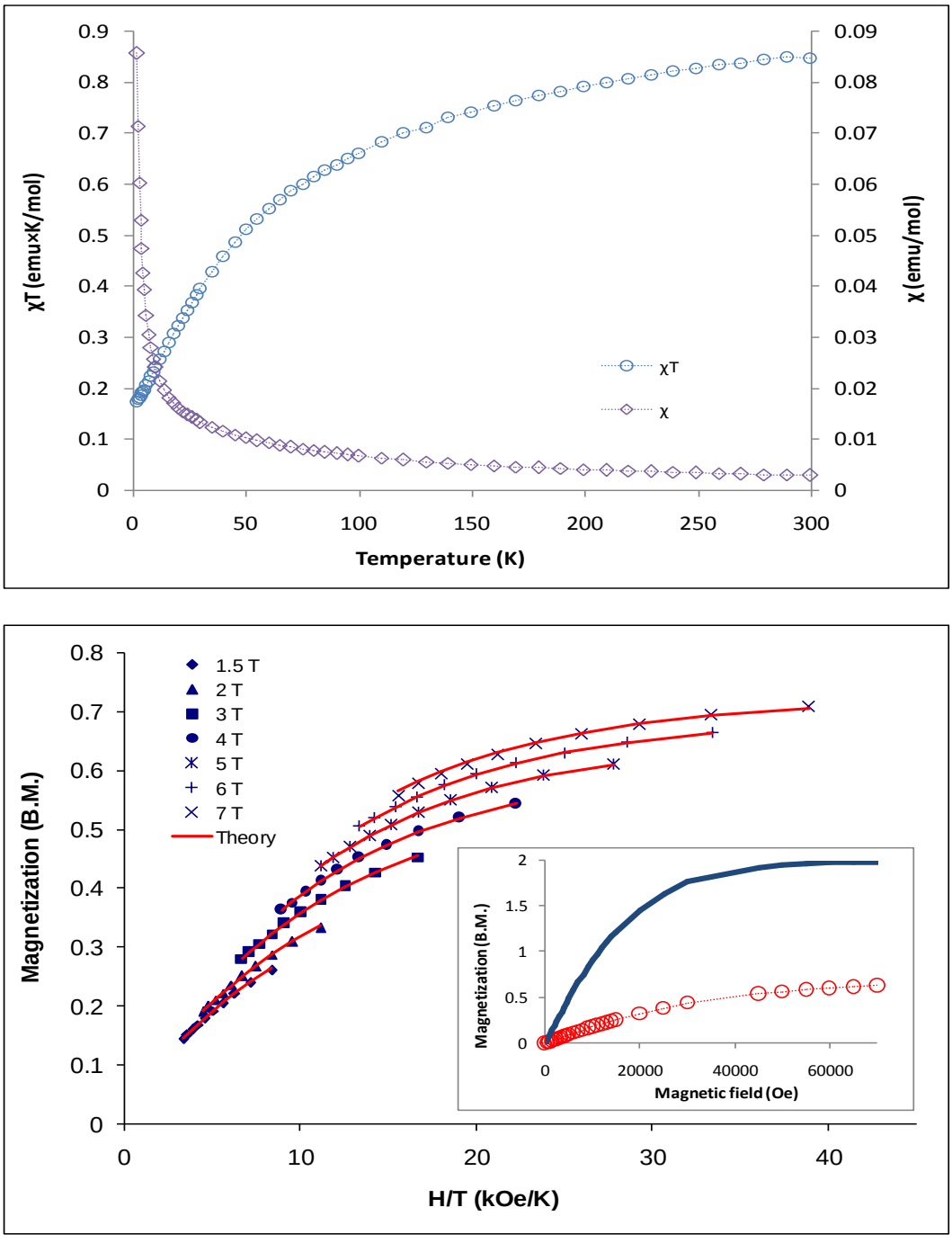

Figure 2.18 (a)Temperature dependence of χ (◊) and χT product (o) for **5**. (b) Reduced magnetization data at different external fields. Solid lines correspond to the best-fit curves using *ANISOFIT* (D = -30.0 cm^{-1}, E = -0.85 cm^{-1}, g = 1.50). Inset: Field dependent magnetization for **5** (o). The solid line corresponds to the Brillouin function (S = 1, g_{avg} = 2.0).

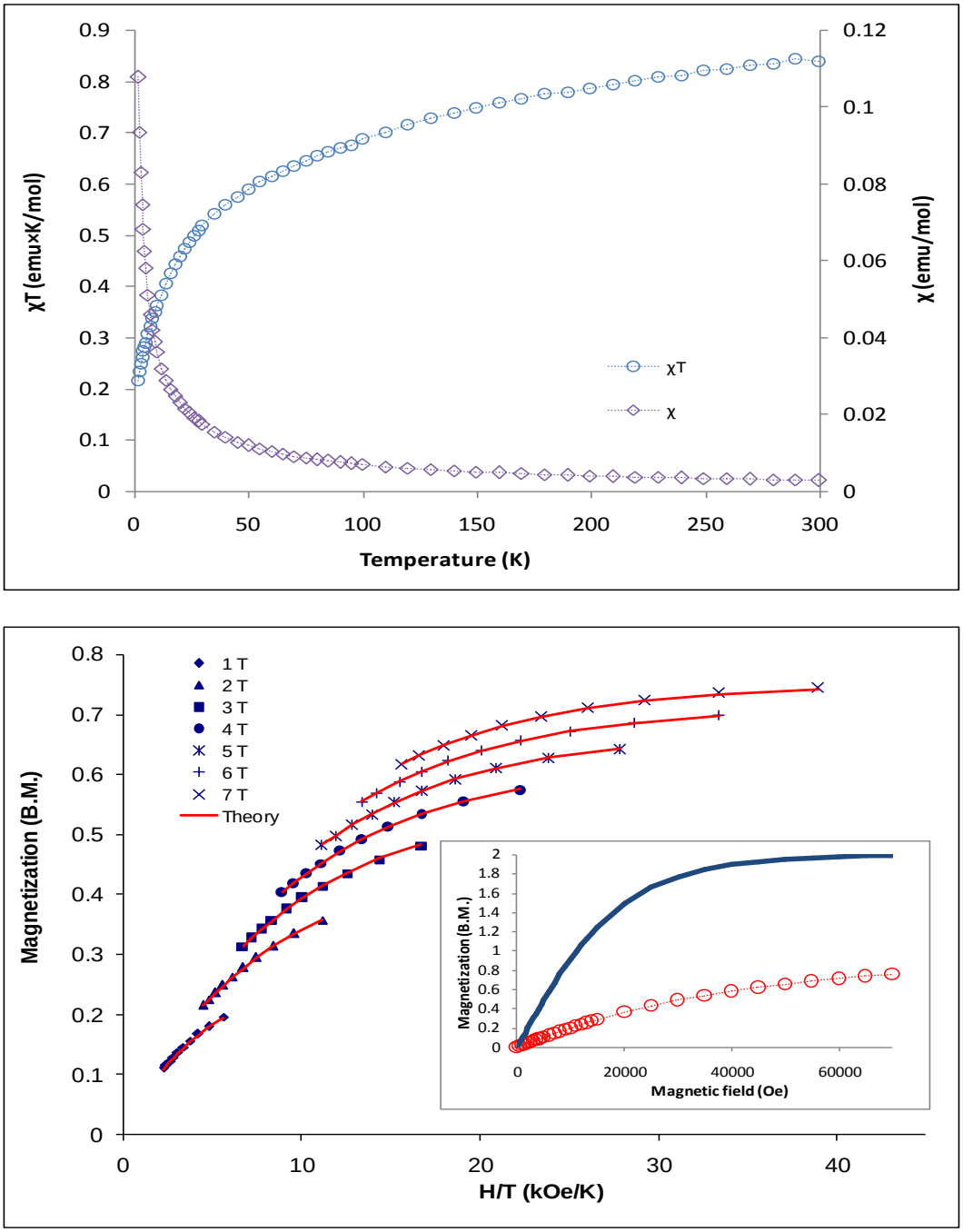

Figure 2.19 (a)Temperature dependence of χ (◊) and χT product (o) for **6**. (b) Reduced magnetization data at different external fields. Solid lines correspond to the best-fit curves using *ANISOFIT* (D = -22.7 cm^{-1}, E = -1.53 cm^{-1}, g = 1.36). Inset: Field dependent magnetization for **6** (o). The solid line corresponds to the Brillouin function (S = 1, g_{avg} = 2.0).

(Et_4N)[Tp*VBr_3] (7). The room-temperature χT vs. T value of 1 emu·K·mol^{-1} is consistent with one isolated V^{III} spin center with g = 2.0, Θ = -50K and TIP of 0.5 x 10^{-3} emu·K·mol^{-1} (Figure 2.20a). The value of χT decreases as the temperature is lowered which can be attributed to zero-field splitting and/or intermolecular interactions. As in the case of compound **3**, the non-superposition of the iso-field lines of the field dependence of the magnetization data at temperatures between 2 and 4.5 K (Figure 2.20b) and the lack of saturation of the magnetization curve for compound **7** even at 7 T indicate the presence of significant zero-field splitting. The fitting of the field dependence of the magnetization data using *ANISOFIT* resulted in D = -22.9 cm^{-1}, E = 0.001 cm^{-1} and g = 1.21. The D value is unexpectedly close to that of **4** although a significant increase was expected as a result of the increased spin-orbit coupling contribution of the halide by replacing the chloride ligand (λ = 530 cm^{-1}) with the heavier bromide (λ = 2530 cm^{-1}). Surprisingly, the compound does not show an ac signal as well despite the large D value.

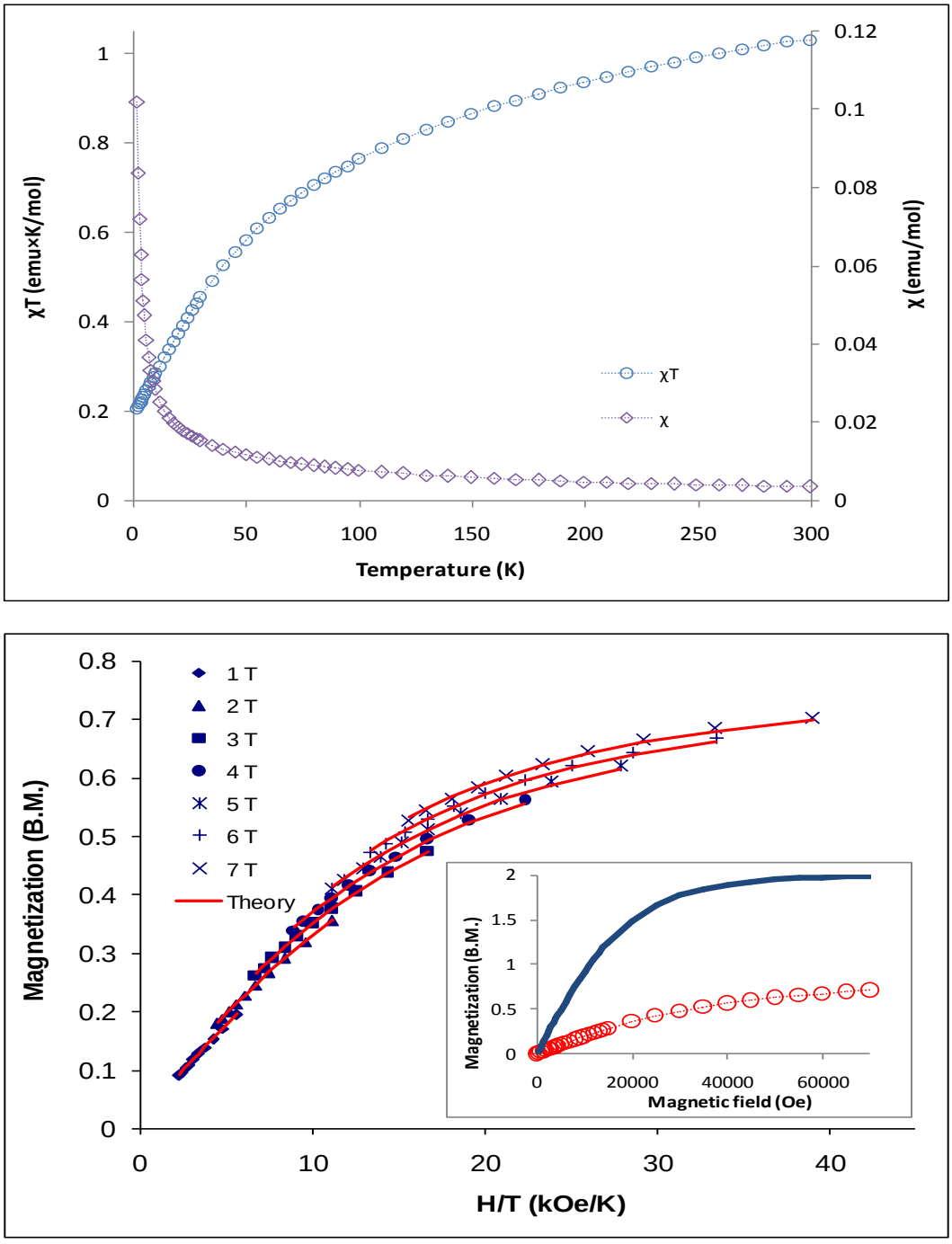

Figure 2.20 (a)Temperature dependence of χ (◊) and χT (o) for **7**. (b) Reduced magnetization data at different external fields. Solid lines correspond to the best-fit curves using *ANISOFIT* (D = -22.9 cm^{-1}, E = 0.001 cm^{-1}, g = 1.21). Inset: Field dependent magnetization for **7 (o)**. The solid line corresponds to the Brillouin function (S = 1, g_{avg} = 2.0).

$(Et_4N)[Tp^*VF_3]\cdot H_2O$ (8). The magnetic properties of a polycrystalline sample of **8** behave very similarly to compound **3**. The room-temperature χT vs. T value of 0.88 emu·K·mol^{-1} is consistent with one isolated V^{III} spin center with g = 1.79, Θ = -4K and TIP = 0.3x10^{-3} emu·K·mol^{-1} (0.88 emu·K·mol^{-1}; Figure 2.21a). The value of χT decreases at lower temperatures which is attributable to zero-field splitting and/or intermolecular interactions. The non-superposition of the iso-field lines of the field dependence of the magnetization data at temperatures between 2 and 4.5 K (Figure 2.21b) and the lack of saturation of the magnetization curve for compound **8** indicate the presence of significant zero-field splitting with a D value of 7.13 cm^{-1} which is significantly smaller than **4** as a result of both smaller trigonal field and smaller spin-orbit coupling contribution of the lighter fluoride ligands.

$[Tp^*V(DMF)_3](PF_6)_2$ (9). The room-temperature χT vs. T value of 1.015 emu·K·mol^{-1} is consistent with an isolated V^{III} complex with g = 1.95 Θ = -5K and TIP = 0.32 x 10^{-6} emu·K·mol^{-1} (C = 1 emu·K·mol^{-1}; Figure 2.22a). The value of χT decreases at lower temperatures which is attributable to zero-field splitting and/or intermolecular interactions. As in the case of compound **3**, the non-superposition of the iso-field lines of the field dependence of the magnetization data at temperatures between 2 and 4.5 K (Figure 2.22b) and the lack of saturation of the magnetization curve for compound **9** indicate the presence of significant zero-field splitting with D value of -19.9 cm^{-1} which is surprisingly comparable to **4** despite the smaller spin orbit coupling of the system.

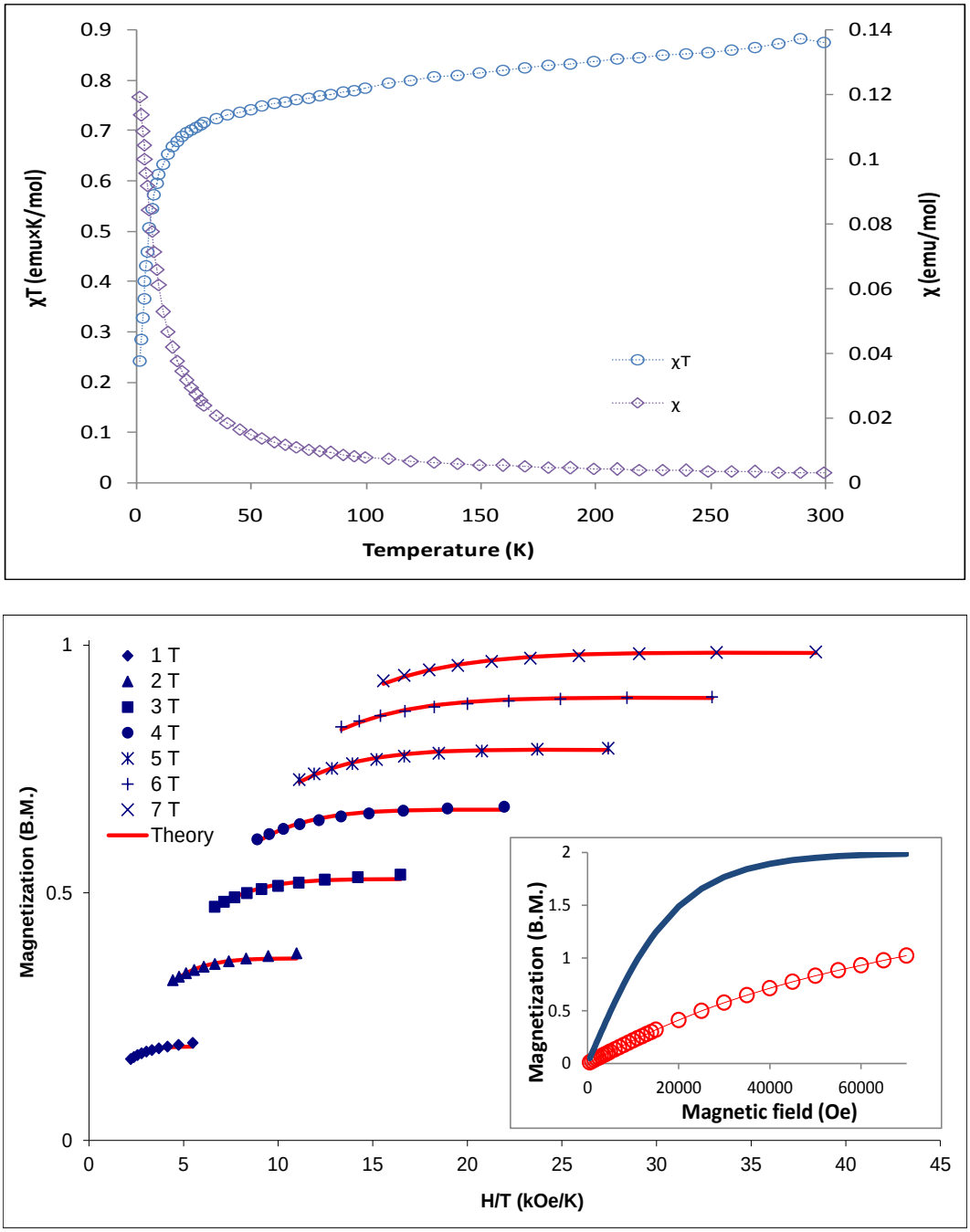

Figure 2.21 (a)Temperature dependence of χ (◊) and χT (o) for **8**. (b) Reduced magnetization data at different external fields. Solid lines correspond to the best-fit curves using *ANISOFIT* (D = 7.13 cm^{-1}, E = -0.124 cm^{-1}, g = 1.51). Inset: Field dependent magnetization for **8 (o)**. The solid line corresponds to the Brillouin function (S = 1, g_{avg} = 2.0).

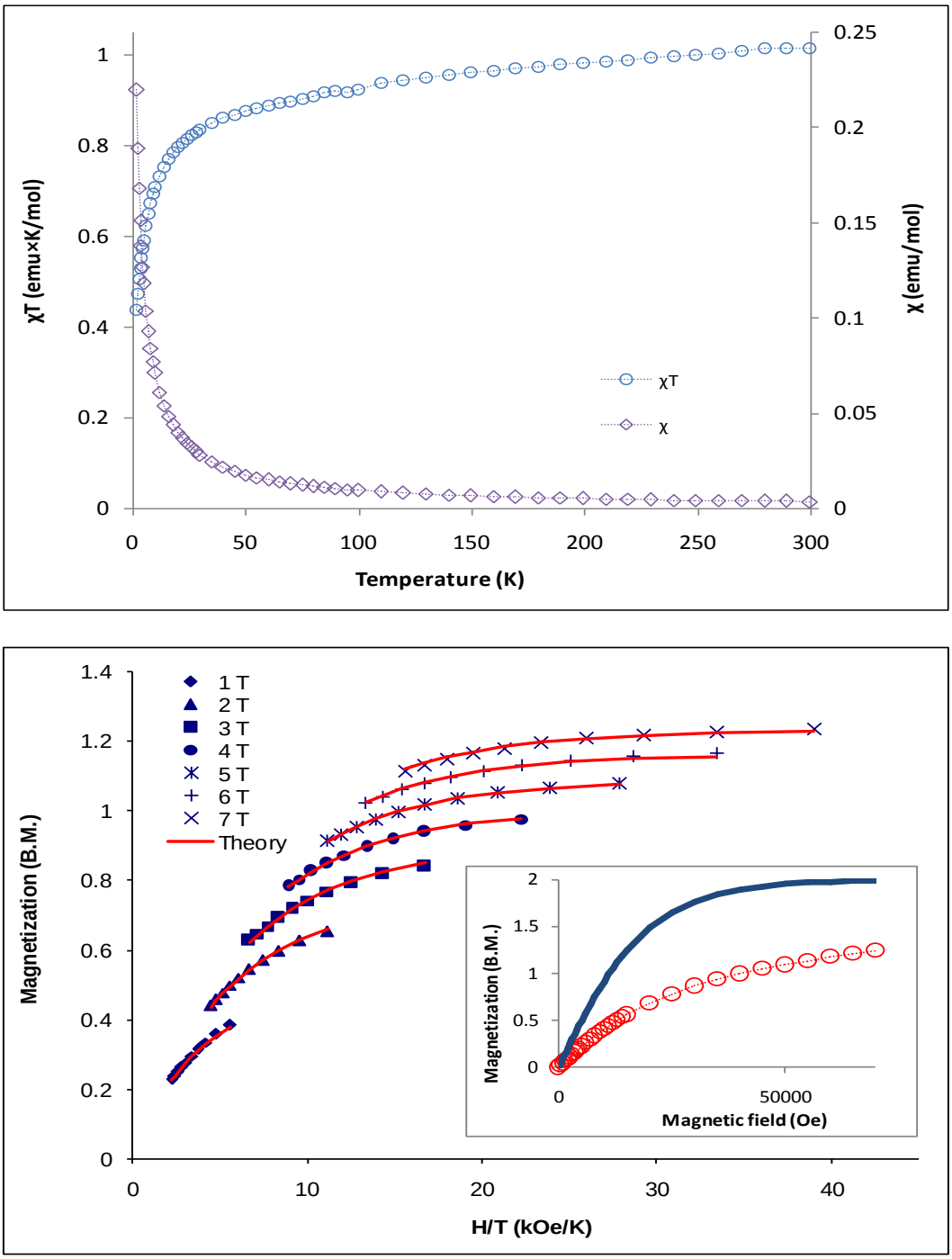

Figure 2.22 (a)Temperature dependence of χ (◊) and χT (o) for **9**. (b) Reduced magnetization data at different external fields. Solid lines correspond to the best-fit curves using *ANISOFIT* (D = -19.9 cm^{-1}, E = 2.19 cm^{-1}, g = 1.92). Inset: Field dependent magnetization for **9 (o)**. The solid line corresponds to the Brillouin function (S = 1, g_{avg} = 2.0).

Table 2.7 ZFS parameters of **1 - 9**

Compound	g	D cm^{-1}	E cm^{-1}
1	1.46	-8.8	2.62
2	1.38	-18.5	2.79
3	1.26	-16.0	3.0
4	1.54	-30.0	-0.81
5	1.50	-30.0	-0.85
6	1.36	-22.76	1.53
7	1.21	-22.9	0.001
8	1.51	7.13	-0.124
9	1.92	-19.9	-2.19

High Field EPR Spectroscopy

Single-crystal HF-HFEPR measurements were carried out using a 35 T resistive magnet with a cavity perturbation technique. The microwave source and detector used were a Millimeter vector network analyzer in combination with a series of schottky diodes and several different frequency multipliers. The experiment was performed at 1.4 K in the frequency range (50-225 GHz). Trials to measure powder spectra on pure sample pressed pellets or pellets of powder dispersed in eicosane were unsuccessful.

Based on the predicted large magnetic anisotropy and the lack of reliability of ZFS parameters extracted from magnetic measurements, single crystal HF-HFEPR measurements were performed on **4** (Figure 2.23). The crystal was rotated about a fixed axis to ensure that the applied field is parallel to the molecular hard plane. Three EPR peaks were observed in the spectrum which correspond to the three different molecular orientation in the crystal as shown in figure 2.24.

The EPR data were simulated using the following Hamiltonian, where φ is the angle between the field and the molecular hard axis:

$$H = DS_z^2 + E\left(S_x^2 - S_y^2\right) + \mu_B \cdot g \cdot B(\cos(\varphi)S_x + \sin(\varphi)\,S_y) \qquad Eq\ 2.1$$

The value of D was calculated indirectly by fitting the observed hard plane transitions revealing a D value of -40 cm^{-1} and E value of -1.1 cm^{-1} with g_x = 1.6, g_y = 1.15 and g_z = 2 which is close to the values extracted from magnetic data.

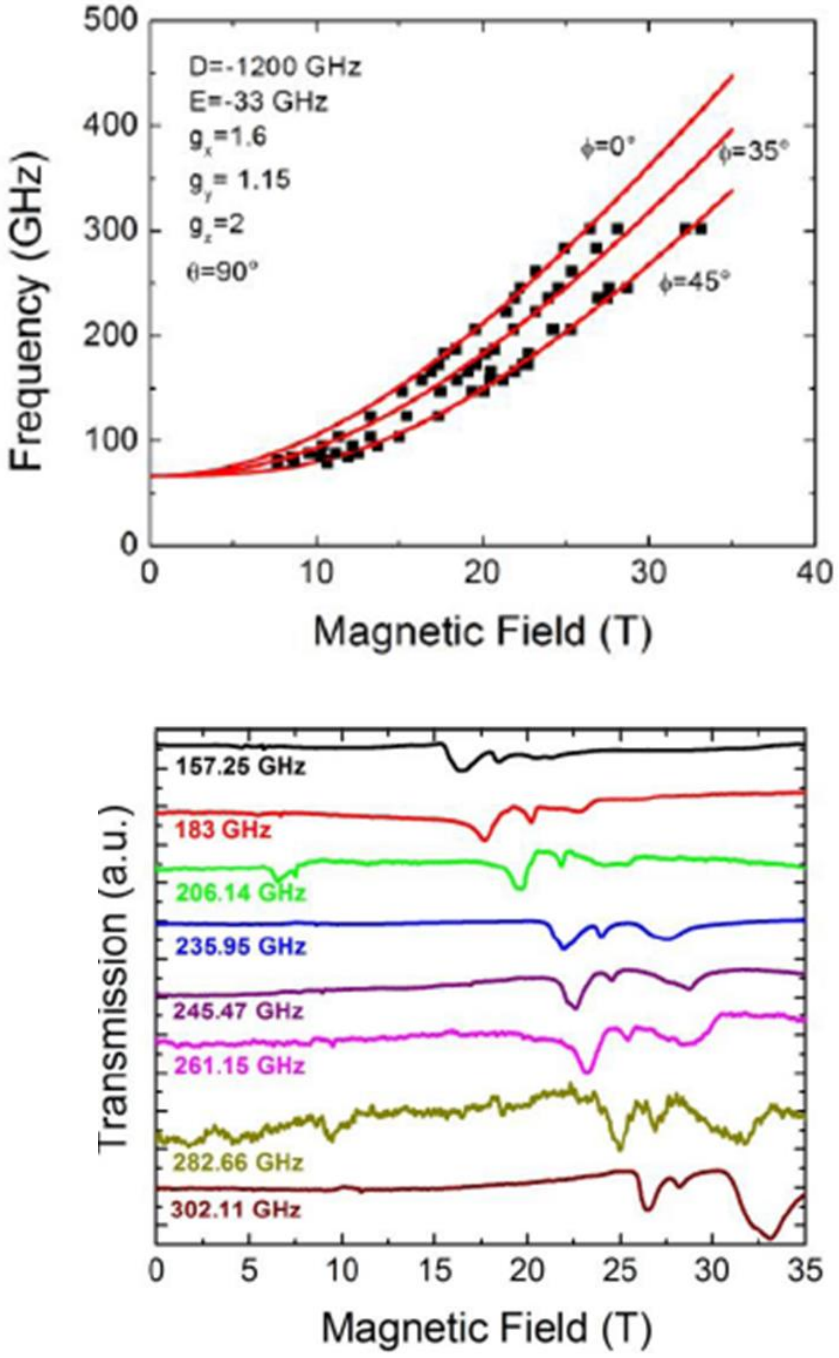

Figure 2.23 EPR peak positions observed for a single crystal of **4**. The solid lines correspond to the best fit employing the Hamiltonian (eq 2.1) and D value of -40 cm^{-1} and E value of -1.1 cm^{-1} with $g_x = 1.6$, $g_y = 1.15$ and $g_z = 2$.

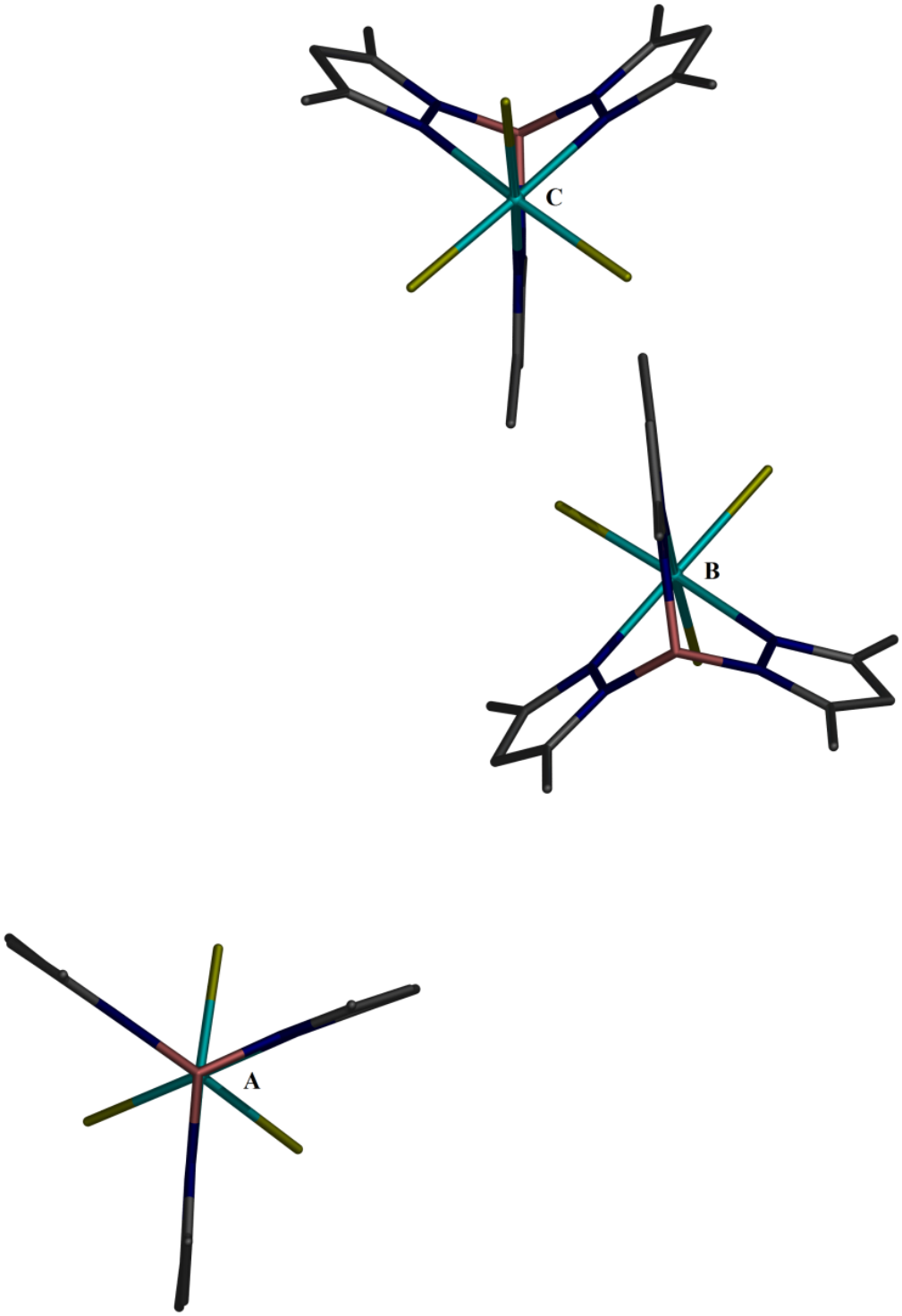

Figure 2.24 Different molecular orientations of the easy axis in **4**

Conclusions

The mononuclear complexes in this chapter highlight the importance of the careful tuning of the local coordination environments of metal ions in order to achieve enhanced single ion anisotropy. The magnetic data indicate that designing mononuclear vanadium complexes with a simple axially distorted pseudo-octahedral coordination environment, such as $A[L_3VX_3]$ (X = F, Cl or Br, $A^+ = Et_4N^+$, nBu_4N^+ or PPN^+ , L_3 = Tp or Tp*, and $[Tp^*V(DMF)_3](PF_6)_2$ can lead to a single ion SMM.

The effects of both axial crystal field distortion and spin-orbit coupling on the magnitude of zero-field splitting parameters in this family of compounds were explored Table 2.7). Both the magnitude of the trigonal field distortion and the spin-orbit coupling were varied by systematically tuning the π-donor ability of the ligand and the ligand spin-orbit coupling contribution. The change of D parameter from **8** (7.13 cm^{-1}) with terminal fluoride ligands to values with larger magnitude and negative sign in the heavier chloride congeners, **4**-**6** (~-30.0 cm^{-1}) supports the previous reports of the heavy halide effect in Nickel analogues.[169,233] The larger axial zero field splitting parameter D in **2** (-18.53 cm^{-1}) and **4** (-30.0 cm^{-1}) compared to **1** (-8.8 cm^{-1}) and (-16.0 cm^{-1}) suggests a direct relationship between the D value and the trigonal crystal field which is larger for the stronger π-donor Tp* ligand in **2** and **4.** The large D value in **9** (-19.9 cm^{-1}) which lacks any spin-orbit coupling contribution from halides supports this conclusion. The control of both factors introduces a relatively untapped strategy for designing and enhancing mononuclear SMM, sometimes referred to as single ion, SMM behavior.

CHAPTER III

NEW VANADIUM (III) CYANIDE BUILDING BLOCKS

The use of a building block approach employing cyanometallate-based SMMs, analogues of Prussian-blue-based high-temperature magnets,[33,35,128] is an alternate strategy for increasing the energy barrier, U_{eff}, and hence the blocking temperature, T_B, observed in traditional oxo-bridged SMMs. In this strategy, relatively large values of D are engendered by controlling the local symmetry of the metal ions which allows for smaller complexes with relatively small spin ground states to exhibit a barrier. For example it is known that the magnetic contribution of the unquenched orbital momenta in degenerate ground states and their mixing with the spin *via* first order spin-orbit coupling induces a strong anisotropy in linear Fe^{III}-CN-Cu^{II} and Fe^{III}-CN-Ni^{II} model complexes.[119,120] For this reason, it is necessary to control cluster architectures to ensure axially distorted local symmetries for metal ions in order to maximize orbital contribution. Structural control can be achieved by using a building block or modular approach in which capping ligands are used to make pre-designed discrete molecular precursors which then self-assemble into a discrete structural architecture rather than growing to form one-, two-, or three-dimensional face-centered cubic PB phases.[116]

The low-valent early 3d transition metals Ti, V, and Cr are excellent candidates for introducing large single ion anisotropy into molecular materials, a topic that was the subject of an interesting theoretical paper by Ruiz and coworkers.[8] In their calculations, in addition to the potential for large ZFS parameters, the diffuse d orbitals of these metals were predicted to give rise to improved overlap with the π and π^* orbitals of the

bridging cyanide ligand resulting in large superexchange constants |J| between metal centers.[125,190] Such large J values are crucial to ensure that the magnetic spin ground state is well-isolated from excited spin states, thereby preventing relaxation via a manifold of excited spin states. In support of this contention is that fact that the combination of V^{II} (t_{2g}^3) and Cr^{III} (t_{2g}^3) metal centers in Prussian blue analogues has led to bulk magnetic ordering temperatures well above room temperature. [34,127,128]

The 3d transition metal ion vanadium (III) ion has been reported to give rise to very strong ferromagnetic interactions in dimeric species[173,174] and often exhibits very large zero-field splitting with axial components |D| up to - 20 cm^{-1}.[173-177] This makes it a very promising building block for SMMs that rely on a moderate spin ground state with a large negative zero-field splitting. Despite these interesting properties and the fact that some vanadium cyanide building blocks were known long time ago,[234-238] including $K_4[V(CN)_6]$,[234] $K_3[VO(CN)_5]$[235] and $Et_4N[V(CN)_6]$,[236] there is very little literature on V^{III} molecular magnetic materials.[32,34,173-185,239] The incorporation of hexacyanovanadate (III) anion $[V^{III}(CN)_6]^{3-}$ into PB-structured materials has proven to be synthetically challenging, presumably due to the ease of oxidation of V^{III} to V^{IV}.[186-188] However few are the examples of vanadium magnetic molecules, there is some key evidence of its potential for enhancing molecular magnetic materials such as $V(TCNE)_2$ and other examples discussed earlier in chapter 1. [33-36,127,183,184,239-241]

Discrete magnetic molecules based on cyanovanadate building blocks are quite rare.[183,189] The only example of a cyanide-bridged cluster containing vanadium (III) was reported by Long and co-workers. The reaction of $[(cyclen)V(CF_3SO_3)_2](CF_3SO_3)$ with

four equivalents of $(Et_4N)CN$ in DMF produces the seven-coordinate complex $[(cyclen)V(CN)_3]$ while using only 1.5 equivalents produces the cage complex, $[(cyclen)_4V_4(CN)_6]^{6+}$ which has a tetrahedral geometry and antiferromagnetic coupling resulting in ground state of S=0. [183]

In the quest for making vanadium (III) cyanide building blocks, salen ligands (salen = N,N'-ethylenebis(salicylimine)) and acac (acac = acetylacetonate) are good capping ligands for dicyanide building blocks. Salen-based cyanide building blocks have been reported for several metals.[242-248] The building block $Na_2[Ru(salen)(CN)_2]$ has been reported by Leung and coworkers in 1989.[242] In 2005, Yeung and coworkers reported the incorporation of this building block into cyanide bridged complexes. [249-251] In addition, β-diketonates have been used as capping ligands in cyanide building blocks.[249,250,252-256]

The syntheses of salen based vanadium (III) precursors of general formula [V(L)Cl(THF)] (where L = salen ligand) have been reported using various synthetic routes. [257,258] The mononuclear acetylacetonate precursors $[M(acac)Cl_2(THF)_2]$ and $[M(acac)_2Cl(THF)]$ where (M= Ti^{III}, V^{III} or Cr^{III}) have been prepared from several different routes including reactions between Hacac and $MCl_3(THF)_3$.[259,260]

In this chapter the syntheses, structural characterization and magnetic studies of new vanadium cyanide building blocks based on acetylacetone and a family of salen-based ligands are reported. The ligands are salen (salen = N,N'-Ethylenebis(salicylimine)), salphen (salphen = N,N'-Phenylenebis(salicylimine)) and 2-methoxysalen (2-methoxysalen = N,N'-Ethylenebis(2-methoxysalicylimine)). Attempts to incorporate them into heterometallic magnetic molecules are also presented.

Experimental

Syntheses

Starting Materials. All chemicals and solvents were of reagent grade quality. The starting material $VCl_3(THF)_3$ (Aldrich) was used as received. The salts $(Et_4N)CN$ and (PPN)CN were synthesized by simple metathesis reaction of KCN with corresponding cation. The tetradentate Schiff base ligands; $salenH_2$, $MeOsalenH_2$, and $salphenH_2$ were prepared according to a literature method.[261] The compounds $V(acac)_2Cl(THF)$, $[V(salen)Cl]_2$, and $\{[Mn(salen)(H_2O)]\}_2(ClO_4)_2$ were synthesized according to reported procedures.[257,259,262] Diethyl ether (Aldrich) and Dimethyl formamide (Alpha Aesar) were used as received. Acetonitrile was dried over 3 Å molecular sieves and distilled prior to use. All syntheses were performed under nitrogen using standard dry box and Schelnk-line techniques.

Physical Measurements. Elemental analyses were performed by Atlantic Microlab Inc. (Norcross, GA). Infrared spectra were recorded as Nujol mulls in the range 400-4000 cm^{-1} on a Nicolet Nexus 470 FTIR spectrophotometer.

[VSalphenClDMF] (10). Sodium hydride (0.21 g, 8.7 mmol) was slowly added to a THF (100 mL) solution of $salphenH_2$ (1.41 g, 4.5 mmol). The suspension was stirred until complete dissolution was achieved to yield a yellow solution. The reagent $VCl_3(THF)_3$ (1.62 g, 4.35 mmol) was then added with stirring which resulted in a reddish maroon solution and the deposition of a finely divided dark brown microcrystalline solid. The solid was collected on a fine frit, washed with THF (2x3 mL) then diethyl ether (3x5 mL). Recrystallization from DMF/diethyl ether resulted in large

red crystals of the product which were collected by filtration and washed with diethyl ether (3x5 mL) and then dried. (Yield = 1.91 g, 92.7%) Elemental analysis: Calcd. for C_{23} H_{21} N_3 O_3 V_1 Cl_1 (**10**): C, 58.30; H, 4.47; N, 8.87; Found: C, 58.23; H, 4.41; N, 8.81. IR(Nujol): ν(C=N) 1661(s) cm^{-1}.

[V(MeOsalen)(Cl)(DMF)] (11). Compound **11** was prepared in a fashion analogous to that described above for compound **10** using $MeOsalenH_2$ (1.48 g, 4.5 mmol). (Yield = 1.8 g, 83%). Elemental analysis: Calcd. for $C_{21}H_{25}ClN_3O_5V$ (**11**): C, 51.92; H, 5.19; Cl, 7.30; N, 8.65; Found: C, 51.81; H, 5.16; N, 8.59. IR(Nujol): ν(C=N) 1620(s) cm^{-1}.

$(Et_4N)_2$[V(acac)$(CN)_4$] (12). A solution of $(Et_4N)CN$ (0.32g, 2 mmol) in 5 mL CH_3CN was added to a solution of $V(acac)_2Cl(THF)$ (0.35 g, 1 mmol) in 10 mL CH_3CN. The color of the reaction mixture turned orange upon stirring overnight. Diethyl ether was slowly added to the orange solution resulting in white precipitate which was collected by filtration then the filtrate was left to stand overnight where more bluish white precipitate formed. The solution was filtered one more time after which time a few drops of diethyl ether were added and the solution was left to stand overnight. Orange crystals of X-ray quality deposited during this time period. The product was collected by filtration collected by filtration then washed with diethyl ether (3x5 mL) then dried. (Yield = 0.14 g, 23%). Elemental analysis: Calcd. for for $C_{25}H_{47}N_6O_2V$ (**12**): C, 58.35; H, 9.21; N, 16.33; Found: C, 58.23; H, 9.16; N, 16.29. IR(Nujol): ν(C≡N) 2046(s) cm^{-1}.

(PPN)[V(acac)$_2$(CN)$_2$]·PPNCl·CH_3CN (13)·CH_3CN. A solution of (PPN)CN (2.3g, 4 mmol) in 5 mL CH_3CN was added to a solution of $V(acac)_2Cl(THF)$ (0.71 g, 2 mmol) in 5 mL CH_3CN which led to a color change from green to dark orange-red and an orange

precipitate after 12 hours. Additional product was obtained by slowly adding diethyl ether to the orange solution. The product was collected by filtration, washed with diethyl ether (3x5 mL) and dried. Recrystallization from acetonitrile/diethyl ether resulted in orange crystals of X-ray quality. (Yield = 2.45 g, 82%). Elemental analysis: Calcd. for $C_{84}H_{74}ClN_4O_4P_4V$ (**13**): C, 71.36; H, 5.28; N, 3.96; Found:): C, 71.31; H, 5.17; N, 3.89. IR(Nujol): ν(C≡N) 2045(s) cm^{-1}.

$(Et_4N)[V(salen)(CN)_2]$ (14). A solution of $(Et_4N)CN$ (0.624g, 4 mmol) in 5 mL of CH_3CN was added to a solution of $[V(salen)Cl]_2$ (0.7g, 1 mmol) in 15 mL of DMF. The reaction mixture was stirred overnight to yield a pale reddish brown precipitate which was collected by filtration. More products were obtained by layering the mother liquor with diethyl ether. The precipitates were combined and washed with diethyl ether (3x5 mL) and dried. X ray quality crystals were obtained by recrystallization from DMF/diethyl ether. (Yield = 0.8 g, 80%). Elemental analysis: Calcd. for $C_{26}H_{34}N_5O_2V$(**14**): C, 62.52; H, 6.86; N, 14.02; Found: C, 62.43; H, 6.78; N, 14.05. IR(Nujol): ν(C≡N) 2104(m), ν(C=N) 1618(s) cm^{-1}.

(PPN)[V(salen)(CN)$_2$] (15). A solution of (PPN)CN (1.15g, 2 mmol) in 5 mL CH_3CN was added to a solution of $[V(salen)Cl]_2$ (0.35g, 0.5 mmol) in 15 mL DMF. The reaction mixture was stirred overnight. The reaction solution was layered with diethyl ether and left overnight which led to the formation of dark reddish-brown X-ray quality crystals. The product was collected by filtration, washed with acetonitrile (1 x 3 mL) followed by diethyl ether (3 x 5 mL) and then dried. (Yield = 0.76 g, 83%). Elemental analysis:

Calcd. for $C_{54}H_{44}N_5O_2P_2V$(**15**): C, 71.44; H, 4.89; N, 7.71; Found: C, 71.37; H, 4.86; N, 7.66. IR(Nujol): ν(C≡N) 2100(s), ν(C=N) 1620(s) cm^{-1}.

(PPN)[V(MeOsalen)(CN)$_2$] (16). A solution of (PPN)CN (1.15g, 2 mmol) in 5 mL of CH_3CN was added to a solution of **11** (0.48 g, 1 mmol) in 15 mL of DMF. The reaction mixture was stirred overnight then layered with diethyl ether and left overnight to yield dark reddish-yellow crystals for X-ray crystallography. The product was collected by filtration, washed with acetonitrile (1 x 3 mL) followed by diethyl ether (3 x 5 mL) and then dried. (Yield = 0.71 g, 73%). Elemental analysis: Calcd. for for $C_{56}H_{48}N_5O_4P_2V$ (**16**): C, 69.49; H, 5.00; N, 7.24; Found: C, 69.43; H, 4.88; N, 7.17. IR(Nujol): ν(C≡N) 2102(s), ν(C=N) 1660 (s) cm^{-1}.

(PPN)[V(salphen)(CN)$_2$]·DMF·2CH$_3$CN (17)·DMF·2CH$_3$CN. A solution of (PPN)CN (1.15g, 2 mmol) in 5 mL of CH_3CN was added to a solution of **10** (0.47 g, 1 mmol) in 15 mL of DMF. The reaction mixture was stirred overnight and layered with diethyl ether which produced dark red-brown crystals. The product was collected by filtration and washed with acetonitrile (1x3mL) followed by diethyl ether (3x5 mL) and then dried. (Yield = 0.91 g, 88%). Elemental analysis: Calcd. for for $C_{61}H_{51}N_6O_3P_2V$ (**17**): C, 70.26; H, 5.17; N, 10.09; Found: C, 70.14; H, 4.89; N, 9.89. IR(Nujol): ν(C≡N) 2102(s), ν(C=N) 1666 (s) cm^{-1}.

[V(salen)(CN)$_2$][Mn(salen)]n·5CH$_3$CN (18). A solution of [Mn(salen)(H_2O)]ClO_4 (176 mg, 0.4 mmol) in 10 mL of CH_3CN was added to a solution of **14** (200 mg, 0.4 mmol) in 5 mL of a 1:1 CH_3CN:DMF solution which led to instantaneous precipitation of a yellow-brown precipitate. The product was collected by filtration, washed with

diethyl ether (3 x 5mL) and dried. (Yield = 0.26 g, 73%). Elemental analysis: Calcd. for $C_{44}H_{43}MnN_{11}O_4V$ (**18**): C, 59.00; H, 4.84; N, 17.20; Found: C, 58.93; H, 4.83; N, 17.14. IR(Nujol): ν(C≡N) 2130(s), ν(C=N) 1621 (s) cm^{-1}.

Single Crystal X-Ray Diffraction

Single crystal X-ray data were collected on a Bruker-APEX II CCD diffractometer at 110 K. Crystals were mounted on cryoloops and placed in the N_2 cryostream. The data sets were collected with Mo Kα radiation (k = 0.71073 Å) as four ω scans at a 0.3 – 0.4° step width. Data integration and processing, Lorentz-polarization and absorption corrections were performed using the Bruker SAINT[220] and SADABS[221] software packages. Solution and refinement of the crystal structures were carried out using the SHELX[222] suite of programs and the graphical interface X-SEED.[223] The structures were solved by direct methods and refined by alternating cycles of full-matrix least-squares methods on F^2 using SHELXL which resolved all non-hydrogen atoms. All non-hydrogen atoms were refined anisotropically at the final refinement cycles. The hydrogen atoms were located from difference Fourier maps, assigned with isotropic displacement factors and included in the final refinement cycles by use of either geometrical constraints (HFIX for hydrogen atoms with parent carbon atoms) or restraints (DFIX for hydrogen atoms with parent nitrogen or oxygen atoms). A summary of the crystallographic data, unit cell parameters, and pertinent data collection and structure refinement parameters are provided in Table 3.1 and Table 3.2. Selected metal–ligand bond distances and angles are provided in Table 3.3 for compounds **10-13,** Table 3.4 for compounds **14-15** and Table 3.5 for compounds **16-17**.

Table 3.1 Crystal structural data and refinement parameters for compounds **10, 12–14**.

Compound	**(10)**	**(12)**	**(13)**	**(14)**
Space group	$P2_1/c$	$P2_12_12_1$	P-1	Fdd2
Unit cell	a = 11.694(2)Å b = 24.123(5)Å c = 7.3026(15)Å β = 91.75(3)°	a = 11.360(2) Å b = 13.530(3) Å c = 18.311(4) Å	a = 9.5928(19)Å b = 12.696(3)Å c = 17.423(4)Å *α = 91.29(3)*° *β* = 105.22(3)° *γ = 108.39(3)*°	a = 21.108(4) Å b = 12.724(3) Å c = 18.699(4) Å
V	2059.1(7)Å^3	2814.5(10) Å^3	1930.1(7)Å^3	5022.3(17) Å^3
Z	4	4	1	8
Density, ρ_{calc}	1.528 g/cm^3	1.215 g/cm^3	1.287 g/cm^3	1.321 g/cm^3
Abs. coeff., μ	0.643 mm^{-1}	0.384 mm^{-1}	0.302 mm^{-1}	0.427 mm^{-1}
Crystal color and habit	dark red plate	yellow needle	orange block	pale red block
Crystal size	0.24 x 0.11 x 0.08 mm	0.21 x 0.1 x 0.05 mm	0.25x0.2x0.08 mm	0.18 x 0.17 x 0.08 mm
Temperature	110 K	110 K	110 K	110 K
Radiation, λ	Mo-Kα, 0.71073 Å	Mo-Kα, 0.71073 Å	Mo-Kα, 0.71073 Å	Mo-Kα, 0.71073 Å
Min. and max. θ	1.69 to 23.92º	1.87 to 23.56º	1.7 to 25.26º	2.16 to 27.45 º
Reflections collected	3181 [R_{int} =0.079]	21932 [R_{int} =0.0743]	18819 [R_{int} = 0.0279]	9827 [R_{int} =0.0221]
Independent reflections	3181	4122	6948	2841
Data/parameters/restraints	3181/282/0	4122/317 /0	6948/470/0	2841/157 /1
R [$F_o > 4\sigma(F_o)$]	R_1 = 0.0603 wR_2 = 0.1273	R_1 = 0.092 wR_2 = 0.24	R_1 = 0.0526 wR_2 = 0.1126	R_1 = 0.0386 wR_2 = 0.0921
G.o.f. on F^2	1.056	1.049	1.037	1.042
Max./min. residual densities, e·Å^{-3}	0.75, -0.58	1.56, -0.48	0.44, –0.49	0.22, -0.25

$R_1 = \Sigma [(F_o - F_o)] / \Sigma (F_o)$. $_wR_2 (F_{o2}) = \{ \Sigma [w(F_{o2} - F_{c2})_2 / \Sigma [w(F_{o2})_2] \}_{1/2}$.

Table 3.2 Crystal structural data and refinement parameters for compounds **15–17**.

Compound	**(15)**	(**16)**	**(17)**
Space group	Pcca	$P2_1/c$	$P2_1/n$
Unit cell	a = 14.294(3)Å b = 12.999(3)Å c = 24.114(5)Å	a = 13.149(3)Å b = 15.671(3)Å c = 14.067(3)Å β = 93.81(3)°	a = 20.534(4) Å b = 13.220(3) Å c = 22.389(5) Å β 111.11(3) °
V	4480.4(16)Å^3	2892.2(10)Å^3	5670(2) Å^3
Z	4	2	4
Density, ρ_{calc}	1.346 g/cm^3	1.218g/cm^3	1.302 g/cm^3
Abs. coeff., μ	0.342 mm^{-1}	0.278 mm^{-1}	0.286 mm^{-1}
Crystal color and habit	red orange plate	red block	red block
Crystal size	0.25 x 0.18 x 0.12 mm	0.23x0.13x0.13 mm	0.20 x 0.20 x 0.10 mm
Temperature	110 K	110 K	110 K
Radiation, λ	Mo-Kα, 0.71073 Å	Mo-Kα, 0.71073 Å	Mo-Kα, 0.71073 Å
Min. and max. θ	2.21 to 27.54º	1.3 to 28.73º	1.81 to 23.32 º
Reflections collected	50227 [R_{int} =0.0442]	33023 [R_{int} = 0.0403]	35151 [R_{int} =0.0814]
Independent reflections	5177	7031	7055
Data/parameters/restraints	5177 /290/0	7031/349/0	7055 /716 /0
R [$F_o > 4\sigma(F_o)$]	R_1 = 0.0384 wR_2 =0.0843	R_1 = 0.085 wR_2 = 0.2436	R_1 = 0.0741 wR_2 = 0.1031
G.o.f. on F^2	1.033	1.060	0.864
Max./min. residual densities, e·Å^{-3}	0.47, -0.40	1.91, –0.42	0.34, -0.41

$R_1 = \Sigma\,[(F_o - F_o)]/\Sigma\,(F_o)$. $_wR_2\,(F_{o2}) = \{\Sigma\,[w(F_{o2} - F_{c2})_2/\Sigma\,[w(F_{o2})_2]\}_{1/2}$.

Table 3.3 Selected metal-ligand bond distances (Å) and bond angles (°) in the crystal structures of compounds **10, 12** and **13.**[a]

[V(salphen)(DMF)Cl] **(10)**			
V(1)-N(1)	2.099(2)	O(1)-V-N(1)	88.0(1)
V(1)-N(2)	2.101(3)	O(1)-V-N(2)	164.1(1)
V(1)-O(1)	1.914(2)	O(1)-V-O(2)	108.81(9)
V(1)-O(2)	1.922(2)	O(1)-V-O(3)	85.92(9)
V(1)-O(3)	2.076(2)	O(1)-V-Cl(1)	89.26(7)
V(1)-Cl(1)	2.378(1)	N(1)-V-N(2)	77.0(1)
		N(1)-V-Cl(1)	100.18(7)
		V(1)- salphen	24.6(6)
$(Et_4N)_2[V(acac)(CN)_4]$ **(12)**			
V(1)-O(1)	1.983(6)	O(1)-V-O(2)	87.0(2)
V(1)-O(2)	1.948(4)	O(1)-V-C(1)	90.4(3)
$V(1)-C\equiv N_{ax}$	2.132(9)	O(1)-V-C(2)	90.3(3)
$V(1)-C\equiv N_{eq}$	2.144(8)	O(1)-V-C(3)	95.5(3)
C≡N	1.12(1)	O(1)-V-C(4)	176.1(3)
		V(1)- C≡N	177.9(7)
		V(1)- acac	22.569(6)
$(PPN)[V(acac)_2(CN)_2]\cdot PPNCl$ **(13)**			
V(1)-O(1)	1.966(2)	O(1)-V-O(2)	88.97(6)
V(1)-O(2)	1.978(2)	O(1)-V-O(1A)	180.00(6)
V(1)-C≡N	2.168(2)	O(1)-V-O(2A)	91.03(6)
O(1)-C(3)	1.277(3)	O(1)-V-C(1)	89.29(7)
C≡N	1.151(3)	O(1)-V-C(1A)	90.71(7)
		O(2)-V-C(1)	89.94(7)
		V(1)- C≡N	179.6(2)
		V(1)- acac	19.169(6)

[a] ax = axial, eq = equatorial

Table 3.4 Selected metal-ligand bond distances (Å) and bond angles (°) in the crystal structures of compounds **14** and **15.**[a]

$(Et_4N)[V(salen)(CN)_2]$ **(14)**			
V(1)-N(2)	2.093(2)	O(1)-V-N(2)	87.30(9)
V(1)-O(1)	1.921(2)	O(1)-V-C(1)	92.0(1)
V(1)-C(1)	2.182(3)	O(1)-V-N(2A)	164.80(9)
O(1)-C(9)	1.326(3)	O(1)-V-O(1A)	107.81(9)
C≡N	1.157(4)	O(1)-V-C(1A)	91.6(1)
		N(2)-V-N(2A)	77.67(9)
		V(1)- C≡N	175.6(2)
		V(1)- salen	19.848(6)
$(PPN)[V(salen)(CN)_2]$ **(15)**			
V(1)-N(2)	2.099(1)	O(1)-V-N(2)	86.82(5)
V(1)-O(1)	1.913(1)	O(1)-V-C(1)	90.01(5)
V(1)-C(1)	2.190(1)	O(1)-V-N(2A)	163.16(5)
O(1)-C(9)	1.321(2)	O(1)-V-O(1A)	109.19(5)
C≡N	1.154(2)	O(1)-V-C(1A)	90.85(5)
		N(2)-V-N(2A)	77.82(5)
		V(1)- C≡N	173.3(1)
		V(1)- salen	24.661(6)

Table 3.5 Selected metal-ligand bond distances (Å) and bond angles (°) in the crystal structures of compounds **16** and **17.**

PPN[V(MeOsalen)$(CN)_2$] **(16)**			
V(1)-N(2)	2.084(3)	O(1)-V-N(2)	87.1(1)
V(1)-O(1)	1.909(2)	O(1)-V-C(1)	92.7(1)
V(1)-C(1)	2.177(3)	O(1)-V-N(2A)	164.3(1)
O(1)-C(9)	1.318(4)	O(1)-V-O(1A)	107.6(1)
C≡N	1.145(4)	O(1)-V-C(1A)	91.4(1)
		N(2)-V-N(2A)	78.9(1)
		V(1)- C≡N	172.0(3)
		V(1)- salen	23.633(6)
PPN[V(salphen)$(CN)_2$] **(17)**			
V(1)-O(1)	1.902(2)	O(1)-V-O(2)	106.7(1)
V(1)-O(2)	1.925(2)	O(1)-V-N(4)	88.3(1)
V(1)-N(3)	2.110(3)	O(1)-V-N(3)	164.2(1)
V(1)-N(4)	2.077(3)	O(1)-V-C(2)	88.7(1)
V(1)-C(1)	2.192(5)	O(1)-V-C(1)	93.4(1)
V(1)-C(2)	2.167(4)	N(3)-V-N(4)	77.1(1)
C≡N	1.147(6)	V(1)- C≡N	177.5(3)
		V(1)- salen	25.78(6)

Results and Discussion

Syntheses and Infrared Spectral Studies

The precursor $[V(acac)_2Cl(THF)]$ was synthesized following the reported procedure.[259] Attempts to prepare $(Et_4N)[(acac)_2V(CN)_2]$ by reacting $[V(acac)_2Cl(THF)]$ with two equivalents of $(Et_4N)CN$ in acetonitrile resulted in yellow crystals of $(Et_4N)_2[acacV(CN)_4]$ **12** (Figure 3.2, Table 3.3) as a result of ligand scrambling as illustrated in scheme 3.1. The reaction of $[V(acac)_2Cl(THF)]$ with two equivalents of (PPN)CN in acetonitrile afforded yellow crystals of the desired product $PPN[(acac)_2V(CN)_2]\cdot PPNCl$, **13** (Figure 3.3, Table 3.3) which is apparently stabilized by co-crystallization with PPNCl. The presence of terminal cyanide in both compounds is evidenced by a $\nu(C\equiv N)$ stretch at 2045 cm^{-1}.

Several trials to incorporate compound **13** into heterometallic molecules were carried out. Compound **13** was reacted with $[Co(dppe)_2(CH_3CN)](BF_4)_2$ leading to $[Co(dppe)_2CN](BF_4)$ as confirmed by X-ray measurements. This result suggests that cyanide groups in **13** are labile. The reaction of **13** with $[Mn(acac)_2(H_2O)](ClO_4)$ resulted in yellow powders with all attempts to crystallize the product using slow diffusion and re-crystallization techniques were unsuccessful. Further attempts were performed with other precursors such as $[M(CH_3CN)_6](BF_4)_2$ {M=Mn,Co and Ni}, and compounds with trans labile coordination sites, $[Mn(salen)(H_2O)]ClO_4$ or $Mn(cyclam)Cl_2$ (Scheme 3.2). The reactions were attempted at low temperatures in order to stabilize the labile cyanide ligands of **13** and to stimulate crystallization of the product but the results were not fruitful.

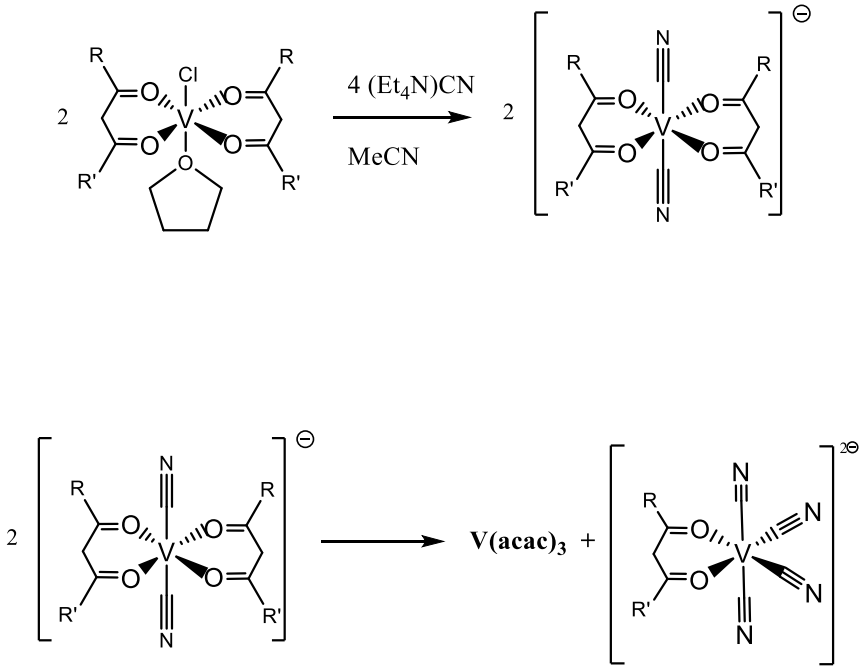

Scheme 3.1 Proposed mechanism of ligand scrambling in **13.**

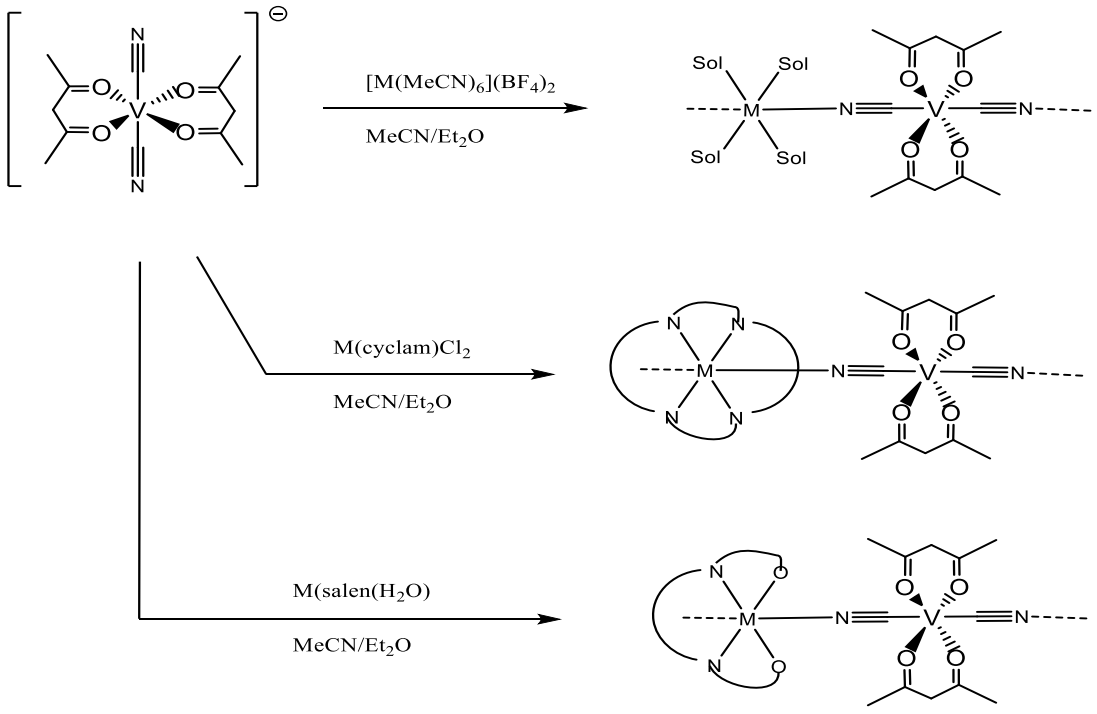

Scheme 3.2 Proposed reactions to incorporate $[V(acac)_2(CN)_2]^-$ building block into 1D chains.

The precursor $[V(salen)Cl]_2$ was reacted with two equivalents of $(Et_4N)CN$ in DMF/CH_3CN resulting in brown powder. Recrystallization from DMF/diethyl ether gave pale red-brown crystals of the dicyanide building block $(Et_4N)[V(salen)(CN)_2]$ (**14**) (Figure 3.4). A similar reaction with two equivalents of (PPN)CN produces $(PPN)[V(salen)(CN)_2]$ (**15**) (Figure 3.5). The same scheme was used to make the analogous building block, $(PPN)[V(MeOsalen)(CN)_2]$ (**16**) (Figure 3.6). The precursor [V(salphen)Cl(THF)] was synthesized according to the literature and recrystallized from DMF/diethyl ether to give red crystals of [V(salphen)Cl(DMF)] (**10**) (Figure 3.1, Table 3.3). Reaction of **10** with two equivalents of $(Et_4N)CN$ in DMF/CH_3CN resulted in a brown powder but no crystals. Reaction of **10** with two equivalents of (PPN)CN in DMF/CH_3CN gave $(PPN)[V(salphen)(CN)_2]\cdot DMF\cdot 2CH_3CN$ (**17**)$\cdot DMF\cdot 2CH_3CN$ (Figure 3.7, Table 3.5). IR spectra of the building blocks are consistent with the presence of cyanide as indicated by the presence of $\nu(C\equiv N)$ stretching frequencies around ~2100 cm^{-1} (Table 3.6). As the data in Table 3.6 indicate, the IR spectra of **14-17** exhibit stretches that are shifted from the energies of the corresponding modes observed for the simple organic cyanide salts and, therefore, are assigned to the terminal cyanides. The presence of coordinated Schiff base ligands is indicated by the $\nu(C=N)$ stretching frequencies of the Schiff base imine group.

Attempts to incorporate this family of building blocks into cyanide-bridged chains through the reaction with other precursors that contain trans labile coordination sites such as manganese (III) salen complexes were performed as illustrated in Scheme

3.3. All the resultant products were found to suffer from the lack of crystallinity. Trials to obtain crystals using different crystal growth techniques were unsuccessful. The reaction of **14** with $[Mn(salen)(H_2O)](ClO_4)$ in DMF/acetonitrile resulted in yellow-brown powders of $[V(salen)(CN)_2][Mn(salen)]n{\cdot}5CH_3CN$ (**18**) (Scheme 3.3). The IR spectrum of **18** exhibits a cyanide stretching frequency at 2130 cm^{-1} which is shifted to higher energy as compared to the building block (2100 cm^{-1}) indicating a bridging rather than a terminal cyanide ligand (Table 3.6).[117] Trials to obtain crystals of **18** using different crystal growth and slow diffusion techniques were unsuccessful.

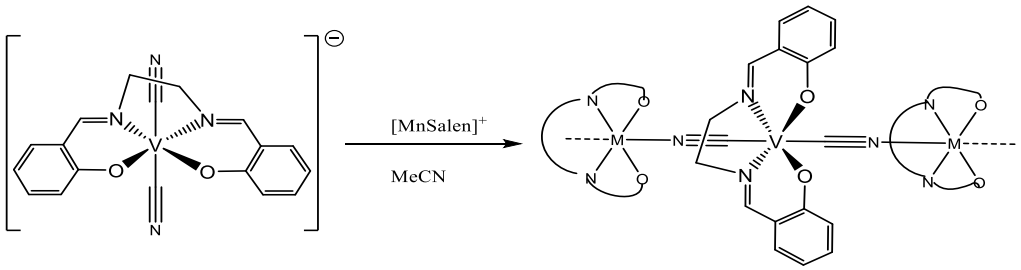

Scheme 3.3 Proposed structure of $[V(salen)(CN)_2][Mn(salen)]n{\cdot}5CH_3CN$ (**18**) 1D chain**.**

Table 3.6 Characteristic infrared cyanide stretches for compounds **13-18** in cm^{-1}

Compound	ν(C≡N) cm^{-1}	ν(C=N) cm^{-1}	
13	2045(m)	-	-
14	2104(s)	1618(s)	1595(s)
15	2100(s)	1620(s)	1597(s)
16	2102(s)	1614(s)	1596(s)
17	2105(s)	1600(s)	1576(s)
18	2130(s)	1621(s)	1599(s)

Single Crystal X-Ray Diffraction Studies

X-ray crystallographic data for **10** revealed that it crystallizes in the monoclinic space group $P2_1/c$ (Table 3.1). The structure consists of discrete neutral molecules with a pseudo-octahedral environment for the central vanadium ion with the N_2O_2 donor sites of the salen ligand filling the equatorial coordination sites and the axial sites being occupied by a terminal chloride and an oxygen atom from DMF molecule (Figure 3.1). Selected bond distances and angles are listed in Table 3.3. The bond distances are very close to the THF adduct that was reported previously except for the V(1)–O(3) distance [2.076(2) Å] which is slightly shorter than the corresponding THF bond [2.155(6) Å].[263] Similarly, the bond angles are comparable to the THF adduct with the angle O1-V-O2 [108.81(9) °] slightly enlarged. The coordination of salphen to vanadium deviates from planarity with the N,O chelate ring forming a dihedral angle of 24.6 °.

Compound **12** crystallizes in the orthorhombic space group $P2_12_12_1$ (Table 3.1). The structure is ionic consisting of a pseudo-octahedral dianion $[V(acac)(CN)_4]^{2-}$ and two isolated Et_4N^+ cations. Two of the equatorial coordination sites in the central vanadium ion are filled with the O donor atoms of the acac ligand while the other two equatorial sites and the axial sites are occupied with carbon donors of terminal cyanide ligands (Figure 3.2). Selected bond distances and angles are provided in table 3.3. The V(1)–O bond distances [1.983(2) Å and 1.948(3) Å] lie within the range of vanadium(III) diketonate complexes.[264] The two equatorial cyanide distances [V(1)–C(1) = 2.132(9) Å, V(1)–C(2) = 2.135(8) Å] and the axial cyanide

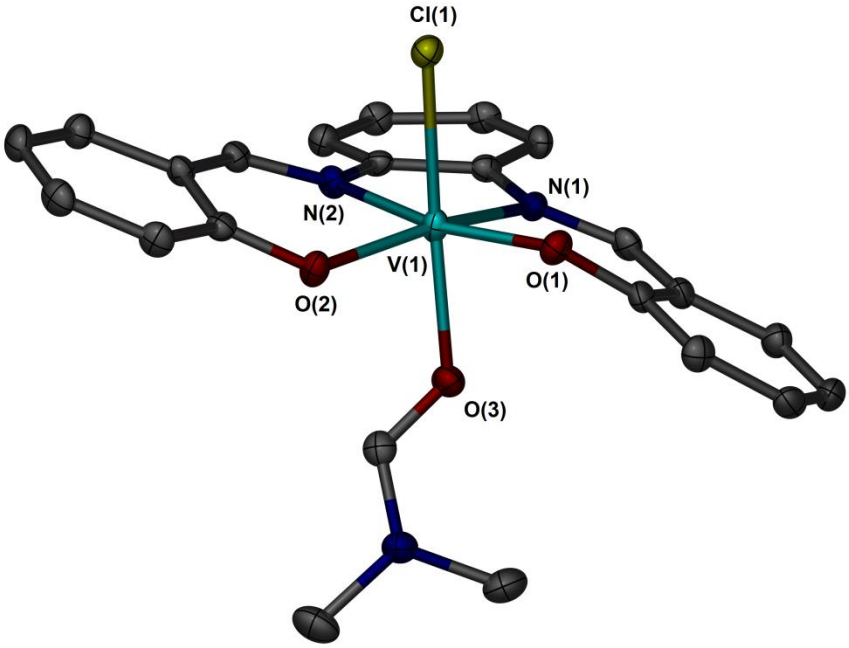

Figure 3.1 Molecular structure of [$V^{(III)}$(salphen)(DMF)Cl] (**10)**. Ellipsoids projected at the 50% probability level. Hydrogen atoms omitted for the sake of clarity.

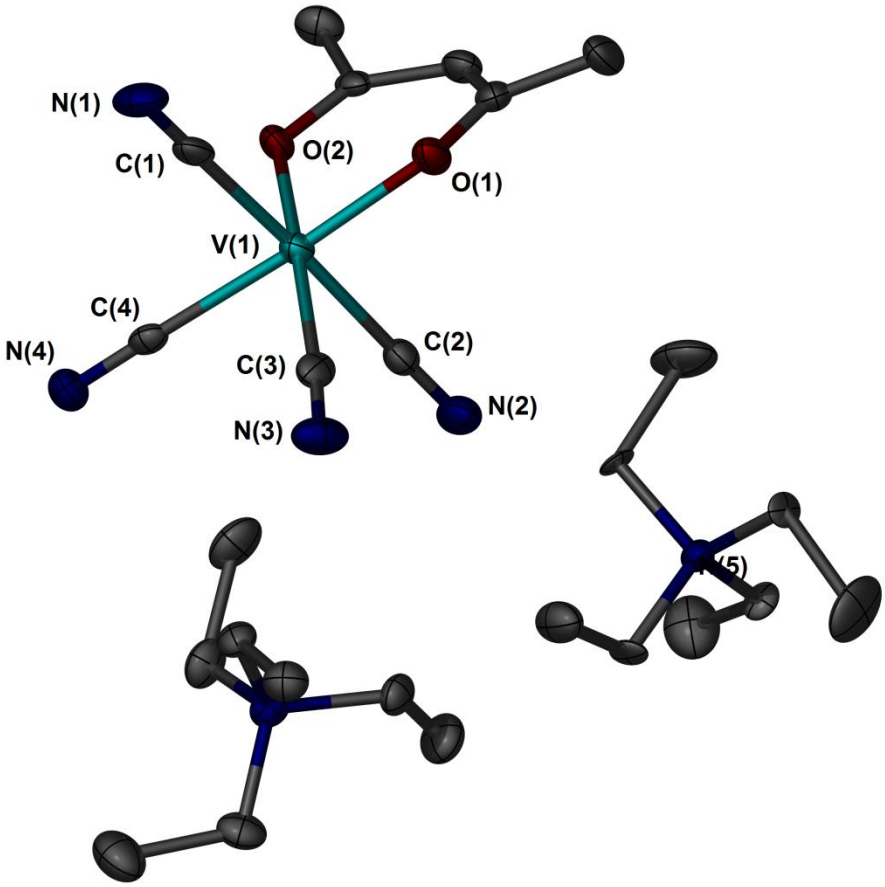

Figure 3.2 Structure of $(Et_4N)_2[V^{(III)}(acac)(CN)_4]$ (**12**). Thermal ellipsoids are drawn at the 50% probability level. Hydrogen atoms omitted for the sake of clarity.

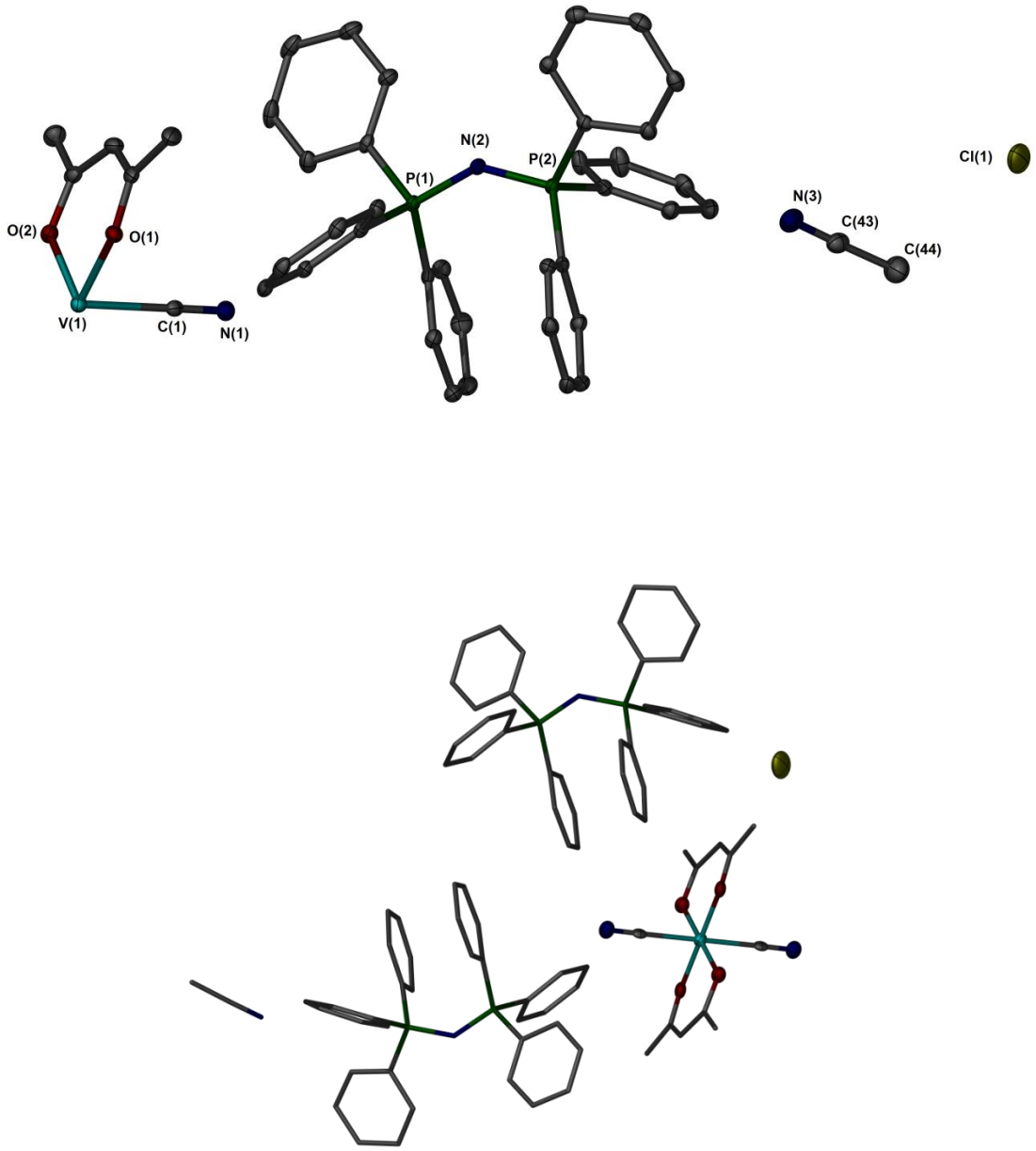

Figure 3.3 Thermal ellipsoid plots of (top) Asymmetric unit (bottom) Molecular structure of (PPN)[$V^{(III)}$ $(acac)_2(CN)_2$]·PPNCl·$2CH_3CN$ (**13**)·$2CH_3CN$. Thermal ellipsoids are drawn at the 30% probability level. Hydrogen atoms are omitted for the sake of clarity.

distances [V(1)–C(3) = 2.122(8) Å, and V(1)–C(4) = 2.144(8) Å] are similar to those reported for $(Et_4N)_3[V(CN)_6]$.[265] The average C≡N bond length is 1.15(1) Å. The cyanide ligands bind to the metal in almost linear fashion with an average angle of V-C≡N = 177.9(3)°; the chelate ring of acac ligand forms a dihedral angle of 22.569°.

Compound **13** crystallizes in the triclinic P-1 space group (Table 3.1) with the anion consisting of a vanadium center with four equatorial O atoms from two acac ligands and two axial cyanide ligands (Figure 3.3). The charge of the anion complex is neutralized with a PPN^+ cation. The co-crystalization of the compound with a (PPN)Cl and an acetonitrile molecule may increase the stability of the dicyanide complex anion and prevent ligand scrambling. Selected bond distances and angles are listed in Table 3.3. The V(1)–O bond distances [1.966(2) Å and 1.978(3) Å] are close to those observed in **12**. The average metal cyanide distance is V(1)–C≡N = 2.168(2) Å which is slightly longer than **12**. The average C≡N bond length is 1.151(3) Å. The cyanide ligands are close to linear with an average angle of V-C≡N = 179.6(2)° and the chelate ring of the acac ligand is slightly twisted with a dihedral angle of 19.169°.

Compound **14** crystallizes in the orthorhombic space group Fdd2 (Table 3.1). The central vanadium ion is in a pseudo-octahedral environment in the complex anion with the N_2O_2 donor atoms of the salen ligand filling the equatorial coordination sites while the axial sites are occupied with carbon donors of axial cyanide ligands (Figure 3.4). The charge of the anion complex is balanced with a $(Et_4N)^+$ cation. Selected

bond lengths and angles are listed in table 3.4. The compound has a V(1)–O(1) bond distance of 1.921(2) Å, and V(1)–N(2) bond distance of 2.093(2) Å which are comparable to those observed in **10**, while the average metal cyanide distance [V(1)–C≡N = 2.182(3) Å] is slightly longer than **12** and **13**. The average C≡N bond is 1.157(2) Å. The cyanide ligands binds to the metal in a slightly bent fashion with an average angle of V-C≡N = 175.6(2) $^{\circ}$, while the chelate ring of salen ligand forms a dihedral angle of 19.848(6) $^{\circ}$.

Compound **15** crystallizes in the orthorhombic space group Pcca (Table 3.2). Selected bond lengths and angles are listed in table 3.4. The complex anion exhibits an identical distorted octahedral coordination environment in the central vanadium ion as **14** (Figure 3.5). The compound has a V(1)–O(1) bond distance of 1.913(1) Å, and V(1)–N(2) bond distance of 2.099(1) Å, while the average metal cyanide distance is V(1)–C≡N = 2.190(1) Å. The average C≡N bond is 1.154(2) Å. Similarly, the cyanide ligands binds to the metal in a slightly bent fashion with an average angle of V-C≡N = 173.3(1) $^{\circ}$, while the N,O chelate ring of salen ligand forms a dihedral angle of 24.661(6) $^{\circ}$.

Compound **16** crystallizes in the monoclinic space group $P2_1/c$ (Table 3.2) with a similar pseudo-octahedral coordination environment in the complex anion with the N_2O_2 donor atoms of the MeOsalen ligand filling the equatorial coordination sites while the axial sites are occupied with carbon donors of axial cyanide ligands (Figure 3.6). The charge of the anion complex is neutralized with PPN^+ cation.

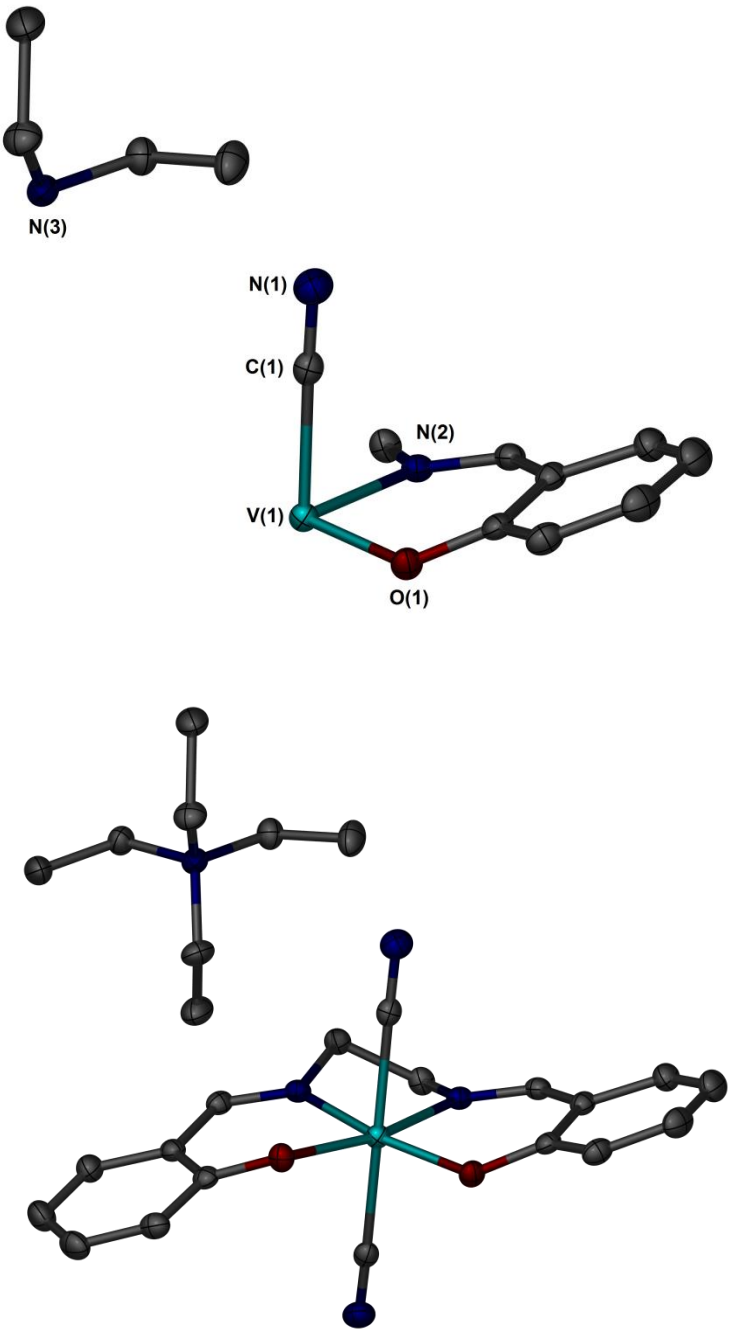

Figure 3.4 Thermal ellipsoid plots of (top) asymmetric unit (bottom) molecular structure of $(Et_4N)[V^{(III)}(salen)(CN)_2]$(**14**). Ellipsoids projected at the 50%probability level. Hydrogen atoms omitted for the sake of clarity.

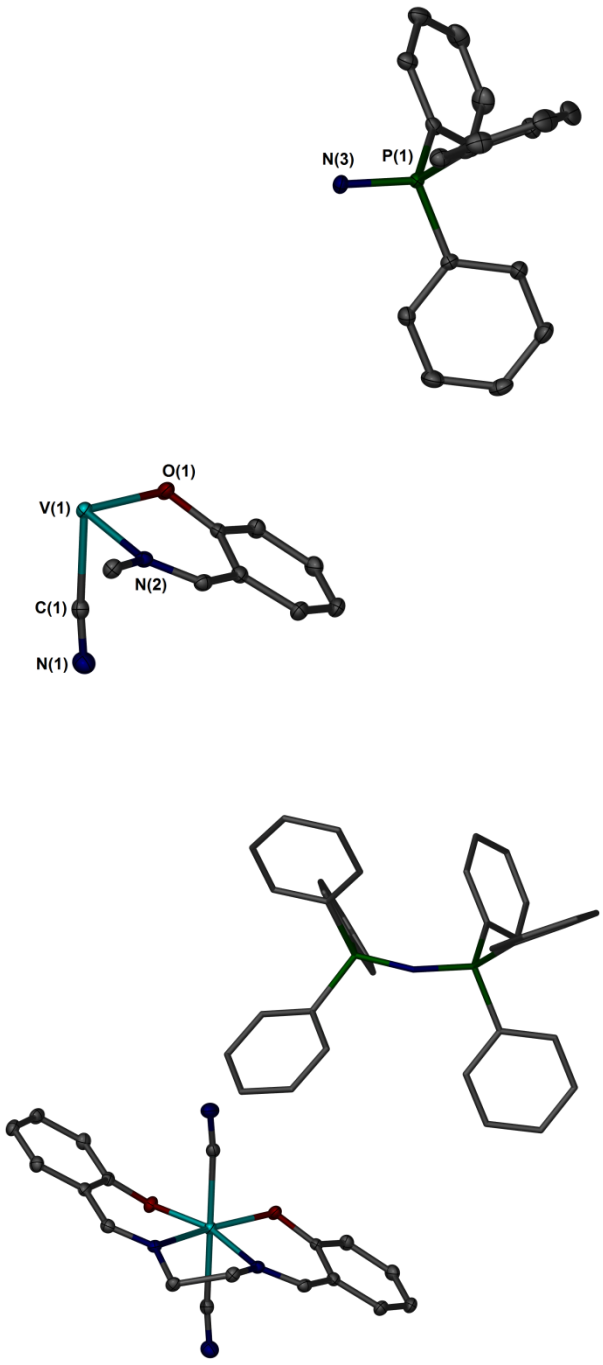

Figure 3.5 Thermal ellipsoid plots of (top) asymmetric unit (bottom) molecular structure of (PPN)[$V^{(III)}$(salen)$(CN)_2$](**15)**. Ellipsoids projected at the 50%probability level. Hydrogen atoms omitted for the sake of clarity.

Selected bond lengths and angles are listed in table 3.5.The compound has bond distances [V(1)–O(1) = 1.909(2) Å, and V(1)–N(2) = 2.084(3) Å] very similar to **14**, while the average metal cyanide distance [V(1)–C≡N = 2.177(3) Å] and the average C≡N bond [1.145(4) Å] are slightly shorter. The metal-cyanide angle [V-C≡N = 172.0(1) °] is a little more bent than **14**, while the N,O chelate ring of MeOsalen ligand forms a similar dihedral angle of 23.633(6) °.

Compound **17** crystallizes in the monoclinic space group $P2_1/n$ (Table 3.2) with the central vanadium ion encountering pseudo octahedral environment in the complex anion. The equatorial coordination sites are filled with the N_2O_2 donor atoms of the salphen ligand, while the axial sites are occupied with carbon donors of axial cyanide ligands (Figure 3.7). Selected bond lengths and angles are listed in table 3.5. The bond distances [V(1)–O(1) = 1.902(2) Å, and V(1)–N(3) = 2.110(3) Å] are very close to **10**. The average metal cyanide distance [V(1)–C≡N = 2.192(3) Å] is similar to that observed in **14-16**. The average C≡N bond is 1.147(6) Å. The cyanide ligands binds to the metal in almost linear fashion with an average angle of V-C≡N = 177.5(1) °, while the N,O chelate ring of salphen ligand forms a dihedral angle of 25.780(6) °. The crystal contains a DMF and two acetonitrile molecules of crystallization

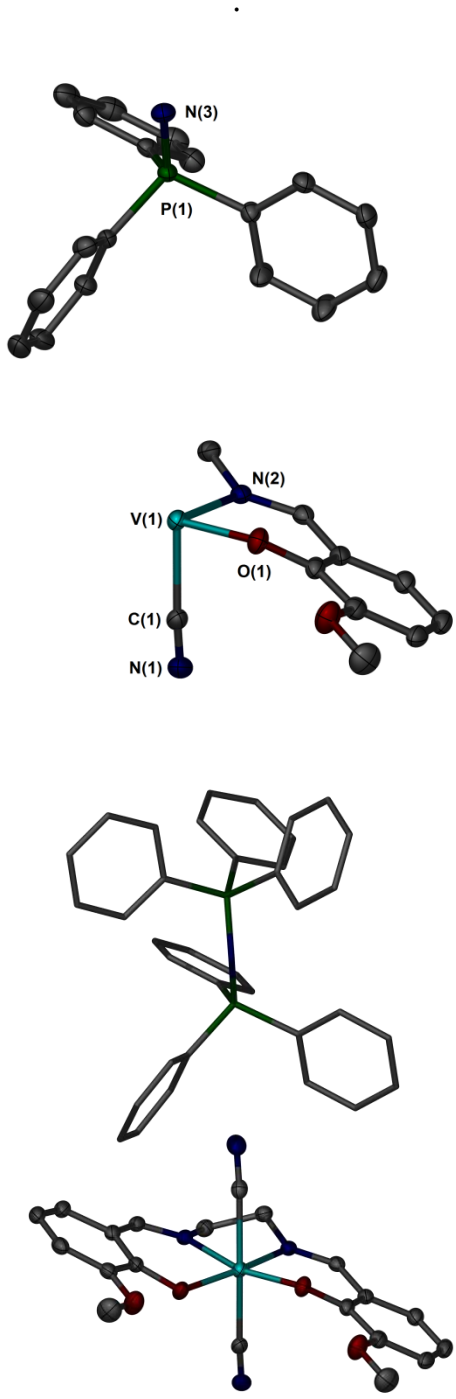

Figure 3.6 Thermal ellipsoid plots of (top) Asymmetric unit (bottom) Molecular structure of (PPN)[$V^{(III)}$(MeOsalen)$(CN)_2$] (**16)**. Ellipsoids projected at the 50%probability level. Hydrogen atoms omitted for the sake of clarity.

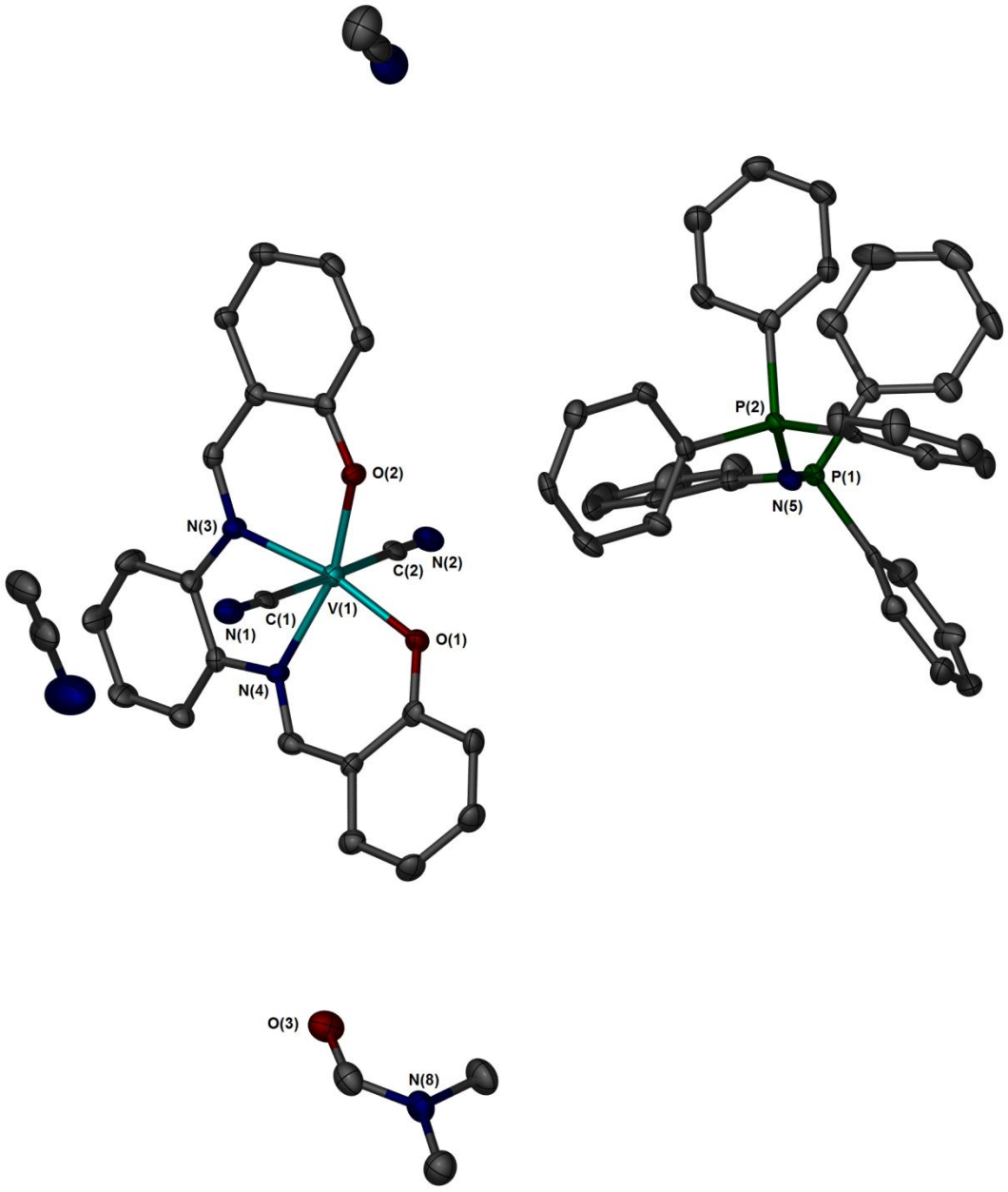

Figure 3.7 Thermal ellipsoid plots of PPN[$V^{(III)}$(salphen)$(CN)_2$]·DMF·2CH_3CN (**17**). Ellipsoids projected at the 50% probability level. Hydrogen atoms omitted for the sake of clarity.

Magnetic Properties

DC magnetic measurements were performed on freshly prepared crushed polycrystalline samples over the temperature range of 2–300 K in an applied magnetic field of 1000 Oe on a Quantum Design SQUID, Model MPMS with 7 Tesla magnet.

$(PPN)[(acac)_2V(CN)_2]\cdot PPNCl$ (13). The χ and χT versus T plots of **13** over the range 1.8 - 300K (Figure 3.8) show a room temperature χT value of 1.05 $emu\cdot mol^{-1}\cdot K$ at 300 K which is consistent with an isolated V^{III} ion with S = 1 and g = 2.05 and temperature-independent paramagnetism (TIP) = $2.0\cdot10^{-4}$ $emu\cdot mol^{-1}$. Upon lowering the temperature, the susceptibility decreases to 0.44 $emu\cdot mol^{-1}\cdot K$ at 2 K (Figure 3.8a), indicating zero field splitting and may be intermolecular dipole-dipole interactions. The magnetization versus field data for **13** (figure 3.8 inset) is consistent with the presence of a single vanadium (III) center. The lack of saturation even at 7 T is not unusual due to the anisotropic nature of V(III). Field-dependent magnetization data at temperatures between 1.8 and 4.5 K show non-superposition of the iso-field lines indicating the presence of large zero-field splitting (Figure 3.8b). The fitting using *ANISOFIT* estimated ZFS parameters of D = -10.0 cm^{-1} and E = 0.01 cm^{-1} with g = 1.98.

$(Et_4N)[V(salen)(CN)_2]$ (14). The room temperature χT value of 0.98 $emu\cdot mol^{-1}\cdot K$ is consistent with one isolated V^{III} ion with S=1 and g = 1.94 and temperature-independent paramagnetism (TIP) = $1.8\cdot10^{-4}$ $emu\cdot mol^{-1}$ (0.98 $emu\cdot K\cdot mol^{-1}$). Upon lowering temperature, the susceptibility decreases to 0.36 $emu\cdot mol^{-1}\cdot K$ at 2 K (Figure 3.9a), which may be due to zero field splitting and some contribution of intermolecular dipole-dipole interactions.

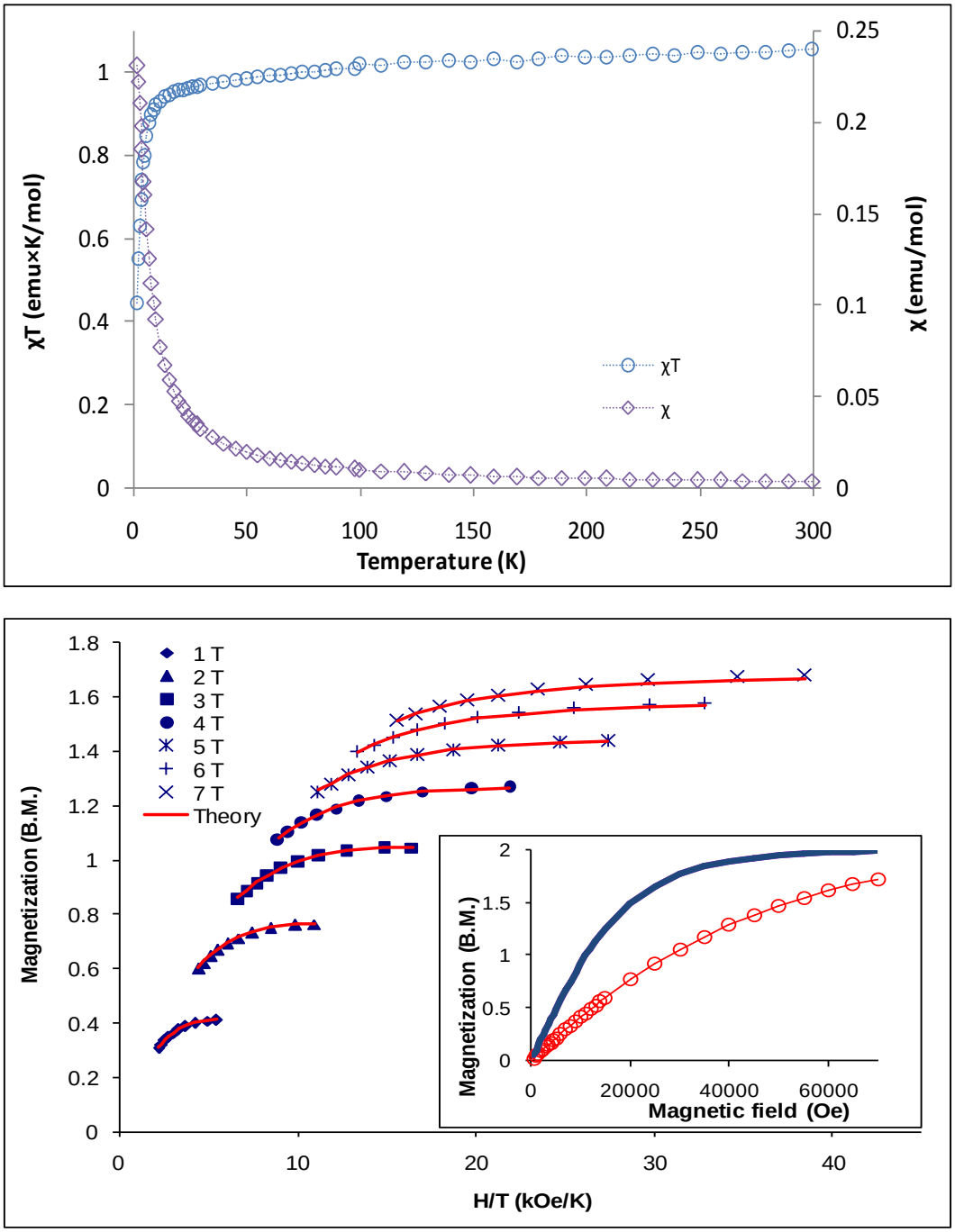

Figure 3.8 (a) Temperature dependence of χ (◊) and χT product (o) for **13** (*S* = 1, *g* = 2.05, TIP = $2.0 \cdot 10^{-4}$ emu mol^{-1}) and (b) reduced magnetization of **13**. Solid lines correspond to the best-fit curves using *ANISOFIT* (D = -10.0 cm^{-1}, E = 0.01 cm^{-1}, *g* = 1.98). Inset: Field-dependent magnetization curve at 1.8 K (o). The solid line corresponds to the Brillion function (S = 1, g_{avg} = 2.0).

The magnetization versus field data for **14** (figure 3.9b inset) is consistent with the presence of single vanadium (III) center. Data of field dependent magnetization at temperatures between 1.8 and 4.5K show a non-superposition of the iso-field lines indicating the presence of large zero field splitting (Figure 3.9b). The fitting using *ANISOFIT* estimated ZFS parameters of D = 5.89 cm^{-1} and E = -0.0108 cm^{-1} with g = 1.89. The magnetization does not saturate even at 7 Tesla.

(PPN)[V(salen)(CN)$_2$] (15). Compound **15** exhibits a room temperature χT value of 1 emu·mol^{-1}·K at 300 K which is consistent with an isolated V^{III} ion with S = 1 and g = 2.03 and temperature-independent paramagnetism (TIP) = $1.0 \cdot 10^{-4}$ emu·mol^{-1} (1.03 emu·K·mol^{-1}). At lower temperatures, the susceptibility decreases to 0.72 emu·mol^{-1}·K at 2 K (Figure 3.10a), which could be attributed to zero field splitting and some contribution of intermolecular dipole-dipole interactions. The magnetization versus field data for **15** (figure 3.10b inset) does not saturate due to strong anisotropy. Field dependent magnetization data at temperatures between 1.8 and 4.5K reveal a non-superposition of the iso-field lines indicating the presence of significant zero field splitting (Figure 3.10b). The fitting using *ANISOFIT* estimated ZFS parameters of D = 3.7 cm^{-1} and E = -0.01 cm^{-1} with g = 2.1.

(PPN)[V(MeOsalen)(CN)$_2$] (16). Compound **16** exhibits a room temperature χT value of 0.93 emu·mol^{-1}·K at 300 K as expected for V^{III} with S = 1 and g = 1.88 and a temperature-independent paramagnetic (TIP) term of $1.8 \cdot 10^{-4}$ emu·mol^{-1}. As the temperature is lowered, the susceptibility decreases to 0.51 emu·mol^{-1}·K at 2 K (Figure 3.11a), indicating zero field splitting and intermolecular dipole-dipole interactions. The

magnetization versus field data for **16** (figure 3.11b inset) is consistent with the presence of single vanadium (III) center but there is no saturation. Field dependent magnetization data at temperatures between 1.8 and 4.5K shows a non-superposition of the iso-field lines indicating the presence of large zero field splitting (Figure 3.11b). The fitting using *ANISOFIT* led to ZFS parameters of D = 4.01 cm^{-1} and E = -0.016 cm^{-1} with g = 1.79.

(PPN)[V(salphen)$(CN)_2$]·DMF·2CH_3CN (17). Compound **17** exhibits a room temperature χT value of 0.89 emu·mol^{-1}·K at 300 K in accord with an isolated V^{III} ion with S = 1 and g = 1.85 and (TIP) = $2.0 \cdot 10^{-4}$ emu·mol^{-1}. Upon lowering temperature, the susceptibility decreases to 0.43 emu·mol^{-1}·K at 2 K (Figure 3.12a), indicating significant zero field splitting and some contribution of intermolecular dipole-dipole interactions. The magnetization versus field data for **17** (figure 3.12b inset) are consistent with the presence of single vanadium (III) center. The lack of saturation even at 7T is probably due to the anisotropic nature of V(III). Field dependent magnetization data between 1.8 and 4.5 K shows a non-superposition of the iso-field lines indicating the presence of large zero field splitting (Figure 3.12b). The fitting using *ANISOFIT* led to ZFS parameters of D = 4.36 cm^{-1} and E = 0.112 cm^{-1} with g = 1.77. ZFS parameters of all the series of vanadium dicyanide building blocks are summarized in table 3.7.

Table 3. 7 ZFS parameters for **13-17.**

Compound	g	D (cm^{-1})	E (cm^{-1})
13	1.98	-10	0.01
14	1.89	5.89	-0.01
15	2.1	3.7	-0.01
16	1.79	4.05	-0.016
17	1.76	4.36	0.112

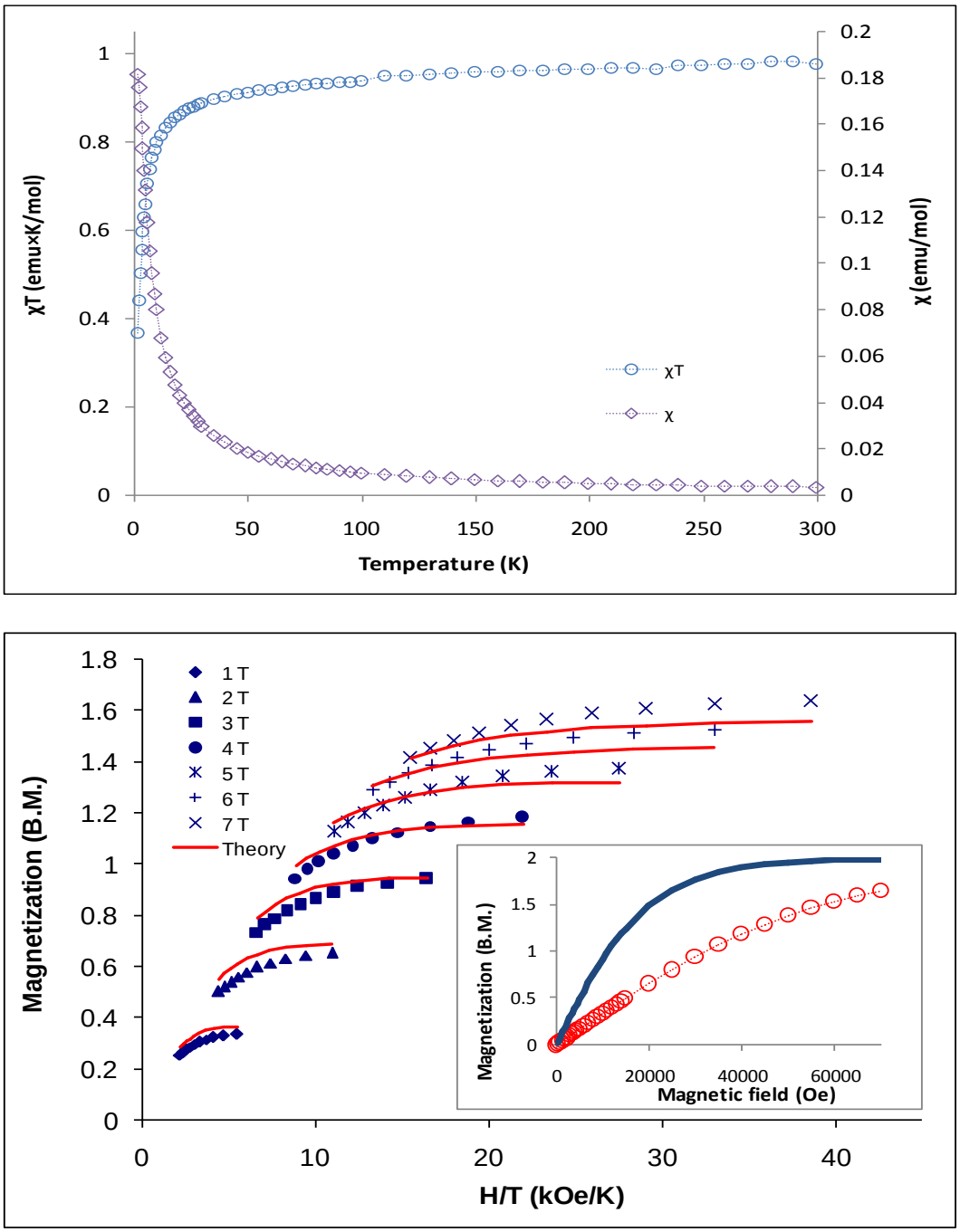

Figure 3.9 (a) Temperature dependence of χ (◊) and χT product (o) for **14** (*S* = 1, *g* = 1.94, TIP = $1.8 \cdot 10^{-4}$ emu mol^{-1}) and (b) reduced magnetization of **14.** Solid lines correspond to the best-fit curves using *ANISOFIT* (D = 5.89, E = -0.01cm^{-1}, *g* = 1.89). Inset: Field-dependent magnetization curve at 1.8 K **(**o**)**. The solid line corresponds to the Brillion function (S = 1, g_{avg} = 2.0).

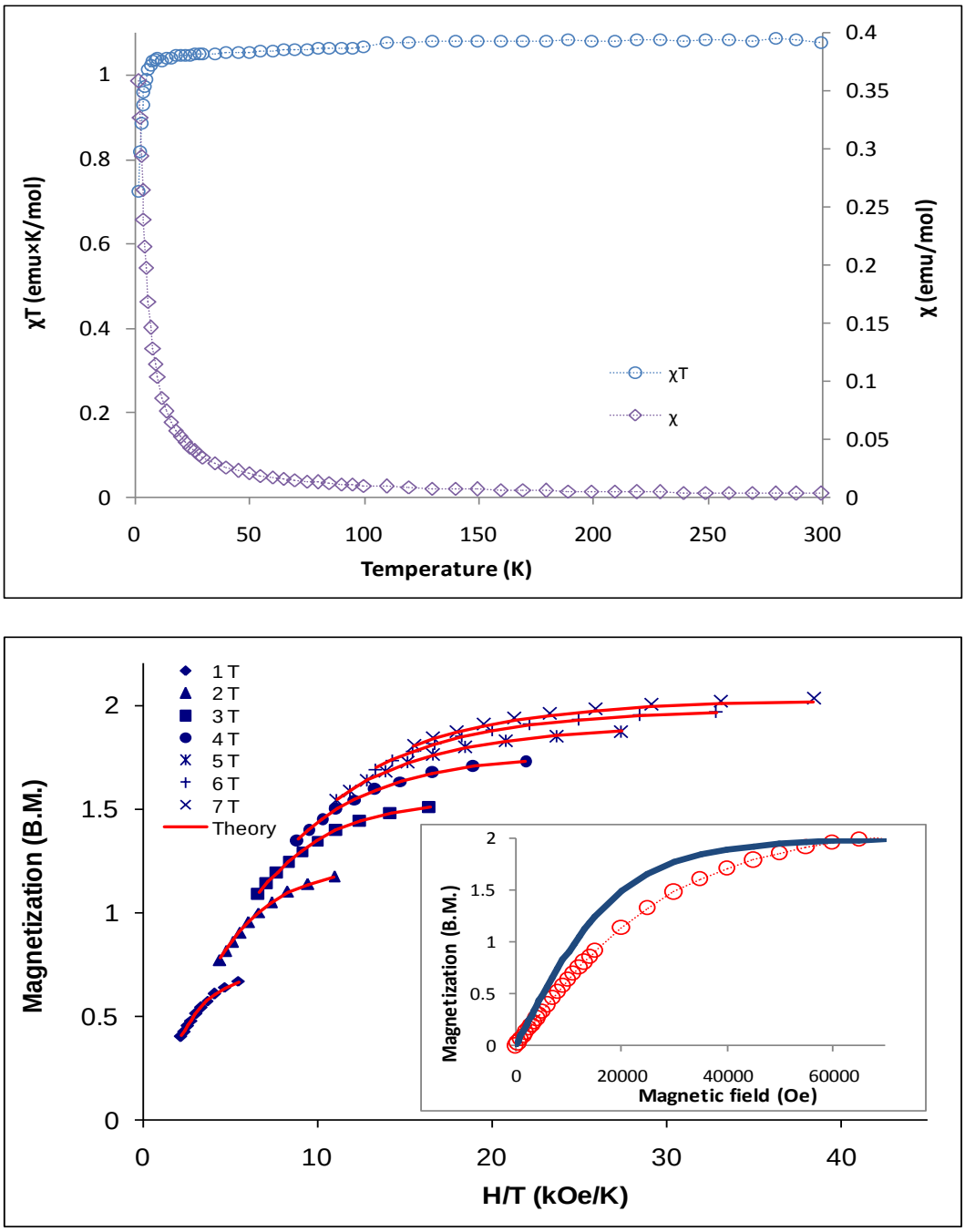

Figure 3.10 (a) Temperature dependence of χ (◊) and χT product (o) for **15** (S = 1, g = 2.03, TIP = $1 \cdot 10^{-4}$ emu mol^{-1}) and (b) reduced magnetization of **15.** Solid lines correspond to the best-fit curves using *ANISOFIT* (D = 3.7, E = -0.01 cm^{-1}, g = 2.1). Inset: Field-dependent magnetization curve at 1.8 K **(**o**)**. The solid line corresponds to the Brillion function (S = 1, g_{avg} = 2.0).

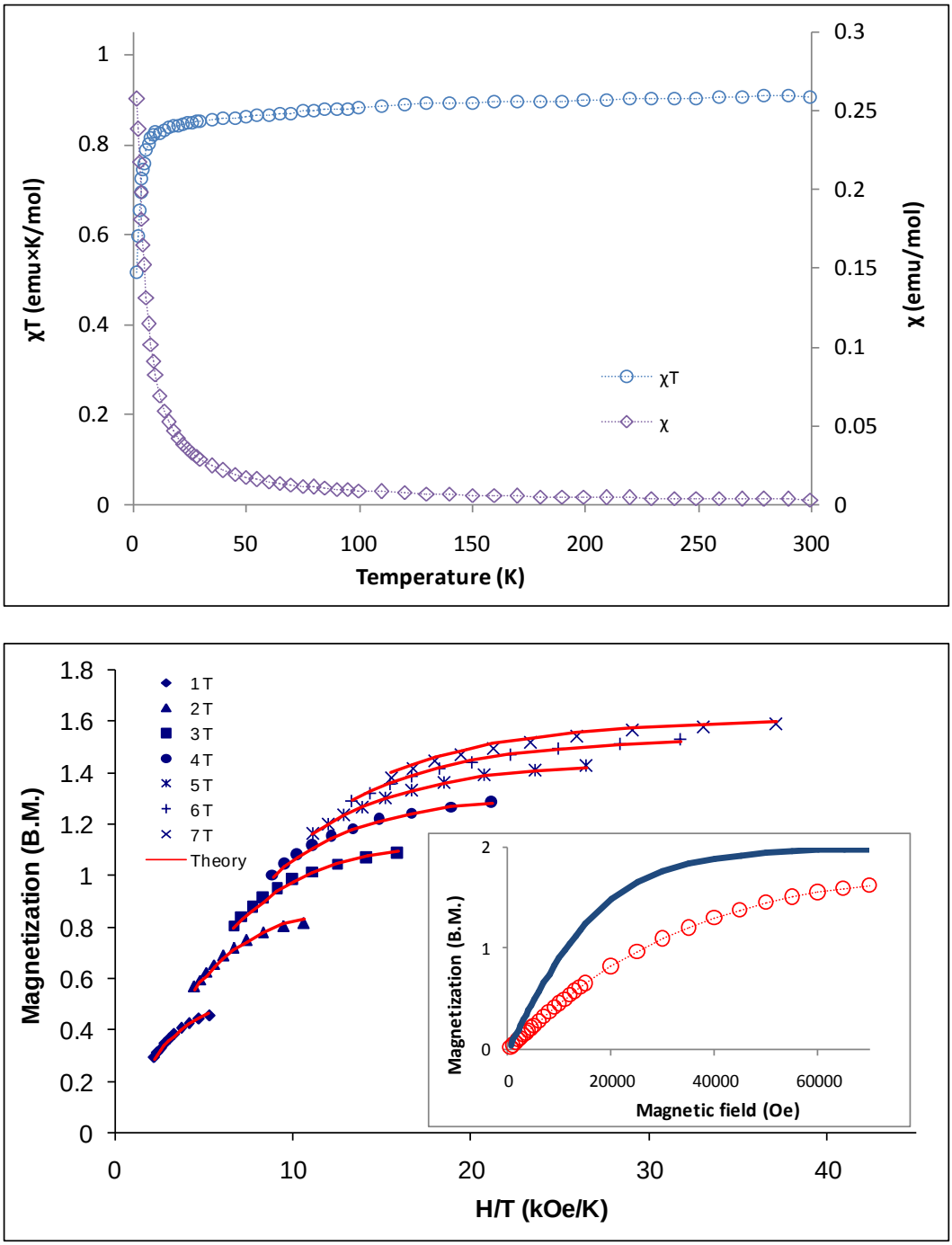

Figure 3.11 (a) Temperature dependence of χ (◊) and χT product (o) for **16** (S = 1, g = 1.88, TIP = $1.8 \cdot 10^{-4}$ emu mol^{-1}) and (b) reduced magnetization of **16**. Solid lines correspond to the best-fit curves using *ANISOFIT* (D = 4.05 cm^{-1}, E = -0.016 cm^{-1}, g = 1.79). Inset: Field-dependent magnetization curve at 1.8 K **(**o**)**. The solid line corresponds to the Brillion function (S = 1, g_{avg} = 2.0).

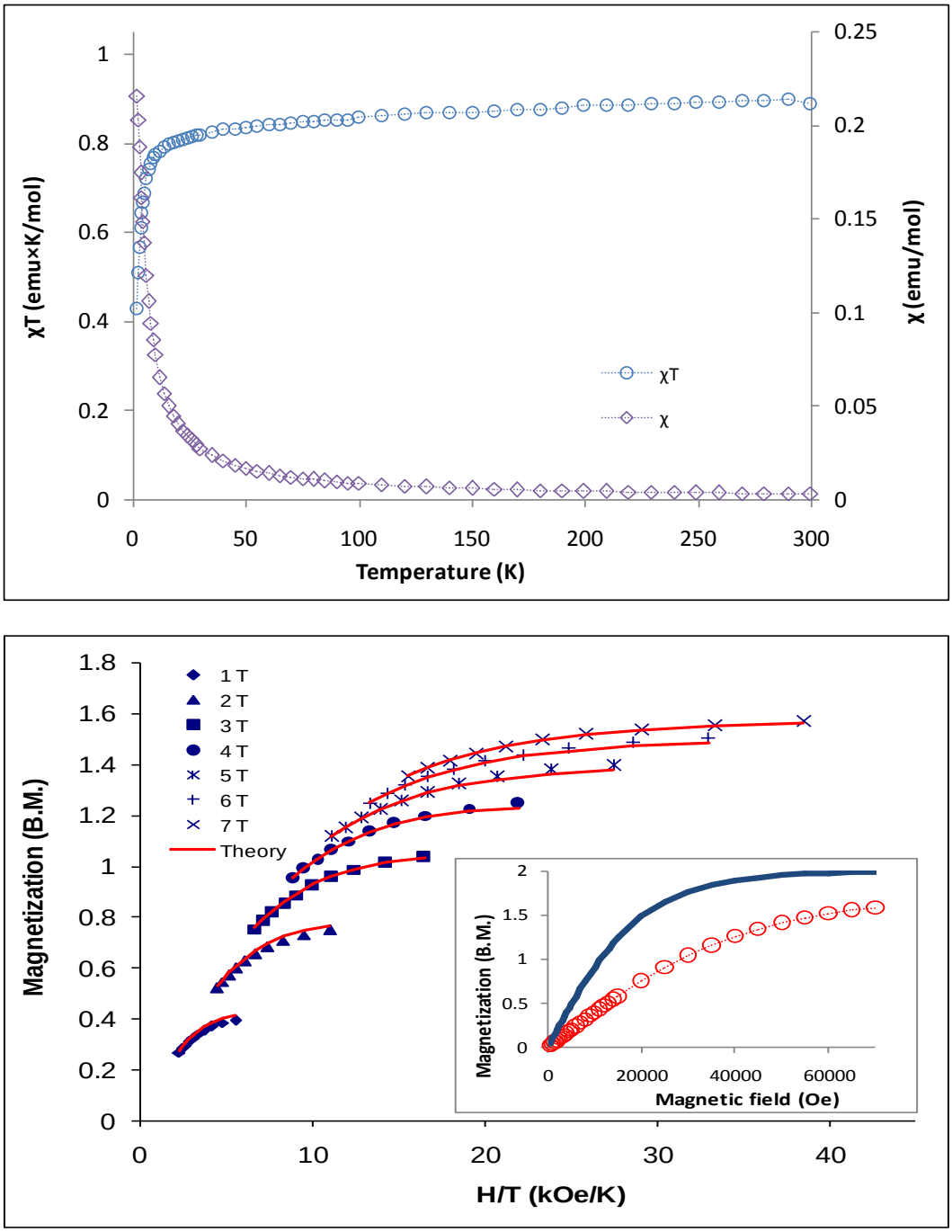

Figure 3.12 (a) Temperature dependence of χ (◊) and χT product (o) for **17** (S = 1, g = 1.83, TIP = $2.0 \cdot 10^{-4}$ emu mol^{-1}) and (b) reduced magnetization of **17**. Solid lines correspond to the best-fit curves using *ANISOFIT* (D = 4.36 cm^{-1}, E = 0.112 cm^{-1}, g = 1.76). Inset: Field-dependent magnetization curve at 1.8 K **(**o**)**. The solid line corresponds to the Brillion function (S = 1, g_{avg} = 2.0).

$[V(salen)(CN)_2][Mn(salen)]_n \cdot 5CH_3CN$ (18). Compound **18** exhibits a room temperature χT value of 3.57 emu·mol^{-1}·K at 300 K, which is consistent with V^{III} ion (S = 1, g = 1.9) and Mn^{III} ion (S =2, g = 1.97) At lower temperatures, the susceptibility decreases to a minimum of 1.79 emu·mol^{-1}·K at 8 K (Figure 3.13a), which can be attributed to antiferromagnetic interactions between metal spins. Decreasing the temperature further results in a slight increase in χT value up to 2.23 emu·mol^{-1}·K at 2 K. The magnetization versus field data for **18** (figure 3.13b) are consistent with the presence of antiferromagnetically coupled vanadium (III) and manganese (III) centers as indicated by a gradual increase and near saturation at 7 T for an S = 1 ground state. The χT versus T data were simulated using a ferrimagnet Heisenberg chain model[266] in addition to incorporating inter-chain interactions, *J'*, in the frame of the mean-field approximation:

$$H = -2J_{Mn-V} \sum_i (S_{Mn,i} \cdot S_{V,i} + S_{Mn,i} \cdot S_{V,i+1}) \qquad (Eq. 3.1)$$

$$\chi = \frac{\chi_{chain}}{1 - \frac{2zJ'}{Ng^2\mu_B^2}\chi_{chain}} \qquad (Eq. 3.2)$$

with (g_{Mn} = 1.95, g_V = 1.85 , J = -4.4 cm^{-1}, zJ' = -0.55 cm^{-1}).

The relaxation dynamics of the compound were studied using ac susceptibility measurements. An "in-phase" and an "out-of-phase" signal were observed in the temperature dependent AC measurements under zero field (Figure 3.14). The frequency dependent AC measurements were fitted using an extended Debye model resulting in an energy barrier of 13.4 cm^{-1} with τ = 1.52x10^{-8} s (Figure 3.15).

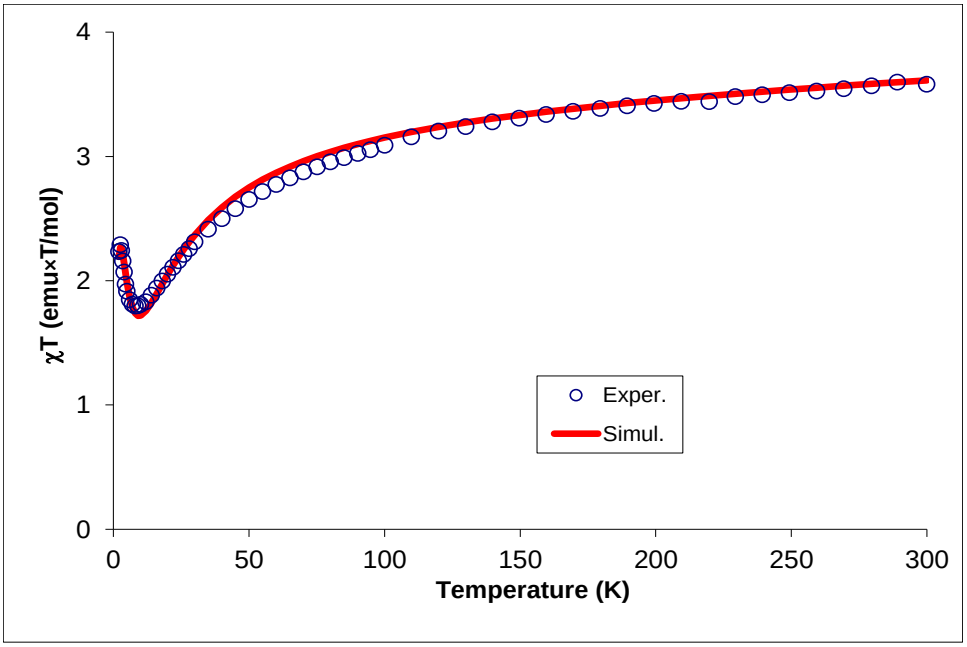

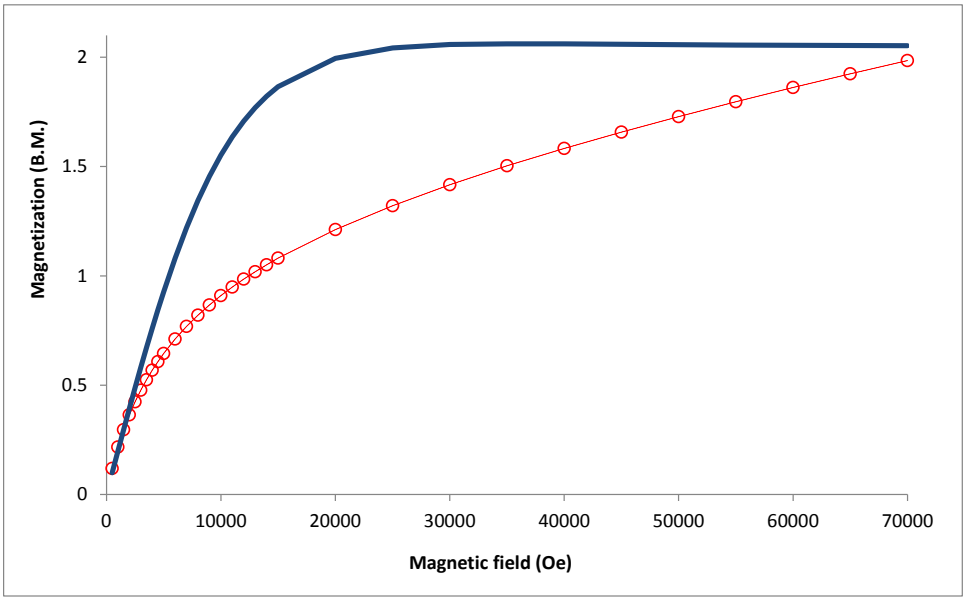

Figure 3.13 (a) Temperature dependence of χT product for **18** (o). The solid line corresponds to the simulation using ferrimagnet Heisenberg chain model (g_{Mn} = 1.95, g_V = 1.85 , J = -4.4 cm^{-1}, zJ' = -0.55 cm^{-1}). (b) field dependent magnetization for **18 (o)**. The solid line corresponds to the Brillion function (S = 1, g_{avg} = 1.95).

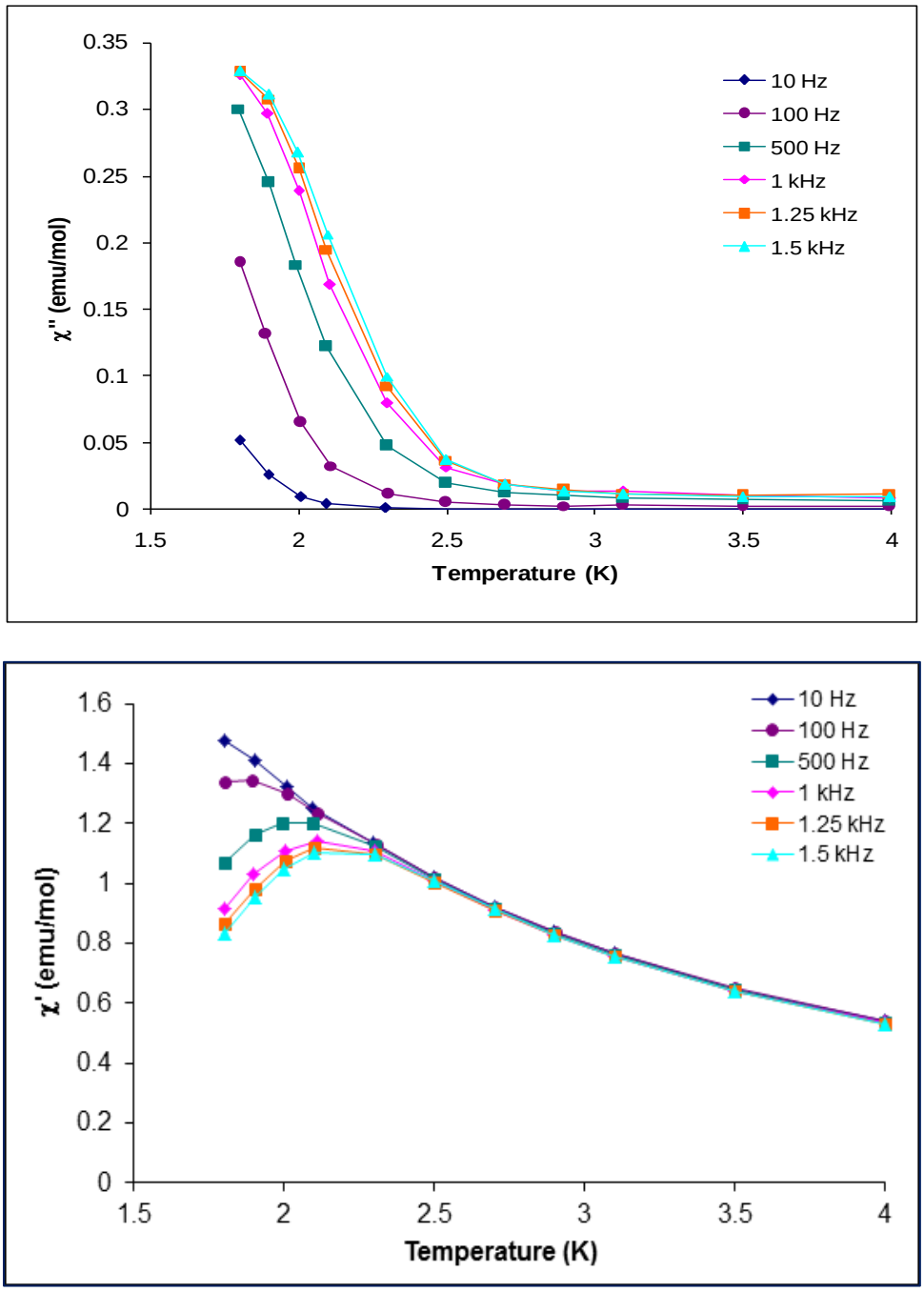

Figure 3.14 Temperature dependence of the imaginary (χ″) part (top) and the real (χ″) part (bottom) of the ac susceptibility for **18** measured under various oscillating frequencies (1-1500 Hz). The solid lines are a guide for the eye.

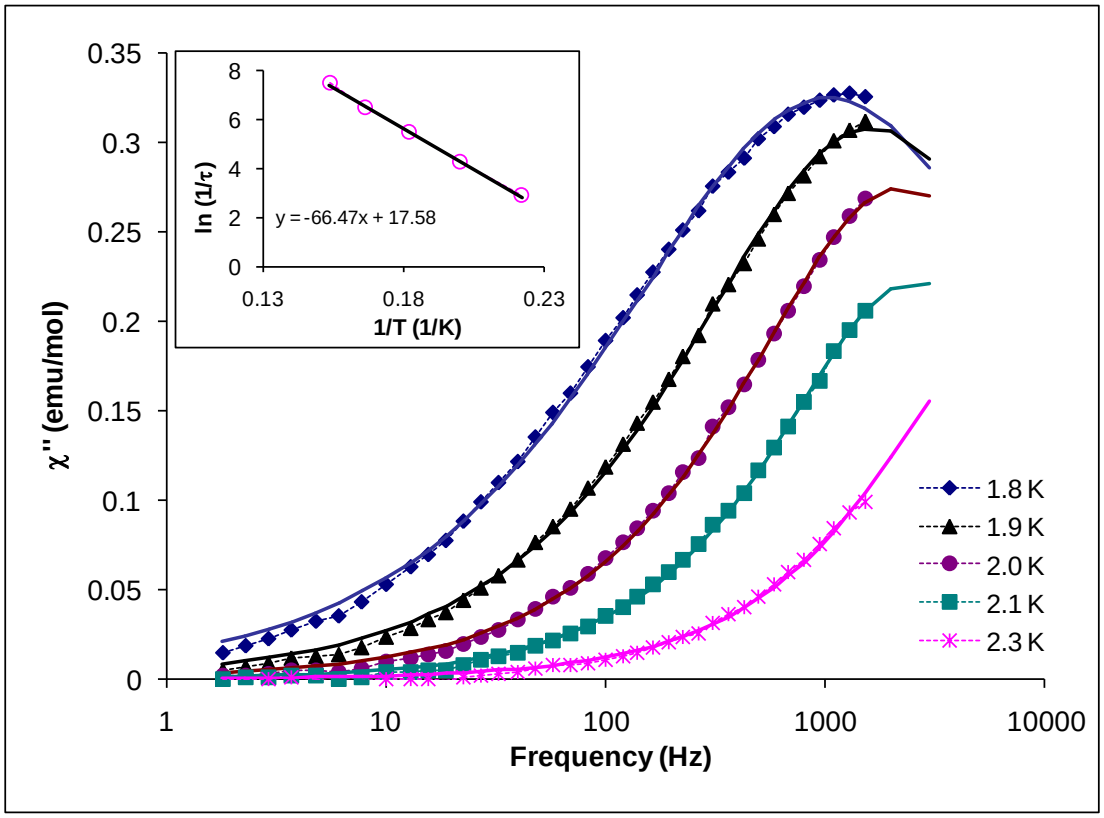

Figure 3.15 Cole-Cole plot for **18**. The solid line represents the least squares fit by a generalized Debye model. Inset: dependence of the logarithm of the relaxation rate ($1/\tau$) on the inverse temperature ($1/T$). The solid line represents the best linear fit to the Arrhenius law (U_{eff} = 13.5 cm^{-1} and τ_0 = 1.52 x 10^{-8} s).

High Field EPR Spectroscopy

Single-crystal HF-HFEPR measurements were carried out in collaboration with Dr Steven Hill in the magnet lab, Tallahassee, Florida. The experiment was performed using a cavity perturbation technique on a 15 T superconducting magnet. The microwave source and detector used were a Millimeter vector network analyzer in combination with a series of schottky diodes and several different frequency multipliers. The experiment temperature was 1.4 K within the frequency range (50-225 GHz).

Based on the predicted large magnetic anisotropy and the lack of reliability of ZFS parameters extracted from magnetic measurements, single crystal HF-HFEPR measurements were performed on **15** (Figure 3.16). The crystal was rotated about a fixed axis to ensure that the applied field is parallel to the molecular easy axis. Two EPR peaks were observed which correspond to the two different molecular orientations in the structure (A and B) as shown in figure 3.17.

The EPR data were simulated using the following Hamiltonian, where φ is the angle between the field and the molecular easy axis:

$$H = DS_z^2 + E\left(S_x^2 - S_y^2\right) + \mu_B \cdot g \cdot B(\cos(\varphi)S_x + \sin(\varphi)\,S_y) \qquad Eq\ 3.3$$

The value of D was calculated indirectly by fitting the observed transitions revealing a D value of 3.8 cm^{-1} and E value of 0.0 cm^{-1} with g_{av} = 1.94 which is close to the values extracted from magnetic data. The unambiguous assignment of the sign of D was not possible due to the lack of rhombic anisotropy (E = 0.0).

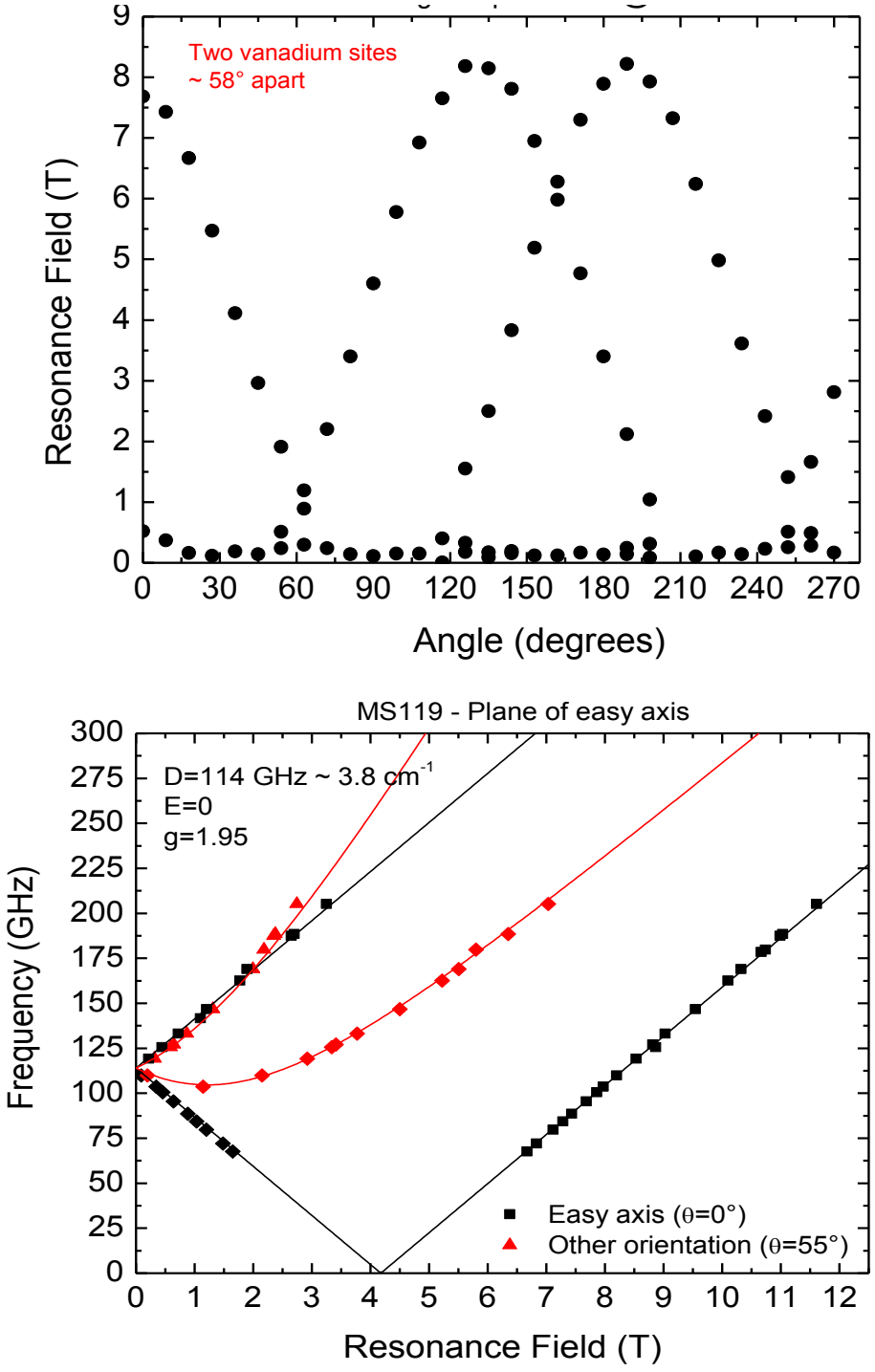

Figure 3. 16 Angle dependence of the EPR spectrum observed for a single crystal of **15** at 110 GHz(top). Frequency dependence of the EPR spectrum of **15**, the solid lines correspond to the best fit employing the Hamiltonian (eq 1).

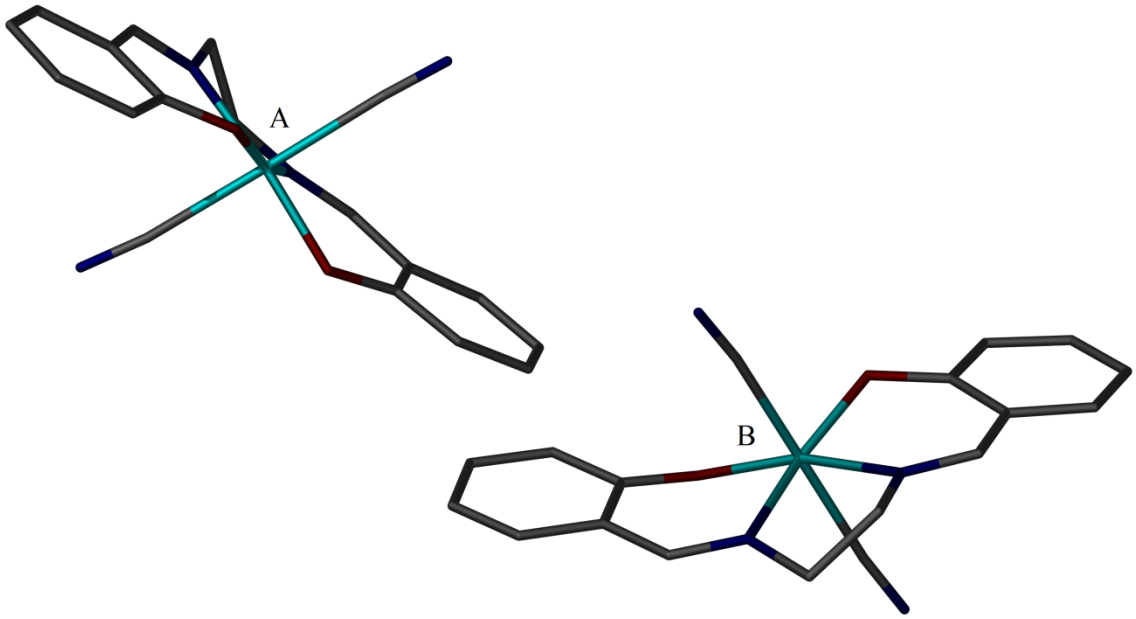

Figure 3. 17 Different molecular orientations of the easy axis in **15**

Conclusions

A family of new anisotropic vanadium cyanide building blocks based on acetylacetonate and salen type ligands were synthesized and structurally characterized The ligands acetylacetonate, salen (salen = N,N'-Ethylenebis(salicylimine)), salphen (salphen = N,N'-Phenylenebis(salicylimine)) and 2-methoxysalen (2-methoxysalen = N,N'-Ethylenebis(2-methoxysalicylimine)) were used. A study of the magnetic properties revealed moderate zfs parameters with D values of -10.0, 5.89, 3.7, 4.05 and 4.36 cm^{-1} for **13-17** respectively which make these building blocks very promising for introducing single ion anisotropy into heterometallic cyanide bridged clusters. The variation of the capping ligand in the salen building block family does not seem to affect the magnitude of D. The magnitude of D for **15** (3.8) was confirmed by HFEPR measurements in collaboration with Dr Steven Hill in the magnet lab, Tallahassee, Florida, however, the assignment of the sign was not possible because of the lack of rhombic anisotropy (E = 0.0). To date, attempts to incorporate them into heterometallic complexes proved to be very challenging due to the high cyanide lability in solution and difficulty in crystallization products presumably due to speciation issues. The reaction of **14** with $[Mn(salen)(H_2O)](ClO_4)$ resulted in powders which we proposed to be **[**$V(salen)(CN)_2][Mn(salen)]_n \cdot 5CH_3CN$ **(18)**. Magnetic studies of **18** were interpreted as being due to an antiferromagnetically coupled cyanide bridged V-CN-Mn 1D chain. The estimated coupling constant is -4.4 cm^{-1}. Susceptibility studies of the ac type led to an estimated energy barrier of 13.5 cm^{-1} with $\tau = 1.52 \times 10^{-8}$ s.

CHAPTER IV

A SERIES OF CYANIDE BRIDGED TRIGONAL BIPYRAMIDAL MOLECULES BASED ON 5D AND 4F METALS

Single Molecule Magnets (SMMs) are a remarkable class of molecules that display magnetic bistability of a molecular origin.[39,78] This magnetic bistability provides an excellent potential for their use as memory storage units of molecular size,[6,7] carriers of quantum bits of information [47,48,56] and components of spintronic devices.[57] Currently, the main challenge in this field is to improve the energy barriers and blocking temperatures in order to make them more feasible for practical applications. Recent studies have focused on increasing the global magnetic anisotropy of the molecule as a key factor for enhancement of SMM properties.[102,114,123,267-269] In this vein, heavy lanthanide and actinide ions are of special interest due to their large spin states accompanied by large single ion anisotropies. Lanthanide elements have a long history of forming materials with extraordinary magnetic properties, including the strongest magnets known, $SmCo_5$ and $Nd_2Fe_{14}B$.[16-18] The properties of these materials are largely a result of the interaction between the lanthanide ions and the conduction band. Synthetic chemists recently began to use f-elements in solution chemistry for the elaboration of single-molecule magnets, resulting in a rapid expansion of the field.[152-155,270-279] Several early examples of the now famous family of double decker complexes studied by Ishikawa and coworkers in 2003[152-155] revealed that individual 4f centers can exhibit slow paramagnetic relaxation of the magnetization up to 40 K.

To understand the SMM behavior in single lanthanide ions, an emerging trend is to control the crystal field and coordination environment.[156-165] The ligand field strength and geometry around the central lanthanide ion have been found to govern the stabilization of the magnetic ground state as well as its isolation from the excited states. A well-isolated ground state is crucial for eliminating thermal relaxation pathways through accessible excited states, thereby increasing the blocking temperatures in lanthanide-based SMMs. Exciting examples that have been reported include organometallic lanthanide complexes[159,160] as well as actinide complexes.[164-168]

In another approach, recent studies showed that, surprisingly, the role of exchange interactions between 4f metal centers is a very important factor.[270,280-286] Long and coworkers reported a family of N_2^{3-} bridged lanthanide dimers that exhibit magnetic hysteresis at a record temperature (14 K) due to the large exchange coupling between lanthanide ions afforded by the interaction of the lanthanide d-orbitals with the N_2^{3-} side-on radical bridges.[282].[50] Several other interesting radical bridged complexes have also been reported.[285-289] Other examples of homo- and heterometallic 4f aggregates are known including Ln_3 triangles,[290-298], Dy_5 pyramids[299,300], 3d-4f TBP [301], 3d-4f octahedron [302], and 5d-4f dimers[303,304]. Powell and coworkers reported an interesting family of Dy_3 triangles showing slow relaxation of magnetization despite the strong antiferromagnetic interaction which leads to a toroidal non-magnetic ground state.[291,294]

Among heterometallic bridged lanthanide compounds, several examples of cyanide bridged d/f cages of different nuclearities and dimensionalities including; dimers,[305-307] 1D chains,[308-315] 2D,[256,316] and 3D networks,[314,317,318] as well as other geometries have

been reported.[256,305-314,316-335] Magnetic exchange interactions with lanthanide ions through bridging cyanides are typically weak, nevertheless interesting magnetic properties have been observed including slow relaxation of the magnetization,[308] long range ordering,[313,317] as well as strong luminescence combined with interesting magnetic properties in multifunctional materials.[327-329] Sieklucka and coworkers reported a detailed study of the ligand-field splitting parameters and the exchange interaction between lanthanide centers and 5d transition metal in a family of cyanide-bridged W^{5+}-CN-Ce^{3+} compounds.[321] The study indicated a ferromagnetic cyanide-mediated {W-CN-Ce} interaction of magnitude $J_{CeW} \approx 2$ cm^{-1}.

In view of the vast expansion of lanthanide molecular magnetism and, in particular, the subset of cyanide bridged d/f complexes, research in this area was pursued in my dissertation studies and I discovered an unprecedented family of cyanide-bridged trigonal bipyramidal (TBP) 5d-4f aggregates of general formula $(Et_4N)_2[(triphosRe(CN)_3)_2(Ln(NO_3)_3)_3]\cdot 4CH_3CN$ (**19**-**27**) where Ln^{III} = La, Ce, Pr, Nd, Sm, Gd, Tb, Dy and Ho respectively. Compounds **25** and **26** exhibit a frequency dependence in the ac susceptibility data at zero field below 3 K, a typical behavior of SMMs.

Experimental

Syntheses

Starting Materials. All chemicals and solvents were of reagent grade quality. The synthesis of the precursor $(Et_4N)[triphosRe(CN)_3]$ was performed according to the

reported procedure. [105] All reactions were carried out under nitrogen using standard Schlenk-line techniques.

Physical Measurements. Elemental analyses were performed by Atlantic Microlab Inc. (Norcross, GA). Infrared spectra were recorded as Nujol mulls in the range 220-4000 cm^{-1} on a Nicolet IR/42 spectrophotometer.

General Procedure: Single crystals were obtained by mixing solutions of $Ln(NO_3)_3 \cdot 6H_2O$ {where Ln = La, Ce, Pr, Nd, Sm, Gd, Tb, Dy or Ho} (0.075 mmol) in 2 mL of CH_3CN with solutions of (Et_4N)[triphosRe$(CN)_3$] (50mg, 0.049 mmol) in acetonitrile (3 mL). After standing overnight, the solutions produced orange-brown crystals of the products $(Et_4N)_2$[(triphosRe$(CN)_3)_2(Ln(NO_3)_3)_3]\cdot 4CH_3CN$ {where Ln = La, Ce, Pr, Nd, Sm, Gd, Tb, Dy or Ho } which were harvested and washed with Et_2O.

$(Et_4N)_2$[(triphosRe$(CN)_3)_2(La(NO_3)_3)_3]\cdot 4CH_3CN$ (19·4CH_3CN). (Yield = 62 mg, 83%). Elemental analysis: Calcd. for $Re_2La_3C_{104}H_{118}N_{17}O_{27}P_6$: C, 41.46; H, 3.95; N, 7.90; Found: C, 41.24; H, 4.06; N, 8.06%. IR (Nujol): ν(C≡N) 2072(m), 2090(m) cm^{-1}.

$(Et_4N)_2$[(triphosRe$(CN)_3)_2(Ce(NO_3)_3)_3]\cdot 4CH_3CN$ (20·4CH_3CN). (Yield = 66 mg, 89%). M. Elemental analysis: Calcd. for $Re_2Ce_3C_{104}H_{118}N_{17}O_{27}P_6$: C, 41.41; H, 3.94; N, 7.89; Found: C, 41.14; H, 4.03; N, 7.86%. IR (Nujol): ν(C≡N) 2073(m), 2091(m) cm^{-1}.

$(Et_4N)_2$[(triphosRe$(CN)_3)_2(Pr(NO_3)_3)_3]\cdot 4CH_3CN$ (21·4CH_3CN). (Yield = 68 mg, 92%). Elemental analysis: Calcd. for $Re_2Pr_3C_{104}H_{118}N_{17}O_{27}P_6$: C, 41.37; H, 3.94; N, 7.88; Found: C, 41.18; H, 3.94; N, 8.08%. IR (Nujol): ν(C≡N) 2073(m), 2092(m) cm^{-1}.

$(Et_4N)_2[(triphosRe(CN)_3)_2(Nd(NO_3)_3)_3]\cdot 4CH_3CN$ ($22\cdot 4CH_3CN$). (Yield = 64 mg, 92%). Elemental analysis: Calcd. for $Re_2Nd_3C_{104}H_{118}N_{17}O_{27}P_6$: C, 41.24; H, 3.93; N, 7.86; Found: C, 41.08; H, 3.96; N, 8.08%. IR (Nujol): ν(C≡N) 2077(m), 2095(m) cm^{-1}.

$(Et_4N)_2[(triphosRe(CN)_3)_2(Sm(NO_3)_3)_3]\cdot 4CH_3CN$ ($23\cdot 4CH_3CN$). (Yield = 65 mg, 87%). Elemental analysis: Calcd. for $Re_2Sm_3C_{104}H_{118}N_{17}O_{27}P_6$: C, 40.99; H, 3.90; N, 7.81; Found: C, 40.81; H, 3.89; N, 7.91%. IR (Nujol): ν(C≡N) 2078(m), 2096(m) cm^{-1}.

$(Et_4N)_2[(triphosRe(CN)_3)_2(Gd(NO_3)_3)_3]\cdot 4CH_3CN$ ($24\cdot 4CH_3CN$). (Yield = 58 mg, 77%). Elemental analysis: Calcd. for $Re_2Gd_3C_{104}H_{118}N_{17}O_{27}P_6$: C, 40.71; H, 3.88; N, 7.76; Found: C, 40.08; H, 3.93; N, 7.78%. IR (Nujol): ν(C≡N) 2086(m), 2101(m) cm^{-1}.

$(Et_4N)_2[(triphosRe(CN)_3)_2(Tb(NO_3)_3)_3]\cdot 4CH_3CN$ ($25\cdot 4CH_3CN$). (Yield = 62 mg, 82%). Elemental analysis: Calcd. for $Re_2Tb_3C_{104}H_{118}N_{17}O_{27}P_6$: C, 40.65; H, 3.87; N, 7.75; Found: C, 40.38; H, 3.86; N, 7.78%. IR (Nujol): ν(C≡N) 2086(m), 2102(m) cm^{-1}.

$(Et_4N)_2[(triphosRe(CN)_3)_2(Dy(NO_3)_3)_3]\cdot 4CH_3CN$ ($26\cdot 4CH_3CN$). (Yield = 64 mg, 84%). Elemental analysis: Calcd. for $Re_2Dy_3C_{104}H_{118}N_{17}O_{27}P_6$: C, 40.50; H, 3.86; N, 7.72; Found: C, 40.08; H, 3.86; N, 7.88%. IR (Nujol): ν(C≡N) 2086(m), 2103(m) cm^{-1}.

$(Et_4N)_2[(triphosRe(CN)_3)_2(Ho(NO_3)_3)_3]\cdot 4CH_3CN$ ($27\cdot 4CH_3CN$). (Yield = 61 mg, 82%). Elemental analysis: Calcd. for $Re_2Ho_3C_{104}H_{118}N_{17}O_{27}P_6$: C, 40.41; H, 3.85; N, 7.70; Found: C, 40.08; H, 3.76; N, 7.78%. IR (Nujol): ν(C≡N) 2087(m), 2105(m) cm^{-1}.

Single Crystal X-Ray Diffraction

X-ray single crystallographic data were collected on a Bruker-APEX CCD diffractometer at 110 K. The data sets were collected with Mo-Kα radiation (k = 0.71073 Å) as four ω-scans at a 0.3 – 0.4° step width. Data integration and processing, Lorentz-polarization and absorption corrections were performed using the Bruker SAINT[220] and SADABS[221] software packages. Solution and refinement of the crystal structures was carried out using the SHELX[222] suite of programs within the graphical interface X-SEED.[223] The structures were solved by direct methods and refined by alternating cycles of full-matrix least-squares methods on F^2, using SHELXTL which resolved all non-hydrogen atoms which were refined anisotropically at the final refinement cycle. The hydrogen atoms were located from difference Fourier maps, assigned with isotropic displacement factors, and included in the final refinement cycles by use of either geometrical constraints (HFIX for hydrogen atoms with parent carbon atoms) or restraints (DFIX for hydrogen atoms with parent nitrogen or oxygen atoms). A summary of the crystallographic data and unit cell parameters, conditions related to data collection and structural refinement statistics is provided in Table 4.1 and Table 4.2. Selected metal–ligand bond distances and angles are given in Table 4.3 for compound **19**, Table 4.4 for compounds **21-22,** Table 4.5 for compounds **23-24** and in Table 4.6 for compounds **25-26**.

Table 4.1 Crystal structural data and refinement parameters for compounds **19-23**

Compound	**(19)**	**(21)**	**(22)**	**(23)**
Space group	*C2/c*	*C2/c*	*C2/c*	*C2/c*
Unit cell	a = 36.170(7) Å b = 13.788(3) Å c = 26.153(5) Å β = 103.07(3)°	*a* = 36.377(7) Å *b* = 13.749(3) Å *c* = 26.090(5) Å β = 104.29(3)°	*a* = 36.469(7) Å *b* = 13.776(3) Å *c* = 26.224(5) Å β = 104.15(3)°	*a* = 36.481(7) Å *b* = 13.726(3) Å *c* =26.184(5) Å β = 103.53(3)°
Unit cell volume, *V*	12704.9 Å^3	12645.1 Å^3	12775(4) Å^3	12692 Å^3
Z	4	4	4	4
Density, ρ_{calc}	1.6305 g/cm^3	1.6720 g/cm^3	1.660 g/cm^3	1.6806 g/cm^3
Abs. coeff., μ	3.037mm^{-1}	3.196mm^{-1}	3.24 mm^{-1}	3.420 mm^{-1}
Crystal color and habit	Orange Block	Orange Block	Orange Block	Orange Block
Crystal size	0.18 x 0.13 x 0.12 mm	0.11 x 0.1 x 0.06 mm	0.27x0.22x0.15 mm	0.14 x 0.11 x 0.09 mm
Temperature	110 K	110 K	110 K	110 K
Radiation, λ	Mo-Kα, 0.71073 Å	Mo-Kα, 0.71073 Å	Mo-Kα, 0.71073 Å	Mo-Kα, 0.71073 Å
Min. and max. θ	1.16 to 27.46º	1.59 to 26.02º	2.27 to 20.70º	2.19 to 25.51º
Reflections collected	64608 [R_{int} =0.0939]	64447 [R_{int} =0.0503]	70942 [R_{int} = 0.0615]	25826[R_{int} =0.0313]
Independent reflections	14379	12434	15300	11712
Data/parameters/restraints	14379/775/0	12434/779 /0	15300/779/0	11712/779 /0
R [$F_o > 4\sigma(F_o)$]	R_1 = 0.0381 wR_2 = 0.0959	R_1 = 0.0358 wR_2 = 0.0918	R_1 = 0.0516 wR_2 = 0.1072	R_1 = 0.0401 wR_2 = 0.0814
G.o.f. on F^2	1.073	1.175	1.081	1.025
Max./min. residual densities, e·Å^{-3}	0.33, -0.37	1.06, -1.59	2.32, –1.17	1.63, -0.76

$R_1 = \Sigma [(F_o - F_o)] / \Sigma (F_o)$. $wR_2 (F_{o2}) = \{ \Sigma [w(F_{o2} - F_{c2})_2 / \Sigma [w(F_{o2})_2] \}_{1/2}$.

Table 4.2 Crystal structural data and refinement parameters for compounds **24-26.**

Compound	**(24)**	**(25)**	**(26)**
Space group	*C2/c*	*C2/c*	*C2/c*
Unit cell	*a* = 36.324(7) Å *b* = 13.822(3) Å *c* = 26.263(5) Å β = 104.03(3)°	*a* = 36.149(7) Å *b* = 13.737(3) Å *c* = 26.215(5) Å β = 103.85(3)°	*a* = 36.167(7) Å *b* = 13.819(3) Å *c* = 26.339(5) Å β = 104.08(3)°
Unit cell volume, *V*	12792(4) Å^3	12640(4) Å^3	12768(4) Å^3
Z	4	4	4
Density, ρ_{calc}	1.678 g/cm^3	1.701 g/cm^3	1.690 g/cm^3
Abs. coeff., μ	3.572 mm^{-1}	3.719 mm^{-1}	3.775 mm^{-1}
Crystal color and habit	Orange Block	Orange Block	Orange Block
Crystal size	0.18 x 0.10 x 0.08 mm	0.25 x 0.18 x 0.12 mm	0.16 x 0.11 x 0.07 mm
Temperature	110 K	110 K	110 K
Radiation, λ	Mo-Kα, 0.71073 Å	Mo-Kα, 0.71073 Å	Mo-Kα, 0.71073 Å
Min. and max. θ	1.16 to 27.83 º	1.59 to 27.64 º	1.58 to 27.43 º
Reflections collected	70413 [R_{int} =0.0802]	70362 [R_{int} =0.0311]	68472 [R_{int} =0.0492]
Independent reflections	14685	14560	14093
Data/parameters/restraints	14685/779/0	14560/779/0	14093/779 /0
R [$F_o > 4\sigma(F_o)$]	R_1 = 0.0942 wR_2 = 0.1261	R_1 = 0.0733 wR_2 = 0.1692	R_1 = 0.0875 wR_2 = 0.1519
G.o.f. on F^2	1.012	1.082	1.066
Max./min. residual densities, e·Å^{-3}	1.34, -1.8	*1.63*, -0.78	1.23, -0.92

$R_1 = \Sigma [(F_o - F_o)] / \Sigma (F_o)$. $_wR_2 (F_{o2}) = \{ \Sigma [w(F_{o2} - F_{c2})_2 / \Sigma [w(F_{o2})_2]\}_{1/2}$.

Table 4.3 Selected bond distances (Å) and bond angles (°) for **19.**

Compound **19**	Distance (Å)		Angle (°)
La(1)–N(1)	2.567(4)	N(1)- La(1)-O(1)	139.7(1)
La (1) – N(3)	2.580(4)	N(1)- La(1)-O(2)	77.4(1)
La(1) – O(1)	2.732(3)	N(1)- La(1)-O(3)	110.2(1)
La(1) – O(2)	2.739(4)	N(1)- La(1)-O(4)	69.6(1)
La(1) – O(3)	2.8100(7)	N(1)- La(1)-O(5)	80.3(1)
La(1) – O(4)	2.606(5)	N(1)- La(1)-O(6)	143.2(1)
La(1) – O(5)	2.567(3)	N(1)- La(1)-O(7)	133.4(1)
La(1) – O(6)	2.556(3)	N(1)- La(1)-O(8)	73.3(1)
La(1) – O(7)	2.575(4)	N(1)- La(1)-N(3)	71.6(1)
La(1) – O(8)	2.600(4)	La(1)- N(1)-C(1)	159.7(4)
Re(1) – C(1)	2.071(4)	La(2)- N(2)-C(2)	158.7(3)
Re(1) – C(2)	2.059(4)	La(3)- N(3)-C(3)	157.8(3)
Re(1) – C(3)	2.077(4)	La(1)- O(1)-La(2)	166.2(1)
C(1) – N(1)	1.157(5)	Re(1)- C(1)-N(1)	171.1(4)
C(2) – N(2)	1.163(5)	Re(1)- C(2)-N(2)	173.0(4)
C(3) – N(3)	1.154(6)	Re(1)- C(3)-N(3)	170.9(4)
La(1) … La(2)	5.399(1)		
La(2) … La(3)	5.399(1)		
La(1) … La(3)	5.609(1)		

Table 4.4 Selected bond distances (Å) and bond angles (°) for **21-22.**

Compound **21**	Distance (Å)		Angle (°)
Pr(1)–N(1)	2.502(4)	N(1)- Pr(1)-O(1)	81.3(1)
Pr(1) – N(3)	2.497(5)	N(1)- Pr(1)-O(2)	115.6(1)
Pr(1) – O(1)	2.665(4)	N(1)- Pr(1)-O(3)	69.0(2)
Pr(1) – O(2)	2.656(4)	N(1)- Pr(1)-O(4)	77.4(1)
Pr(1) – O(3)	2.7821(7)	N(1)- Pr(1)-O(5)	142.9(1)
Pr(1) – O(4)	2.588(4)	N(1)- Pr(1)-O(6)	126.5(1)
Pr(1) – O(5)	2.514(4)	N(1)- Pr(1)-O(7)	71.9(2)
Pr(1) – O(6)	2.513(4)	N(1)- Pr(1)-O(8)	71.9(2)
Pr(1) – O(7)	2.530(5)	N(1)- Pr(1)-N(3)	140.7(2)
Pr(1) – O(8)	2.560(5)	Pr(1)- N(1)-C(1)	165.7(2)
Re(1) – C(1)	2.078(5)	Pr(2)- N(2)-C(2)	155.7(5)
C(1) – N(1)	1.147(7)	Pr(3)- N(3)-C(3)	160.9(4)
Pr(1) … Pr(2)	5.260(1)	Pr(1)- O(1)-Pr(2)	157.3(4)
Pr(1) … Pr(3)	5.561(1)	Re(1)- C(1)-N(1)	170.9(5)
Compound **22**	Distance (Å)		Angle (°)
Nd(1)–N(1)	2.497(4)	N(1)- Nd(1)-O(1)	77.6(1)
Nd(1) – N(3)	2.501(4)	N(1)- Nd(1)-O(2)	72.2(1)
Nd(1) – O(1)	2.640(3)	N(1)- Nd(1)-O(3)	72.1(1)
Nd(1) – O(2)	2.642(4)	N(1)- Nd(1)-O(4)	81.5(1)
Nd(1) – O(3)	2.7832(6)	N(1)- Nd(1)-O(5)	139.7(2)
Nd(1) – O(4)	2.580(4)	N(1)- Nd(1)-O(6)	142.8(2)
Nd(1) – O(5)	2.589(6)	N(1)- Nd(1)-O(7)	76.4(1)
Nd(1) – O(6)	2.546(6)	N(1)- Nd(1)-O(8)	75.2(1)
Nd(1) – O(7)	2.511(4)	N(1)- Nd(1)-N(3)	141.1(1)
Nd(1) – O(8)	2.503(4)	Nd(1)- N(1)-C(1)	157.1(4)
Re(1) – C(1)	2.071(5)	Nd(2)- N(2)-C(2)	161.1(4)
C(1) – N(1)	1.155(7)	Nd(3)- N(3)-C(3)	154.8(4)
Nd(1) … Nd(2)	5.2382(9)	Nd(1)- O(1)-Nd(2)	166.6(1)
Nd(1) … Nd(3)	5.564(1)	Re(1)- C(1)-N(1)	170.6(4)

Table 4.5 Selected bond distances (Å) and bond angles (°) for **23-24.**

Compound **23**	Distance (Å)		Angle (°)
Sm(1)–N(1)	2.459(4)	N(1)- Sm(1)-O(1)	77.4(1)
Sm(1) – N(3)	2.453(4)	N(1)- Sm(1)-O(2)	72.6(1)
Sm(1) – O(1)	2.628(3)	N(1)- Sm(1)-O(3)	77.2(1)
Sm(1) – O(2)	2.611(3)	N(1)- Sm(1)-O(4)	75.2(1)
Sm(1) – O(3)	2.472(3)	N(1)- Sm(1)-O(5)	81.0(1)
Sm(1) – O(4)	2.466(4)	N(1)- Sm(1)-O(6)	71.2(1)
Sm(1) – O(5)	2.539(3)	N(1)- Sm(1)-O(7)	139.9(1)
Sm(1) – O(6)	2.7724(6)	N(1)- Sm(1)-O(8)	143.1(1)
Sm(1) – O(7)	2.563(5)	N(1)- Sm(1)-N(3)	140.3(1)
Sm(1) – O(8)	2.512(5)	Sm(1)- N(1)-C(1)	158.4(4)
Re(1) – C(1)	2.068(5)	Sm(2)- N(2)-C(2)	161.6(4)
C(1) – N(1)	1.159(7)	Sm(3)- N(3)-C(3)	156.7(4)
Sm(1) … Sm(2)	5.1953(9)	Sm(1)- O(1)-Sm(2)	166.9(1)
Sm(1) … Sm(3)	5.544(1)	Re(1)- C(1)-N(1)	170.4(4)
Compound **24**	Distance (Å)		Angle (°)
Gd(1)–N(1)	2.431(6)	N(1)- Gd(1)-O(1)	77.5(2)
Gd(1) – N(3)	2.431(5)	N(1)- Gd(1)-O(2)	72.7(2)
Gd(1) – O(1)	2.624(4)	N(1)- Gd(1)-O(3)	77.1(2)
Gd(1) – O(2)	2.604(5)	N(1)- Gd(1)-O(4)	75.1(2)
Gd(1) – O(3)	2.467(5)	N(1)- Gd(1)-O(5)	81.2(2)
Gd(1) – O(4)	2.456(5)	N(1)- Gd(1)-O(6)	71.5(2)
Gd(1) – O(5)	2.523(5)	N(1)- Gd(1)-O(7)	142.9(2)
Gd(1) – O(6)	2.7639(7)	N(1)- Gd(1)-O(8)	139.6(2)
Gd(1) – O(7)	2.482(8)	N(1)- Gd(1)-N(3)	140.1(2)
Gd(1) – O(8)	2.537(8)	Gd(1)- N(1)-C(1)	159.2(5)
Re(1) – C(1)	2.056(7)	Gd(2)- N(2)-C(2)	161.9(5)
C(1) – N(1)	1.159(9)	Gd(3)- N(3)-C(3)	157.5(5)
Gd(1) … Gd(2)	5.196(1)	Gd(1)- O(1)-Gd(2)	167.5(2)
Gd(1) … Gd(3)	5.527(1)	Re(1)- C(1)-N(1)	169.5(6)

Table 4.6 Selected bond distances (Å) and bond angles (°) for **25-26**.

Compound **25**	Distance (Å)		Angle (°)
Tb(1)–N(1)	2.409(7)	N(1)- Tb(1)-O(1)	72.7(2)
Tb(1) – N(3)	2.401(6)	N(1)- Tb(1)-O(2)	77.3(2)
Tb(1) – O(1)	2.580(7)	N(1)- Tb(1)-O(3)	71.6(2)
Tb(1) – O(2)	2.603(6)	N(1)- Tb(1)-O(4)	81.9(2)
Tb(1) – O(3)	2.7604(7)	N(1)- Tb(1)-O(5)	142.1(3)
Tb(1) – O(4)	2.506(6)	N(1)- Tb(1)-O(6)	139.7(3)
Tb(1) – O(5)	2.470(9)	N(1)- Tb(1)-O(7)	75.1(2)
Tb(1) – O(6)	2.523(8)	N(1)- Tb(1)-O(8)	76.7(2)
Tb(1) – O(7)	2.450(7)	N(1)- Tb(1)-N(3)	140.1(2)
Tb(1) – O(8)	2.457(5)	Tb(1)- N(1)-C(1)	159.5(6)
Re(1) – C(1)	2.059(8)	Tb(2)- N(2)-C(2)	161.2(6)
C(1) – N(1)	1.15(1)	Tb(3)- N(3)-C(3)	159.5(6)
Tb(1) … Tb(2)	5.160(1)	Tb(1)- O(1)-Tb(2)	167.9(2)
Tb(1) … Tb(3)	5.521(1)	Re(1)- C(1)-N(1)	170.5(7)
Compound **26**	Distance (Å)		Angle (°)
Dy(1)–N(1)	2.387(7)	N(1)- Dy(1)-O(1)	77.0(2)
Dy(1) – N(3)	2.379(7)	N(1)- Dy(1)-O(2)	73.1(3)
Dy(1) – O(1)	2.621(6)	N(1)- Dy(1)-O(3)	71.1(2)
Dy(1) – O(2)	2.576(7)	N(1)- Dy(1)-O(4)	81.3(2)
Dy(1) – O(3)	2.7743(7)	N(1)- Dy(1)-O(5)	75.2(2)
Dy(1) – O(4)	2.496(6)	N(1)- Dy(1)-O(6)	77.5(2)
Dy(1) – O(5)	2.447(7)	N(1)- Dy(1)-O(7)	139.7(3)
Dy(1) – O(6)	2.444(5)	N(1)- Dy(1)-O(8)	142.9(3)
Dy(1) – O(7)	2.524(8)	N(1)- Dy(1)-N(3)	139.1(3)
Dy(1) – O(8)	2.471(9)	Dy(1)- N(1)-C(1)	160.5(7)
Re(1) – C(1)	2.074(8)	Dy(2)- N(2)-C(2)	162.5(6)
C(1) – N(1)	1.15(1)	Dy(3)- N(3)-C(3)	159.2(7)
Dy(1) … Dy(2)	5.186(1)	Dy(1)- O(1)-Dy(2)	167.5(2)
Dy(1) … Dy(3)	5.549(1)	Re(1)- C(1)-N(1)	169.7(7)

Results and Discussion

Syntheses and Infrared Spectroscopy

The reaction of (Et_4N)[triphosRe$(CN)_3$] with $Ln(NO_3)_3 \bullet 6H_2O$ in acetonitrile resulted in orange crystals of the target compounds. The compounds are air stable, but loss of interstitial solvent occurs after the crystals are removed from their mother liquor. In addition, if the crystals of compounds **19-27** are left to stand for ~ 1 month in the mother liquor they slowly decompose to yield a green solution and an unidentified white powder.

The IR data for the [triphosRe$(CN)_3]^-$ ion and compounds **19-27** are summarized in Table 4.7. Compounds **19-27** exhibit characteristic bands in the ν(C≡N) stretching region. A comparison of the observed IR data to the ν(C≡N) stretching frequencies for the precursor anions helps in assigning the cyanide bands in the new compounds to either bridging or terminal CN^- ligands. The IR spectrum of **19** confirms the existence of bridging cyanide by the appearance of cyanide stretches at 2072 and 2090 cm^{-1} which are higher than those for the [triphosRe$(CN)_3]^-$ ion (2060 and 2070 cm^{-1}).[336] The presence of nitrate anions is indicated by the absorptions at 1292, 1089, 834 cm^{-1}. Similarly, the IR spectra of **20-27** exhibit characteristic peaks for nitrate anions as well as two cyanide stretching frequencies that are shifted to higher frequencies as compared to the corresponding mode of the [triphosRe$(CN)_3]^-$ ion (Table 4.7), therefore, these modes are reasonable to assign to bridging cyanides.

Table 4.7 Selected infrared spectral data (cm^{-1}) for **19-27.**

Compound	ν(C≡N) cm^{-1}			(NO_3) cm^{-1}		Ref
[triphosRe$(CN)_3$]$^-$	2060	2070	-	-	-	[336]
19	2072	2090	1292	1089	834	This work
20	2073	2091	1291	1090	834	This work
21	2073	2092	1291	1090	834	This work
22	2077	2095	1292	1090	835	This work
23	2078	2096	1292	1090	835	This work
24	2086	2101	1296	1090	836	This work
25	2086	2102	1297	1091	835	This work
26	2086	2103	1298	1091	836	This work
27	2087	2105	1297	1092	836	This work

Single Crystal X-Ray Diffraction Studies

X-ray crystallographic measurements of the compounds revealed an iso-structural family that crystallizes in the C2/c space group (Table 4.1, Table 4.2). The molecular structures (**19** is shown in Figure 4.1, Figure 4.2) consist of a trigonal bipyramidal core of two [triphosRe$(CN)_3]^-$ anions in the axial positions, bridged through cyanide ligands to three lanthanide ions in the equatorial positions. Three nitrate anions further bridge the lanthanide ions in the plane with two additional chelating nitrate anions coordinated above and below the plane (Figure 4.1). Two tetraethyl ammonium cations exist to balance the charge of the dianionic cluster along with four acetonitrile molecules. Selected bond distances and angles are listed in Table 4.3, 4.4 and 4.5. As illustrated for **19** in Figure 4.1, the local coordination environment around each ten-coordinate lanthanide ion is nearly identical to form a distorted hexadecahedral polyhedron with a N_2O_8 coordination sphere; O_4 donor atoms of the bridging nitrate and O_4 donor atoms of the chelating nitrate with bond lengths which are in the range of bond lengths for previously reported lanthanide complexes.[337-339] The two apical sites are occupied by nitrogen atoms from cyanide groups with a La(1)-N(1) bond of 2.600(4) Å. The La(1)–N(1)–C(1) angle is significantly bent, 159.7(4)° whereas the angle Re(1)-C(1)-N(1) is 171.1(4) °. The bridging oxygen bond angle La(1)–O(1)–La(2) is 166.2(1) ° and the Ln1...Ln2 shortest contact is 5.160 Å. A packing diagram projected in the *ac*-plane is provided in Figure 4.2, which shows the arrangement of the TBPs in 3D. The shortest intermolecular Ln --- Ln distance is 11.098 Å.

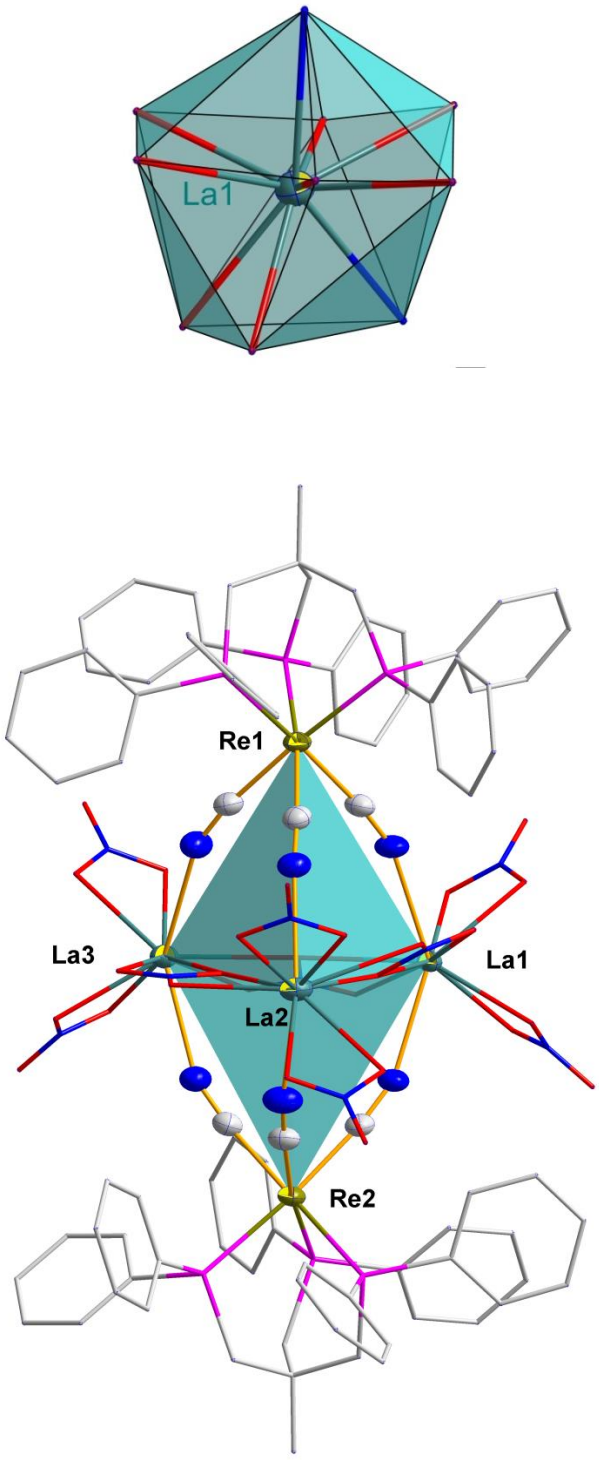

Figure 4.1 (a) Distorted hexadecahedral polyhedron of La^{3+} center. (b) plot of $[(triphosRe(CN)_3)_2(La(NO_3)_3)_3]^{2-}$ dianion in (**19**). Ellipsoids are projected at the 50% probability level and hydrogen atoms were omitted for the sake of clarity.

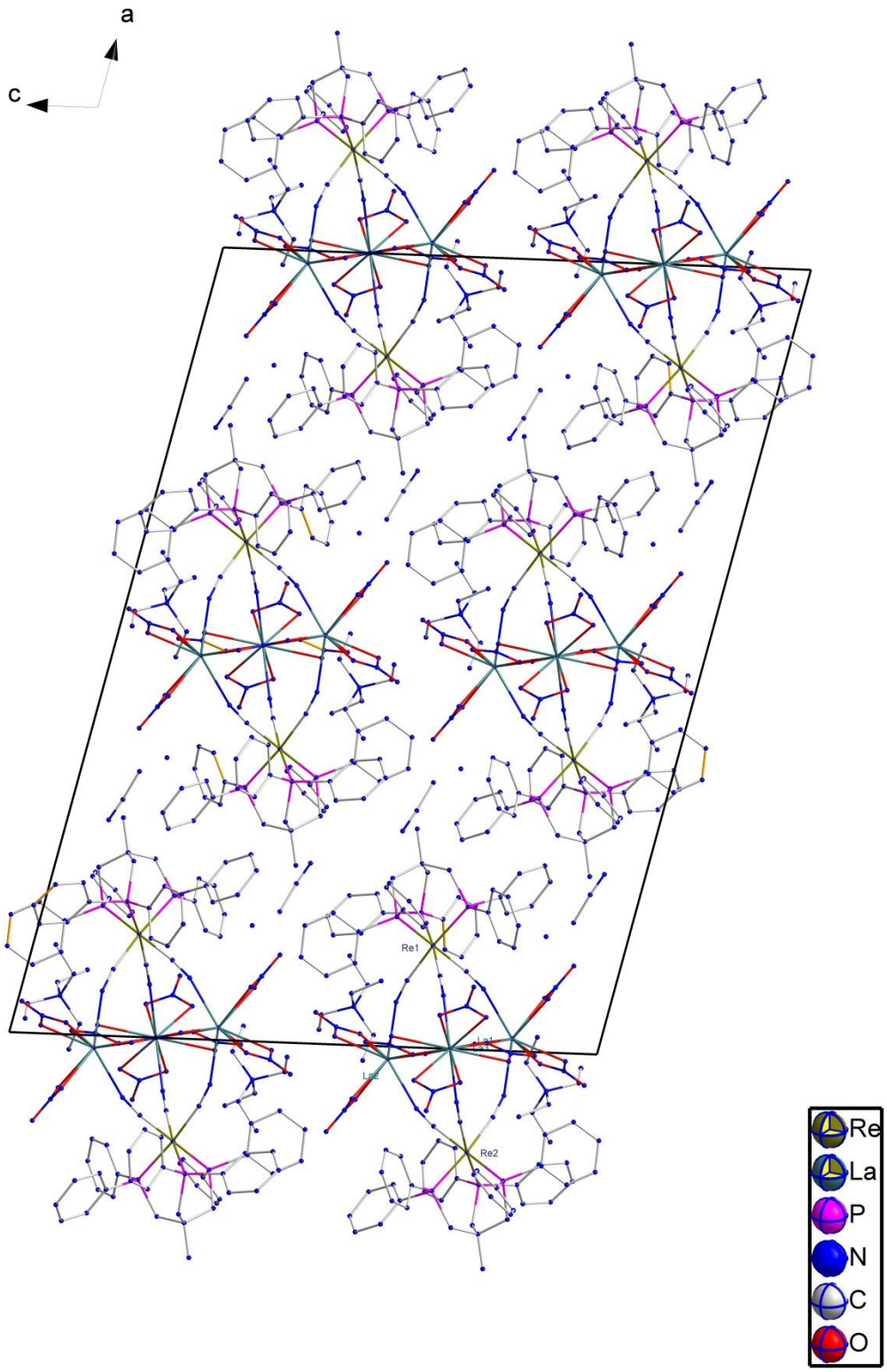

Figure 4.2 Molecular representation of the crystal packing of **19** in the *ac*-plane.

Magnetic Properties

Magnetic susceptibility measurements in the DC mode were performed on crushed single crystals of the title compounds with the use of a Quantum Design MPMS-XL SQUID magnetometer operating in the temperature range of 1.8-300 K at 1000 G. AC magnetic susceptibility measurements were performed on the same sample with an oscillating field of 5 Oe. Simulation of the magnetic susceptibility curves were carried out using PHI[340] for **19** or MAGPACK[341] for **24**.

$(Et_4N)_2[(triphosRe(CN)_3)_2(La(NO_3)_3)_3]\cdot 4CH_3CN$ (19·4CH$_3$CN). Temperature-dependent magnetic susceptibility data for **19** were fitted using PHI.[340] It's dominated by the signature of large temperature independent paramagnetism (TIP) of Re(II) (figure 4.3a). The room temperature χT value of 1.42 emu.K.mol^{-1} for **19** is in a good agreement with 2 isolated Re(II) ions with one unpaired electron each (C = 0.65) and (χTIP = 2.49x10^{-3} emu.K.mol^{-1}). The χT value gradually decreases as the temperature is lowered as result of the large TIP reaching a minimum of 0.63 emu.K.mol^{-1} at 2K. Similar behavior was previously noted in case of the Re(II) precursor itself.[336] The magnetization versus field data of **19** (Figure 4.3b inset) is consistent with the presence of two Re(II) ions only following a Brillion function (S=1/2, g=1.78).

$(Et_4N)_2[(triphosRe(CN)_3)_2(Ce(NO_3)_3)_3]\cdot 4CH_3CN$ (20·4CH$_3$CN). The room temperature χT value of 2.82 emu.K.mol^{-1} for **20** is consistent with two Re(II) ions (S=1/2, g = 1.87) and three Ce(III) ions (g = 0.85, J= 5/2) (C= 3) (figure 4.4a). The χT curve displays a smooth monotonic decrease with lowering temperature until 10K, followed by a sharp decrease reaching a minimum of 0.64 emu.K.mol^{-1} at 2K. This

decrease in χT is mostly due to the depopulation of Stark excited sublevels of Ce(III)[321] and possibly antiferromagnetic exchange interaction between the metal ions. The magnetization versus field data of **20** (Figure 4.4b, inset) is comparable with the presence of two Re(II) ions and three Ce(III) ions. The lack of saturation even at 7 T is attributed to the anisotropic nature of both Re(II) and Ce(III).[321] The field dependence of the magnetization data at temperatures between 1.8 and 4.5 K reveal a non-superposition of the iso-field lines which indicates strong spin-orbit coupling (Figure 4.4b). No significant features were observed in the AC-susceptibility data measured down to 1.8 K.

$(Et_4N)_2[(triphosRe(CN)_3)_2(Pr(NO_3)_3)_3]\cdot 4CH_3CN$ ($21\cdot 4CH_3CN$). The room temperature χT value of 5.12 emu.K.mol^{-1} for **21** is consistent with two Re(II) ions (S=1/2, g = 1.88) and three Pr(III) ions (g = 0.8, J= 4) (C= 5.47) (figure 4.5a). The χT gradually decreases at lower temperatures reaching a minimum of 0.64 emu.K.mol^{-1} at 2K giving a Weiss constant of -44 K. This decrease in χT mainly is due to the depopulation of Stark excited sublevels of Pr(III) and possibly weak antiferromagnetic exchange interactions between the metal ions.[339] The lack of saturation in the magnetization versus field data of **21** (Figure 4.4b, inset) even at 7 T is due to the anisotropic nature of both Re(II) and Pr(III) ions. The field dependence of the magnetization data at temperatures between 1.8 and 4.5 K show a non-superposition of the iso-field lines indicating the presence of significant spin orbit coupling (Figure 4.5b). No significant features were observed in the AC susceptibility data measured down to 1.8 K.

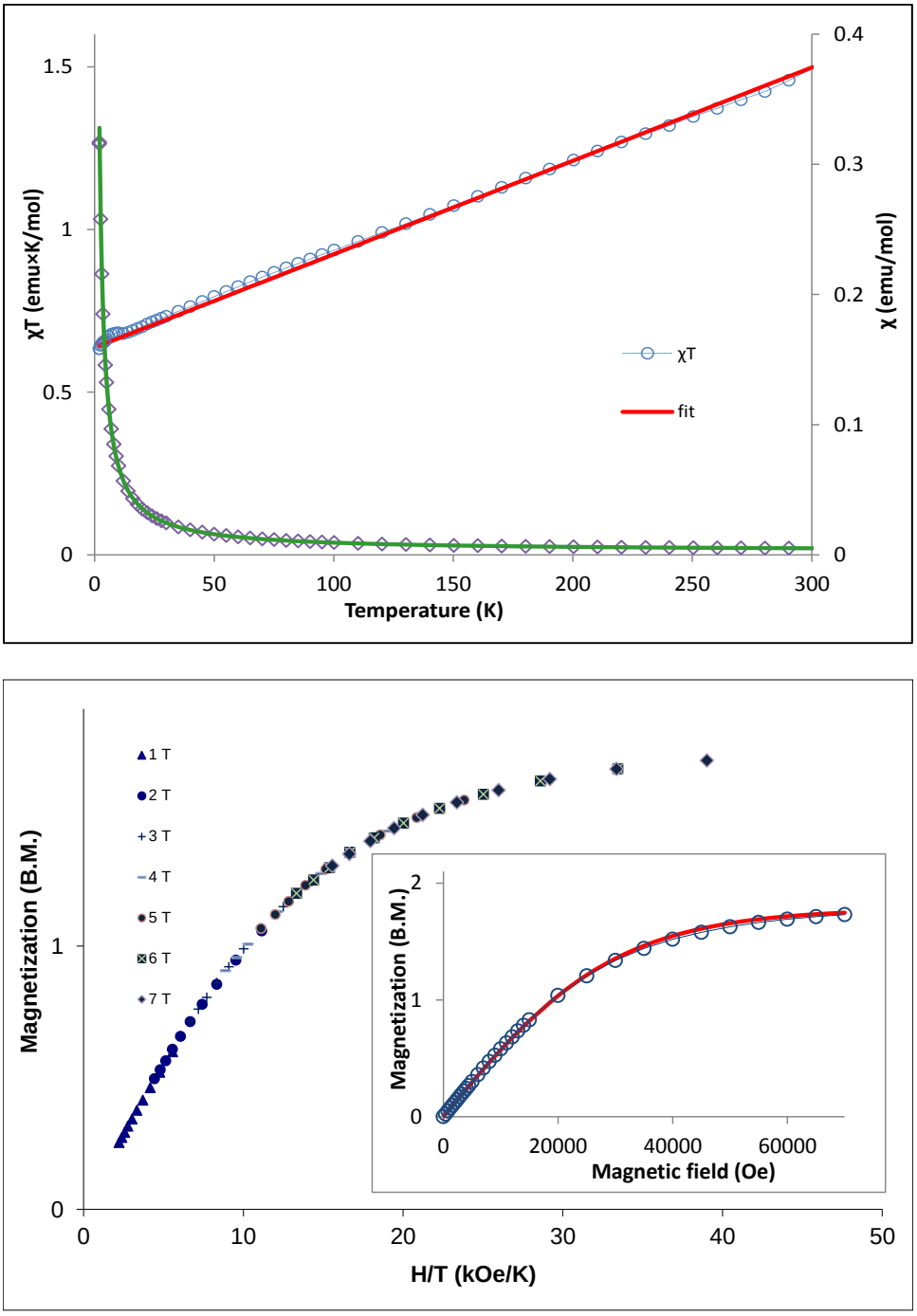

Figure 4.3 (a) Temperature dependence of χ (◊) and χT product (o) for **19**. Solid line corresponds to fit using PHI (S=1/2, g = 1.88 and TIP =2.49 x10^{-3}). (b) Reduced magnetization data at different external fields. Inset: field dependent magnetization **(**o**)**. The solid line corresponds to the Brillion function (S = 1/2, g_{avg} = 1.78).

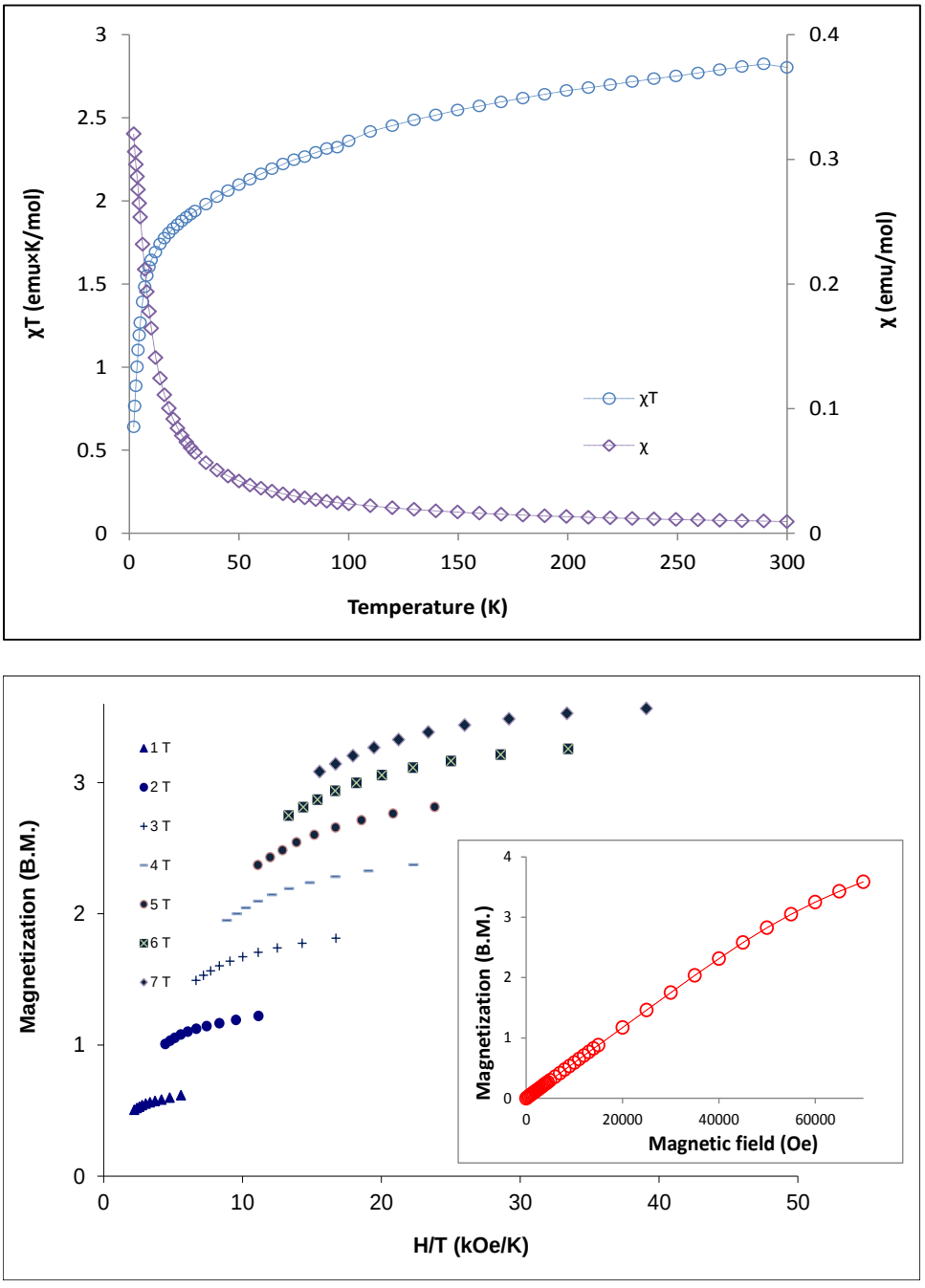

Figure 4.4 (a) Temperature dependence of χ (◊) and χT product (o) for **20**. (b) Reduced magnetization data at different external fields. Inset: field dependent magnetization for **20** (o).

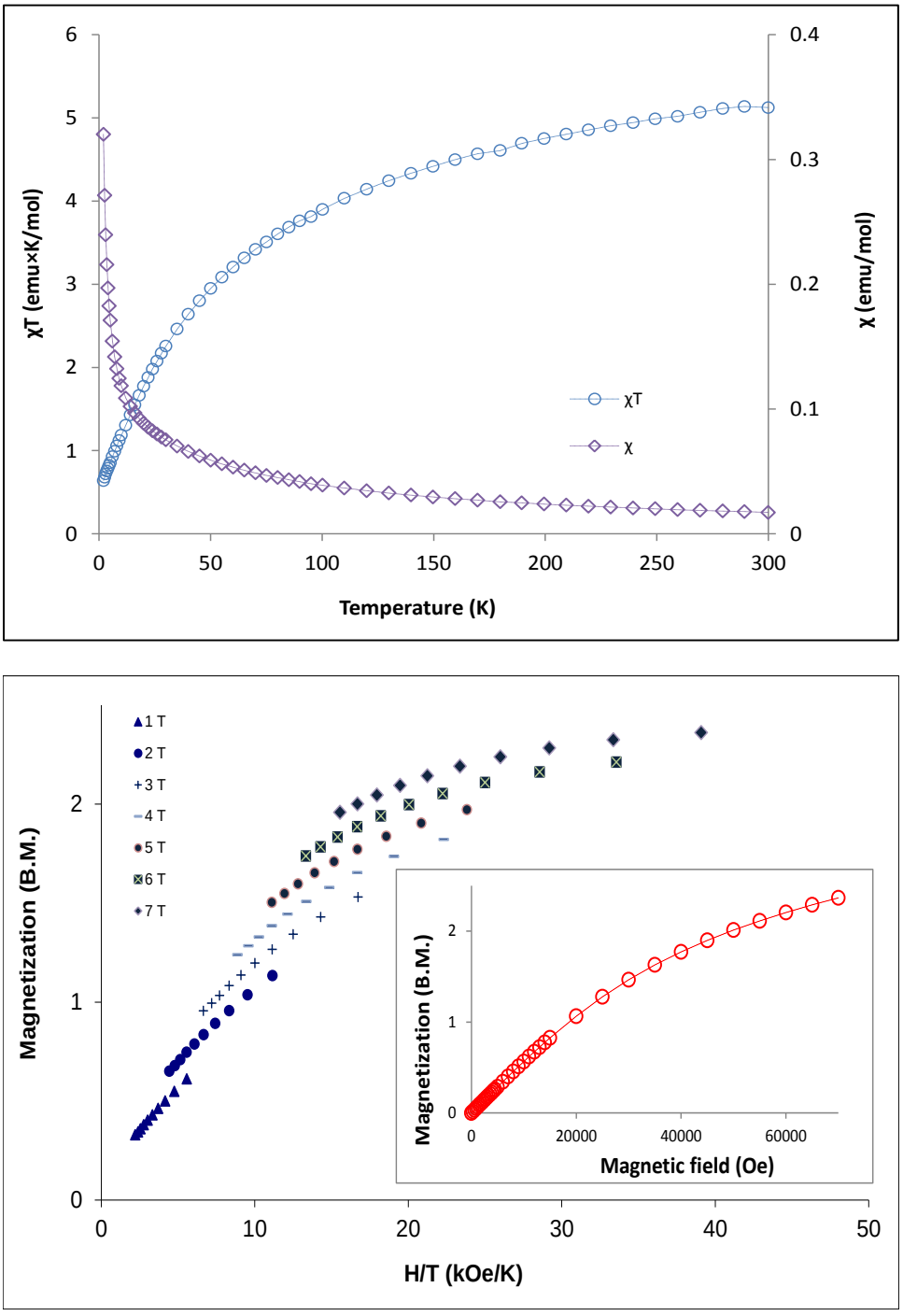

Figure 4.5 (a) Temperature dependence of χ (◊) and χT product (o) for **21**. (b) Reduced magnetization data at different external fields. Inset: field dependent magnetization for **21**(o).

$(Et_4N)_2[(triphosRe(CN)_3)_2(Nd(NO_3)_3)_3]\cdot 4CH_3CN$ ($22\cdot 4CH_3CN$). The room temperature χT value of 5.02 emu.K.mol^{-1} for **22** is consistent with two Re(II) ions (S = 1/2, g = 1.87) and three Nd(III) ions (g = 0.72, J= 4.5) (C= 5.46) (Figure 4.6a). The χT curve shows a monotonic decrease at lower temperatures down to 10 K followed by a sharper decrease reaching a minimum of 1.44 emu.K.mol^{-1} at 2 K giving a Weiss constant of -49 K. This decrease in χT might be an indication of both depopulation of Stark excited sublevels of Nd(III) and possibly antiferromagnetic exchange interaction between the metal ions. The lack of saturation the magnetization versus field data of **22** (Figure 4.6b, inset) even at 7T is considered to be a result of the anisotropic nature of both Re(II) and Nd(III) ions. The field dependence of the magnetization data at temperatures between 1.8 and 4.5 K show a non-superposition of the iso-field lines indicating the presence of significant spin orbit coupling (Figure 4.6b). No significant features were observed in the AC susceptibility data.

$(Et_4N)_2[(triphosRe(CN)_3)_2(Sm(NO_3)_3)_3]\cdot 4CH_3CN$ ($23\cdot 4CH_3CN$). The room temperature χT value of 1.75 emu.K.mol^{-1} for **23** is consistent with two R(II) ions (S=1/2, g = 1.8) and three Sm(III) ions (g = 0.56, J= 1/2) (C= 0.7) (Figure 4.7a). The χT gradually decreases at lower temperature until 7K where a sharper decrease occurs reaching a minimum of 0.41 emu.K.mol^{-1} at 2K giving a Weiss constant of -1.25 K. This decrease in χT might be an indication of antiferromagnetic exchange interaction between the metal ions. The lack of saturation even at 7T is probably due to the anisotropic nature of both Re(II) and Sm(III). No out-of-phase signals were observed in the AC-susceptibility data measured down to 1.8 K.

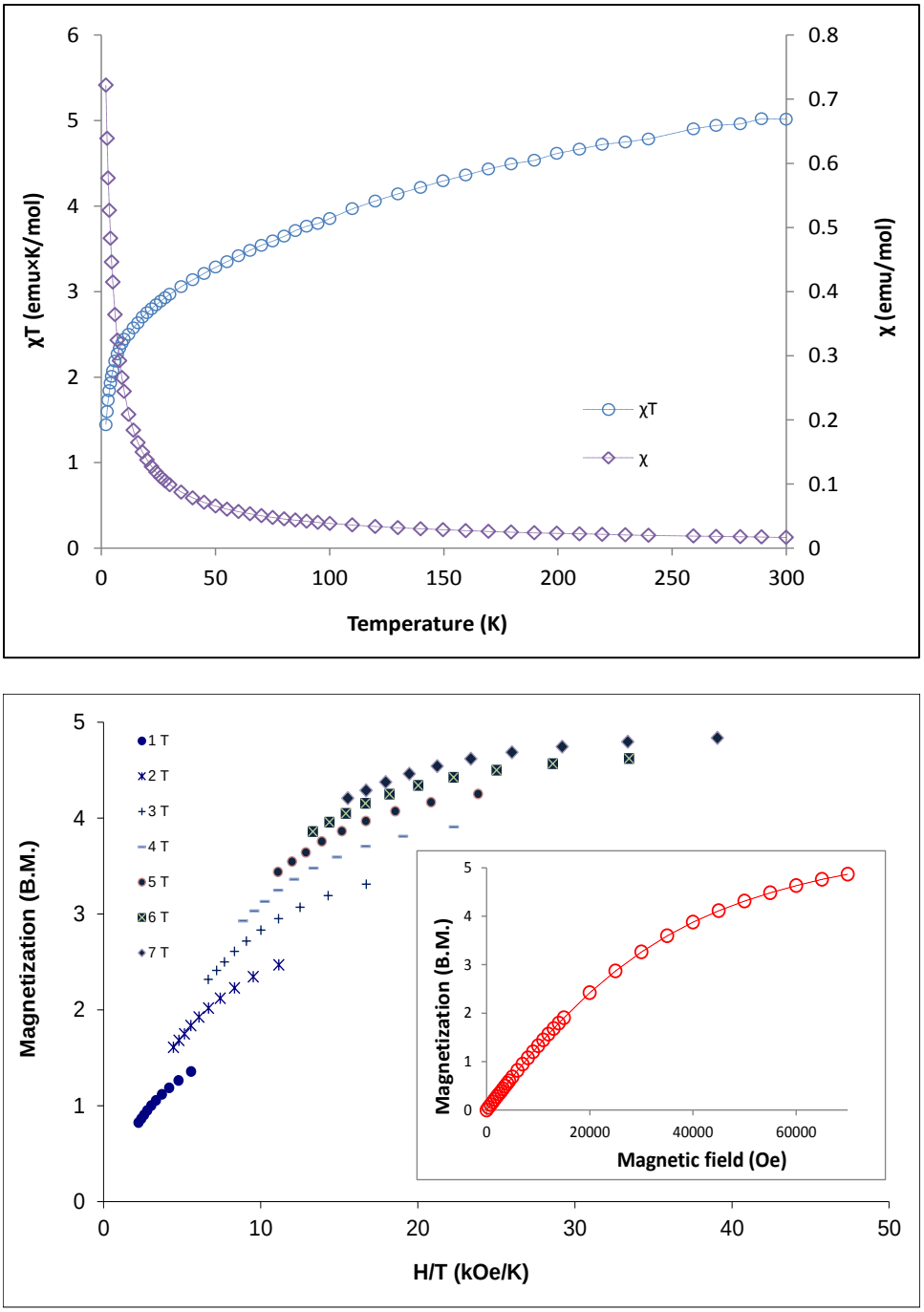

Figure 4.6 (a) Temperature dependence of χ (◊) and χT product (o) for **22**. (b) Reduced magnetization data at different external fields. Inset: field dependent magnetization for **22** (o).

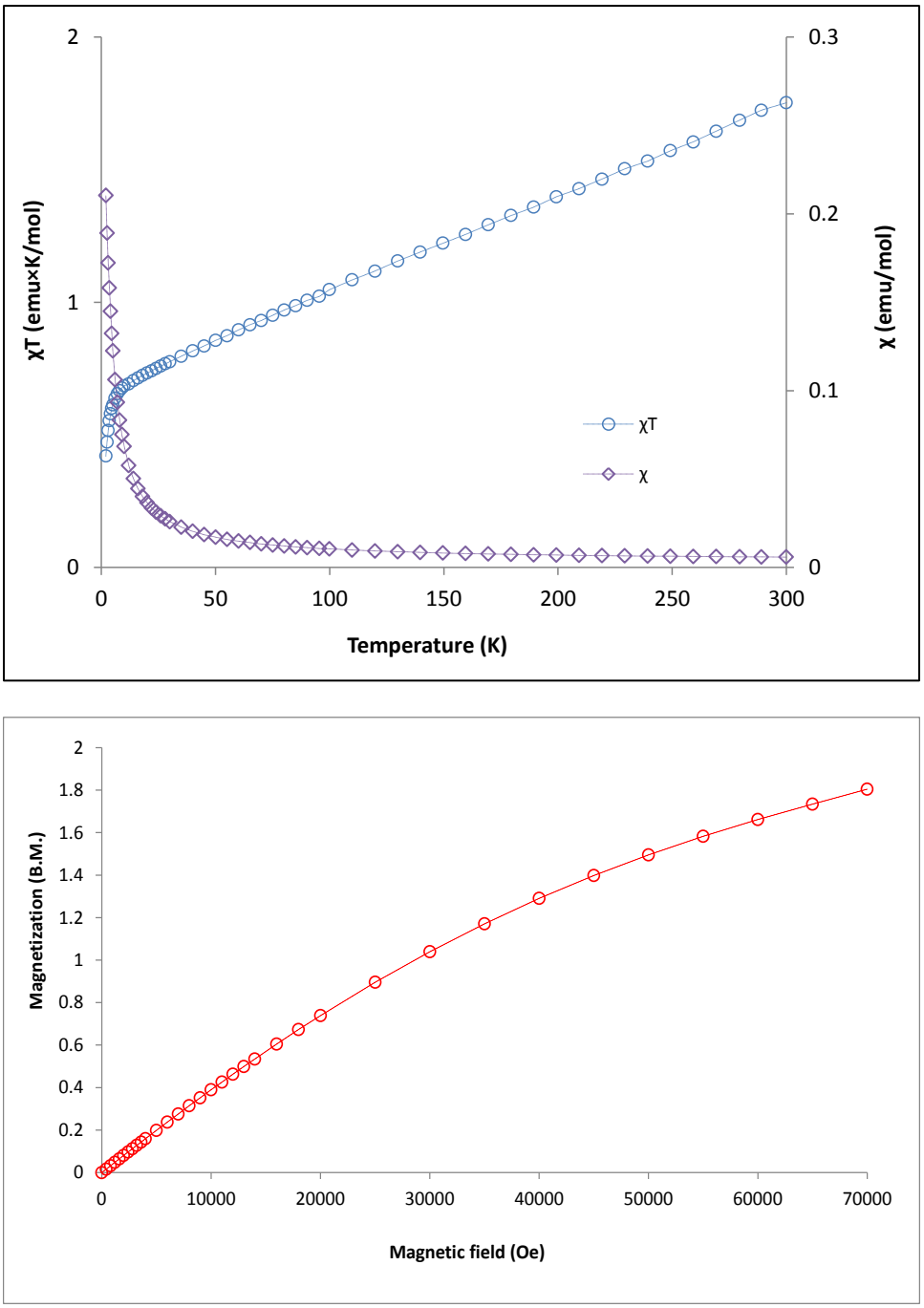

Figure 4.7 (a) Temperature dependence of χ (◊) and χT product (o) for **23**. (b) Reduced magnetization data at different external fields. Inset: field dependent magnetization for **23** (o).

$(Et_4N)_2[(triphosRe(CN)_3)_2(Gd(NO_3)_3)_3]\cdot 4CH_3CN$ ($24\cdot 4CH_3CN$). The room temperature χT value of 24.6 emu.K.mol^{-1} for **24** is consistent with two Re(II) ions (S = 1/2, g = 1.87) and three Gd(III) ions (g = 2, J= 3.5) (C= 24.1) (Figure 4.8a). The χT slowly decreases with lowering temperature reaching a minimum of 20.7 emu.K.mol^{-1} at 4 K then increases to 21.7 at 2 K giving a Weiss constant of -1.6 K which may be an indication of antiferromagnetic exchange interactions between the metal ions. Simulation of the χT data was carried out using MAGPACK resulting in an antiferromagnetic cyano-mediated {Re-CN-Gd} interaction of the magnitude $J_{ReGd} \approx -0.25$ cm^{-1} as compared to a weaker antiferromagnetic nitrato mediated {Re-CN-Gd} interaction of the magnitude $J_{GdGd} \approx -0.02$ cm^{-1}

The magnetization versus field data of **24** (Figure 4.8b, inset) are consistent with the presence of two Re(II) ions and three Gd(III) ions. The lack of saturation even at 7 T (20.3 μ_B) is likely due to the anisotropic nature of Re(II) and the presence of low lying excited states as indicated by the non-superposition of the iso-field lines of the field dependence of the magnetization data at temperatures between 2 and 4.5 K (Figure 4.8b). No significant features were observed in the AC susceptibility measurements.

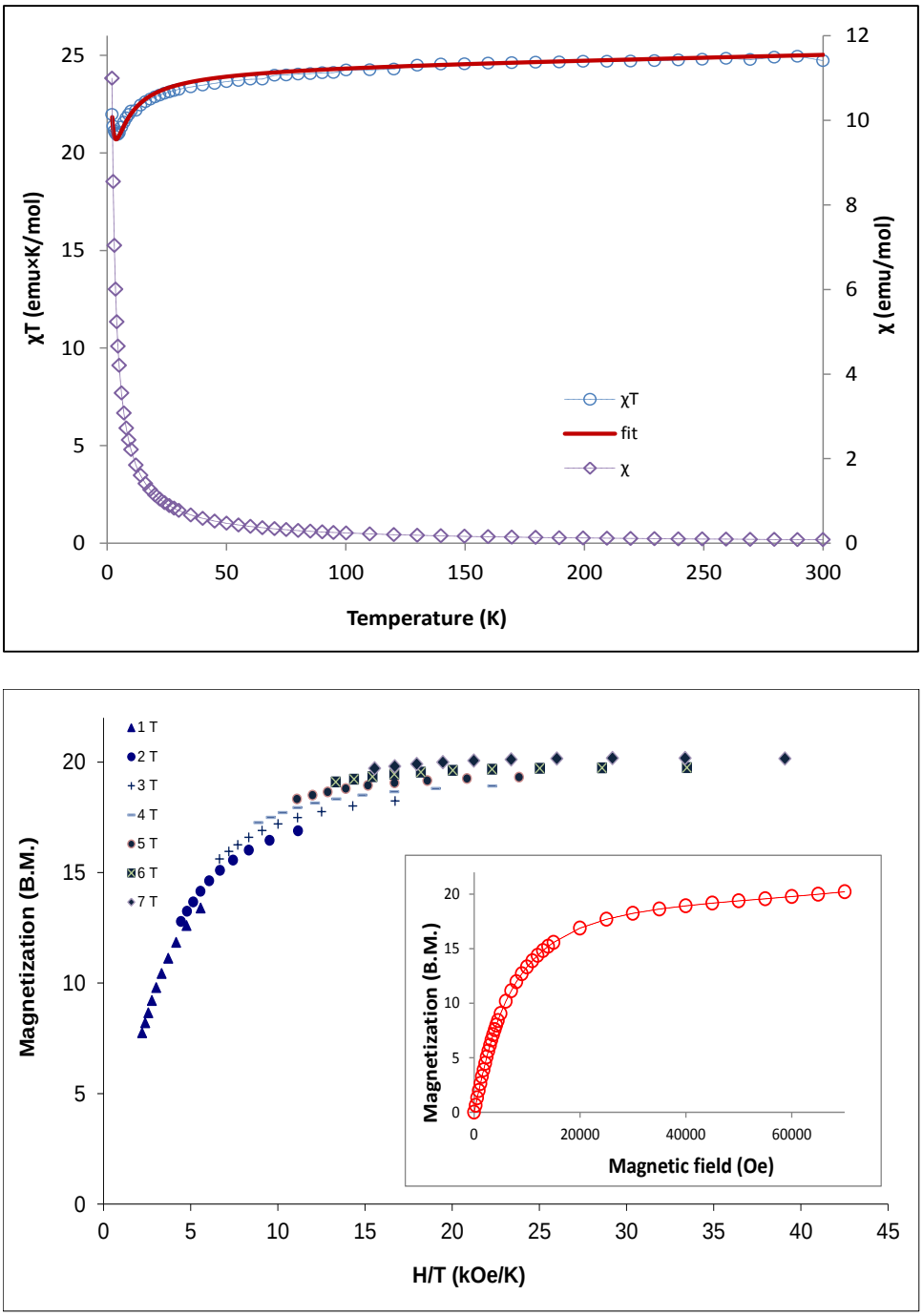

Figure 4.8 (a) Temperature dependence of χ (◊) and χT product (o) for **24**. (b) Reduced magnetization data at different external fields. Inset: field dependent magnetization for **24** (o).

$(Et_4N)_2[(triphosRe(CN)_3)_2(Tb(NO_3)_3)_3]\cdot 4CH_3CN$ ($25\cdot 4CH_3CN$). The room temperature χT value of 34.6 emu.K.mol^{-1} for **25** is in accord with two non-interacting Re(II) (S=1/2, g = 1.88) and three Tb(III) ions (g = 1.45, J= 6) (C= 33.8) (Figure 4.9a). The χT slowly decreases on lowering temperature and then increases back to a maximum of 42 emu.K.mol^{-1} at 2 K giving Θ = -6 K which can be attributed to the depopulation of excited sublevels of Tb(III) and possibly antiferromagnetic interactions. The magnetization versus field data (Figure 4.9b, inset) reveals a fast increase in slope below 0.6 T followed by a slow increase up to 15.4 μ_B at 7 T which is consistent with the value calculated for three uncorrelated Tb(III) ions (3x4.5 μ_B) and two uncorrelated Re(II) magnetic moments (2x1 μ_B). The field dependence of the magnetization data at temperatures between 2 and 4.5 K exhibit a non-superposition of the iso-field lines indicating the presence of significant spin orbit coupling (Figure 4.9b). Given the anisotropic nature of the compounds, the AC susceptibility studies were carried out for **25**. An obvious temperature dependence of χ'' was observed below 4 K (Figure 4.10a) indicating slow relaxation of the magnetization, a characteristic of SMM behavior but with no maxima being observed. The energy barriers and relaxation times were approximated following a method reported by Bartolome et. al.[342] based on the equation:

$$\ln\left(\frac{x''}{x'}\right) = \ln(\omega\tau_\circ) + \frac{E_a}{kBT} \qquad Eq\ 4.1$$

The calculated energy barrier and relaxation time for **25** are 8.49 cm^{-1} and 1.51 x 10^{-8} s resepctively (Figure 4.10b). Appying a 1000 Oe DC field led to an energy barrier of 5.86 cm^{-1} and relaxation time of 3.6x10^{-7} s(Figure 4.11)

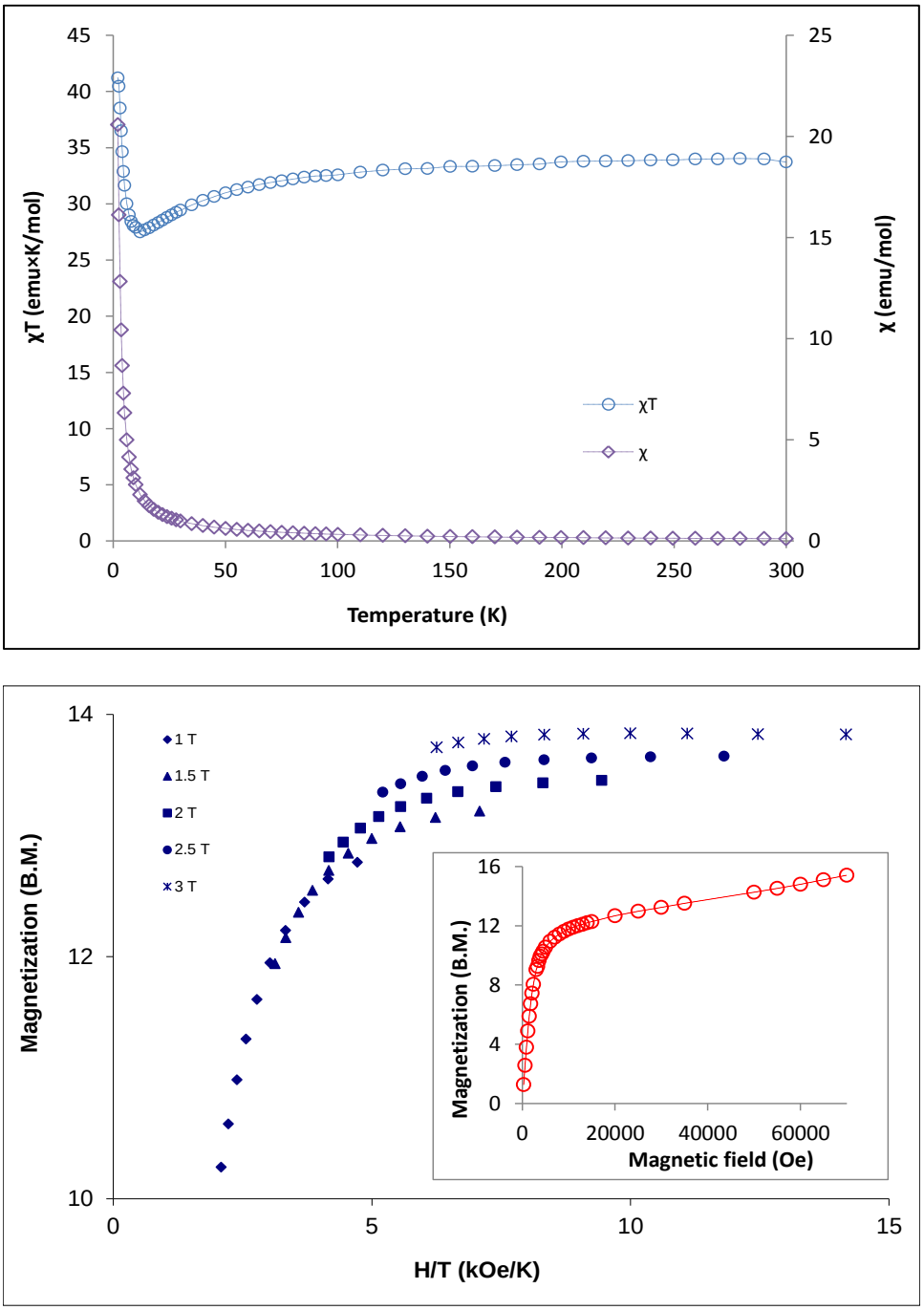

Figure 4.9 (a) Temperature dependence of χ (◊) and χT product (o) for **25**. (b) Reduced magnetization data at different external fields. Inset: field dependent magnetization for **25** (o).

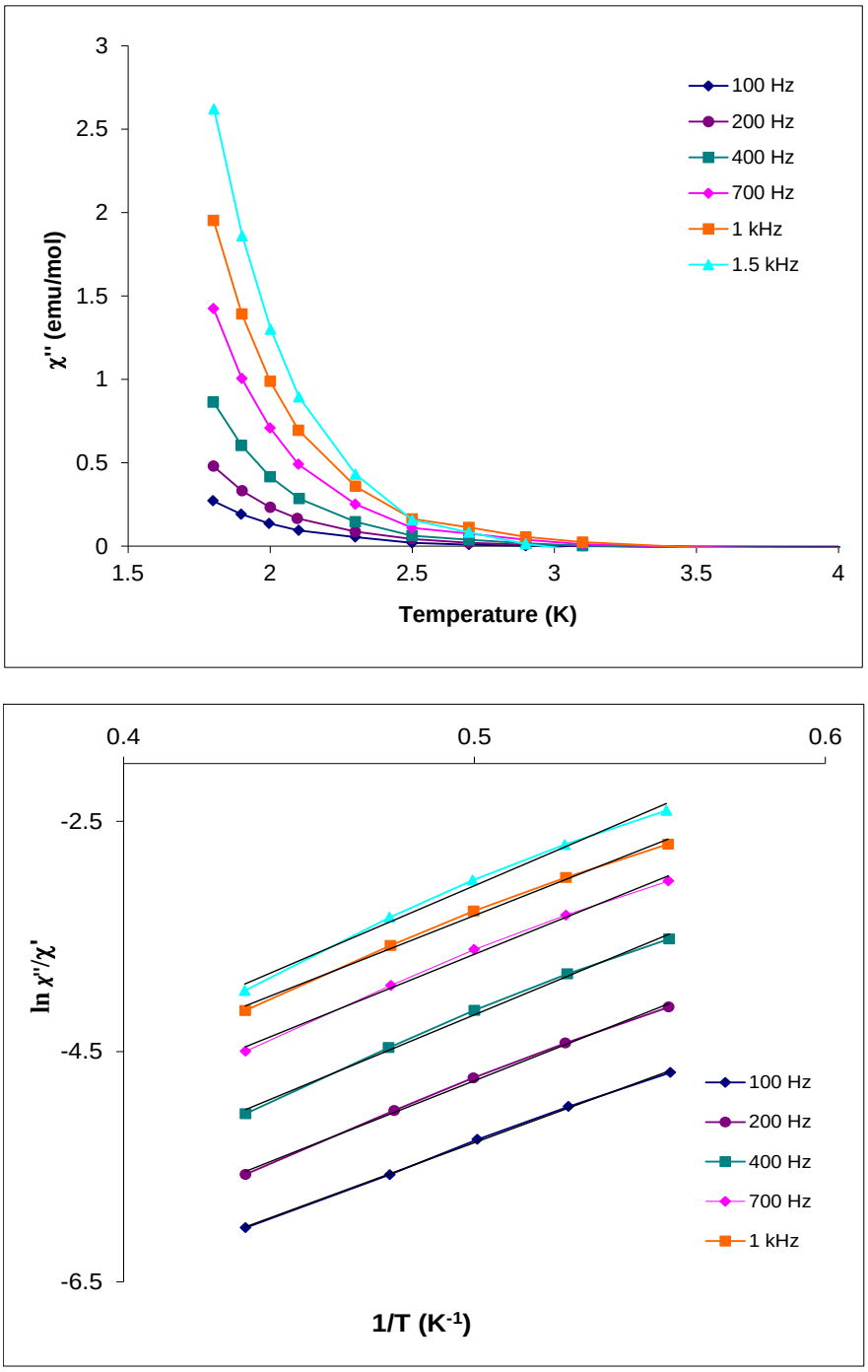

Figure 4.10 Temperature dependence of the out-of-phase AC susceptibility of **25** (top) and fit of the temperature dependence of the AC susceptibility data for **25** (bottom) under a zero applied DC field.

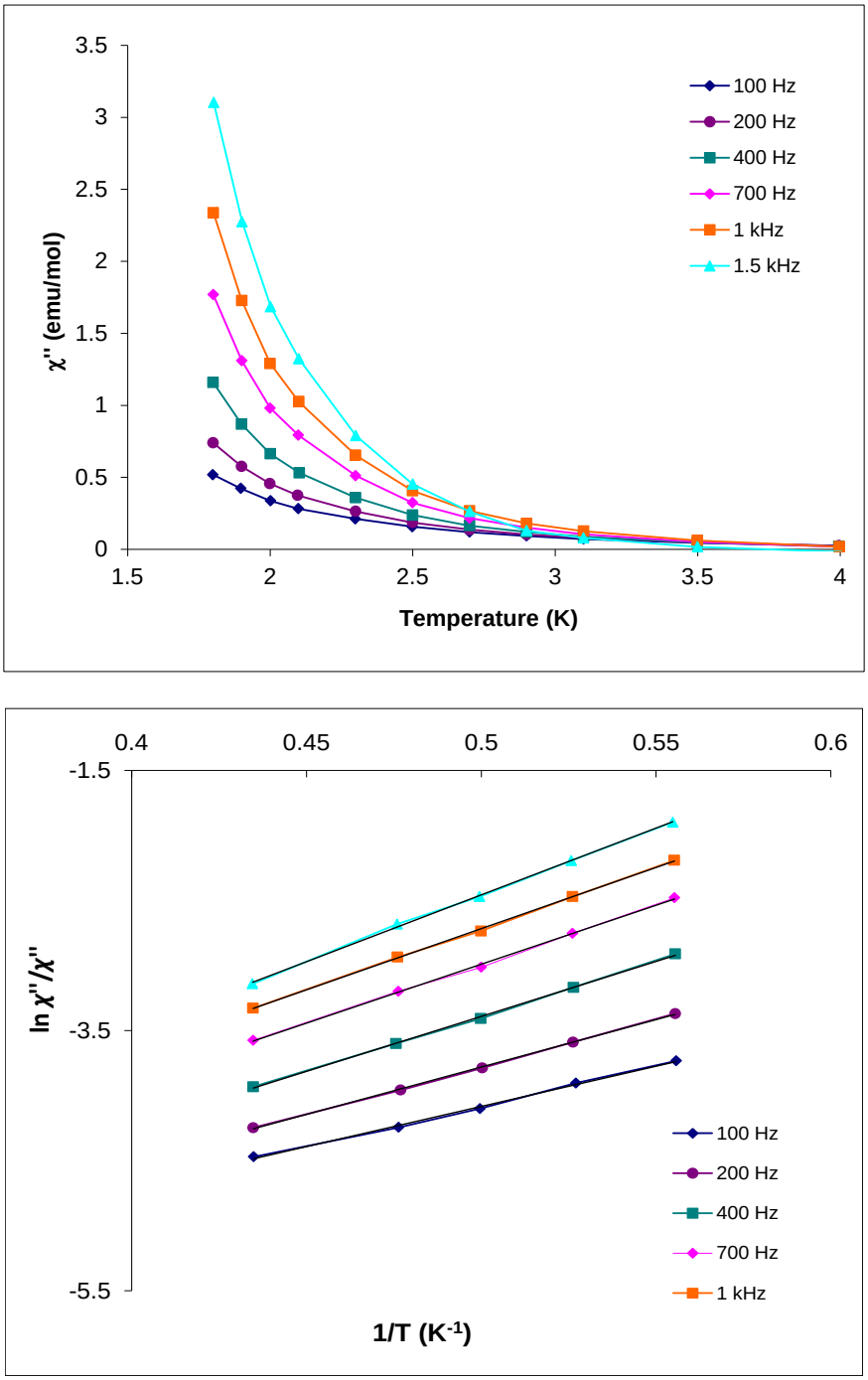

Figure 4.11 Temperature dependence of the out-of-phase AC susceptibility of **25** (top) and fit of the temperature dependence of the AC susceptibility of **25** (bottom) under a 1000 Oe DC applied field.

$(Et_4N)_2[(triphosRe(CN)_3)_2(Dy(NO_3)_3)_3]\cdot 4CH_3CN$ ($26\cdot 4CH_3CN$). The room temperature χT value of 48.5 emu.K.mol^{-1} for **26** matches two non-interacting Re(II) ions (S=1/2, g = 1.9) and three Dy(III) ions (g = 1.41, J= 15/2) (C= 48.2). Similarly, the χT slowly decreases at lower temperatures and then increases to a maximum of 33.9 emu.K.mol-1 at 2 K giving; the Weiss constant is -7 K. This decrease in χT is an indication of both depopulation of Stark excited sublevels of Dy(III) and a possible antiferromagnetic exchange interaction between the metal ions. Similar behavior was observed for **26** (Figure 4.12 inset) with a maximum of 19.8 μ_B at 7T. This value is consistent with that calculated for three uncorrelated Dy(III) magnetic moments (3 x 5.23 μ_B) and two uncorrelated Re(II) magnetic moments (2 x 1μ_B). Given the anisotropic nature of the compounds, the AC susceptibility studies were performed for **26**. An obvious temperature dependence of χ'' was observed below 4K (Figure 4.13) indicating slow paramagnetic relaxation of the magnetization which is indicative of SMM behavior but no maxima were observed. The energy barriers and relaxation times were roughly evaluated following Bartolome method[342] based on the following equation:

$$\ln\left(\frac{x''}{x'}\right) = \ln(\omega\tau_\circ) + \frac{E_a}{kBT} \qquad Eq\ 4.2$$

The calculated energy barrier and relaxation time for **26** were estimated to be 2.9 cm^{-1} and 6x10^{-7} s respectively. The measurements were repeated under a 1000 Oe applied DC field resulting in an increase in the energy barrier to 4.2 cm^{-1} with a relaxation time of 7.36x10^{-7} s (Figure 4.14)

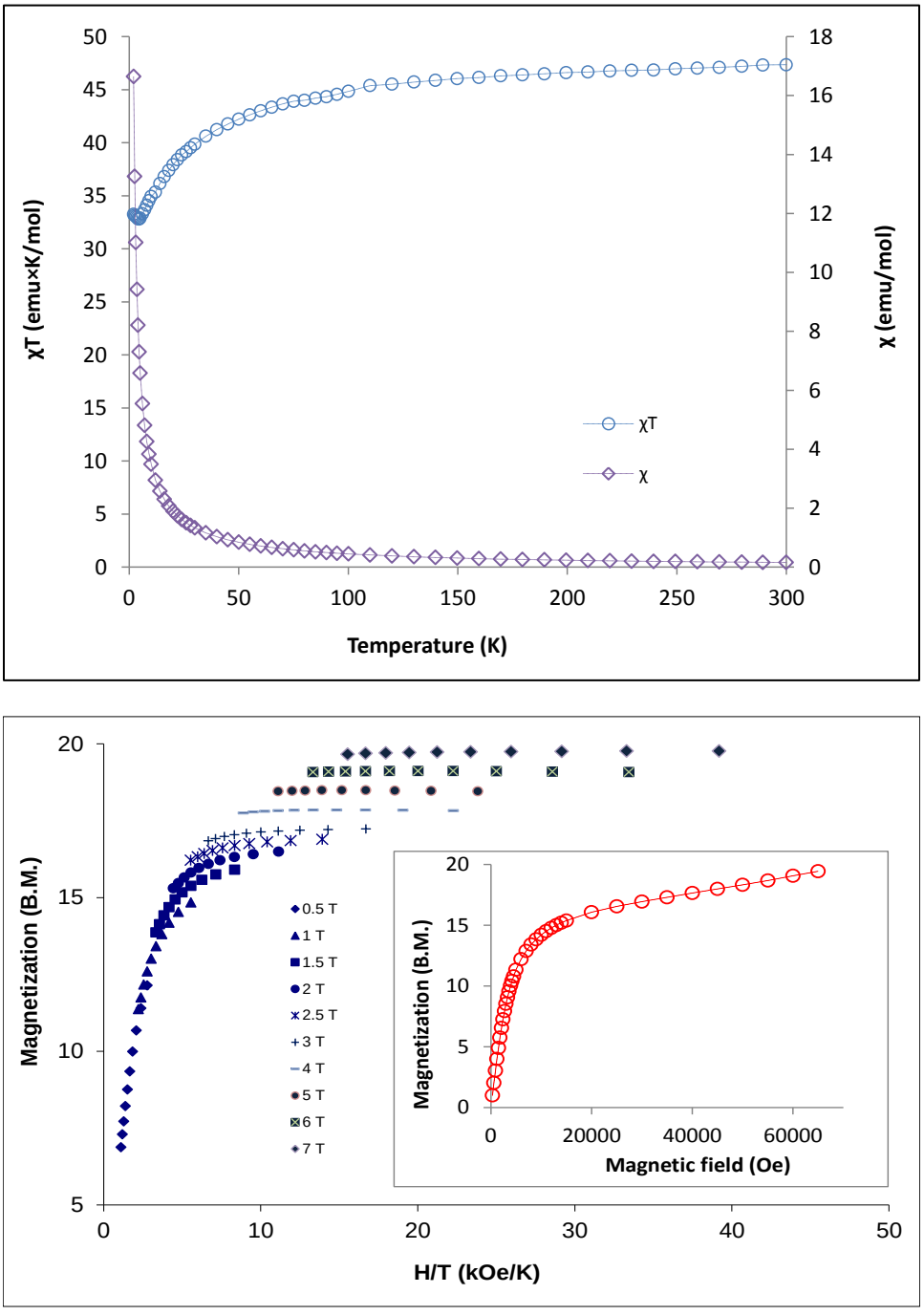

Figure 4.12 (a) Temperature dependence of χ (◊) and χT product (o) for **26**. (b) Reduced magnetization data at different external fields. Inset: field dependent magnetization for **26** (o).

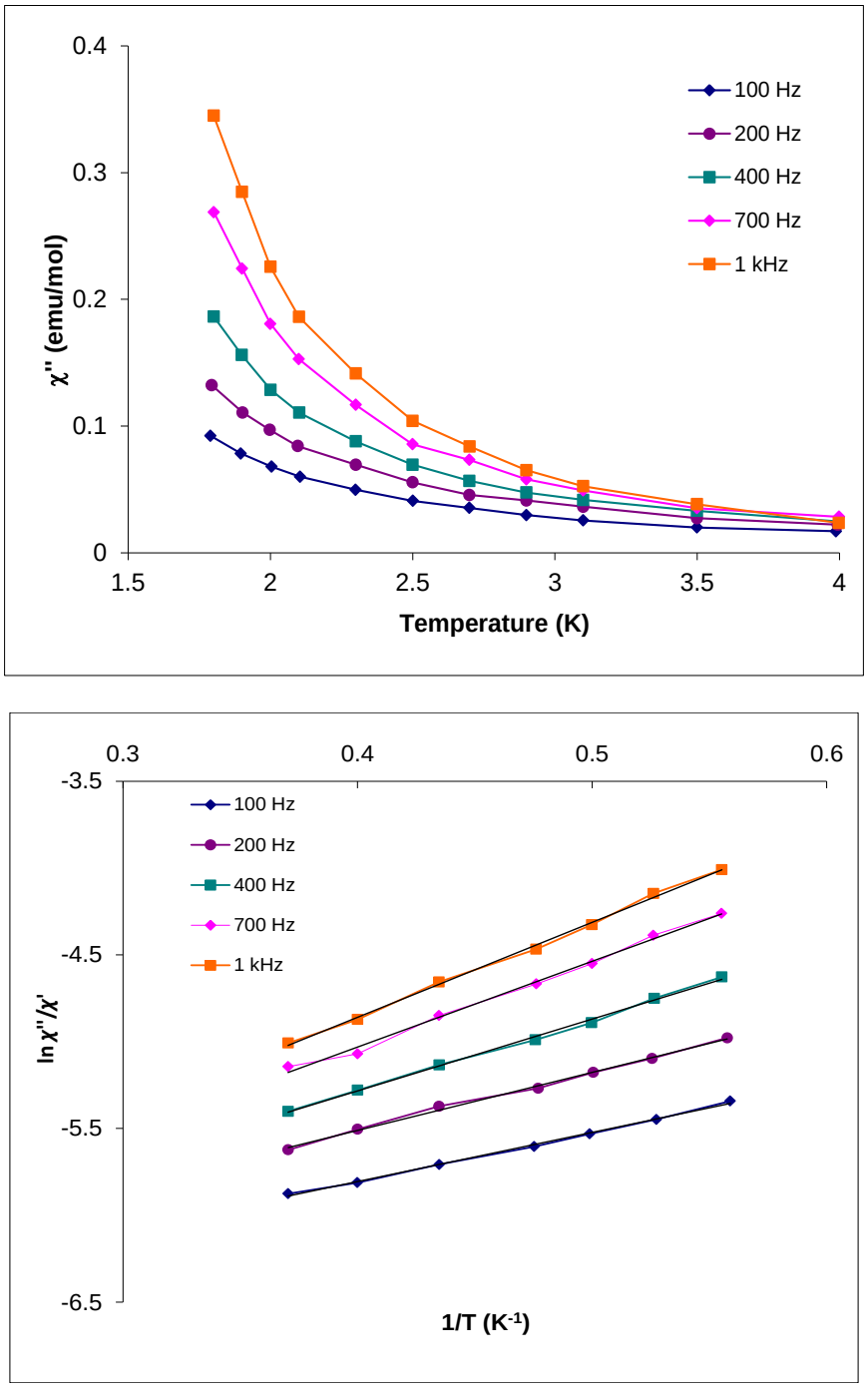

Figure 4.13 Temperature dependence of the out-of-phase ac susceptibility of **26** (top), and fit of Temperature dependence of ac susceptibility of **26** (bottom) under a zero DC applied field.

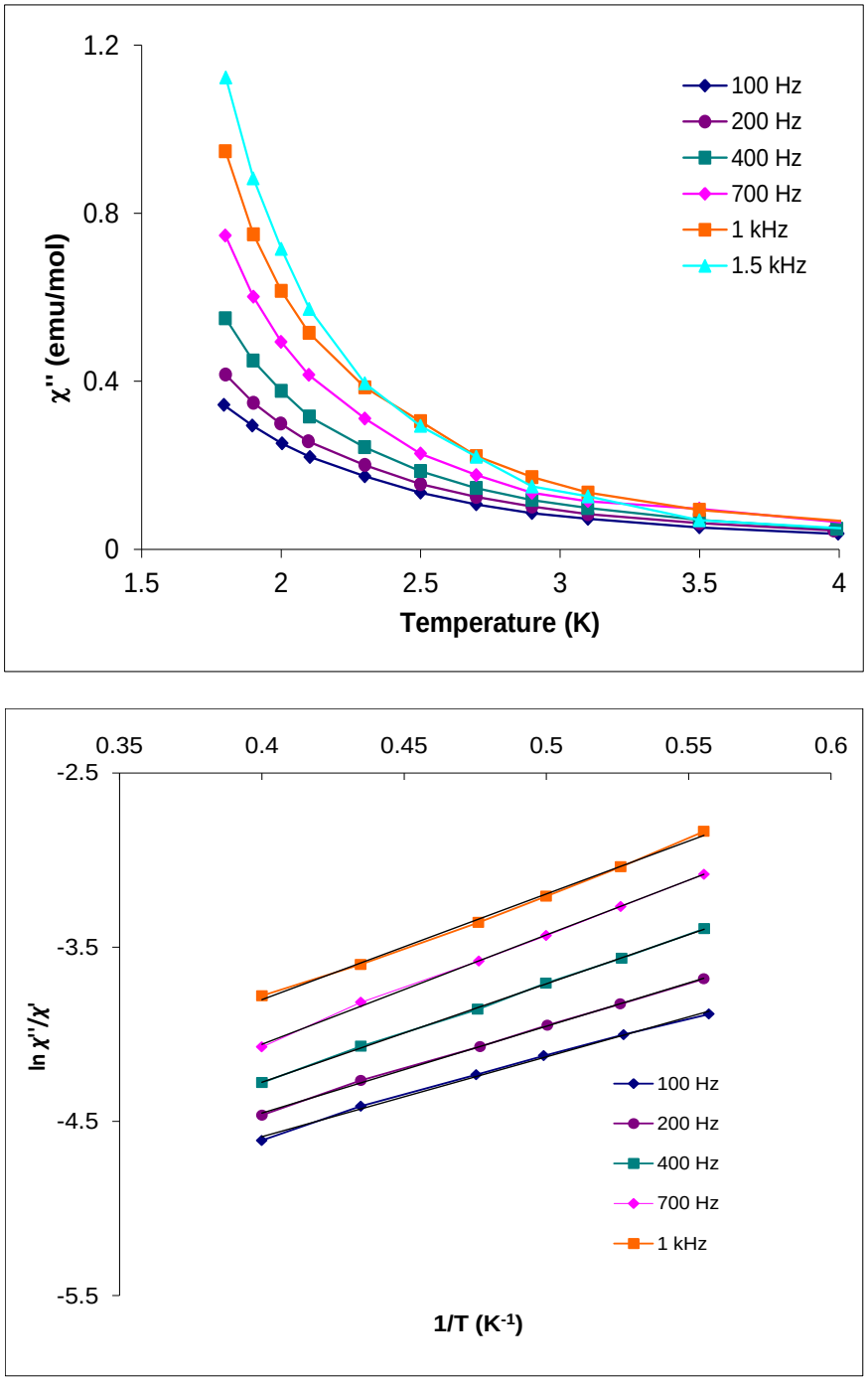

Figure 4.14 Temperature dependence of the out-of-phase AC susceptibility data of **26** (top) and fit of the temperature dependence of AC susceptibility of **26** (bottom) under a 1000Oe DC applied field.

$(Et_4N)_2[(triphosRe(CN)_3)_2(Ho(NO_3)_3)_3]\cdot 4CH_3CN$ ($27\cdot 4CH_3CN$). The magnetic behavior of 27 was investigated as shown in the temperature dependence of χ and χTas well as magnetization measurements (Figure 4.15). The room temperature χT value of 42 emu.K.mol^{-1} for **27** is consistent with two non-interacting Re(II) ions (S=1/2, g = 1.8) and three non-interacting Ho(III) ions (g = 1.25, J= 8) as well as a large TIP (χ_{TIP} = 2.0x10^{-3}) (C= 42.85). The χT value slowly decreases as the temperature is lowered and then it reaches a minimum of 12 emu.K.mol^{-1} at 2 K with a Weiss constant of -9 K (Figure 4.15). This monotonic decrease in χT value might be an indication of both the depopulation of Stark excited sub-levels of the Ho(III) ions and possibly antiferromagnetic exchange interactions between the different metal ions. The field dependence of the magnetization data at temperatures between 2 and 4.5 K exhibit a non-superposition of the iso-field lines indicating the presence of significant spin orbit coupling (Figure 4.15b).

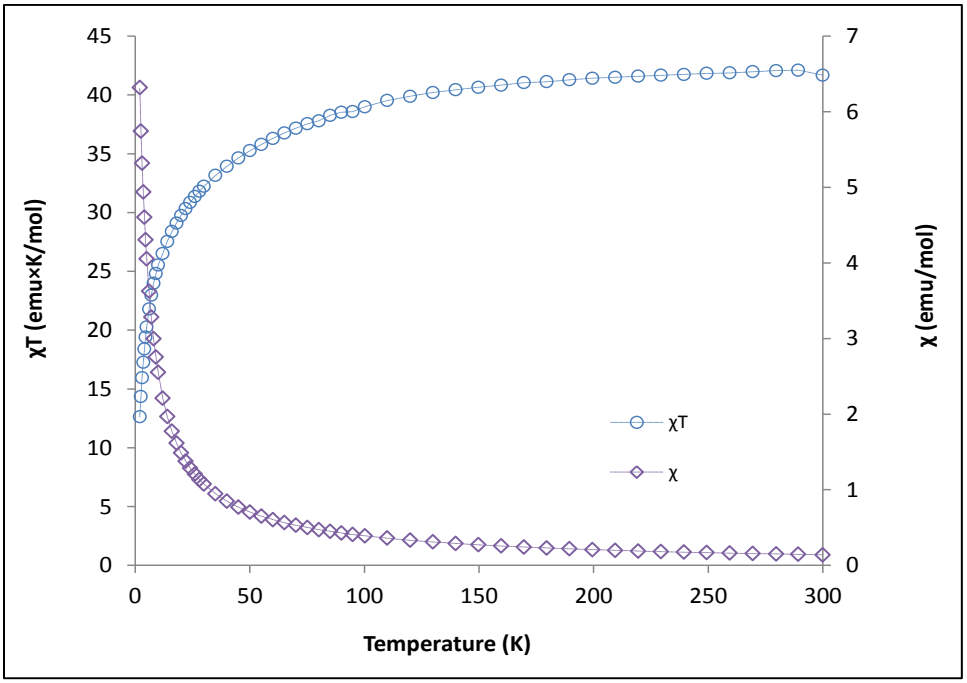

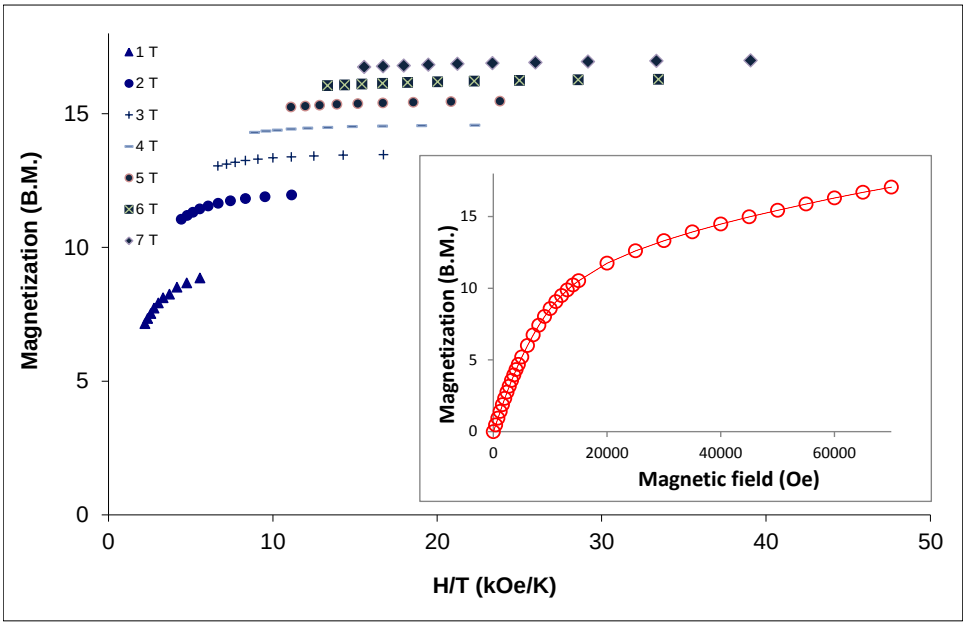

Figure 4. 15 (a) Temperature dependence of χ (◊) and the χT product (o) for **27**. (b) Reduced magnetization data at different external fields. Inset: field dependent magnetization for **27** (o).

Conclusions

A homologous series of 5d/4f cyanide bridged aggregates of general formula $(Et_4N)_2[(triphosRe(CN)_3)_2(Ln(NO_3)_3)_3]\cdot 4CH_3CN$ (**19**-**27**) where Ln = La, Ce, Pr, Nd, Sm, Gd, Tb, Dy and Ho were synthesized and structurally characterized. The family of compounds described in this chapter represents the first family of cyanide-bridged lanthanide containing TBPs which adds valuable information to our reservoir of compounds with TBP geometry. The SQUID studies of the magnetic properties revealed a variety of magnetic responses. Compounds **25** and **26** exhibit slow paramagnetic relaxation of magnetization at zero field below 3 K, indicative of SMM behavior. The relaxation dynamics parameters were estimated by fitting the temperature dependence of the AC data resulting in an energy barrier of 8.49 cm^{-1} and relaxation time of 1.51 x 10^{-8} s for **25** and a barrier of 2.9 cm^{-1} with relaxation time of 6x10^{-7} s in case of **26**. The AC measurements were repeated for both compounds under 1000 Oe applied DC field resulting in a decrease in the energy barrier in **25** and an increase in case of **26**. The nearly symmetric ligand field around the lanthanide centers affects the properties by providing more accessible low-lying excited states that serve to enhance the relaxation rate of the magnetization.

CHAPTER V

CONCLUSIONS AND FUTURE OUTLOOK

The growing need for new and improved technologies for electronics and magnets has sparked a huge upsurgence of research in the design of potential alternatives to conventional materials in order to overcome the current limitations on the particle size and functionality. This areas is commonly referred to as spintronics. [57-62] In the past few decades, molecular magnetic materials have come to the forefront owing to advantages which include ease of synthesis and processing due to higher solubilities, low temperature self-assembly and improved mechanical flexibility.[19-21] Additionally, molecular materials offer systematic approaches for the study of structure-properties relationships in order to gain a deeper understanding of what affects magnetic interactions in order to better modify and tune the properties. The molecular nature of these materials opens up new horizons for combining different physical properties into multifunctional magnetic materials.[21-29,34,57]

The discovery of single molecule magnets (SMMs) represents a major breakthrough in the field of magnetism and, indeed, coordination chemistry in general.[39] The variety of available molecular materials with diverse dimensionalities, nuclearities, and compositions has opened up important new venues for chemical approaches to the preparation of electronic and magnetic devices with unprecedented precision at the nanoscale.[41] These devices represent potential candidates for use as memory storage units of molecular size,[6,7,42,81] as carriers of quantum bits of information for quantum computing purposes[44-56,60,81] and as components of spintronic devices.[56-62]

In response to the challenge of making SMMs with more readily accessible blocking temperatures and longer relaxation times, different approaches have been launched. [103-108,112,114] The main focus in the early stages was towards increasing the total spin as a tool for enhanced properties, [103-108] but recent theoretical studies clearly suggest that we should focus synthetic efforts on enhancing the global anisotropy of metal complexes rather than the spin, S, for obtaining higher barriers in SMMs. [114,115] Early 3d transition metals as well as 4d and 5d transition metals are excellent candidates for introducing large single-ion anisotropy into clusters.[125,126] In the vein of increasing anisotropy with spin-orbit coupling, heavy lanthanide and actinide ions are another source of special interest plus they have larger spin states than 3d metal ions and some of the trivalent ions exhibit Ising-type single ion anisotropy.[152-155]

The work described in this dissertation highlights my efforts to isolate and characterize new building blocks suitable for incorporating highly the anisotropic early transition 3d metal ion V(III) and the 5d metal ion Re(II) as well as lanthanides into heterometallic molecular magnetic materials, and gives insight into the different factors affecting zero-field splitting as a source for single ion anisotropy. In Chapter II, attempts at rational control of the local coordination environment of the metal ions in order to ensure larger orbital contributions to their magnetic moments are presented. The synthesis of a series of trigonally distorted mononuclear V(III) complexes is presented with emphasis on the effect of both the magnitude of the trigonal field and the ligand spin-orbit coupling contribution on the zero-field splitting parameters. In this series, the magnitude of the trigonal field distortion was systematically varied depending on the

differences in ligand field strength for specific ligand combinations; the magnitude of the spin-orbit coupling in the system was varied using ligand spin-orbit coupling contributions (the heavy-halide effect).[169,233,343] The mononuclear complexes in this chapter highlight the importance of careful tuning of the local coordination environments of metal ions in order to achieve enhanced single ion anisotropy. The change of D parameter from **8** (7.13 cm^{-1}) with terminal fluoride ligands to values with larger magnitude and negative sign in the heavier chloride congeners, **4**-**6** (~-30.0 cm^{-1}) supports the previous reports of the heavy halide effect in Nickel analogues.[169,233] Replacing Tp ligand in **1** and **3** with the stronger π donor, Tp*, in **2** and **4** (Tp = *tris*(*-1*-pyrazolyl)borohydride), Tp* = *tris*(*3*,*5*-dimethyl-*1*-pyrazolyl)borohydride)) resulted an axial zero field splitting parameter D_z of -18.5 for **2** and -30.0 cm^{-1} for **4** versus -8.8 for **1** and -16.0 cm^{-1} for **3** as calculated by fitting the iso-field lines in magnetization curves. These results suggest a direct relationship between the D value and the trigonal crystal field which is larger for the stronger π-donor Tp* ligand in **2** and **4.** The large D value in **9** (-19.9 cm^{-1}) which lacks any spin-orbit coupling contribution from halides supports this conclusion. A more accurate determination of the magnitude of D in **4** was achieved using HF-HFEPR in collaboration with Prof. Steven Hill at the National High Field Magnet Lab, Tallahassee, Florida. The EPR measurements on single crystal samples of **4** provided a more accurate value for the zero-field splitting which is -40.0 cm^{-1}, an even higher value than was estimated from magnetic data. Efforts to measure the remaining compounds in the family are ongoing as it is necessary to wait for more magnet time.

These findings are promising in terms of using the strategy of tweaking axial crystal field distortions to enhance single ion anisotropy. In fact, the control of both factors, crystal field and spin-orbit coupling effects in a single compound is a relatively untapped strategy, and one which is ideal for designing enhanced mononuclear SMMs, sometimes (albeit a misnomer) referred to as single ion, single molecule magnets (SIMs). The magnetic data indicate that designing mononuclear vanadium(III) complexes with a simple axially distorted pseudo-octahedral coordination environment, such as $A[L_3VX_3]$ (X = F, Cl or Br, A^+ = Et_4N^+, nBu_4N^+ or PPN^+ , L_3 = Tp or Tp*, and $[Tp^*V(DMF)_3](PF_6)_2$ can lead to a SIM. The ac susceptibility studies for **4** revealed an out-of-phase ac signal below 3.5 K under a 1000 Oe dc field. The fitting of Cole-Cole plots using the Debye model yielded $\tau_o = 5 \times 10^{-5}$ s and $U_{eff} = 4.0$ cm^{-1}. Hysteresis loops were collected using a micro-SQUID on easy-axis oriented single crystal samples. The results of temperature-dependence magnetization measurements reveal butterfly shape hysteretic behavior for **4** at low temperatures (Figure 2.17), which is typical for mononuclear SMMs due to rapid quantum tunneling.[76] Theoretical calculations using complete active space (CAS) methods and ligand field analysis were initiated in collaboration with Prof. Frank Neese at the Max Planck institute, Mulheim, Germany in order to gain a deeper understanding of what affect SMM behavior in this type of complex.

The results presented in Chapter III describe the syntheses and the structural, spectroscopic and magnetic studies of a new series of cyanide building blocks suitable for incorporating the highly anisotropic vanadium(III) ion into cyanide bridged

molecular materials. The ligands acetylacetonate, salen (salen = N,N'-Ethylenebis(salicylimine)), salphen (salphen = N,N'-Phenylenebis(salicylimine)) and 2-methoxysalen (2-methoxysalen = N,N'-Ethylenebis(2-methoxysalicylimine)) were used. A study of the magnetic properties revealed moderate zero-field splitting parameters with D_z values of -10.0, 5.89, 3.7, 4.05 and 4.36 cm^{-1} for **13-17** respectively which make these building blocks very promising for introducing single-ion anisotropy into heterometallic cyanide bridged clusters. The variation of the capping ligand in the salen building block family does not seem to affect the magnitude of D_z. The magnitude of D_z for **15** (3.8) was confirmed by HF-HFEPR measurements in collaboration with Dr Steven Hill in the National High Magnetic Field Laboratory (NHMFL), in Tallahassee, Florida, however, the assignment of the sign of D was not possible because of the lack of rhombic anisotropy (E = 0.0). To date, attempts to incorporate these building blocks into heterometallic complexes have proven to be very challenging due to the high cyanide lability in solution and difficulty in crystallization presumably due to the presence of multiple products in solution. The reaction of **14** with $[Mn(salen)(H_2O)](ClO_4)$ resulted in powders which we propose to be **[**$V(salen)(CN)_2][Mn(salen)]_n \cdot 5CH_3CN$ **(18)** on the basis of elemental analysis and magnetic studies which are in accord with an antiferromagnetically coupled cyanide bridged V-CN-Mn 1D chain. The estimated exchange coupling constant is -4.4 cm^{-1}. Susceptibility studies of the ac type led to an estimated energy barrier of 13.5 cm^{-1} with $\tau = 1.52 \times 10^{-8}$ s. Synthetic efforts towards finding the optimum conditions for incorporating these interesting building blocks into heterometallic complexes will continue to be pursued.

Chapter IV outlines the use of capping ligands as a viable synthetic route to isolating various heterometallic discrete molecules. The results presented in this chapter describe the structural and magnetic properties of a series of lanthanide-containing trigonal bipyramidal (TBP) molecules of general formula $(Et_4N)_2[(triphosRe(CN)_3)_2(Ln(NO_3)_3)_3]\cdot 4CH_3CN$ (**19**-**27**) where Ln = La, Ce, Pr, Nd, Sm, Gd, Tb, Dy and Ho. These compounds constitute the first cyanide-bridged lanthanide containing TBPs and their investigation adds valuable information to the literature of rare earth compounds in various architectures. The SQUID studies revealed a variety of magnetic behavior including the fact that compounds **25** and **26** exhibit slow paramagnetic relaxation of magnetization at zero field below 3 K which hints at SMM behavior. Frequency dependent ac measurements of **26** revealed the appearance of a second relaxation process under an applied field. The nearly symmetric ligand field around the lanthanide centers affects the properties by providing more accessible low-lying excited states that serve to enhance the relaxation rate of the magnetization.

Overall, the work presented in this dissertation provides insight into new methods for enhancing magnetic properties via control of metal ion coordination environments using ligand donor properties and ligand spin-orbit coupling contributions (Chapter II) and provides clear evidence for the potential of the use of vanadium(III) as a means of incorporating single-ion anisotropy into cyanide bridged molecular materials (Chapter III). Additionally, the work highlights the use of cyanide precursors for the synthesis of new magnetic molecular materials containing lanthanides as a source of single ion anisotropy (Chapter IV).

REFERENCES

(1) Dunbar, K. R. *Inorg. Chem.* **2012**, *51*, 12055.

(2) Powell, A. K. *Nature Chem.* **2010**, *2*, 351.

(3) Rentschler, E.; Affronte, M.; Massobrio, C.; Rabu, P. *Solid State Sci.* **2009**, *11*, 970.

(4) Gatteschi, D.; Bogani, L.; Cornia, A.; Mannini, M.; Sorace, L.; Sessoli, R. *Solid State Sci.* **2008**, *10*, 1701.

(5) Murrie, M.; Price, D. J. *Annu. Rep. Prog. Chem., Sect. A: Inorg. Chem.* **2007**, *103*, 20.

(6) Coronado, E.; Dunbar, K. R. *Inorg. Chem.* **2009**, *48*, 5047.

(7) Gatteschi, D.; Sessoli, R.; Villain, R. *Molecular Nanomagnets*; Oxford University Press: Oxford, 2006.

(8) Mroziński, J. *Coord. Chem. Rev.* **2005**, *249*, 2534.

(9) Yakhmi, J. V. *Macromol. Symp.* **2004**, *212*, 141.

(10) Gatteschi, D.; Sessoli, R. *J. Magn. Magn. Mater.* **2004**, *272*, 1030.

(11) Boca, R. *Theoretical Foundations of Molecular Magnetism*; Elsevier: New York, 1999.

(12) Miller, J. S.; Epstein, A. J. *MRS Bull.* **2000**, *25*, 21.

(13) Clemente-Juan, J. M.; Coronado, E. *Coord. Chem. Rev.* **1999**, *193-5*, 361.

(14) Kahn, O. *Molecular Magnetism*; VCH Publishers: New York, 1999.

(15) Miller, J. S.; Epstein, A. J.; Reiff, W. M. *Acc. Chem. Res.* **1988**, *21*, 114.

(16) Bovda, O. M.; Bovda, V. A.; Chebotarev, V. V.; Chen, C. H.; Fedorchenko, V. D.; Higgins, A. K.; Medvedev, O. V.; Onischenko, L. V.; Tortika, O. S. *Metallofiz. Noveishie Tekhnol.* **2010**, *32*, 135.

(17) Givord, D.; Li, H. S.; Moreau, J. M. *Solid State Commun.* **1984**, *50*, 497.

(18) Hou, Y. L.; Xu, Z. C.; Peng, S.; Rong, C. B.; Liu, J. P.; Sun, S. H. *Adv. Mater.* **2007**, *19*, 3349.

(19) Kurmoo, M. *Chem. Soc. Rev.* **2009**, *38*, 1353.

(20) Verdaguer, M.; Bleuzen, A.; Marvaud, V.; Vaissermann, J.; Seuleiman, M.; Desplanches, C.; Scuiller, A.; Train, C.; Garde, R.; Gelly, G.; Lomenech, C.; Rosenman, I.; Veillet, P.; Cartier, C.; Villain, F. *Coord. Chem. Rev.* **1999**, *190-192*, 1023.

(21) Coronado, E.; Day, P. *Chem. Rev.* **2004**, *104*, 5419.

(22) Sato, O. *J. Solid State Electrochem.* **2007**, *11*, 773.

(23) Dei, A. *Angew. Chem., Int. Ed.* **2005**, *44*, 1160.

(24) Arimoto, Y.; Ohkoshi, S.; Zhong, Z. J.; Seino, H.; Mizobe, Y.; Hashimoto, K. *J. Am. Chem. Soc.* **2003**, *125*, 9240.

(25) Coronado, E.; Galan-Mascaros, J. R.; Gomez-Garcia, C. J.; Laukhin, V. *Nature* **2000**, *408*, 447.

(26) Gutlich, P.; Garcia, Y.; Goodwin, H. A. *Chem. Soc. Rev.* **2000**, *29*, 419.

(27) Palacio, F.; Miller, J. S. *Nature* **2000**, *408*, 421.

(28) Verdaguer, M. *Science* **1996**, *272*, 698.

(29) Gutlich, P.; Hauser, A.; Spiering, H. *Angew. Chem., Int. Ed.* **1994**, *33*, 2024.

(30) Bleaney, B.; Bowers, K. D. *Proc. R. Soc. London, A* **1952**, *214*, 451.

(31) Miller, J. S. *Polyhedron* **2009**, *28*, 1596.

(32) Shultz, D. A.; Kumar, R. K.; Bin-Salamon, S.; Kirk, M. L. *Polyhedron* **2005**, *24*, 2876.

(33) Entley, W. R.; Girolami, G. S. *Science* **1995**, *268*, 397.

(34) Ferlay, S.; Mallah, T.; Ouahes, R.; Veillet, P.; Verdaguer, M. *Nature* **1995**, *378*, 701.

(35) Mallah, T.; Thiebaut, S.; Verdaguer, M.; Veillet, P. *Science* **1993**, *262*, 1554.

(36) Manriquez, J. M.; Yee, G. T.; McLean, R. S.; Epstein, A. J.; Miller, J. S. *Science* **1991**, *252*, 1415.

(37) Gutlich, P.; Garcia, Y.; Woike, T. *Coord. Chem. Rev.* **2001**, *219*, 839.

(38) Guetlich, P.; Goodwin, H. A. *Top. Curr. Chem.* **2004**, *233*, 1.

(39) Sessoli, R.; Gatteschi, D.; Caneschi, A.; Novak, M. A. *Nature* **1993**, *365*, 141.

(40) Sessoli, R.; Tsai, H. L.; Schake, A. R.; Wang, S. Y.; Vincent, J. B.; Folting, K.; Gatteschi, D.; Christou, G.; Hendrickson, D. N. *J. Am. Chem. Soc.* **1993**, *115*, 1804.

(41) Seo, D. M.; Meenakshi, V.; Teizer, W.; Zhao, H.; Dunbar, K. R. *J. Magn. Magn. Mater.* **2006**, *301*, 31.

(42) Meijer, G. I. *Science* **2008**, *319*, 1625.

(43) Wernsdorfer, W. *Nat. Mater.* **2007**, *6*, 174.

(44) Tejada, J.; Chudnovsky, E. M.; del Barco, E.; Hernandez, J. M.; Spiller, T. P. *Nanotechnology* **2001**, *12*, 181.

(45) Affronte, M.; Troiani, F.; Ghirri, A.; Carretta, S.; Santini, P.; Corradini, V.; Schuecker, R.; Muryn, C.; Timco, G.; Winpenny, R. E. *Dalton Trans.* **2006**, 2810.

(46) Bertaina, S.; Gambarelli, S.; Tkachuk, A.; Kurkin, I. N.; Malkin, B.; Stepanov, A.; Barbara, B. *Nat. Nanotechnol.* **2007**, *2*, 39.

(47) Lehmann, J.; Gaita-Arino, A.; Coronado, E.; Loss, D. *J. Mater. Chem.* **2009**, *19*, 1672.

(48) Bertaina, S.; Shim, J. H.; Gambarelli, S.; Malkin, B. Z.; Barbara, B. *Phys. Rev. Lett.* **2009**, *103*.

(49) Stamp, P. C. E. *Nature* **2008**, *453*, 167.

(50) Stepanenko, D.; Trif, M.; Loss, D. *Inorg. Chim. Acta* **2008**, *361*, 3740.

(51) Schlegel, C.; van Slageren, J.; Manoli, M.; Brechin, E. K.; Dressel, M. *Phys. Rev. Lett.* **2008**, *101*.

(52) Lehmann, J.; Gaita-Arino, A.; Coronado, E.; Loss, D. *Nat. Nanotechnol.* **2007**, *2*, 312.

(53) Leuenberger, M. N.; Loss, D.; Poggio, M.; Awschalom, D. D. *Phys. Rev. Lett.* **2002**, *89*.

(54) Leuenberger, M. N.; Loss, D. *Nature* **2001**, *410*, 789.

(55) Tejada, J. *Polyhedron* **2001**, *20*, 1751.

(56) Timco, G. A.; Carretta, S.; Troiani, F.; Tuna, F.; Pritchard, R. J.; Muryn, C. A.; McInnes, E. J. L.; Ghirri, A.; Candini, A.; Santini, P.; Amoretti, G.; Affronte, M.; Winpenny, R. E. P. *Nat. Nanotechnol.* **2009**, *4*, 173.

(57) Camarero, J.; Coronado, E. *J. Mater. Chem.* **2009**, *19*, 1678.

(58) Sanvito, S. *Spin Transport and Magnetism*; Taylor & Francis, New York: 2012.

(59) Katoh, K.; Isshiki, H.; Komeda, T.; Yamashita, M. *Chemistry – An Asian Journal* **2012**, *7*, 1154.

(60) Bogani, L.; Wernsdorfer, W. *Nat. Mater.* **2008**, *7*, 179.

(61) Chappert, C.; Fert, A.; Van Dau, F. N. *Nat. Mater.* **2007**, *6*, 813.

(62) Bogani, L.; Wernsdorfer, W. *Inorg. Chim. Acta* **2008**, *361*, 3807.

(63) Carlin, R. L. *Magnetochemistry*; Springer-Verlag Berlin, 1986.

(64) Van Niekerk, J. N.; Schoening, F. R. L. *Acta Crystallogr.* **1953**, *6*, 227.

(65) Van Niekerk, J. N.; Schoening, F. R. L. *Nature* **1953**, *171*, 36.

(66) Barclay, G. A.; Harris, C. M.; Hoskins, B. F.; Kokot, E. *Proc. Chem. Soc., London* **1961**, 264.

(67) Kokot, E.; Martin, R. L., *Inorg. Chem.* **1964**, *3*, 1306.

(68) Moreland, J. A.; Doedens, R. J. *Inorg. Chem.* **1978**, *17*, 674.

(69) Dickman, M. H.; Doedens, R. J. *Inorg. Chem.* **1981**, *20*, 2677.

(70) Porter, L. C.; Doedens, R. J. *Inorg. Chem.* **1984**, *23*, 997.

(71) Anderson, P. W. *Phys Rev* **1959**, *115*, 2.

(72) Good-enough, J. B. *Phys. Chem. Solids* **1958**, *6*, 287.

(73) Kanamori, J. *Phys. Chem. Solids* **1959**, *10*, 87.

(74) Hay, P. J.; Thibeault, J. C.; Hoffmann, R. *J. Am. Chem. Soc.* **1975**, *97*, 4884.

(75) Willett, R.; Gatteschi, D.; Kahn, O. *Magneto-structural Correlation in Exchange Coupled Systems*; Kluwer: Dordrecht, The Netherlands 1985.

(76) Kahn, O. *Angew. Chem.* **1985**, *97*, 837.

(77) Caneschi, A.; Gatteschi, D.; Sessoli, R.; Barra, A. L.; Brunel, L. C.; Guillot, M. *J. Am. Chem. Soc.* **1991**, *113*, 5873.

(78) Christou, G.; Gatteschi, D.; Hendrickson, D. N.; Sessoli, R. *MRS Bull.* **2000**, *25*, 66.

(79) Aromi, G.; Brechin, E. K. *Single-Molecule Magnets and Related Phenomena;* Springer-Verlag, Berlin: 2006.

(80) Christou, G.; Gatteschi, D.; Hendrickson, D. N.; Sessoli, R. *MRS Bull.* **2011**, *25*, 66.

(81) Gatteschi, D.; Sessoli, R. *Angew. Chem., Int. Ed.* **2003**, *42*, 268.

(82) Thomas, L.; Lionti, F.; Ballou, R.; Gatteschi, D.; Sessoli, R.; Barbara, B. *Nature* **1996**, *383*, 145.

(83) Wernsdorfer, W. *Handbook of Advanced Magnetic Materials*; Liu, Y., Sellmyer, D., Shindo, D., Eds.; Springer, New York: 2006.

(84) Ruiz-Molina, D.; Christou, G.; Hendrickson, D. N. *Mol. Cryst. Liq. Cryst.* **2000**, *343*, 335.

(85) Lis, T. *Acta Crystallogr B* **1980**, *36*, 2042.

(86) Christou, G. *Polyhedron* **2005**, *24*, 2065.

(87) Torres, F.; Hernández, J. M.; Bohigas, X.; Tejada, J. *Appl. Phys. Lett.* **2000**, *77*.

(88) Eppley, H. J.; Tsai, H.-L.; de Vries, N.; Folting, K.; Christou, G.; Hendrickson, D. N. *J. Am. Chem. Soc.* **1995**, *117*, 301.

(89) Pederson, M. R.; Khanna, S. N. *Phys. Rev. B* **1999**, *60*, 9566.

(90) Arom, G.; Aubin, S. M. J.; Bolcar, M. A.; Christou, G.; Eppley, H. J.; Folting, K.; Hendrickson, D. N.; Huffman, J. C.; Squire, R. C.; Tsai, H.-L.; Wang, S.; Wemple, M. W. *Polyhedron* **1998**, *17*, 3005.

(91) Tasiopoulos, A. J.; Wernsdorfer, W.; Abboud, K. A.; Christou, G. *Inorg. Chem.* **2005**, *44*, 6324.

(92) Soler, M.; Wernsdorfer, W.; Sun, Z.; Ruiz, D.; Huffman, J. C.; Hendrickson, D. N.; Christou, G. *Polyhedron* **2003**, *22*, 1783.

(93) Brockman, J. T.; Abboud, K. A.; Hendrickson, D. N.; Christou, G. *Polyhedron* **2003**, *22*, 1765.

(94) Murugesu, M.; Wernsdorfer, W.; Abboud, K. A.; Brechin, E. K.; Christou, G. *Dalton Trans.* **2006**, *0*, 2285.

(95) Chakov, N. E.; Lee, S.-C.; Harter, A. G.; Kuhns, P. L.; Reyes, A. P.; Hill, S. O.; Dalal, N. S.; Wernsdorfer, W.; Abboud, K. A.; Christou, G. *J. Am. Chem. Soc.* **2006**, *128*, 6975.

(96) Chakov, N. E.; Abboud, K. A.; Zakharov, L. N.; Rheingold, A. L.; Hendrickson, D. N.; Christou, G. *Polyhedron* **2003**, *22*, 1759.

(97) Soler, M.; Wernsdorfer, W.; Sun, Z.; Huffman, J. C.; Hendrickson, D. N.; Christou, G. *Chem. Commun.* **2003**, *0*, 2672.

(98) King, P.; Wernsdorfer, W.; Abboud, K. A.; Christou, G. *Inorg. Chem.* **2005**, *44*, 8659.

(99) Soler, M.; Artus, P.; Folting, K.; Huffman, J. C.; Hendrickson, D. N.; Christou, G. *Inorg. Chem.* **2001**, *40*, 4902.

(100) Artus, P.; Boskovic, C.; Yoo, J.; Streib, W. E.; Brunel, L.-C.; Hendrickson, D. N.; Christou, G. *Inorg. Chem.* **2001**, *40*, 4199.

(101) Tsai, H.-L.; Eppley, H. J.; de Vries, N.; Folting, K.; Christou, G.; Hendrickson, D. N. *J. Chem. Soc., Chem. Commun.* **1994**, *0*, 1745.

(102) Rinehart, J. D.; Long, J. R. *Chem. Sci.* **2011**, *2*, 2078.

(103) Abbati, G. L.; Cornia, A.; Caneschi, A.; Fabretti, A. C.; Mortalo, C. *Inorg. Chem.* **2004**, *43*, 4540.

(104) Abbati, G. L.; Caneschi, A.; Cornia, A.; Fabretti, A. C.; Pozdniakova, Y. A.; Shchegolikhina, O. I. *Angew. Chem., Int. Ed.* **2002**, *41*, 4517.

(105) Müller, A.; Luban, M.; Schröder, C.; Modler, R.; Kögerler, P.; Axenovich, M.; Schnack, J.; Canfield, P.; Bud'ko, S.; Harrison, N. *ChemPhysChem* **2001**, *2*, 517.

(106) Müller, A.; Sarkar, S.; Shah, S. Q. N.; Bögge, H.; Schmidtmann, M.; Sarkar, S.; Kögerler, P.; Hauptfleisch, B.; Trautwein, A. X.; Schünemann, V. *Angew. Chem. Int. Ed.* **1999**, *38*, 3238.

(107) Müller, A.; Krickemeyer, E.; Das, S. K.; Kögerler, P.; Sarkar, S.; Bögge, H.; Schmidtmann, M.; Sarkar, S. *Angew. Chem. Int. Ed.* **2000**, *39*, 1612.

(108) Müller, A.; Das, S. K.; Kögerler, P.; Bögge, H.; Schmidtmann, M.; Trautwein, A. X.; Schünemann, V.; Krickemeyer, E.; Preetz, W. *Angew. Chem. Int. Ed.* **2000**, *39*, 3413.

(109) Ako, A. M.; Hewitt, I. J.; Mereacre, V.; Clérac, R.; Wernsdorfer, W.; Anson, C. E.; Powell, A. K. *Angew. Chem. Int. Ed.* **2006**, *45*, 4926.

(110) Murugesu, M.; Takahashi, S.; Wilson, A.; Abboud, K. A.; Wernsdorfer, W.; Hill, S.; Christou, G. *Inorg. Chem.* **2008**, *47*, 9459.

(111) Tasiopoulos, A. J.; Vinslava, A.; Wernsdorfer, W.; Abboud, K. A.; Christou, G. *Angew. Chem. Int. Ed.* **2004**, *43*, 2117.

(112) Milios, C. J.; Vinslava, A.; Wernsdorfer, W.; Moggach, S.; Parsons, S.; Perlepes, S. P.; Christou, G.; Brechin, E. K. *J. Am. Chem. Soc.* **2007**, *129*, 2754.

(113) Thomas, L.; Lionti, F.; Ballou, R.; Gatteschi, D.; Sessoli, R.; Barbara, B. *Nature* **1996**, *383*, 145.

(114) Waldmann, O. *Inorg. Chem.* **2007**, *46*, 10035.

(115) Ruiz, E.; Cirera, J.; Cano, J.; Alvarez, S.; Loose, C.; Kortus, J. *Chem. Commun.* **2008**, *0*, 52.

(116) Wang, X. Y.; Avendano, C.; Dunbar, K. R. *Chem. Soc. Rev.* **2011**, *40*, 3213.

(117) Shatruk, M.; Avendano, C.; Dunbar, K. R. In *Prog. Inorg. Chem.*; John Wiley & Sons, Inc.: 2009, p 155.

(118) Ruiz, E.; Rodríguez-Fortea, A.; Alvarez, S.; Verdaguer, M. *Chem.–Eur. J.* **2005**, *11*, 2135.

(119) Atanasov, M.; Busche, C.; Comba, P.; El Hallak, F.; Martin, B.; Rajaraman, G.; van Slageren, J.; Wadepohl, H. *Inorg. Chem.* **2008**, *47*, 8112.

(120) Atanasov, M.; Comba, P.; Daul, C. A. *J. Phys. Chem. A* **2006**, *110*, 13332.

(121) Levy, P. M. *B Am Phys Soc* **1969**, *14*, 409.

(122) Tsukerblat, B. S.; Tarantul, A.; Muller, A. *J. Mol. Struct.* **2007**, *838*, 124.

(123) Palii, A.; Tsukerblat, B.; Klokishner, S.; Dunbar, K. R.; Clemente-Juan, J. M.; Coronado, E. *Chem. Soc. Rev.* **2011**, *40*, 3130.

(124) Tsukerblat, B. S.; Palii, A. V.; Ostrovsky, S. M.; Kunitsky, S. V.; Klokishner, S. I.; Dunbar, K. R. *J. Chem. Theory Comput.* **2005**, *1*, 668.

(125) Weihe, H.; Gudel, H. U. *Comments Inorg. Chem.* **2000**, *22*, 75.

(126) Entley, W. R.; Treadway, C. R.; Girolami, G. S. *Mol. Cryst. Liq. Cryst. Sci. Technol., Sect. A* **1995**, *273*, 153.

(127) Hatlevik, O.; Buschmann, W. E.; Zhang, J.; Manson, J. L.; Miller, J. S. *Adv. Mater.* **1999**, *11*, 914.

(128) Holmes, S. M.; Girolami, G. S. *J. Am. Chem. Soc.* **1999**, *121*, 5593.

(129) Berlinguette, C. P.; Vaughn, D.; Canada-Vilalta, C.; Galan-Mascaros, J. R.; Dunbar, K. R. *Angew. Chem. Int. Ed.* **2003**, *42*, 1523.

(130) Freedman, D. E.; Jenkins, D. M.; Iavarone, A. T.; Long, J. R. *J. Am. Chem. Soc.* **2008**, *130*, 2884.

(131) Sokol, J. J.; Hee, A. G.; Long, J. R. *J. Am. Chem. Soc.* **2002**, *124*, 7656.

(132) Schelter, E. J.; Karadas, F.; Avendano, C.; Prosvirin, A. V.; Wernsdorfer, W.; Dunbar, K. R. *J. Am. Chem. Soc.* **2007**, *129*, 8139.

(133) Choi, H. J.; Sokol, J. J.; Long, J. R. *Inorg. Chem.* **2004**, *43*, 1606.

(134) Ferbinteanu, M.; Miyasaka, H.; Wernsdorfer, W.; Nakata, K.; Sugiura, K.; Yamashita, M.; Coulon, C.; Clerac, R. *J. Am. Chem. Soc.* **2005**, *127*, 3090.

(135) Choi, H. J.; Sokol, J. J.; Long, J. R. *Inorg. Chem.* **2004**, *43*, 1606.

(136) Pedersen, K. S.; Dreiser, J.; Nehrkorn, J.; Gysler, M.; Schau-Magnussen, M.; Schnegg, A.; Holldack, K.; Bittl, R.; Piligkos, S.; Weihe, H.; Tregenna-Piggott, P.; Waldmann, O.; Bendix, J. *Chem. Commun.* **2011**, *47*, 6918.

(137) Pedersen, K. S.; Schau-Magnussen, M.; Bendix, J.; Weihe, H.; Palii, A. V.; Klokishner, S. I.; Ostrovsky, S.; Reu, O. S.; Mutka, H.; Tregenna-Piggott, P. L. W. *Chem.–Eur. J.* **2010**, *16*, 13458.

(138) Tregenna-Piggott, P. L. W.; Sheptyakov, D.; Keller, L.; Klokishner, S. I.; Ostrovsky, S. M.; Palii, A. V.; Reu, O. S.; Bendix, J.; Brock-Nannestad, T.; Pedersen, K.; Weihe, H.; Mutka, H. *Inorg. Chem.* **2008**, *48*, 128.

(139) Dreiser, J.; Pedersen, K. S.; Schnegg, A.; Holldack, K.; Nehrkorn, J.; Sigrist, M.; Tregenna-Piggott, P.; Mutka, H.; Weihe, H.; Mironov, V. S.; Bendix, J.; Waldmann, O. *Chem.–Eur. J.* **2013**, *19*, 3693.

(140) Harris, T. D.; Coulon, C.; Clerac, R.; Long, J. R. *J. Am. Chem. Soc.* **2011**, *133*, 123.

(141) Freedman, D. E.; Harman, W. H.; Harris, T. D.; Long, G. J.; Chang, C. J.; Long, J. R. *J. Am. Chem. Soc.* **2010**, *132*, 1224.

(142) Harman, W. H.; Harris, T. D.; Freedman, D. E.; Fong, H.; Chang, A.; Rinehart, J. D.; Ozarowski, A.; Sougrati, M. T.; Grandjean, F.; Long, G. J.; Long, J. R.; Chang, C. J. *J. Am. Chem. Soc.* **2010**, *132*, 18115.

(143) Jurca, T.; Farghal, A.; Lin, P. H.; Korobkov, I.; Murugesu, M.; Richeson, D. S. *J. Am. Chem. Soc.* **2011**, *133*, 15814.

(144) Mossin, S.; Tran, B. L.; Adhikari, D.; Pink, M.; Heinemann, F. W.; Sutter, J.; Szilagyi, R. K.; Meyer, K.; Mindiola, D. J. *J. Am. Chem. Soc.* **2012**, *134*, 13651.

(145) Zadrozny, J. M.; Long, J. R. *J. Am. Chem. Soc.* **2011**, *133*, 20732.

(146) Zadrozny, J. M.; Liu, J.; Piro, N. A.; Chang, C. J.; Hill, S.; Long, J. R. *Chem. Commun.* **2012**, *48*, 3927.

(147) Zhu, Y.-Y.; Wang, B.-W.; Gao, S. *Chem. Sci.* **2013**.

(148) Vallejo, J.; Castro, I.; Ruiz-Garcia, R.; Cano, J.; Julve, M.; Lloret, F.; De Munno, G.; Wernsdorfer, W.; Pardo, E. *J. Am. Chem. Soc.* **2012**, *134*, 15704.

(149) Zadrozny, J. M.; Atanasov, M.; Bryan, A. M.; Lin, C. Y.; Rekken, B. D.; Power, P. P.; Neese, F.; Long, J. R. *Chem. Sci.* **2013**, *4*, 125.

(150) Weismann, D.; Sun, Y.; Lan, Y.; Wolmershäuser, G.; Powell, A. K.; Sitzmann, H. *Chem.–Eur. J.* **2011**, *17*, 4700.

(151) Buchholz, A.; Eseola, A. O.; Plass, W. *C. R. Chim.* **2012**, *15*, 929.

(152) Ishikawa, N. *Polyhedron* **2007**, *26*, 2147.

(153) Ishikawa, N.; Sugita, M.; Ishikawa, T.; Koshihara, S.-y.; Kaizu, Y. *J. Am. Chem. Soc.* **2003**, *125*, 8694.

(154) Ishikawa, N.; Sugita, M.; Ishikawa, T.; Koshihara, S.-y.; Kaizu, Y. *J. Phys. Chem. B* **2004**, *108*, 11265.

(155) Ishikawa, N.; Sugita, M.; Wernsdorfer, W. *J. Am. Chem. Soc.* **2005**, *127*, 3650.

(156) Baldoví, J. J.; Clemente-Juan, J. M.; Coronado, E.; Gaita-Ariño, A. *Polyhedron* **2013**.

(157) Liu, J.-L.; Yuan, K.; Leng, J.-D.; Ungur, L.; Wernsdorfer, W.; Guo, F.-S.; Chibotaru, L. F.; Tong, M.-L. *Inorg. Chem.* **2012**, *51*, 8538.

(158) Chilton, N. F.; Langley, S. K.; Moubaraki, B.; Soncini, A.; Batten, S. R.; Murray, K. S. *Chem. Sci.* **2013**, *4*, 1719.

(159) Jiang, S. D.; Wang, B. W.; Sun, H. L.; Wang, Z. M.; Gao, S. *J. Am. Chem. Soc.* **2011**, *133*, 4730.

(160) Jiang, S.-D.; Liu, S.-S.; Zhou, L.-N.; Wang, B.-W.; Wang, Z.-M.; Gao, S. *Inorg. Chem.* **2012**, *51*, 3079.

(161) Le Roy, J. J.; Jeletic, M. S.; Gorelsky, S. I.; Korobkov, I.; Ungur, L.; Chibotaru, L. F.; Murugesu, M. *J. Am. Chem. Soc.* **2013**.

(162) Chen, G. J.; Guo, Y. N.; Tian, J. L.; Tang, J. K.; Gu, W.; Liu, X.; Yan, S. P.; Cheng, P.; Liao, D. Z. *Chem.–Eur. J.* **2012**, *18*, 2484.

(163) Antunes, M. A.; Pereira, L. C. J.; Santos, I. C.; Mazzanti, M.; Marçalo, J.; Almeida, M. *Inorg. Chem.* **2011**, *50*, 9915.

(164) Moro, F.; Mills, D. P.; Liddle, S. T.; van Slageren, J. *Angew. Chem. Int. Ed.* **2013**, 52, 3430.

(165) Rinehart, J. D.; Long, J. R. *J. Am. Chem. Soc.* **2009**, *131*, 12558.

(166) Monreal, M. J.; Wright, R. J.; Morris, D. E.; Scott, B. L.; Golden, J. T.; Power, P. P.; Kiplinger, J. L. *Organometallics* **2013**.

(167) Coutinho, J. T.; Antunes, M. A.; Pereira, L. C. J.; Bolvin, H.; Marcalo, J.; Mazzanti, M.; Almeida, M. *Dalton Trans.* **2012**, *41*, 13568.

(168) Baldovi, J. J.; Cardona-Serra, S.; Clemente-Juan, J. M.; Coronado, E.; Gaita-Arino, A. *Chem. Sci.* **2013**, *4*, 938.

(169) Ye, S. F.; Neese, F. *J. Chem. Theory Comput.* **2012**, *8*, 2344.

(170) Karunadasa, H. I.; Arquero, K. D.; Berben, L. A.; Long, J. R. *Inorg. Chem.* **2010**, *49*, 4738.

(171) Palii, A. V.; Ostrovsky, S. M.; Klokishner, S. I.; Tsukerblat, B. S.; Berlinguette, C. P.; Dunbar, K. R.; Galan-Mascaros, J. R. *J. Am. Chem. Soc.* **2004**, *126*, 16860.

(172) Palii, A. V.; Clemente-Juan, J. M.; Coronado, E.; Klokishner, S. I.; Ostrovsky, S. M.; Reu, O. S. *Inorg. Chem.* **2010**, *49*, 8073.

(173) Castro, S. L.; Sun, Z. M.; Grant, C. M.; Bollinger, J. C.; Hendrickson, D. N.; Christou, G. *J. Am. Chem. Soc.* **1998**, *120*, 2365.

(174) Knopp, P.; Wieghardt, K.; Nuber, B.; Weiss, J.; Sheldrick, W. S. *Inorg. Chem.* **1990**, *29*, 363.

(175) Tidmarsh, I. S.; Batchelor, L. J.; Scales, E.; Laye, R. H.; Sorace, L.; Caneschi, A.; Schnack, J.; McInnes, E. J. *Dalton Trans.* **2009**, 9402.

(176) Shaw, R.; Tuna, F.; Wernsdorfer, W.; Barra, A. L.; Collison, D.; McInnes, E. J. L. *Chem. Commun.* **2007**, 5161.

(177) Krzystek, J.; Fiedler, A. T.; Sokol, J. J.; Ozarowski, A.; Zvyagin, S. A.; Brunold, T. C.; Long, J. R.; Brunel, L. C.; Telser, J. *Inorg. Chem.* **2004**, *43*, 5645.

(178) Tregenna-Piggott, P. L. W.; Weihe, H.; Bendix, J.; Barra, A. L.; Gudel, H. U. *Inorg. Chem.* **1999**, *38*, 5928.

(179) Kumagai, H.; Kitagawa, S. *Chem. Lett.* **1996**, 471.

(180) Castro, S. L.; Sun, Z.; Grant, C. M.; Bollinger, J. C.; Hendrickson, D. N.; Christou, G. *J. Am. Chem. Soc.* **1998**, *120*, 2365.

(181) Papoutsakis, D.; Grohol, D.; Nocera, D. G. *J. Am. Chem. Soc.* **2002**, *124*, 2647.

(182) Dujardin, E.; Ferlay, S.; Phan, X.; Desplanches, C.; Moulin, C. C. D.; Sainctavit, P.; Baudelet, F.; Dartyge, E.; Veillet, P.; Verdaguer, M. *J. Am. Chem. Soc.* **1998**, *120*, 11347.

(183) Lee, I. S.; Long, J. R. *Dalton Trans.* **2004**, 3434.

(184) Tomono, K.; Tsunobuchi, Y.; Nakabayashi, K.; Ohkoshi, S. *Inorg. Chem.* **2010**, *49*, 1298.

(185) Zhou, P. H.; Xue, D. S.; Luo, H. Q.; Yao, J. L.; Shi, H. G. *Nanotechnology* **2004**, *15*, 27.

(186) Nelson, K. J.; Daniels, M. C.; Reiff, W. M.; Troff, S. A.; Miller, J. S. *Inorg. Chem.* **2007**, *46*, 10093.

(187) Nelson, K. J.; Miller, J. S. *Inorg. Chem.* **2008**, *47*, 2526.

(188) Nelson, K. J.; Giles, I. D.; Troff, S. A.; Arif, A. M.; Miller, J. S. *Inorg. Chem.* **2006**, *45*, 8922.

(189) Li, D. F.; Parkin, S.; Wang, G. B.; Yee, G. T.; Holmes, S. M. *Inorg. Chem.* **2006**, *45*, 2773.

(190) Brechin, E. K.; Boskovic, C.; Wernsdorfer, W.; Yoo, J.; Yamaguchi, A.; Sanudo, E. C.; Concolino, T. R.; Rheingold, A. L.; Ishimoto, H.; Hendrickson, D. N.; Christou, G. *J. Am. Chem. Soc.* **2002**, *124*, 9710.

(191) Chakov, N. E.; Wernsdorfer, W.; Abboud, K. A.; Christou, G. *Inorg. Chem.* **2004**, *43*, 5919.

(192) Atanasov, M.; Comba, P.; Daul, C. A. *Inorg. Chem.* **2008**, *47*, 2449.

(193) Tregenna-Piggott, P. L. W.; Sheptyakov, D.; Keller, L.; Klokishner, S. I.; Ostrovsky, S. M.; Palii, A. V.; Reu, O. S.; Bendix, J.; Brock-Nannestad, T.; Pedersen, K.; Weihe, H.; Mutka, H. *Inorg. Chem.* **2009**, *48*, 128.

(194) Pedersen, K. S.; Schau-Magnussen, M.; Bendix, J.; Weihe, H.; Palii, A. V.; Klokishner, S. I.; Ostrovsky, S.; Reu, O. S.; Mutka, H.; Tregenna-Piggott, P. L. W. *Chem.–Eur. J.* **2010**, *16*, 13458.

(195) Maganas, D.; Sottini, S.; Kyritsis, P.; Groenen, E. J. J.; Neese, F. *Inorg. Chem.* **2011**, *50*, 8741.

(196) Zadrozny, J. M.; Liu, J. J.; Piro, N. A.; Chang, C. J.; Hill, S.; Long, J. R. *Chem. Commun.* **2012**, *48*, 3927.

(197) Palii, A. V.; Ostrovsky, S. M.; Klokishner, S. I.; Tsukerblat, B. S.; Schelter, E. J.; Prosvirin, A. V.; Dunbar, K. R. *Inorg. Chim. Acta* **2007**, *360*, 3915.

(198) Clarke, J. G.; MacKinnon, J. A. *Can. J. Phys.* **1971**, *49*, 1539.

(199) Foner, S.; Low, W. *Phys Rev* **1960**, *120*, 1585.

(200) Carlin, R. L.; Schwartz, R. W. *J. Am. Chem. Soc.* **1970**, *92*, 6763.

(201) Pryce, M. H. L.; Runciman, W. A. *Discussions of the Faraday Society* **1958**, *26*, 34.

(202) Dolder, S.; Spichiger, D.; Tregenna-Piggott, P. L. W. *Inorg. Chem.* **2003**, *42*, 1343.

(203) Hitchman, M. A.; McDonald, R. G.; Smith, P. W.; Stranger, R. *J. Chem. Soc., Dalton Trans.* **1988**, *0*, 1393.

(204) Tregenna-Piggott, P. L.; Best, S. P. *Inorg. Chem.* **1996**, *35*, 5730.

(205) Landry-Hum, J.; Bussiere, G.; Daniel, C.; Reber, C. *Inorg. Chem.* **2001**, *40*, 2595.

(206) Piper, T. S.; Carlin, R. L. *Inorg. Chem.* **1963**, *2*, 260.

(207) Alonso, P. J.; Fornies, J.; Garcia-Monforte, M. A.; Martin, A.; Menjon, B. *Chem. Commun.* **2001**, 2138.

(208) Barra, A. L.; Brunel, L. C.; Gatteschi, D.; Pardi, L.; Sessoli, R. *Acc. Chem. Res.* **1998**, *31*, 460.

(209) Hagen, W. R. *Coord. Chem. Rev.* **1999**, *190–192*, 209.

(210) Tregenna-Piggott, P. L.; Weihe, H.; Bendix, J.; Barra, A. L.; Gudel, H. U. *Inorg. Chem.* **1999**, *38*, 5928.

(211) Morosin, B.; Montgomery, H. *Acta Crystallogr. Sec. B* **1969**, *25*, 1354.

(212) Krzystek, J.; Fiedler, A. T.; Sokol, J. J.; Ozarowski, A.; Zvyagin, S. A.; Brunold, T. C.; Long, J. R.; Brunel, L.-C.; Telser, J. *Inorg. Chem.* **2004**, *43*, 5645.

(213) van Dam, P. J.; Klaassen, A. A. K.; Reijerse, E. J.; Hagen, W. R. *J. Magn. Reson.* **1998**, *130*, 140.

(214) Krzystek, J.; Park, J. H.; Meisel, M. W.; Hitchman, M. A.; Stratemeier, H.; Brunel, L. C.; Telser, J. *Inorg. Chem.* **2002**, *41*, 4478.

(215) Desrochers, P. J.; Telser, J.; Zvyagin, S. A.; Ozarowski, A.; Krzystek, J.; Vicic, D. A. *Inorg. Chem.* **2006**, *45*, 8930.

(216) Collison, D.; Helliwell, M.; Jones, V. M.; Mabbs, F. E.; McInnes, E. J. L.; Riedi, P. C.; Smith, G. M.; Pritchard, R. G.; Cross, W. I. *J. Chem. Soc., Faraday Trans.* **1998**, *94*, 3019.

(217) Ruamps, R.; Maurice, R.; Batchelor, L.; Boggio-Pasqua, M.; Guillot, R.; Barra, A. L.; Liu, J.; Bendeif, E.-E.; Pillet, S.; Hill, S.; Mallah, T.; Guihéry, N. *J. Am. Chem. Soc.* **2013**.

(218) Rehder, D.; Gailus, H.; Schmidt, H. *Acta Crystallogr C* **1998**, *54*, 1590.

(219) Kimehunt, E.; Spartalian, K.; Derusha, M.; Nunn, C. M.; Carrano, C. J. *Inorg. Chem.* **1989**, *28*, 4392.

(220) *SMART and SAINT*; Siemens Analytical X-ray Instruments Inc. : Madison, WI, 1996.

(221) Sheldrick., G. M. *SADABS: A program for absorption correction with the Bruker SMART system*; University of Göttingen: Germany, 2008.

(222) Sheldrick, G. M. *Acta Crystallogr. Sec. A* **2008**, *64*, 112.

(223) Barbour, L. J. *J. Supramol. Chem.* **2003**, *1*, 189.

(224) Oshiki, T.; Mashima, K.; Kawamura, S.; Tani, K.; Kitaura, K. *Bull. Chem. Soc. Jpn.* **2000**, *73*, 1735.

(225) Clark, R. J. H.; Nyholm, R. S.; Scaife, D. E. *J. Chem. Soc. A* **1966**, 1296.

(226) Cotton, F. A.; Lewis, G. E.; Schwotzer, W. *Inorg. Chem.* **1986**, *25*, 3528.

(227) Neumann, R.; Assael, I. *J. Am. Chem. Soc.* **1989**, *111*, 8410.

(228) Knopp, P.; Wieghardt, K. *Z Naturforsch B* **1991**, *46*, 1077.

(229) Aidoudi, F. H.; Byrne, P. J.; Allan, P. K.; Teat, S. J.; Lightfoot, P.; Morris, R. E. *Dalton Trans.* **2011**, *40*, 4324.

(230) Kime-Hunt, E.; Spartalian, K.; DeRusha, M.; Nunn, C. M.; Carrano, C. J. *Inorg. Chem.* **1989**, *28*, 4392.

(231) Shores, M. P.; Sokol, J. J.; Long, J. R. *J. Am. Chem. Soc.* **2002**, *124*, 2279.

(232) Zadrozny, J. M.; Long, J. R. *J. Am. Chem. Soc.* **2011**, *133*, 20732.

(233) Chen, J. J.; Du, M. L. *Physica B* **1996**, *228*, 409.

(234) Jagner, S. *Acta Chem. Scand. A* **1975**, *29*, 255.

(235) Jagner, S.; Vannerbe.Ng *Acta Chem. Scand.* **1973**, *27*, 3482.

(236) Nelson, K. J.; Miller, J. S. *Inorg. Chem.* **2008**, *47*, 2526.

(237) Petersen, E. *Z. Anorg. Chem.* **1904**, *38*, 342.

(238) Schmid, V.; Linder, R.; Marian, C. M. *Eur. J. Inorg. Chem.* **2006**, 1588.

(239) Verdaguer, M.; Bleuzen, A.; Train, C.; Garde, R.; de Biani, F. F.; Desplanches, C. *Philos. T. Roy. Soc. A* **1999**, *357*, 2959.

(240) Hashimoto, K.; Ohkoshi, S. C. *Philos. T. Roy. Soc. A* **1999**, *357*, 2977.

(241) Freedman, D. E.; Jenkins, D. M.; Long, J. R. *Chem. Commun.* **2009**, 4829.

(242) Leung, W. H.; Che, C. M. *Inorg. Chem.* **1989**, *28*, 4619.

(243) Guo, J. F.; Yeung, W. F.; Lau, P. H.; Wang, X. T.; Gao, S.; Wong, W. T.; Chui, S. S.; Che, C. M.; Wong, W. Y.; Lau, T. C. *Inorg. Chem.* **2010**, *49*, 1607.

(244) Zhang, D.; Zhao, Z.; Chen, K.; Chen, X. *Synth. React. Inorg., Met.-Org., Nano-Met. Chem.* **2012**, *43*, 273.

(245) Albores, P.; Seeman, J.; Rentschler, E. *Dalton Trans.* **2009**, *0*, 7660.

(246) Man, W.-L.; Kwong, H.-K.; Lam, W. W. Y.; Xiang, J.; Wong, T.-W.; Lam, W.-H.; Wong, W.-T.; Peng, S.-M.; Lau, T.-C. *Inorg. Chem.* **2008**, *47*, 5936.

(247) Zhang, Q.; Zhou, H.; Shen, X.; Zhou, H.; Yang, Y. *New J. Chem.* **2013**, *37*, 941.

(248) Zhang, D.; Wang, H.; Chen, Y.; Zhang, L.; Tian, L.; Ni, Z.-H.; Jiang, J. *Dalton Trans.* **2009**, *0*, 9418.

(249) Yeung, W. F.; Lau, P. H.; Lau, T. C.; Wei, H. Y.; Sun, H. L.; Gao, S.; Chen, Z. D.; Wong, W. T. *Inorg. Chem.* **2005**, *44*, 6579.

(250) Guo, J. F.; Wang, X. T.; Wang, B. W.; Xu, G. C.; Gao, S.; Szeto, L.; Wong, W. T.; Wong, W. Y.; Lau, T. C. *Chem.–Eur. J.* **2010**, *16*, 3524.

(251) Lay, P. H.; Yeung, W. F.; Man, W. L.; Lau, T. C.; Wei, H. Y.; Sun, H. L.; Gao, S.; Chen, Z. D.; Wong, W. T. *Abstr. Pap. Am. Chem. Soc.* **2005**, *229*, 144.

(252) Kashiwabara, K.; Katoh, K.; Ohishi, T.; Fujita, J.; Shibata, M. *Bull. Chem. Soc. Jpn.* **1982**, *55*, 149.

(253) Ohishi, T.; Kashiwabara, K.; Fujita, J. *Bull. Chem. Soc. Jpn.* **1983**, *56*, 1553.

(254) Suzuki, T.; Kashiwabara, K.; Kita, M.; Fujita, J.; Kaizaki, S. *Inorg. Chim. Acta* **1998**, *281*, 77.

(255) Toma, L. M.; Toma, L. D.; Delgado, F. S.; Ruiz-Perez, C.; Sletten, J.; Cano, J.; Clemente-Juan, J. M.; Lloret, F.; Julve, M. *Coord. Chem. Rev.* **2006**, *250*, 2176.

(256) Yeung, W. F.; Lau, T. C.; Wang, X. Y.; Gao, S.; Szeto, L.; Wong, W. T. *Inorg. Chem.* **2006**, *45*, 6756.

(257) Chapman, K. W.; Southon, P. D.; Weeks, C. L.; Kepert, C. J. *Chem Commun (Camb)* **2005**, 3322.

(258) Evans, D. F.; Missen, P. H. *J. Chem. Soc., Dalton Trans.* **1987**, 1279.

(259) Seidel, W.; Kreisel, G. *Z. Anorg. Allg. Chem.* **1989**, *577*, 229.

(260) Manzer, L. E. *Inorg. Chem.* **1978**, *17*, 1552.

(261) McAuliffe, C. A.; Nabhan, A.; Pritchard, R. G.; Watkinson, M.; Bermejo, M.; Sousa, A. *Acta Crystallogr. Sect. C: Cryst. Struct. Commun.* **1994**, *C50*, 1676.

(262) Przychodzen, P.; Lewinski, K.; Balanda, M.; Pelka, R.; Rams, M.; Wasiutynski, T.; Guyard-Duhayon, C.; Sieklucka, B. *Inorg. Chem.* **2004**, *43*, 2967.

(263) Gambarotta, S.; Mazzanti, M.; Floriani, C.; Chiesi-Villa, A.; Guastini, C. *Inorg. Chem.* **1986**, *25*, 2308.

(264) J. Bonitatebus Jr, P.; K. Mandal, S. *Chem. Commun.* **1998**, 939.

(265) Nelson, K. J.; Giles, I. D.; Troff, S. A.; Arif, A. M.; Miller, J. S. *Inorg. Chem.* **2006**, *45*, 8922.

(266) Seiden, J. *J. Physique Lett.* **1983**, *44*, 947.

(267) Accorsi, S.; Barra, A.-L.; Caneschi, A.; Chastanet, G.; Cornia, A.; Fabretti, A. C.; Gatteschi, D.; Mortalò, C.; Olivieri, E.; Parenti, F.; Rosa, P.; Sessoli, R.; Sorace, L.; Wernsdorfer, W.; Zobbi, L. *J. Am. Chem. Soc.* **2006**, *128*, 4742.

(268) Bernot, K.; Bogani, L.; Caneschi, A.; Gatteschi, D.; Sessoli, R. *J. Am. Chem. Soc.* **2006**, *128*, 7947.

(269) Kahn, O. *Philos. T. Roy. Soc. A* **1999**, *357*, 3005.

(270) Magnani, N.; Colineau, E.; Eloirdi, R.; Griveau, J. C.; Caciuffo, R.; Cornet, S. M.; May, I.; Sharrad, C. A.; Collison, D.; Winpenny, R. E. P. *Phys. Rev. Lett.* **2010**, *104*.

(271) Lin, P.-H.; Burchell, T. J.; Ungur, L.; Chibotaru, L. F.; Wernsdorfer, W.; Murugesu, M. *Angew. Chem. Int. Ed.* **2009**, *48*, 9489.

(272) Guo, Y.-N.; Xu, G.-F.; Gamez, P.; Zhao, L.; Lin, S.-Y.; Deng, R.; Tang, J.; Zhang, H.-J. *J. Am. Chem. Soc.* **2010**, *132*, 8538.

(273) Rinehart, J. D.; Fang, M.; Evans, W. J.; Long, J. R. *Nat Chem* **2011**, *3*, 538.

(274) Jiang, S.-D.; Wang, B.-W.; Sun, H.-L.; Wang, Z.-M.; Gao, S. *J. Am. Chem. Soc.* **2011**, *133*, 4730.

(275) Watanabe, A.; Yamashita, A.; Nakano, M.; Yamamura, T.; Kajiwara, T. *Chem.–Eur. J.* **2011**, *17*, 7428.

(276) Gonidec, M.; Biagi, R.; Corradini, V.; Moro, F.; De Renzi, V.; del Pennino, U.; Summa, D.; Muccioli, L.; Zannoni, C.; Amabilino, D. B.; Veciana, J. *J. Am. Chem. Soc.* **2011**, *133*, 6603.

(277) Gonidec, M.; Luis, F.; Vilchez, A.; Esquena, J.; Amabilino, D. B.; Veciana, J. *Angew. Chem., Int. Ed.* **2010**, *49*, 1623.

(278) Zhang, P.; Guo, Y.-N.; Tang, J. *Coord. Chem. Rev.* **2013**, *257*, 1728.

(279) Ishikawa, N.; Mizuno, Y.; Takamatsu, S.; Ishikawa, T.; Koshihara, S.-y. *Inorg. Chem.* **2008**, *47*, 10217.

(280) Kozimor, S. A.; Bartlett, B. M.; Rinehart, J. D.; Long, J. R. *J. Am. Chem. Soc.* **2007**, *129*, 10672.

(281) Rinehart, J. D.; Bartlett, B. M.; Kozimor, S. A.; Long, J. R. *Inorg. Chim. Acta* **2008**, *361*, 3534.

(282) Rinehart, J. D.; Fang, M.; Evans, W. J.; Long, J. R. *J. Am. Chem. Soc.* **2011**, *133*, 14236.

(283) Cremades, E.; Gomez-Coca, S.; Aravena, D.; Alvarez, S.; Ruiz, E. *J. Am. Chem. Soc.* **2012**, *134*, 10532.

(284) Abbas, G.; Lan, Y. H.; Kostakis, G.; Anson, C. E.; Powell, A. K. *Inorg. Chim. Acta* **2008**, *361*, 3494.

(285) Rajeshkumar, T.; Rajaraman, G. *Chem. Commun.* **2012**, *48*, 7856.

(286) Rinehart, J. D.; Fang, M.; Evans, W. J.; Long, J. R. *Nature Chem.* **2011**, *3*, 538.

(287) Bernot, K.; Pointillart, F.; Rosa, P.; Etienne, M.; Sessoli, R.; Gatteschi, D. *Chem. Commun.* **2010**, *46*, 6458.

(288) Caneschi, A.; Gatteschi, D.; Sessoli, R.; Rey, P. *Acc. Chem. Res.* **1989**, *22*, 392.

(289) Demir, S.; Zadrozny, J. M.; Nippe, M.; Long, J. R. *J. Am. Chem. Soc.* **2012**, *134*, 18546.

(290) Costes, J. P.; Dahan, F.; Nicodeme, F. *Inorg. Chem.* **2001**, *40*, 5285.

(291) Tang, J. K.; Hewitt, I.; Madhu, N. T.; Chastanet, G.; Wernsdorfer, W.; Anson, C. E.; Benelli, C.; Sessoli, R.; Powell, A. K. *Angew. Chem., Int. Ed.* **2006**, *45*, 1729.

(292) Hewitt, I. J.; Lan, Y. H.; Anson, C. E.; Luzon, J.; Sessoli, R.; Powell, A. K. *Chem. Commun.* **2009**, 6765.

(293) Hewitt, I. J.; Tang, J.; Madhu, N. T.; Anson, C. E.; Lan, Y.; Luzon, J.; Etienne, M.; Sessoli, R.; Powell, A. K. *Angew. Chem., Int. Ed.* **2010**, *49*, 6352.

(294) Lin, S. Y.; Wernsdorfer, W.; Ungur, L.; Powell, A. K.; Guo, Y. N.; Tang, J. K.; Zhao, L.; Chibotaru, L. F.; Zhang, H. J. *Angew. Chem., Int. Ed.* **2012**, *51*, 12767.

(295) Lin, S. Y.; Zhao, L.; Guo, Y. N.; Zhang, P.; Guo, Y.; Tang, J. K. *Inorg. Chem.* **2012**, *51*, 10522.

(296) Xu, G. F.; Gamez, P.; Tang, J. K.; Clerac, R.; Guo, Y. N.; Guo, Y. *Inorg. Chem.* **2012**, *51*, 5693.

(297) Xue, S.; Chen, X.-H.; Zhao, L.; Guo, Y.-N.; Tang, J. *Inorg. Chem.* **2012**, *51*, 13264.

(298) Yang, F.; Yan, P. F.; Li, Q.; Chen, P.; Li, G. M. *Eur. J. Inorg. Chem.* **2012**, 4287.

(299) Blagg, R. J.; Muryn, C. A.; McInnes, E. J. L.; Tuna, F.; Winpenny, R. E. P. *Angew. Chem., Int. Ed.* **2011**, *50*, 6530.

(300) Gamer, M. T.; Lan, Y.; Roesky, P. W.; Powell, A. K.; Clerac, R. *Inorg. Chem.* **2008**, *47*, 6581.

(301) Birk, T.; Pedersen, K. S.; Thuesen, C. A.; Weyhermuller, T.; Schau-Magnussen, M.; Piligkos, S.; Weihe, H.; Mossin, S.; Evangelisti, M.; Bendix, J. *Inorg. Chem.* **2012**, *51*, 5435.

(302) Xiang, H.; Lu, W. G.; Zhang, W. X.; Jiang, L. *Dalton Trans.* **2013**, *42*, 867.

(303) Pointillart, F.; Bernot, K.; Sessoli, R.; Gatteschi, D. *Inorg. Chem.* **2010**, *49*, 4355.

(304) Okazawa, A.; Nojiri, H.; Ishida, T.; Kojima, N. *Polyhedron* **2011**, *30*, 3140.

(305) Cunningham, B. P.; Kautz, J. A. *J. Chem. Crystallogr.* **2000**, *30*, 671.

(306) Figuerola, A.; Diaz, C.; Ribas, J.; Tangoulis, V.; Granell, J.; Lloret, F.; Mahía, J.; Maestro, M. *Inorg. Chem.* **2002**, *42*, 641.

(307) Hulliger, F.; Landolt, M.; Vetsch, H. *J. Solid State Chem.* **1976**, *18*, 283.

(308) Dhers, S.; Sahoo, S.; Costes, J.-P.; Duhayon, C.; Ramasesha, S.; Sutter, J.-P. *CrystEngComm* **2009**, *11*, 2078.

(309) Ma, S.-L.; Ren, S. *J. Inorg. Organomet. Polym. Mater.* **2009**, *19*, 382.

(310) Tanase, S.; Evangelisti, M.; de Jongh, L. J.; Smits, J. M. M.; de Gelder, R. *Inorg. Chim. Acta* **2008**, *361*, 3548.

(311) Ikeda, S.; Hozumi, T.; Hashimoto, K.; Ohkoshi, S.-i. *Dalton Trans.* **2005**, *0*, 2120.

(312) Tanase, S.; de Jongh, L. J.; Prins, F.; Evangelisti, M. *ChemPhysChem* **2008**, *9*, 1975.

(313) Prins, F.; Pasca, E.; de Jongh, L. J.; Kooijman, H.; Spek, A. L.; Tanase, S. *Angew. Chem.* **2007**, *119*, 6193.

(314) Withers, J. R.; Ruschman, C.; Parkin, S.; Holmes, S. M. *Polyhedron* **2005**, *24*, 1845.

(315) Zhao, H.; Lopez, N.; Prosvirin, A.; Chifotides, H. T.; Dunbar, K. R. *Dalton Trans.* **2007**, *0*, 878.

(316) Hozumi, T.; Ohkoshi, S.-i.; Arimoto, Y.; Seino, H.; Mizobe, Y.; Hashimoto, K. *J. Phys. Chem. B* **2003**, *107*, 11571.

(317) Zhou, H.; Diao, G.-W.; Qian, S.-Y.; Yang, X.-Z.; Yuan, A.-H.; Song, Y.; Li, Y.-Z. *Dalton Trans.* **2012**, *41*, 10690.

(318) Tanase, S.; Prins, F.; Smits, J. M. M.; de Gelder, R. *CrystEngComm* **2006**, *8*, 863.

(319) Hulliger, F.; Landolt, M.; Vetsch, H. *J. Solid State Chem.* **1976**, *18*, 307.

(320) Mullica, D. F.; Farmer, J. M.; Cunningham, B. P.; Kautz, J. A. *J. Coord. Chem.* **2000**, *49*, 239.

(321) Kozieł, M.; Pełka, R.; Rams, M.; Nitek, W.; Sieklucka, B. *Inorg. Chem.* **2010**, *49*, 4268.

(322) Sieklucka, B.; Podgajny, R.; Korzeniak, T.; Nowicka, B.; Pinkowicz, D.; Kozieł, M. *Eur. J. Inorg. Chem.* **2011**, *2011*, 305.

(323) Sutter, J.-P.; Dhers, S. b.; Rajamani, R.; Ramasesha, S.; Costes, J.-P.; Duhayon, C.; Vendier, L. *Inorg. Chem.* **2009**, *48*, 5820.

(324) Nowicka, B.; Korzeniak, T.; Stefańczyk, O.; Pinkowicz, D.; Chorąży, S.; Podgajny, R.; Sieklucka, B. *Coord. Chem. Rev.* **2012**, *256*, 1946.

(325) Przychodzen, P.; Lewinski, K.; Pelka, R.; Balanda, M.; Tomala, K.; Sieklucka, B. *Dalton Trans.* **2006**, *0*, 625.

(326) Visinescu, D.; Toma, L. M.; Fabelo, O.; Ruiz-Pérez, C.; Lloret, F.; Julve, M. *Inorg. Chem.* **2013**, *52*, 1525.

(327) Chelebaeva, E.; Larionova, J.; Guari, Y.; Ferreira, R. A. S.; Carlos, L. D.; Paz, F. A. A.; Trifonov, A.; Guérin, C. *Inorg. Chem.* **2009**, *48*, 5983.

(328) Chelebaeva, E.; Larionova, J.; Guari, Y.; Sa Ferreira, R. A.; Carlos, L. D.; Almeida Paz, F. A.; Trifonov, A.; Guerin, C. *Inorg. Chem.* **2008**, *47*, 775.

(329) Long, J.; Chelebaeva, E.; Larionova, J.; Guari, Y.; Ferreira, R. A. S.; Carlos, L. D.; Almeida Paz, F. A.; Trifonov, A.; Guérin, C. *Inorg. Chem.* **2011**, *50*, 9924.

(330) Perrier, M.; Long, J.; Paz, F. A. A.; Guari, Y.; Larionova, J. *Inorg. Chem.* **2012**, *51*, 6425.

(331) Ma, S.-L.; Ren, S.; Ma, Y.; Liao, D.-Z. *J. Chem. Sci. (Bangalore, India)* **2009**, *121*, 421.

(332) Yuan, A.-H.; Southon, P. D.; Price, D. J.; Kepert, C. J.; Zhou, H.; Liu, W.-Y. *Eur. J. Inorg. Chem.* **2010**, *2010*, 3610.

(333) Qian, S.-Y.; Yuan, A.-H. *Acta Crystallogr. Sect. E* **2011**, *67*, m845.

(334) Przychodzeń, P.; Pełka, R.; Lewiński, K.; Supel, J.; Rams, M.; Tomala, K.; Sieklucka, B. *Inorg. Chem.* **2007**, *46*, 8924.

(335) Alexandru, M.-G.; Visinescu, D.; Madalan, A. M.; Lloret, F.; Julve, M.; Andruh, M. *Inorg. Chem.* **2012**, *51*, 4906.

(336) Schelter, E. J.; Bera, J. K.; Bacsa, J.; Galan-Mascaros, J. R.; Dunbar, K. R. *Inorg. Chem.* **2003**, *42*, 4256.

(337) Wang, J.-H.; Yan, P.-F.; Li, G.-M.; Zhang, J.-W.; Chen, P.; Suda, M.; Einaga, Y. *Inorg. Chim. Acta* **2010**, *363*, 3706.

(338) Gao, T.; Yan, P.-F.; Li, G.-M.; Hou, G.-F.; Gao, J.-S. *Inorg. Chim. Acta* **2008**, *361*, 2051.

(339) Kusrini, E. *Inorg. Chim. Acta* **2010**, *363*, 2533.

(340) Chilton, N. F.; Anderson, R. P.; Turner, L. D.; Soncini, A.; Murray, K. S. *J. Comput. Chem.* **2013**.

(341) Borrás-Almenar, J. J.; Clemente-Juan, J. M.; Coronado, E.; Tsukerblat, B. S. *J. Comput. Chem.* **2001**, *22*, 985.

(342) Bartolome, J.; Filoti, G.; Kuncser, V.; Schinteie, G.; Mereacre, V.; Anson, C. E.; Powell, A. K.; Prodius, D.; Turta, C. *Phys. Rev. B* **2009**, *80*.

(343) Goswami, T.; Misra, A. *J. Phys. Chem. A* **2012**, *116*, 5207.